Modulation of optoelectronic properties of layered two-dimensional materials by strain, twist and dielectric engineering

विद्या वाचस्पति की
उपाधि की अपेक्षाओं की आंशिक पूर्ति में प्रस्तुत शोध प्रबंध

A thesis submitted in partial fulfilment of the requirements of the degree of Doctor of Philosophy

द्वारा / By

तमघ्नो चौधरी/ Tamaghna Chowdhury

पंजीकरण सं. / Registration No:
२०१७२०३१/ 20172031

शोध प्रबंध पर्यवेक्षक / Thesis Supervisor:
डॉ. अतीकुर रहमान / Dr. Atikur Rahman

भारतीय विज्ञान शिक्षा एवं अनुसंधान संस्थान पुणे
INDIAN INSTITUTE OF SCIENCE EDUCATION AND RESEARCH PUNE
2024

Dedicated to the memories of my grandparents.....

Certificate

Certified that the work incorporated in the thesis entitled "Modulation of optoelectronic properties of layered two-dimensional materials by strain, twist, and dielectric engineering" submitted by **Tamaghna Chowdhury** was carried out by the candidate, under my supervision. The work presented here or any part of it has not been included in any other thesis submitted previously for the award of any degree or diploma from any other university or institution.

Atikur Rahman

Date: July 29, 2024

(Dr. Atikur Rahman)
Supervisor

Declaration

Name of Student: Tamaghna Chowdhury
Reg. No: 20172031
Thesis Supervisor(s): Dr Atikur Rahman
Department: Physics
Date of joining program: 01.08.2017
Date of Pre-Synopsis Seminar: 20.02.2024

Title of Thesis: **Modulation of optoelectronic properties of layered two-dimensional materials by strain twist and dielectric engineering.**

I declare that this written submission represents my idea in my own words and where others' ideas have been included; I have adequately cited and referenced the original sources. I declare that I have acknowledged collaborative work and discussions wherever such work has been included. I also declare that I have adhered to all principles of academic honesty and integrity and have not misrepresented or fabricated or falsified any idea/data/fact/source in my submission. I understand that violation of the above will be cause for disciplinary action by the Institute and can also evoke penal action from the sources which have thus not been properly cited or from whom proper permission has not been taken when needed.

The work reported in this thesis is the original work done by me under the guidance of **Dr Atikur Rahman.**

Tamaghna Chowdhury

Date: July 29, 2024 (Tamaghna Chowdhury)

Acknowledgements

"The philosophers have only interpreted the world in various ways. The point however is to change it."
- Theses On Feuerbach.

I am deeply thankful for the immense support I received throughout my Integrated MS and PhD program at IISER Pune. To begin with, I wish to express my gratitude to my supervisor, Dr. Atikur Rahman for his guidance and support in last seven years. I deeply appreciate his regard for independent research and his confidence in permitting us to investigate new research questions. I also extend my gratitude to my Commonwealth Split-site supervisor at the University of Manchester, Prof. Artem Mishchenko, for his guidance and support. His passion for fundamental physics research is contagious and has consistently inspired me to put in extra effort. I wish to express my gratitude to Prof. G V Pavan Kumar and Dr. Sreejith G J, members of my research advisory committee, for their continuous support, constructive feedback, invaluable suggestions, and recommendations. Also, Prof. Pavan is a highly valued collaborator who has consistently inspired me to pursue excellence in basic physics research. Working in the condensed matter physics group at the University of Manchester provided me with the inspiring opportunity to closely interact with Sir Andre Geim, Noble Prize winner for the discovery of graphene and Prof. Irina Grigorieva. It was a truly enriching experience to be part of the same research group as them. I also extend my gratitude to Prof. Sandip Ghosh and Mr Dibyasankar Das from TIFR Mumbai, Prof. Kausik Majumdar from IISC Bengaluru, Prof. Goutam Sheet from IISER Mohali, and Prof. Prasenjit Ghosh from IISER Pune for their productive collaborations. I also wish to extend my appreciation to Prof. Andres Castellanos Gomez for hosting me during my visit to his laboratory in ICMM-CSIC, Madrid, Spain. I am also grateful to Dr Shouvik Datta and Dr Ashish Arora from IISER Pune for engaging in numerous scientific discussions.

I wish to express my gratitude to all my colleagues from IISER Pune and the University of Manchester for creating an excellent research atmosphere. Special thanks go to Sagnik Chatterjee for his invaluable assistance with theoretical calculations and for managing all the paperwork required to send samples to me in Manchester. His support was crucial,

and without it, my last research project would not have been successful. I also thank Dr Sumaiya Parveen, Dr Vrinda Narayanan P, Dr Divya Nechiyil, and Dr Ayesha Rahman for their valuable advice and encouragement. I am grateful to Manisha and Sudipta, my fellow lab members, for their support. I express my appreciation to Dr Diptabrata Paul from Prof. G V Pavan Kumar's lab for our productive collaboration that led to the publication of my first research paper. The beginning of the project during the COVID-19 pandemic, while we were both restricted to our homes, highlights the successful results of our collaboration. I want to express my thanks to Dr Qian Yang, Amit Singh, Pablo Diaz Nunez, Ziwei Wang, Mengjie Feng, Stephen Tipper, Bilal Ahmed Gani and Ivan Timokhin for their crucial help in conducting experiments in Manchester.

Beyond the professional domain, the moments spent in IISER Pune Hostel 2 will remain etched in my memory forever. I extend my heartfelt thanks to my friends Arnab Laha, Ratheejit Ghosh, Diptabrata Paul, Abhijit Chatterjee, Roopsali Banerjee, Sagnik Chatterjee, Shubhayan Chakraborty, Arunabha Sen, Amit Bhunia, Jyotirmoy Ganguly, Sanchayita di, Souvik Panda, Swagata, Ishika and Saptashwa Chakraborty. Our engaging discussions on sports, literature, music, and politics are fond memories. The memories of watching together the UEFA Champions League, Copa America 2021 and 2024, Finalissima, FIFA World Cup 2022, and Cricket World Cup 2019, 2023, and 2024 will forever hold a special place in my heart. The emotional roller coaster ride we experienced during those moments is something that I will always cherish. The memories of our monsoon bike rides are unforgettable. Perhaps we should consider writing our own "Motorcycle Diaries". I have learned a great deal from each of you and I appreciate your constant presence and support.

I want to express my thanks to my friends in Manchester - Sudipa Halder, Avishek Basu, Sumanta Laha, Shubhra Kamal Nandi, Amit Singh, Komal Sareen, Konoya di, Sagar da, Soham Pal, James Lourembam and Dipta Sengupta - for their support in helping me adjust to a new place. The times we spent together, watching matches at Old Trafford, Etihad, and Lord's, exploring the UK, and cooking, are moments that I will always hold dear. I am also grateful to my landlords, Martin Hayes Gleave and Steve of Montgomery House, Manchester, UK for their help. I would like to extend my gratitude to my favourite sports teams-the Indian cricket and football teams, Mohun Bagan club, and FC Barcelona- and my favourite athlete, Lionel Messi, for giving me a life outside of academia.

Words fall short in expressing the depth of gratitude I feel for the love and support I have received from family, friends, and teachers. I want to acknowledge the tremendous sacrifices my parents Debjit Chowdhury and Sraboni Chowdhury (Sengupta) have made throughout my life, solely with the aim of ensuring my happiness and well-being. Looking forward, I

am committed to reciprocating and striving to bring them the same level of support and joy in the coming years. Once more, I reflect on how my late grandparents Kantimoy Choudhury, Ranjit Sengupta, Aruna Choudhury and Kalyani Sengupta, to whom I dedicate this thesis, would have been filled with happiness and pride if they were alive today. Their influential role in shaping my life continues to be a source of deep appreciation. I would also like to express my gratitude to my maternal uncle and aunt, Sujit, Bijit Sengupta and Chumki, Rima Sengupta, as well as my paternal aunt, Indrani Sarkar, for their unwavering support.

I extend my gratitude to my school teachers - Mr Shankar Roy, Mr Parthasarathi Panigrahi, Mrs Tapasi Banerjee, Mrs Babita Adhikary, Mr Kasuhik Ghanti, Ujjwal Mukherjee, late BLM Sir (DAV Rupnarayanpur) and Mr Paresh Chandra Banerjee (Chittaranjan High School (Eng. Med.)). Their teaching played a crucial role in inspiring me to pursue a career in basic science. I thank Prof. Debashish Biswas, Prof. Ruma Ray, Prof. Dhruba Banerjee, Prof. Argha Deb, Prof. Tapas Ranjan Midya, Mr Nirmal Kumar Bhattacharya and Mr Swarup Kumar Nandi for their teaching and advice during my B.Sc.(Physics Honours) days in Jadavpur University. I am also grateful to Dr Bijay Agarwalla, Dr Sreejith G. J., Dr Suneeta Vardarajan, Prof. Deepak Dhar and Prof. Sunil Mukhi for their excellent teaching during my MSc (Physics) at IISER Pune. I would like to express my gratitude to my hometown friends from Chittaranjan, namely Anurag Chatterjee, Mahananda Bose, Riddhi Adhikary, Rick Chakraborty, Sk. Ramiz Ahmed, Sumit Roy and Archies Dubey, for their unwavering support. I extend my gratitude to Uttaran Dutta, my senior at Jadavpur University and later a ‘mentor’ in Pune, for his continuous support.

Finally, my sincere gratitude goes to the IISER Pune, the University of Manchester and the Commonwealth Scholarship Commission administrations for their essential assistance and support. I extend my thanks to each of the different fellowship agencies that I have been associated with throughout my PhD. Specifically, I appreciate the support from the Council for Scientific and Industrial Research (CSIR) and the Prime Minister’s Research Fellowship (PMRF) scheme, Ministry of Education, Government of India, for providing research fellowship and funding national and international travel for conference presentations. Additionally, I express my gratitude to the Commonwealth Scholarship Commission, Foreign Commonwealth and Development Office (FCDO), United Kingdom, for fully supporting my one-year stay at the University of Manchester through the Split-site program. I also acknowledge partial funding from The Abdus Salam ICTP for attending a workshop on twistronics in Trieste, Italy.

"...I, the eternal wonder, of the Creator of the universe. The furious Shiva shines on my forehead, like a royal medallion of victory!"
- ‘Bidrohi (The Rebel)’, Kazi Nazrul Islam.

Abstract

Since Sir Andre Geim and Sir Kostya Novoselov successfully isolated graphene in Manchester in 2004, numerous layered two-dimensional (2D) materials have been uncovered. Among these, transition metal dichalcogenides (TMDs) (WS_2, MoS_2) and group-IV monochalcogenides (GeS) have garnered significant attention recently because of their distinctive electrical and optical characteristics. Several external elements, such as the surrounding dielectric medium, mechanical strain, and twisting, can greatly affect these properties. The dielectric medium in the vicinity can impact charge carrier screening and exciton creation, while mechanical strain can be employed to adjust the material's band structure. Alternatively, a moiré pattern may develop when two layers of 2D materials are rotated relative to one another. This twist-induced superlattice can dramatically alter the electronic properties of the material.

This thesis explores the utilization of these external perturbations to uncover novel optoelectronic properties in layered 2D materials. First, the tensile strain-induced brightening of momentum-forbidden 'dark' exciton in monolayer WS_2 by placing them on nanotextured substrates will be discussed. This is shown by photoluminescence and Raman measurements, supported by theoretical calculations. Excitons and trions are quasiparticles that arise due to the interaction of electrons and holes in semiconductors. Further, the modulation of exciton and trion formation in monolayer WS_2 by dielectric and substrate engineering will be discussed. We conducted a systematic investigation of surface defects by progressively increasing the distance between the WS_2 monolayer and the substrate. This approach allowed us to accurately adjust the exciton and trion contributions in the photoluminescence (PL) spectra of WS_2. Additionally, excitation power-dependent measurements on dielectric-engineered and patterned substrates provided insights into the mechanism behind PL modulation in monolayer WS_2. Next, the emergence of ferroelectricity due to a twist in germanium sulfide nanowires will be discussed. GeS is a material with inversion symmetry and therefore ferroelectricity is forbidden. The production of twisted nanowires using low-pressure chemical vapour deposition (LPCVD) will be covered. In this regard, the details for the development of a custom-built LPCVD system will also be discussed. The electrical measurement, piezoelectric force microscopy (PFM), second-harmonic generation

(SHG) spectroscopy, and theoretical results that confirm the presence of unconventional ferroelectricity in twisted GeS nanowires will also be discussed in the thesis.

Furthermore, I will discuss our most recent findings on electronic transport in the graphene-MoS_2 heterostructure and provide an account of an inexpensive, custom-built transfer stage system crucial for fabricating 2D van der Waals heterostructures. The thesis wraps up by highlighting the major experimental findings and suggesting some potential avenues for future research based on these results.

Synopsis

The research detailed in this thesis explores the modulation of optoelectronic characteristics of layered two-dimensional materials through strain, dielectric, and twist engineering. Specifically, the generation of bright exciton, dark exciton, and trion in monolayer TMD, using WS_2 as an example, is examined through dielectric, substrate, and strain engineering. Conversely, the discovery of room-temperature ferroelectricity in twisted germanium sulfide nanowires was achieved through stacking engineering. Thus, this thesis is primarily divided into two sections: Chapters 3 and 4 examine the influence of strain and dielectric on the optical emission (photoluminescence (PL) and Raman) properties of monolayer 2D TMDs, while Chapter 5 explores the impact of symmetry breaking resulting from twisting in germanium sulfide nanowires. Meanwhile, Chapter 2 covers the development of custom-built apparatuses (LPCVD and transfer stage) essential to producing high-quality samples necessary for the previously described studies. Below, we describe the organization of this thesis and offer brief summaries of each chapter.

Chapter 1: Introduction

In Chapter 1, we provide an overview of two-dimensional (2D) layered materials. We provide a concise explanation of the characteristics of 2D layered materials, which serve as the model system for the following chapters of this thesis, namely graphene, transition metal dichalcogenides (TMDs), hexagonal boron nitride (hBN) and group-IV monochalcogenides. We then elaborate on the various types of excitons observed in 2D materials, such as bright excitons, spin-forbidden dark excitons, momentum-forbidden dark excitons, and defect-bound excitons, along with their importance in optical emission. We then discuss three critical techniques-strain, dielectric modification, and twist-employed throughout this thesis to alter the optoelectronic characteristics of 2D layered materials. We provide a concise explanation of how strain and dielectric influence the band structure, which in turn affects the photoluminescence properties of 2D materials. Next, we describe the emergence of unconventional ferroelectricity due to twist which causes symmetry breaking in 2D materials.

Chapter 2: Instrumentation: Synthesis and Transfer

The chapter discusses the synthesis and transfer techniques for one-dimensional (1D) GeS nanowires and two-dimensional (2D) van der Waals heterostructures. Among preparation methods, low-pressure chemical vapour deposition (LPCVD) is noted for its ability to produce high-quality 2D compounds. The study explores the growth of 1D nanowires from 2D GeS using vapour-liquid-solid (VLS) growth in low-pressure chemical vapour deposition (LPCVD), a method that can achieve high yields and control the thickness of the wire. The ability to control the twisting configuration of van der Waals structures is emphasized, as it affects their electrical and optical characteristics. The optimal conditions for growing twisted GeS nanowires are discussed, including the importance of low pressure and a particular range of gas flow rates.

The chapter also explores the setup and components of a home-built LPCVD system used for growing twisted GeS nanowires and a custom-built transfer stage for creating van der Waals heterostructures. The details include the components and step-by-step procedures for both setups, emphasizing the effectiveness, cost-efficiency, and customizability of these home-built systems compared to commercial setups. In conclusion, the chapter outlines the successful development and application of these home-built systems in synthesizing twisted GeS nanowires and fabricating vdWHs.

Chapter 3: Brightening of dark excitons in WS_2 via tensile strain-induced excitonic valley convergence

In this chapter, the experimental observation of momentum-forbidden $K\Lambda$ dark excitons was reported by placing monolayer (ML) WS_2 on top of nanotextured substrates, which imparts tensile strain, modifying its electronic band-structure. Temperature-dependent photoluminescence (PL) and Raman measurements on the strained and unstrained were performed on ML WS_2 samples. For calculating electronic bandstructure, the lattice structure was relaxed using ultrasoft pseudopotential with Perdew-Burke-Ernzerhof (PBE) exchange-correlation functionals alongside plane waves implemented in the QUANTUM ESPRESSO package. The brightening of the dark exciton is described well by the strong exciton-phonon coupling observed in our PL and Raman experiments supported by our theoretical calculations. In addition to offering a tuning knob for light-matter interactions in two-dimensional materials, our results pave the way to designing ultrasensitive strain-sensing devices based on TMDs.

Chapter 4: Modulation of trion and exciton formation in monolayer WS_2 by dielectric and substrate engineering

This chapter discusses the influence of the dielectric environment (hBN, SiO_2/Si and air) on the PL of TMD monolayers, in this case, WS_2. The PL spectra of monolayer WS_2 are

mainly dominated by free carrier and excitonic recombination. The effect of substrate defects on the PL of TMDs has been investigated by varying the excitation laser power in each of these cases. We have also studied the influence of the nature of the charge carried by substrate defects on PL. Our study reveals that suspending and inserting an hBN layer has two distinct effects on the ratio of exciton and trion intensity with increasing excitation power. Our findings will have a profound impact on tailoring single-photon emission processes from the defects of 2D materials and fabricating excitons and valleytronic devices.

Chapter 5: Stacking engineered room temperature ferroelectricity in twisted GeS nanowires

In this chapter, experimental observation of ferroelectric order at room temperature by introducing Eshelby twist in Germanium sulfide (GeS) nanowires is discussed. The twisted GeS nanowires were synthesized by the low-pressure chemical vapour deposition (LPCVD) technique using gold as the catalyst. Raman scattering, powder X-ray diffraction (PXRD), transmission electron microscopy (TEM), selected area electron diffraction (SAED), and energy dispersive X-ray analysis (EDS) were performed to confirm the chemical composition and crystallinity of the twisted nanowire. Electrical studies (I-V characteristics and gate dependence), piezoresponse force microscopy (PFM), and second harmonic generation spectroscopy (SHG) measurements were performed on these twisted nanowires to show the emergence of ferroelectricity and broken inversion symmetry, respectively. Our experimental observations are further supported by density functional theory (DFT) calculations which showed that the inversion symmetry is broken because of the twist in the GeS nanowire system.

Chapter 6: Conclusions and future directions

In this chapter, we wrap up the thesis with a succinct summary of the presented works and their future perspectives, both fundamentally and technologically. Additionally, we showcase preliminary findings on electronic transport studies of graphene-MoS_2 heterostructures, including optical spectroscopy, photoresponse investigation, and photocurrent spectroscopy. These experiments aim to reveal the mechanisms of charge and energy transfer and the impact of graphene on band nesting in monolayer TMDs.

List of Publications

This thesis comprises publications numbered 1, 2, 3, 4, and 5 from the list below, with publications 6 and 7 being excluded. * = Corresponding author, † = equal contribution.

1. **Tamaghna Chowdhury**† , Diptabrata Paul† , Divya Nechiyil, Gokul M.A., Kenji Watanabe, Takashi Taniguchi, G. V. Pavan Kumar and Atikur Rahman*, *Modulation of exciton and trion formation in WS_2 by dielectric and substrate engineering.*
   2D Materials, 8, 045032 (2021).

2. **Tamaghna Chowdhury**, Chetna Taneja, Aastha Vasdev, Prasenjit Ghosh, Goutam Sheet, G.V. Pavan Kumar and Atikur Rahman*, *Stacking Engineered Room temperature ferroelectricity in twisted Germanium sulfide.*
   Advanced Electronic Materials, 8, 2101158 (2022).

3. **Tamaghna Chowdhury***, Sagnik Chatterjee, Dibyasankar Das, Ivan Timokhin, Pablo Díaz Núñez, Gokul M.A., Suman Chatterjee, Kausik Majumdar, Prasenjit Ghosh, Artem Mishchenko*, and Atikur Rahman*, *Brightening of Dark Excitons in WS_2 via Tensile Strain-Induced Excitonic Valley Convergence*.
   Physical Review B (Letter), 110, L081405 (2024).

4. **Tamaghna Chowdhury**, Sudipta Majumder, Sagnik Chatterjee, and Atikur Rahman, *Effect of charge and energy transfer in Graphene-MoS_2 interface on electrical mobility and photoresponse*, **manuscript under preparation (2024)**.

5. **Tamaghna Chowdhury**, Sagnik Chatterjee, Ivan Timokhin, Pablo Díaz Núñez, Gokul M.A., Artem Mishchenko, and Atikur Rahman, *Understanding the effect of dielectric environment on the optical properties of monolayer WS_2 though low-temperature Raman and PL spectroscopy,* **manuscript under preparation (2024)**.

6. Vrinda Narayanan P, Gokul M. A., **Tamaghna Chowdhury**, Chandan Singh, Mukul Kabir, Takashi Taniguchi, Kenji Watanabe and Atikur Rahman, *Giant enhancement of photoresponse through dielectric engineering in mixed dimensional van der Waals heterostructure.*
   Advanced Materials Interfaces, 9, 2102054 (2022).

7. Sagnik Chatterjee[†,*], **Tamaghna Chowdhury**[†,*], Pablo Díaz Núñez, Nicholas Kay, Manisha Rajput, Sooyeon Hwang, Ivan Timokhin, Prasenjit Ghosh, Artem Mishchenko, and Atikur Rahman[*]. *Effects of Reduced Interlayer Interactions on the K-point Excitons of MoS_2 Nanoscrolls*,
arXiv:2404.12250 (2024). (submitted, under review)

Selected Conferences/ workshop presentations:

1. *Stacking engineered room temperature ferroelectricity in twisted germanium sulfide nanowires*, **Tamaghna Chowdhury (presenting author)**, Workshop on Twistronics and Moire Materials: Bridging Theory and Experiments, The Abdus Salam Centre for Theoretical Physics(ICTP), Trieste, Italy, January 2024. **(poster presentation)**

2. *Tensile strain induced brightening of momentum forbidden dark excitons in monolayer WS_2*, **Tamaghna Chowdhury (presenting author)**, Recent Progress in Graphene and 2D Materials Research (RPGR), Bengaluru, India, November, 2023.
(contributed talk)

3. *Modulation of dark excitons in WS_2 by substrate engineering.*, **Tamaghna Chowdhury (presenting author)**, 2D Transition Metal Dichalcogenides Conference, Churchill College, University of Cambridge, UK, June 2023. **(poster presentation)**

4. *Growth and characterization of twisted Germanium sulfide nanostructures.*, **Tamaghna Chowdhury (presenting author)**, International Conference on Nano science and Technology (ICONSAT), Kolkata, India, March 2020. **(poster presentation)**

Contents

Chapter 1

Introduction

Graphene research has experienced rapid development in recent years, evolving into a well-developed discipline that intersects materials science, solid-state physics, and engineering [1–4]. This remarkable progress has ignited a burgeoning interest in a broad range of two-dimensional materials (2DMs) that exhibit varied electronic characteristics[5, 6]. Graphene, with its extraordinary attributes, has emerged as an exceptional framework for exploring nanoscale physics and for developing an advanced generation of electronics characterized by their ultrathin structure, flexibility and high speed. However, graphene also presents several challenges that have yet to be fully addressed [1–4].

In contrast to graphene's limitations, other 2DMs offer enhanced versatility, encompassing a range of semiconductors, conductors with varying bandgaps (such as WS_2, and MoS_2), and insulators like hexagonal boron nitride (hBN). This vast collection of 2DMs, each with adjustable material features, paves the way for heterogeneous integration at the nanometer scale (see Figure 1.1). Such integration can result in newly formed hybrid compositions that exhibit entirely new physics and facilitate novel capabilities[4].

Normally, a monolayer of a 2DM consists of a covalently bonded lattice that is only one or a few atoms thick. In contrast to conventional nanostructures, which have dangling bonds and surface trap states, these atomic sheets free from dangling bonds frequently exhibit outstanding electronic and optical characteristics. Moreover, the completely saturated bonds on their surfaces indicate that interactions among adjacent layers of 2DMs are primarily governed by van der Waals forces. The lack of covalent bonds enables the combination of significantly different materials without the limitations of crystal lattice mismatch, offering substantial flexibility in merging 2DMs with diverse nanoscale materials[4].

Combining 2DMs to form various van der Waals heterostructures (vdWHs) has unlocked new functions and applications that were not achievable before. Early attempts at combining vdWHs with other nanomaterials primarily concentrated on combining 2DLMs with zero-dimensional (0D) and one-dimensional (1D) nanostructures[7–10]. For instance, the integration with 0D nanomaterials, such as quantum dots and plasmonic nanoparticles, has led to the development of remarkable devices like high-speed broadband photodetectors[8].

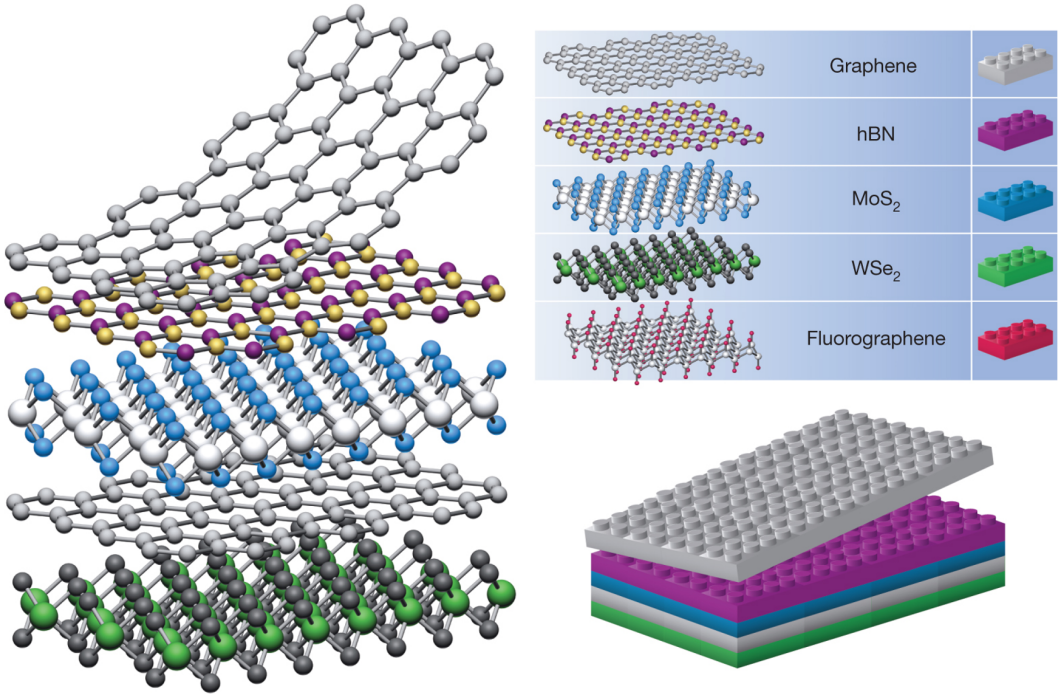

FIGURE 1.1: Assembling vdWHs can be likened to assembling Lego blocks. Each 2D crystal acts as a Lego piece, enabling the construction of a vast array of layered structures. This atomic-scale Lego conceptually resembles molecular beam epitaxy but follows different construction principles and utilizes a distinct set of materials. Adapted with permission from [6].

Similarly, 1D nanostructures, including nanowires and nanoribbons, have been combined with 2DLMs to create a new class of ultra-thin transistors characterized by remarkable speed and adaptability[9, 10].

The innovative 1D-2D and 0D-2D vdWHs represent a significant advancement in nano-scale material integration, enabling the creation of devices with remarkable performance characteristics. More recently, the focus has shifted towards the vertical stacking of different 2DMs to create 2D-2D heterostructures and moiré heterostructures. Such 2D-2D heterostructures offer exciting possibilities to regulate and manage the production, confinement, and movement of charge carriers, excitons, photons, and phonons on an atomic level, thus enabling the creation of specialized devices with improved features[4, 11].

Semiconductor nanowires have typically been created using standard three-dimensional (3D) crystalline materials. In contrast, layered crystals, which are made up of sheets bonded covalently and held by the weaker van der Waals forces, constitute an innovative class of

materials that exhibit properties absent in 3D crystals. Forming nanowires from these layered materials has the potential to reveal novel structural and optoelectronic features [12–15].

The realization of this vision is achieved through the synthesis and emergent characteristics of vdW nanowires derived from layered crystals, integrating vapour-liquid-solid (VLS) growth alongside van der Waals epitaxy. An illustration of this is the conversion of germanium (II) sulfide (GeS), a 2D/layered chalcogenide semiconductor with an anisotropic structure, into nanowires via the VLS process. These van der Waals nanowires crystallize with layers oriented along the wire axis and demonstrate bright, size-dependent band-edge luminescence. The tendency of these nanowires to form screw dislocations, a feature commonly observed in layered crystals, imparts remarkable properties absent in 3D-crystalline nanowires.

A notable feature is the Eshelby twist, caused by the torque applied to the ends of a cylindrical solid due to the axial dislocation stress field. This creates a chiral configuration in the layered nanowires, forming spontaneous and size-adjustable twist moiré patterns between the van der Waals layers along the wires. Custom growth protocols facilitate the formation of intricate structures unattainable in planar van der Waals stacks, such as homojunction connecting twisted (dislocated) and regular layered (dislocation-free) segments, along with a smooth transition of helical moiré patterns driven by a continuously variable Eshelby twist[12, 13].

1.1 Two dimensional layered materials

1.1.1 Graphene

Graphene, composed of a single layer of carbon atoms bonded covalently in a honeycomb structure, demonstrates an impressive range of excellent physical properties, such as extraordinary mechanical strength and superior electrical conductivity. Particularly, graphene's charge carriers, in its nature as a zero-bandgap semi-metal, possess very high mobility, rendering it a highly conductive two-dimensional material (2DM) and a crucial element in diverse vdWHs[4, 16].

Graphene's one-atom-thick structure and nonzero density of states provide partial optical and electrostatic transparency along with an adjustable work function, making it a distinctive component for vdWH devices (see Fig. 1.2). Bernal-stacked AB bilayer graphene represents the most basic homogeneous vdWHs. It has distinct properties, such as four pseudospin flavors, and enables a bandgap to be induced by a vertical electric field. In contrast, misaligned

(non-Bernal) graphene layers act similarly to individual monolayers, highlighting the subtle nature of interlayer interactions depending on their stacking orientation[4, 17].

In summary, graphene's exceptional properties and its role in vdWHs have significantly advanced the field of nanotechnology, leading to innovative device architectures and applications. The ongoing exploration of vdWH integration strategies promises to unlock new functionalities and enhance the performance of nanoscale devices, further expanding the potential of this dynamic field[18].

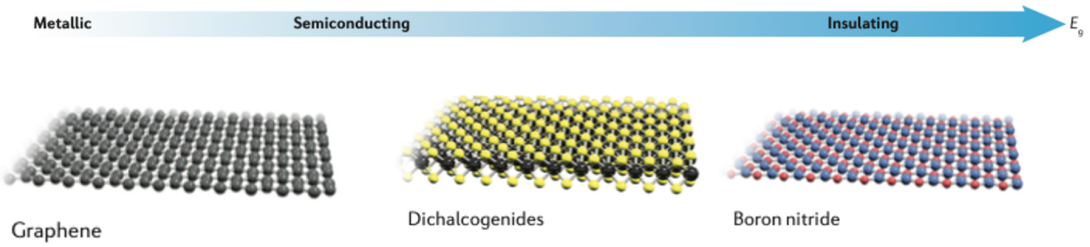

FIGURE 1.2: A wide range of 2DMs demonstrates different chemical compositions, atomic structures, and electronic characteristics, with bandgaps that increase progressively from left to right. Adapted with permission from [4].

1.1.2 Transition metal dichalcogenides

Transition metal dichalcogenides (TMDs) set themselves apart from semi-metallic graphene and insulating hBN by offering a wide range of layered materials with tunable electronic properties and varying bandgaps. TMDs, denoted by the chemical formula MX_2 (where M denotes a transition metal, usually molybdenum or tungsten, and X signifies a chalcogenide such as sulfur, selenium, or tellurium), can be sourced from both natural minerals and fabricated bulk crystals, or created through chemical vapour deposition (CVD) methods (see Figure 1.2)[19, 20].

Besides molybdenum and tungsten, other metals such as rhenium, zirconium, tantalum, hafnium etc., along with non-transition metals like gallium, tin, and bismuth, can form stable TMDs. Well-studied TMDs, including MoS_2, $MoSe_2$, WS_2, and WSe_2, show a bandgap that changes from indirect in their bulk form to direct in monolayers. These materials also exhibit noteworthy features such as valley polarization, lattice symmetry-induced valley Hall effect, and superconductivity. Generally, TMDs have bandgaps ranging from approximately 1 to 2 eV and exhibit carrier mobility around 100 $cm^2V^{-1}s^{-1}$ at room temperature[4, 5].

The exploration of TMDs within vdWHs and their integration with other 2D materials like graphene and BN herald new possibilities for advanced device architectures and functionalities. Understanding the diverse electronic properties and potential applications of TMDs is crucial for pushing the boundaries of nanotechnology and developing next-generation electronic devices[4].

1.1.3 Hexagonal boron nitride

hBN, commonly known as white graphite, is very similar to graphite. It has a similar honeycomb structure in which boron and nitrogen atoms replace each carbon atom pair in the unit cell, forming a wide-band gap insulator. Bulk hBN crystals, akin to graphite, can be exfoliated into one or several atomic layers. These layers are extensively researched for various uses, such as flat insulating substrates, encapsulation materials, atomically thin tunnelling barriers, and defect-free dielectrics. Moreover, the combination of nitrogen, carbon and boron enables the formation of doped or alloyed layers with tunable electronic characteristics, facilitating bandgap engineering and the implementation of both p-type and n-type doping. This adaptability makes hBN a significant material in the creation of advanced nanodevices and heterostructures, where it can enhance performance and functionality (see Figure1.2)[4, 11, 21–23].

1.1.4 Group-IV monochalcogenide

Graphene, hBN, and TMDs are ideal materials for creating vertical van der Waals stacks and growing lateral heterostructures. This versatility arises from the ease of monolayer growth and isolation, their straightforward polymorphism, and their fixed stoichiometry (e.g., MX_2). However, layered crystals that differ from these properties offer new opportunities for unconventional heterostructures. A notable example includes group IV monochalcogenide semiconductors, capable of creating different layered phases with diverse amounts of chalcogen. As an example, tin sulfides have multiple phases: SnS_2, Sn_2S_3, and SnS, each with unique properties. SnS_2 has a trigonal layered structure and demonstrates high carrier mobility in field-effect transistors, along with a potential role as a photocatalyst. Monochalcogenides such as GeS (MX, M= Sn, Ge; X: S, Se) are orthorhombic crystals with anisotropic transport properties, valleytronics and optoelectronic applications. Additionally, they exhibit outstanding characteristics such as in-plane ferroelectricity. These characteristics make them promising for various state-of-the-art applications [24].

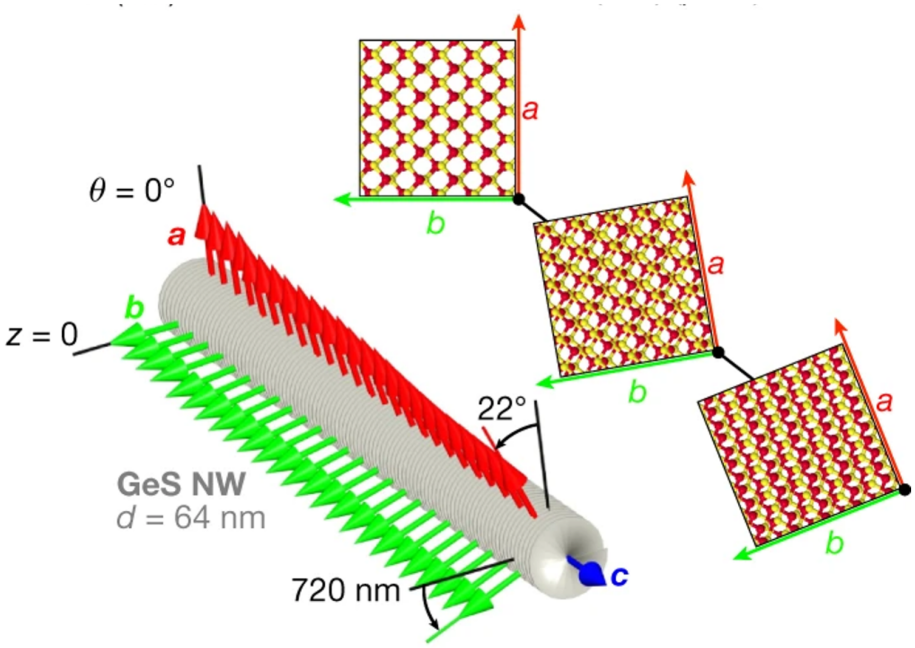

FIGURE 1.3: An illustration showing how the moiré registry changes along chiral GeS nanowires and how the (a, b) crystal axes rotate. Adapted with permission from [13].

Group IV monochalcogenides and their related alloys with similar structures offer additional pathways for creating heterostructures. Because of their open architecture and increased surface activity, compounds like SnS usually form thicker multilayer crystals (surpassing 50 nm, or roughly 100 layers and above). These structures, exhibiting {110} vertical side facets, can act as nucleation sites for the lateral growth of another monochalcogenide (e.g., GeS), creating lateral heterostructures akin to those formed with 2D TMDs. These heterostructures possess well-defined, atomically bonded lateral interfaces that span multiple vdW layers. Another exciting frontier involves transforming 2D/layered crystals into a three-dimensional form by utilizing lattice mismatch between different monochalcogenides. $Ge_{1-x}Sn_xS$ alloy nanoribbons, which have edges containing a high concentration of SnS, endure compressive stress along the edges that generates managed axial twisting. The distinct structure, characterized by a seamless shift from flat to vertical alignment and the ability to sustain propagating polariton modes, renders these 3D nanoribbons highly suitable for applications in energy and information transmission [13, 24].

Adjustable and stable minor interlayer rotation angles can be achieved by departing from

a planar geometry. Within van der Waals nanowires featuring axial screw dislocations, Eshelby twists form chiral growth spirals, and the interlayer twist angle can be adjusted by changing the radius R of the wire (with b representing the Burgers vector). In VLS nanowire synthesis, the radius R is determined by the dimensions of the growth catalyst, allowing precise adjustment through the selection of nanocatalysts composed of metal particles (see Figure 1.3). In the case of twisted GeS van der Waals nanowires, the radius R spans from greater than 100 nm to nearly 7.5 nm, translating into interlayer twists from below 0.002°to 0.32°for a Burgers vector corresponding to a single unit cell. This approach for attaining precisely controllable interlayer twists showcases several distinctive characteristics: minor interlayer twists are supported by the presence of the screw dislocation; the ensuing twist is cast onto a helicoid surface instead of a flat plane. Moreover, this distinctive geometry facilitates continuously adjustable interlayer twists and twist homojunction, which is unattainable in planar configurations[12, 14].

1.2 Excitons in layered semiconductors

TMDs and vdWHs represent a novel paradigm for the study of fundamental exciton physics. The combination of reduced dielectric screening and pronounced spatial confinement (see figure 1.4) in these materials leads to an exceptionally strong Coulomb interaction, which gives rise to a variety of many-body effects. This includes the generation of various forms of excitons, like optically permitted excitons and non-radiative dark excitons, as well as interlayer exciton states with spatial separation. These excitonic states exhibit binding energies of $\simeq 0.5$ eV which is significantly higher than those found in traditional materials such as GaAs, ranging from ten to a hundred times larger. As a result, excitonic characteristics in TMDs persist at room temperature, significantly influencing both the non-equilibrium dynamics of these materials and the optical response. Additionally, other quasiparticles, including biexcitons and trions, have been also detected in monolayer TMDs[25].

The field of TMD exciton physics gained significant momentum when K. F. Mak et al. [19] demonstrated that MoS_2 shifts from being an indirect bandgap semiconductor in bulk form to being a direct bandgap semiconductor in monolayer form. This transition leads to a significantly increased photoluminescence (PL)[25–28].

The TMD PL/absorption shows the presence of two prominent resonances known as A and B excitons. These resonances are the result of spin-orbit coupling in these materials with heavy transition metal atoms, which lifts the spin degeneracy of both the conduction and valence bands. Although splitting in the conduction band due to spin-orbit coupling is relatively small, the separation in the valence band is $\simeq 200$ meV in Mo-based TMDs and up to 400 meV in W-based TMDs. Consequently, two distinct optical transitions are possible,

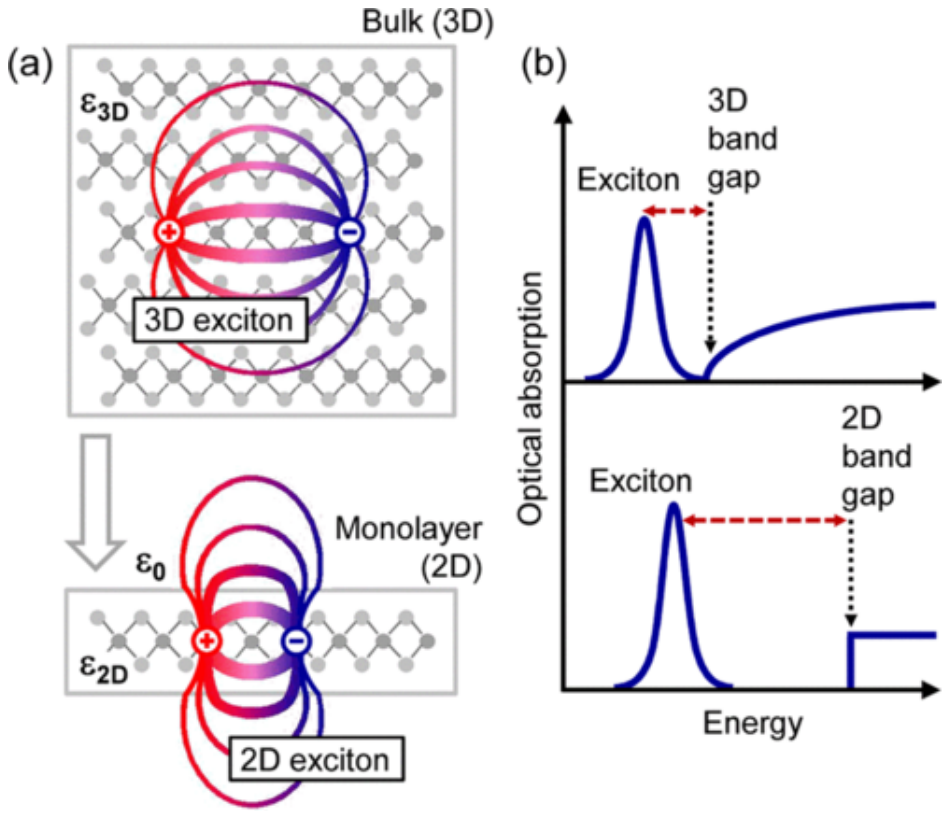

FIGURE 1.4: (a) Spatial depiction of electrons and holes forming excitons in the three-dimensional bulk material and a nearly two-dimensional monolayer. The variations in the dielectric environment are symbolically represented by distinct dielectric constants ϵ_{3D} and ϵ_{2D} as well as the vacuum permittivity ϵ_0. (b) Schematic representation of how dimensionality affects electronic and excitonic properties through optical absorption. The change from 3D to 2D is anticipated to result in a rise in both the band gap and the exciton binding energy (shown by the dashed red line). For simplicity, the excited excitonic states and Coulomb corrections for continuous absorption have been excluded. Adapted with permission from [29].

involving holes in the upper and lower energy spin valence bands. This unique interplay of spin, orbit, and layer degrees of freedom in TMDs offers rich opportunities for exploring new physical phenomena and potential applications in optoelectronic devices[25, 30, 31].

1.2.1 Exciton binding energy

Several experimental methods allow for the determination of the excitonic binding energy E_b, defined as the difference in energy between the renormalized free-particle bandgap E_0 and the absolute value of the exciton transition energy E_X. E_0 is measured by scanning tunnelling spectroscopy (STS), and E_X is measured by PL measurements. Their difference gives an E_b of 0.55 eV for monolayer $MoSe_2$. The E_b of the exciton ground state is also estimated to be $\simeq$ 0.3 eV for monolayer WS_2 placed on top of a SiO_2 substrate[29, 32, 33].

In TMDs, excitons differ substantially from the hydrogen Rydberg series. This is because of the nonlocal dielectric screening as a result of the heterogeneous dielectric environment surrounding the TMDs. E_b can also be extracted using one- and two-photon spectroscopy, which addresses s-type and p-type excitonic states, and states respectively. From these experiments, E_b was estimated to be $\simeq$ 0.55 eV for monolayer $MoSe_2$ placed on top of graphene and 0.37 eV for WSe_2 on SiO_2/ Si substrate [25, 34].

Recent research has shown that the E_b can be modified by hundreds of meV by manipulating the dielectric environment. It is possible to create in-plane dielectric heterostructures with spatially dependent E_b. Strain can also be utilized to influence the optical characteristics of 2DMs. It is also shown that excitonic resonances change dramatically towards lower energy when subjected to tensile strain, according to studies. This shift is predominantly caused by a decrease in the electronic band gap, while the E_b varies relatively little [25, 35].

1.2.2 Dark exciton

In addition to bright excitons, understanding the optical characteristics and dynamics of TMDs relies heavily on the optically inaccessible dark excitonic states (see Figure 1.5). These dark excitons can be categorized into spin-forbidden and momentum-forbidden excitons. Their existence has been indirectly demonstrated through temperature-dependent PL experiments, which show an increase in the PL intensity with an increase in the temperature in W-based TMDs. The presence of dark excitons, which have a lower energy level than bright excitons, can explain this behaviour. At reduced temperatures, the majority of excitons settle into these dark states, which notably diminishes the light emission efficiency. As the temperature rises, the excitons tend to occupy the higher-energy bright exciton states within the light cone, resulting in an increase in photoluminescence [31, 36–39].

1.2.2.1 Spin-forbidden dark exciton

In TMDs derived from Mo and W, the spin-orbit coupling that removes the spin degeneracy of the conduction band exhibits unique features (refer to Figure 1.5). As a result, in $MoSe_2$ and MoS_2, the bright excitons are the lowest energy states. However, in W-based TMDs, the spin-forbidden dark excitons are the energetically lowest. This observation is consistent with the temperature-dependent PL experiment. For the first time, low-temperature magneto-PL studies under high magnetic fields showcased the brightening of these states. The dark excitons in the magneto-PL spectra of W-based TMDs are distinctly visible as peaks, approximately 50 meV lower than the bright exciton[25, 40–42].

An alternative approach has been used to activate spin-forbidden dark excitonic states by coupling to surface plasmons. Dark excitons possess dipole moment perpendicular to the plane of the material; therefore, they can couple to the surface plasmons[25, 43].

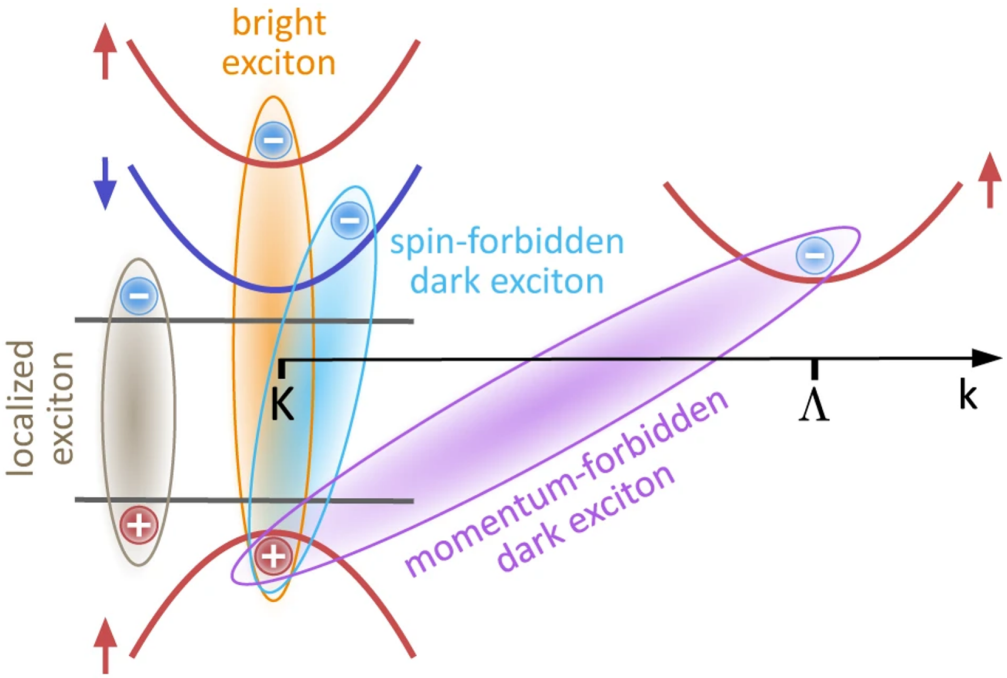

FIGURE 1.5: In monolayer TMDs and their heterostructures, different types of excitons can be found. Excitons are electron-hole pairs bound by Coulomb forces (depicted as ovals). Momentum-forbidden dark excitons involve electrons and holes situated in different valleys within momentum space, making them inaccessible to light due to the absence of necessary momentum transfer. Spin-forbidden dark excitons are made up of holes and electrons with opposite spins, which light cannot access because of the lack of spin-flip. Localized excitons are formed when holes and electrons are trapped in impurity-induced potentials. Adapted with permission from [25].

1.2.2.2 Momentum-forbidden dark exciton

Significant scattering channels for exciton-phonon interactions are presented by intervalley dark excitons. The dark $K\Lambda$ excitons, which are thought to constitute the energetically lowest ground state in tungsten-based TMDs, are of particular interest. These excitons have an electron at the Λ valley and a hole at the K valley (see Figure 1.5). A recent STS study shows that the Λ valley is $\simeq$ 80 meV below the K valley in monolayer WSe_2. Furthermore, for

MoS_2 and WSe_2, strain-dependent PL measurements, which assess relative spectral changes between the K and Λ valleys, exhibit opposite behavior[37].

Recent work shows that in W-based TMDs, scattering of optical and acoustic phonons into $K\Lambda$ exciton states leads to considerable linewidth broadening of bright excitons, even at low temperatures. The strain can also regulate the linewidth of excitons in TMDs. The A exciton linewidth significantly narrows with strain and becomes more symmetric for materials based on Se, but it does not change for WS_2 and increases for MoS_2. Exciton-phonon scattering alterations brought on by strain are the cause of these effects[25].

Furthermore, recent PL measurements have shown evidence of radiative recombination paths to momentum-forbidden states aided by phonons. The activation of these excitons in the presence of high-dipole molecules is predicted by theoretical work. A novel exciton brightening by effective exciton-molecule coupling may be used for dark-exciton-based molecule identification.[44, 45]

Ultimately, the experimental detection of momentum-forbidden dark states can be achieved by examining the intra-excitonic 1s-2p transition. Examining the optical response immediately following optical excitation and subsequent to exciton thermalization has both experimentally and theoretically confirmed the transition of bright exciton populations into the lowest energy momentum-forbidden dark excitonic states in monolayer WSe_2[36, 38, 46].

1.2.3 Defect-bound exciton

In TMDs, impurities may cause electrons and holes to be captured in potential wells, resulting in localized excitons. The vivid 1s exciton transitions are represented by a large peak in the PL spectra of TMDs at room temperature. At lower temperatures, beneath the bright 1s excitons, numerous additional spectral resonances appear due to the confinement of free excitons in local potential wells. As the temperature increases and the thermal energy exceeds the trapping potential, excitons previously confined in local potential wells are released, leading to the disappearance of the narrow spectral lines at the lower energy end[25, 47].

It has recently been demonstrated that the prominent single-photon emission from TMD monolayers is caused by these localized excitons[48, 49].

1.3 Strain engineering in layered materials

Strain is a key factor in controlling the electrical and optical properties of TMDCs, as evidenced by recent theoretical and experimental studies. Compared to conventional semiconductors, TMDCs have a remarkable mechanical strength that enables the application of large strains to modify their band structures. According to atomic force microscopy (AFM)

studies and density functional theory (DFT) calculations, the fracture stress of suspended monolayer MoS_2 is $\simeq$ one-eighth of its Young's modulus. Notably, bulk silicon usually fractures at strains of 1.5% or less, but MoS_2 monolayers have a maximum strain at fracture surpassing 10%[50–54].

Large-scale applications of macroscopically homogeneous strains are possible, whereas, at the nanoscale, inhomogeneous strains provide a way to form spatially variable band structures within 2D TMDCs. Localized strain variations, for instance, are produced by wrinkles in MoS_2[55].

The remarkable strain tolerance exhibited by 2D TMDCs offers a viable method for continuously adjusting their electrical and optical characteristics, spurring the rapid advancement of research into strain-induced modifications-based optoelectronic devices. Numerous theoretical studies and experimental investigations have shown how strain alters the optoelectronic properties of 2D materials. For instance, in monolayer MoS_2, a biaxial tensile strain of 10-15% can result in a semiconductor-to-metal phase change, while a uniaxial strain of about 2% can trigger a direct-to-indirect bandgap transition[56–59].

Raman spectroscopy is widely used to determine the structure of TMDCs by examining the interlayer van der Waals interactions, electron-phonon interactions, and long-range Coulomb interactions between atoms. As an illustration, the shifts in the Raman peaks corresponding to the A_{1g} (out-of-plane) and E^1_{2g} (in-plane) modes show how sensitive the phonon spectra of TMDCs are to applied strain[60, 61].

Therefore, strain engineering is essential for improving our knowledge of the optical and electrical characteristics of 2D materials and their possible uses in devices[55].

1.3.1 PL of layered materials under strain

Various spectroscopic studies have shown the potential of TMDCs as a great platform for continuously modifying electronic band structures and optical properties through applied strain (see Figure 1.6a). For example, under tensile strain, the peak positions in the absorption and photoluminescence spectra of 2D TMDCs show a linear redshift for both A and B excitons (see Figure 1.6b). Redshift rates in the monolayer MoS_2 absorption spectrum are -68 ± 5 meV/% for the B exciton and -64 ± 5 meV/% for the A exciton (see Figure 1.6c). Monolayer WSe_2 exhibits redshift rates of -50 ± 3 and -54 ± 2 meV/% for the B and A excitons, respectively. Furthermore, redshift rates of -45 ± 7 meV/% for the A exciton in MoS_2 monolayers, -53 ± 10 meV/% for the A exciton, and 129 ± 20 meV/% for the indirect bandgap in MoS_2 bilayers are observed for the PL spectral peaks in relation to tensile strain(see Figure 1.6d and f)[50, 62–64].

Beyond the observed redshift, large strains can induce a transition between direct and indirect bandgaps in TMDCs. For example, an indirect peak appears in WS_2 monolayers

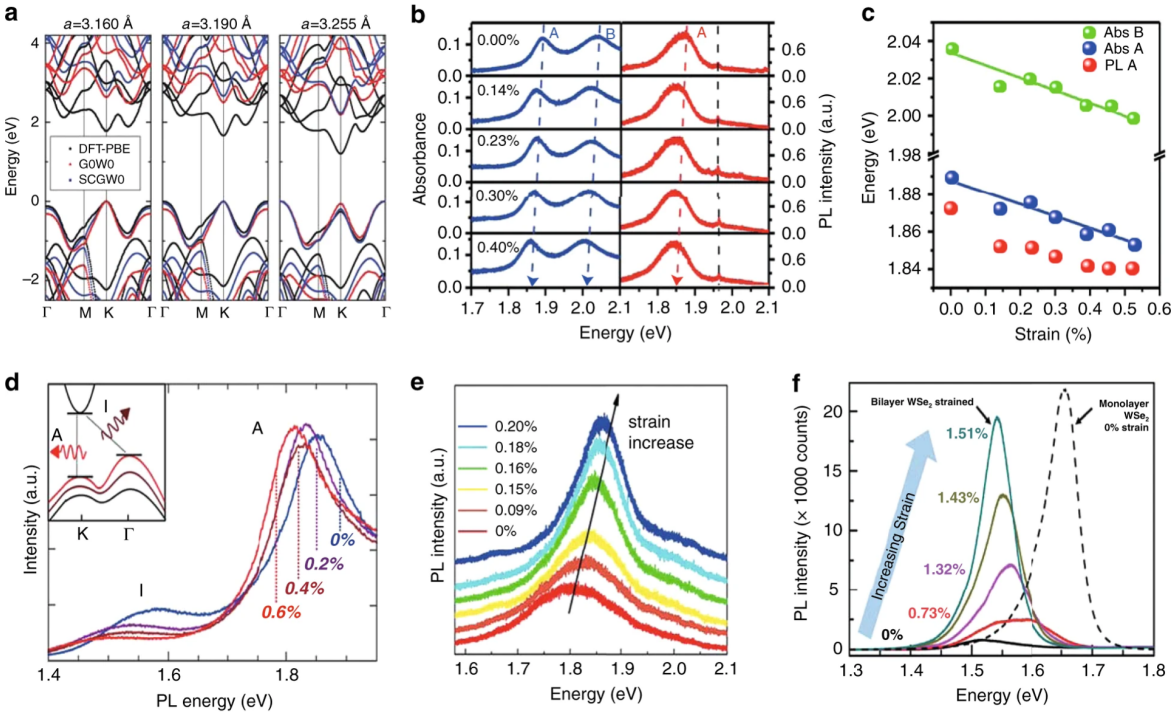

FIGURE 1.6: a) The band structures of monolayer MoS_2 were computed using Density Functional Theory (DFT), G_0W_0, and $SCGW_0$ methods for lattice constants of 3.225 Å, 3.190 Å, and 3.160 Å, corresponding to 3%, 1%, and 0% tensile strains, respectively. b, c) The photoluminescence (PL) and absorption spectra of monolayer MoS_2 were examined under different tensile strains(uniaxial). It is important to note that the dashed black line superimposed on the PL spectra in (b) represents the polymethyl methacrylate (PMMA) PL peak, not the B exciton's. The data points taken from (b) are fitted linearly by the lines in (c).d) Analysis was done on the PL spectra of bilayer MoS_2 under uniaxial tensile strain, which increased from 0% to 0.6%. The bilayer MoS_2 indirect bandgap is highlighted in the inset. e) Trilayer MoS_2 PL spectra were collected at different biaxial compressive strains. f) Solid lines indicate the strained bilayer and dashed lines indicate the unstrained monolayer. The PL spectra of the bilayer WSe_2 under various uniaxial tensile strains were compared with those of the unstrained monolayer WSe_2. Adapted with permission from [55].

strained beyond 2.5%, while in WSe_2 bilayers a significant enhancement in PL intensity is observed at 0. 73% uniaxial tensile strain due to an indirect-to-direct transition. These tunable optical properties have driven research into utilizing strain-related characteristics such as input laser intensity, temperature, and voltage to quantify strains in TMDCs, further expanding their potential applications in optoelectronics and strain sensors[55].

Local inhomogeneous strains offer additional ways to modify the optical characteristics of 2D materials at the nanoscale through local strain engineering. A notable example is the

exciton funnel effect, where the electronic band structure of a zigzag MoS_2 ribbon is modified under strain, causing excitons to migrate to regions with lower band gaps before recombination. This effect has been observed in PL spectra of A excitons on the top of wrinkles in MoS_2, indicating that local strains can confine excitons. The funnelling of photogenerated excitons towards high-strain regions holds promise for applications in single-photon sources for quantum communications and networks, as well as in photovoltaic devices like solar cells[55, 58].

Furthermore, the application of homogeneous strain to TMDCs can result in a significant enhancement due to the transition from an indirect to direct band structure. This phenomenon underlines the importance of strain engineering in exploring and optimizing the optoelectronic properties of 2D materials for advanced device applications[55].

1.4 Dielectric engineering in two-dimensional materials

In two-dimensional 2D TMDs, the combined dielectric screening from the material layer and its surrounding environment significantly influences both exciton-binding energies and quasiparticle (QP) gaps[26, 65]. However, the shifts caused by dielectric screening in the QP gap and exciton-binding energy are opposite, making it challenging to experimentally isolate and discern their individual contributions. Early efforts to comprehend optical gaps in the context of the surrounding dielectric environment produced ambiguous findings. These studies typically used substrates and/or capping layers made of fused silica or oxides like SiO_2, MgO, and sapphire[66].

Recent experimental work has demonstrated that the encapsulation of 2D materials, such as hBN, TMDs and graphene, significantly affects the optical bandgap in ways consistent with theoretical predictions. This development has introduced a novel approach to optical gap engineering through the use of dielectric engineering and encapsulation approaches[65, 67]. Controlling the optoelectronic properties of 2D materials requires an understanding of the physics underlying the dielectric screening effect on the optical gap. We can outline a model to illustrate this concept. The effect of dielectric screening on the electron-electron interaction in 2D materials can be understood by considering a thin slab of width d, placed between two different dielectrics with permittivities ϵ_1 and ϵ_2. The Rytova-Keldysh (RK) potential describes the electrostatic potential due to a charge bound to the slab in the limit as $d \to 0$[68, 69].

$$V_{RK}(q) = \frac{e^2}{2\varepsilon_0\varepsilon_m} \frac{1}{q(r_0 q + 1)}, \tag{1.1}$$

where $r_0/2\pi$ represents the thin slab's 2D polarizability, and $\epsilon_m = (\epsilon_1 + \epsilon_2)/2$ is the average dielectric constant of the surrounding environment. The static dielectric function, which is

linear in q, is given by $\epsilon_{2D}(q) = V_{RK}(q)/V_0(q) = \epsilon_m(1 + r_0 q)$, where $V_0(q) = e^2/(2\epsilon q)$ is the vacuum Coulomb potential's two-dimensional Fourier transform. Consequently, the dielectric constant in 2D materials depends on intrinsic characteristics (r_0) and extrinsic qualities (ϵ_m), in contrast to bulk materials where it is an intrinsic attribute. The RK potential's inverse Fourier transform is:

$$V_{\mathrm{RK}}(r) = \frac{2\pi e^2}{\varepsilon_0 \varepsilon_m r_0} \left[H_0\left(\frac{r}{r_0}\right) - Y_0\left(\frac{r}{r_0}\right) \right] \tag{1.2}$$

The optical bandgap is essentially the QP bandgap adjusted by the exciton-binding energy. By solving the Wannier equation, which is comparable to a hydrogen-like equation that describes an exciton, one can find the exciton-binding energy[29, 66].

$$\left(-\frac{\nabla_{\mathbf{r}}^2}{2\mu} + V(r) - E_g - E_{n\ell} \right) \psi_{n\ell}(\mathbf{r}) = 0, \tag{1.3}$$

The relative coordinate between the electron and hole is indicated by r, the QP bandgap is represented by E_g, the reduced mass is shown by $\mu = \frac{m_e m_h}{m_e + m_h}$, the exciton wave function is indicated by $\psi_{nl}(r)$, and the principal (angular) quantum numbers are n (l). The 2D polarizability r_0, the effective masses, and the external dielectric constant ϵ_m are the inputs for this equation when the RK potential is used.

1.5 Unconventional ferroelectricity due to twist in layered materials

Ferroelectric materials are crystals that exhibit inherent charge polarization with multiple stable directions for the polarization vector, influenced by the lattice symmetry. The transition between these stable polarization states can be manipulated using an external electric field, enabling a range of applications such as non-volatile memory, microwave components, transistors, and sensors [70, 71]. Ferroelectric semiconductors are especially noteworthy because they could enable field-effect transistors with extra functionalities, such as data storage. Finding appropriate materials that maintain ferroelectric properties at room temperature and can be fabricated into thin films demanded by the microelectronics sector has been challenging[70, 72]. This requirement is particularly difficult for traditional oxides because of their subpar interface quality, which restricts the homogenous ferroelectric layer thicknesses that can be practically achieved. A different approach is to utilize layered crystals which can be either cleaved or developed into ultrathin layers while maintaining their surface integrity. Thus far, only a limited number of these materials have been confirmed

experimentally, such as out-of-plane $CuInP_2S_6$, in-plane ferroelectric SnTe as well as both in-plane and out-of-plane ferroelectricity in various phases of In_2Se_3[73–76].

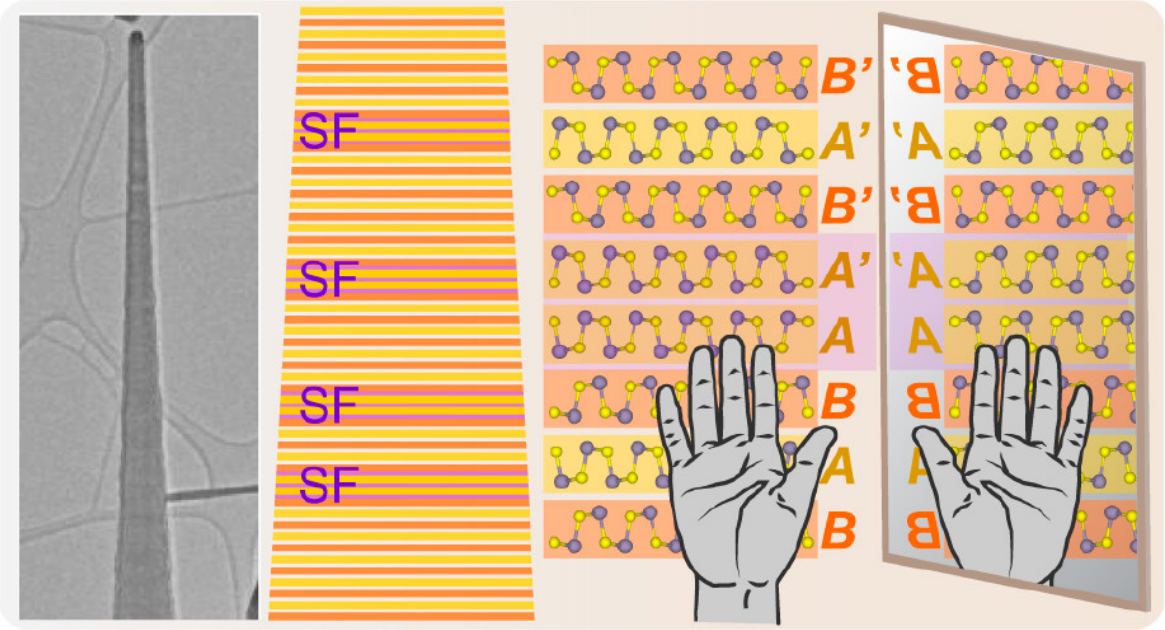

FIGURE 1.7: Diagram illustrating how stacking faults cause symmetry breaking in van der Waals nanowires. SF stands for stacking fault. Adapted with permission from [14].

In recent times, a novel trend has developed in fabricating genuine 2D ferroelectrics, leveraging interfacial charge transfer within stacked heterostructures composed of 2D materials. The construction of van der Waals heterostructures by sequentially stacking different 2D crystals has advanced into a refined area of study, enabling the creation of extremely sharp and clean interfaces and the precise control of the rotational (twist) angle between neighbouring layers. The inclusion of twist results in the formation of moiré superlattices, characterized by a periodic alteration in the local arrangement of atoms. When the twist angles are minimal ($\theta \leq 2°$), 2D atomic lattices with comparable unit cell sizes frequently experience significant reconstruction. This happens because the gain in energy from the preferred stacking arrangements compensates for the strain induced in the lattice. Recent studies have demonstrated that these commensurate domains exhibit ferroelectricity in slightly twisted hexagonal boron nitride, a wide band-gap insulator, as well as in semimetallic WTe_2. This ferroelectricity enables the switching of domain types through the application of an external electric field and the sliding of atomic planes along the interface. The vdWHs possess broken inversion symmetry and, when combined with the asymmetric atomic arrangement at the interface of two 2D crystals, they facilitate ferroelectric domains with alternate out-of-plane polarization organized into a twist-regulated network[70, 77–80].

Recently, a novel method for symmetry breaking in van der Waals materials was proposed: the incorporation of stacking faults that diminish symmetry within a centrosymmetric

stacked host crystal. This was illustrated using nanowires of group IV monochalcogenides (MX, where M = Ge or Sn; X = Se or S), which are anisotropic vdW crystals[81]. There has been interest in MX monochalcogenides as ferroelectrics due to theoretical forecasts of multiferroic order where in-plane ferroelectricity is coupled with ferroelasticity at temperatures above room temperature[82, 83]. Nevertheless, achieving ferroelectricity in group IV monochalcogenides poses considerable difficulties.

Single 2D layers form in an anisotropic, non-centrosymmetric arrangement and have shown ferroelectric polarization for SnSe and SnS. Obtaining monolayers of these materials continues to be challenging through both growth methods and exfoliation. Experimental realization of symmetry breaking in the few-layer regime is also difficult. The MX family of crystals possesses an orthorhombic structure (space group Pnma) with puckered layers organized in an A-B stacking sequence. The thickness has a direct impact on ferroelectricity because, within centrosymmetric A-B stacking, only an odd number of layers disrupt the balance between A and B layers, leading to a resultant electric polarization. It is clearly challenging to precisely manage the number of layers[14].

GeS nanowires produced through a vapour-liquid-solid (VLS) method have become significant in the fields of nanophotonics, optoelectronics, and 3D twistronics[12, 84]. GeSe, which is notable for its use in optoelectronic and photovoltaics applications because of its 1.3 eV direct band gap, high carrier mobility, and superb environmental stability, is also suitable for VLS growth, although it appears as large ribbons[85]. Density functional theory (DFT) demonstrates that metastable A-A' stacking in GeSe possesses reduced formation energies compared to GeS. Additionally, it reveals that the A-A' stacking faults exhibit lower energy than the A-A stacking sequence with aligned A-layers. First-principles calculations show that the ferroelectricity similar to a-single MX monolayer arises due to the local symmetry breaking from A-A' stacking. The experimental observations of areas with a high concentration of stacking faults show reduced symmetry through second harmonic generation. The disruption of symmetry caused by stacking faults in otherwise centrosymmetrically aligned MX nanowires could be a potential pathway to developing vdW ferroelectric[14].

Chapter 2

Instrumentation: Synthesis and Transfer

2.1 Introduction

2.1.1 Synthesis of 1D GeS nanowire

Two-dimensional (2D) compound materials are considered highly promising for various applications, including electronics, optoelectronics, sensors, and flexible devices. This is due to their high carrier mobility, adjustable bandgaps, large specific surface area, atomic-level thickness, and a range of other advantageous properties. Among the various methods for preparing 2D compound materials, chemical vapour deposition (CVD) stands out as particularly promising. It allows for the growth of high-quality 2D compound materials at a reasonable cost. Considerable efforts have been dedicated to enhancing the CVD growth of 2D compound materials, focusing on achieving large domain sizes, controllable layer numbers, rapid growth rates, and high-quality characteristics[86].

We investigated the development of one-dimensional (1D) nanowires derived from layered 2D GeS (see crystal structure of GeS in Figure 2.1a). In recent times, quasi-1D chalcogenides like $Ta_2Pd_3Se_8$ and $TaSe_3$ have been obtained by exfoliating bulk materials. Initial studies have examined their properties, revealing that $Ta_2Pd_3Se_8$ exhibits semiconducting behavior[87], while $TaSe_3$ displays metallic or semimetallic characteristics [88]. Research has mainly concentrated on fibres or bundles in which many fundamental 1D units are bound together by weak van der Waals interactions. Although the morphology of these fibres or nanowires is dictated by the 1D configuration of their constituent parts, a different method for quasi-1D van der Waals materials involves transforming a two-dimensional (2D) layered crystal into a nanowire form. This can be achieved by employing bottom-up synthesis methods, like vapour-liquid-solid (VLS) growth, which is well-known for producing nanowires from three-dimensional materials [89]. This method also provides the advantages of generating a high yield of wires simultaneously and regulating the wire thickness by adjusting the growth catalyst dimension [90–92]. The ability to control the twisting configuration

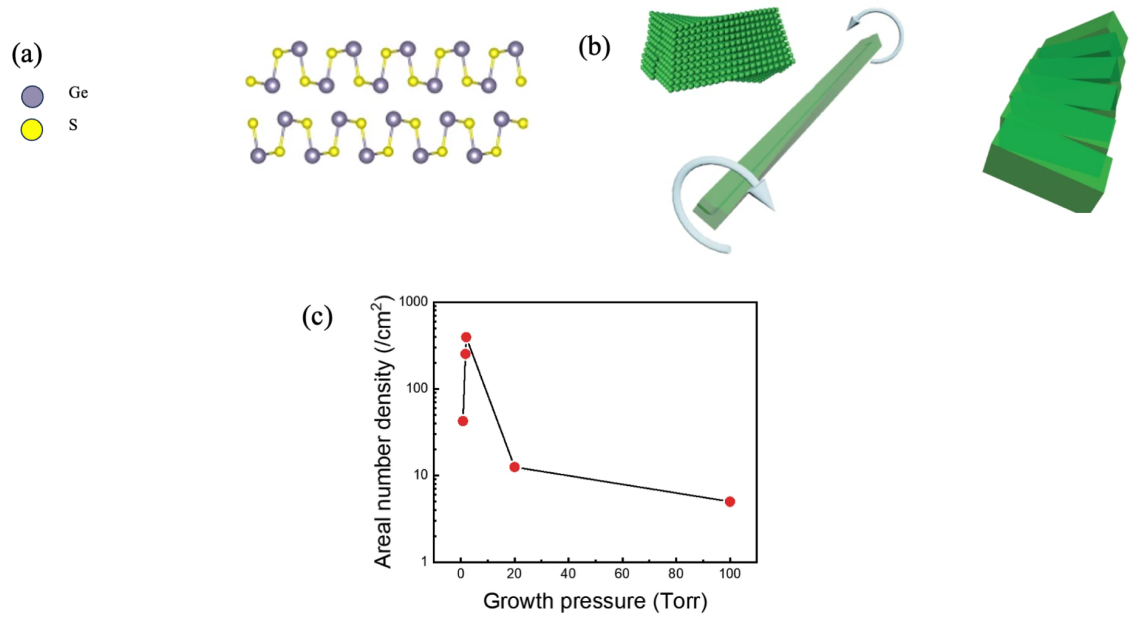

FIGURE 2.1: (a) GeS layered crystal framework (b) Schematics demonstrating the formation process of mesoscale GeS structures with notable twisting. The evolution of a nanowire displaying an Eshelby twist. (c) The density of twisted GeS structures per unit substrate area as a function of growth pressure. Adapted with permission from [12].

of van der Waals structures offers a novel dimension for modifying their electrical and optical characteristics. The twist angle markedly affects the excitons, electronic states, and phonons of the twisted structures through interlayer coupling, resulting in distinct optical, electric, and spintronic characteristics. Twisted van der Waals structures are commonly created through a transfer-stacking method, though this approach is not ideal for materials with robust interlayer interactions. Simple bottom-up fabrication techniques may offer a different approach to producing twisted van der Waals structures. Nevertheless, the Eshelby twist, associated with a screw dislocation, enables the formation of these structures from nanoscopic to mesoscopic scales. Axial screw dislocations are first incorporated into nanowires growing along the stacking direction during the synthesis process. This method produces van der Waals nanostructures that consistently twist, with their twist rates being dependent on the nanowires' radii. Compounds such as germanium sulfide (GeS) have the capability to develop into nanowires following the van der Waals stacking direction (perpendicular to the planes). Introducing the Eshelby twist into these nanowires naturally results in twisting between the successive layers (Figure 2.1b). Low-pressure chemical vapour deposition (LPCVD) is a process in which twisted GeS nanowires can be grown. Low pressure and flow rate of carrier gas an essential conditions for the growth of twisted nanowires. The study by Liu et. al. [12] showed that there is an optimum pressure and carrier gas flow range for which the aerial number density of twisted GeS nanowires is the highest (see Figure

2.1c). Hence, a custom-built LPCVD (Low-Pressure Chemical Vapor Deposition) system was designed to synthesize twisted GeS nanowires for the investigation of their unique optoelectronic properties.[12, 93–97].

2.1.2 2D van der Waals Heterostructure fabrication setup

The extraction of graphene and other two-dimensional (2D) materials represented a notable advancement in the field of physics [98, 99]. Since then, the development of transfer methods allowing for the precise placement of 2D materials has been one of the most important breakthroughs in this field [11, 100]. These accurate transfer methods have enabled the creation of synthetic materials by stacking different 2D materials (refer to Fig. 2.2), leading to the formation of so-called van der Waals heterostructures (vdWHs) [101, 102]. Generally,

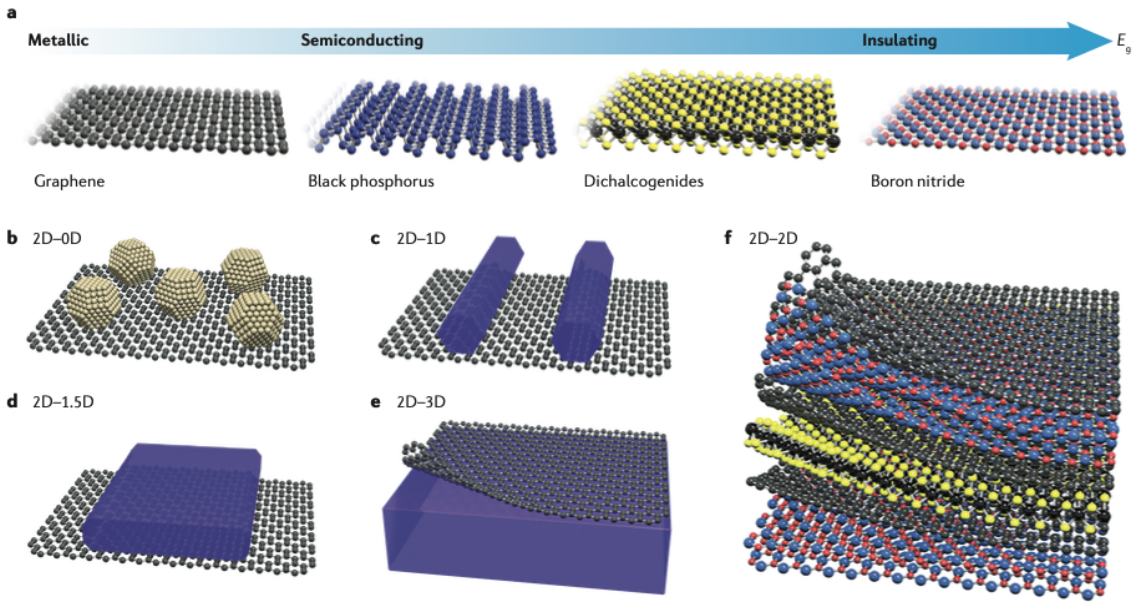

FIGURE 2.2: A diverse collection of 2DMs demonstrates a range of chemical compositions, electronic properties, and atomic structure, with an increasing bandgap from left to right. Panels b-f illustrate vdWHs created by integrating the 2DMs, which are free of dangling bonds, with various materials: 0D nanoparticles or quantum dots (panel b), 1D nanowires (panel c), 1.5D nanoribbons (panel d), 3D bulk materials (panel e), and 2D nanosheets (panel f). Adapted with permission from [4].

a monolayer of 2DMs comprises a lattice that is bonded covalently and is just one or a few atoms thick. These atomic layers lack dangling bonds, endowing them with remarkable optical and electrical properties, in contrast to common nanostructures that experience surface trap states and dangling bonds. The entirely saturated bonds on the surface indicate that the interactions among adjacent layers of 2DMs are typically governed by van der Waals forces. As there are no direct chemical bonds, van der Waals interactions allow the combination

of significantly different materials without the need for crystal lattice compatibility. This allows for great versatility in integrating 2DMs with various nanoscale materials, leading to the formation of diverse vdWHs with unique functionalities that were not possible before [101].

Commercial setups for fabricating 2D heterostructures are available on the market, but they tend to be expensive and offer limited opportunities for customization to meet specific experimental requirements. Therefore, a custom-built transfer stage was set up in the laboratory using commercially available components.

2.2 Low-pressure chemical vapour deposition (LPCVD) setup

2.2.1 Vapor-Liquid-Solid nanowire growth mechanism

In the VLS process, Au nanoparticle acts as a nanowire growth catalyst. As the growth temperature is well above the eutectic temperature, a liquid drop is formed whose majority content is Au and other contents are Ge and S. This Ge and S content in the liquid drop is due to the accumulation of GeS molecules on the tip of the liquid drop which comes from GeS vapour in LPCVD. These GeS molecules then diffuse through the catalyst liquid drop and form the GeS nanowire (see Fig. 2.3). Since GeS has a layered anisotropic crystal structure (see Figure 2.1a), it crystallizes as layers along the wire axis with an Eshelby axial dislocation at the center[15].

2.2.2 Procedure of synthesis

TABLE 2.1: Summary of the components of the home-built LPCVD system

Description	Specification	Quantity
Split-type single zone tube furnace	Nabertherm (max. temp.1100 °C)	1
Mass-flow controllers (MFC)	MKS	2
Argon gas and Forming gas	Commercial gas cylinders	1 each
Both end open transparent quartz tube	25 mm outer diameter, can withstand vacuum up to 10^{-3} Torr, antsLAB™	1
Alumina boat	15 ml, antsLAB™	2
Pressure gauge	Digital Pirani gauge with dual gauge head, ACE instruments	1
Liquid nitrogen	commercial liquid nitrogen supplied in 30 L dewar (cryocan, IOCL)	1
Vapor sublimation trap	stainless steel tube with NW16 and NW40 flange, custom made by FOURVAC	1
Vacuum Pump	Pfeiffer Duo 3	1
Germanium sulfide powder	Sigma-Aldrich	One 5 gm bottle
Stainless steel bellows	0.5 inch outer diameter	2
Au-coated silicon substrate	3-5 nm Au-coated Silicon, coating done by thermal vapour deposition/ sputtering	3
Metal wool	stainless steel	500 gms

A home-built LPCVD system was set up in the laboratory for the synthesis of twisted germanium sulfide (GeS) nanowires (see Figure 2.4). The ingredients required for setting up a LPCVD system are listed in Table 2.1:

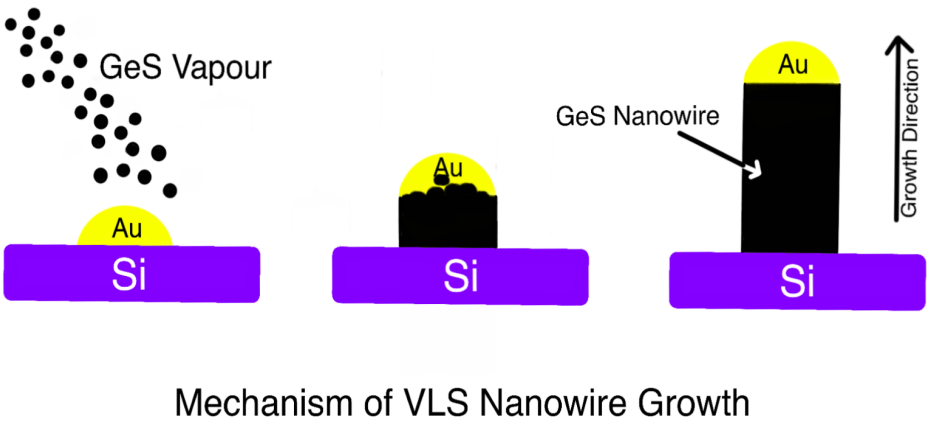

FIGURE 2.3: Vapour-Liquid-Solid (VLS) growth mechanism: 3 nm Au-coated Si substrate dewets at the growth temperature of 270-300 °C to form an array of Au nanoparticles and the GeS vapour starts to accumulate (left). As the growth temperature is well above the eutectic temperature, a liquid drop is formed whose majority content is Au and other contents are Ge and S. The GeS molecules accumulate at the bottom and Au is at the tip (middle). As more amount of GeS vapour accumulates on the bottom, the nanowire grows in size with Au at the tip (right).

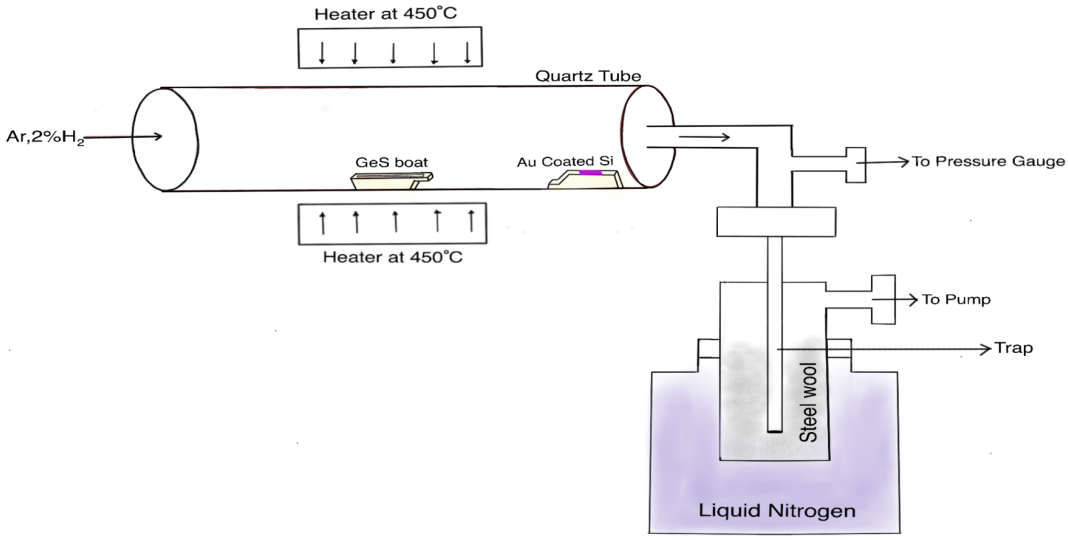

FIGURE 2.4: Schematic of Low-pressure chemical vapour deposition (LPCVD) setup.

As shown in the schematic Fig. 2.4 a single zone split type tube furnace was used for the LPCVD process. A 25 mm, pre-cleaned quartz tube was placed inside the tube furnace

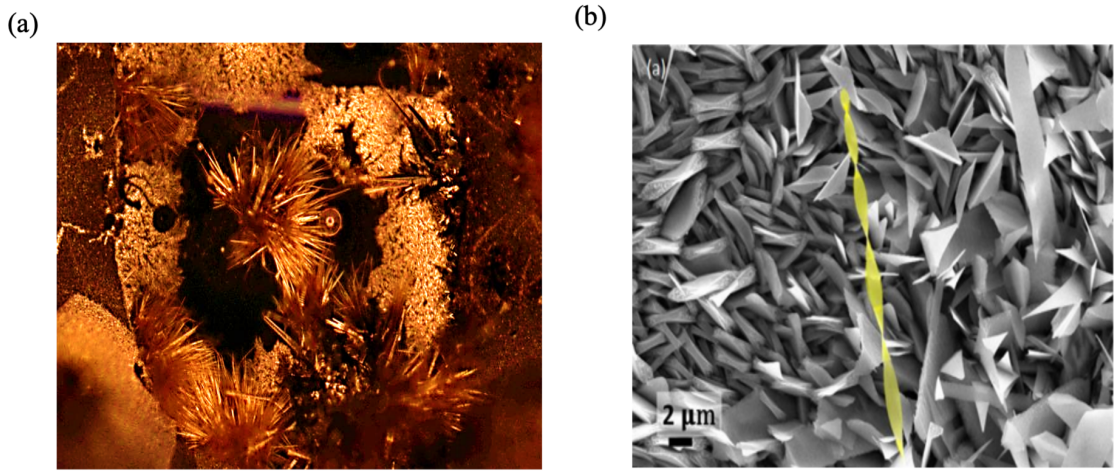

FIGURE 2.5: (a) Optical Microscope image of the forest of GeS nanowires can be seen on the growth substrate in the dark field mode. (b) FESEM image of a twisted GeS nanowire highlighted in yellow.

for LPCVD. The temperature gradient of the furnace was determined for 450°C furnace temperature, beforehand. A steep gradient in temperature was observed towards both ends. 30 mg of GeS powder was put inside the alumina boat and was kept at the centre of the quartz tube where the temperature was 450°C. Another inverted alumina boat was placed inside the quartz tube, towards the end (downstream), where the temperature is 270°C. Three pieces of 3 nm Au-coated Si substrate were placed on top of the inverted boat. The tube was closed on both sides by using O-rings, vacuum grease and metal connectors to maintain the low pressure. The inlet (left-hand side in Fig. 2.4) was connected to the Ar gas cylinder and the flow was controlled using a mass flow controller (MFC). The outlet was connected to the vacuum pump through a vacuum sublimation trap dipped inside liquid nitrogen. A sufficient amount of steel wool was placed inside the trap to increase the effective surface area. The vapour sublimation trap captures vapours and solidifies them before they can flow back into the quartz tube, preventing contamination of Au-coated Si substrates. Additionally, it stops gases from entering and damaging the vacuum pump. A digital pirani gauge was also attached to monitor the pressure. A safety valve was also placed to prevent any accidents. The vacuum pump was turned on and sufficient time was allowed to reach the base pressure. Initially, a flow rate of 500 sccm Ar gas was set for 30 minutes to remove any oxygen present inside the tube. This procedure is known as flushing. After flushing the flow of Ar was decreased to 100 sccm and the furnace temperature was set to 450°C with 5°C/ s ramping rate. At this rate, it takes around $\sim$ 90 mins to reach 450°C. Once the temperature

reached 420 °C, the Ar gas flow was decreased to 0 sccm and forming gas (Ar/ 2% H_2) flow was switched on with a flow rate of 50 sccm which resulted in 1-2 Torr pressure inside the quartz tube. The 450 °C, 1-2 Torr pressure and 50 sccm gas flow were maintained for 30 mins and then the furnace was allowed to cool to room temperature naturally. During the cooling cycle when the temperature reaches 420 °C, forming gas flow was decreased to 0 sccm and the Ar gas flow was increased to 100 sccm. The flow rate is maintained till the room temperature is achieved. Once it reached room temperature the vacuum pump was switched off and the Ar flow rate was increased to 500 sccm until the ambient pressure was achieved. After this, the inlet and outlet metal connectors were carefully opened to take out the substrates. After that, the substrates were observed under an optical microscope in dark field mode. The substrates show a forest of nanowires as can be seen in the optical microscope image Fig.2.5a. An SEM image of the growth substrate shows a twisted GeS nanowire (highlighted in yellow) Fig. 2.5b [15].

2.3 2D van der Waals heterostructure fabrication setup

2.3.1 Components and design

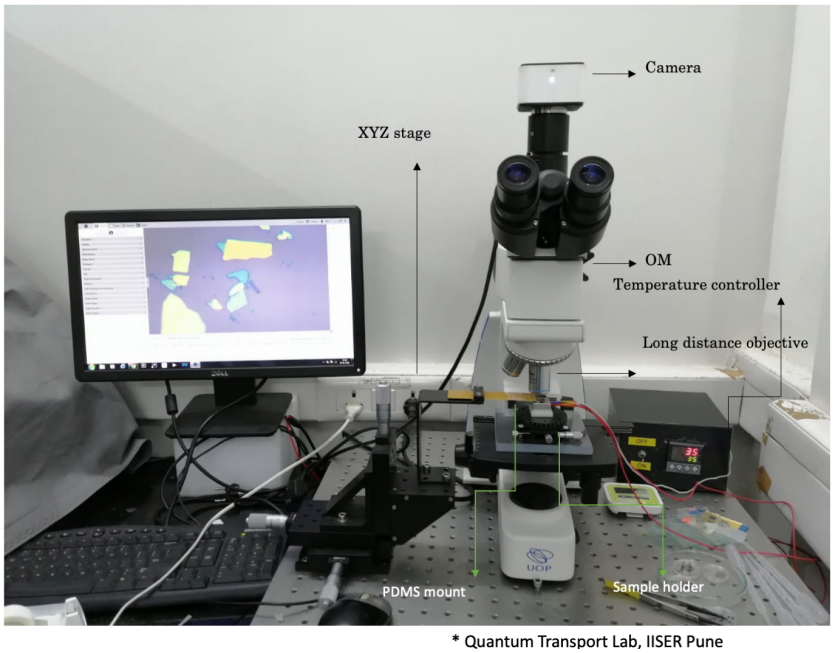

FIGURE 2.6: Photograph of the home-built transfer stage setup showing various parts and accessories.

A home-built transfer stage was set up (see Fig. 2.6) using the components listed in Table 2.2 Fig. 2.6 depicts the system used for transferring 2D materials. The system is composed

TABLE 2.2: Summary of the components of the home-built transfer stage setup

Component	Specification/ Quantity
Optical breadboard	Steel, custom-made by FOURVAC
Rubber damping sheets	4
Optical microscope body	UoP
XYZ stage	2 (one for sample stage and one for PDMS stamp holder)
Heater	Catridge heater hotend for 3D printer, 12 V, 40 W
Thermocouple	K-type
PID temperature controller	One, PID-500
Long-distance objective lens	One
Power supply	12 V
PCB Board	with hole at one end for attaching a transparent coverslip
CMOS Camera	MIchrome 6
Toggle switch	1
Computer	for seeing the camera image
Coverslip	Transparent, 0.15 mm thickness
Scotch-tape	1-roll
Silicone-elastomer kit	Sylgard®184, Dow-corning

of an optical microscope with a long-distance objective lens, a white light source, an XYZ stage (sample/substrate stage) and an XYZ stage (stamp stage). All the components are mounted on a stainless steel optical breadboard. A CMOS camera is attached to the optical microscope with an HDMI output attached to a computer. The sample stage also contains a heater and a thermocouple controlled by a PID temperature controller placed in a rectangular black box. The PDMS stamp is glued using feviqwick to a transparent glass coverslip which is attached to a circular hole cut on a PCB board using scotch tape. The PCB board is then attached to the XYZ stamp stage in a cantilever-like geometry. This particular arrangement resolves any transparency-related issue that is often encountered when a thick glass slide is used. A double-sided carbon tape is placed on the sample stage and the silicon or other substrates are placed on top of that for firm attachment.

2.3.2 Transfer process

2.3.2.1 Transfer process for exfoliated materials using PPC

PDMS stamp was made by mixing PDMS liquid and the hardener in a 10:1 ratio and was subsequently cured at 90 °C for 30 min. A small PDMS stamp was cut from the big PDMS sheet using a biopsy punch. The small stamp was then attached to a glass cover slip. The PDMS stamp was first placed firmly on top of the glass cover slip and a small drop of feviqwick was placed close to the stamp. After that, the drop of feviqwick was slowly dragged

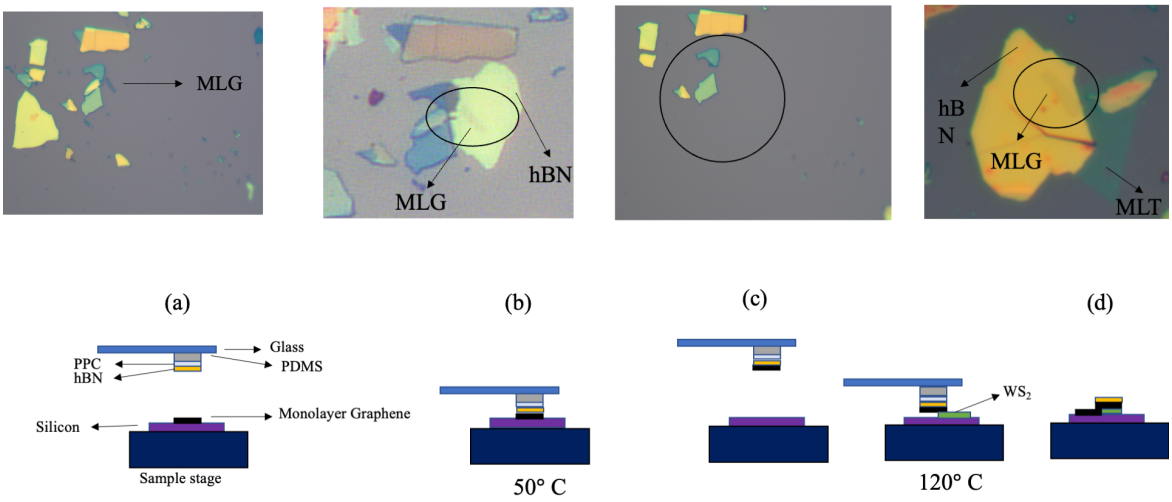

FIGURE 2.7: Steps for transfer of exfoliated layers: (a) Optical microscope image shows the exfoliated monolayer graphene on 285 nm SiO_2/Si substrate. The monolayer will be picked up using PDMS/PPC/hBN aligned on top of it. (b) The PDMS/PPC/hBN stack was lowered and placed on top of the monolayer graphene. The sample stage was heated to 50 °C. (c) The monolayer graphene was picked up using the PDMS/PPC/hBN stack and the corresponding region in the SiO_2/Si substrate can be seen empty. (d) The PDMS/PPC/hBN/graphene stack was placed on top of a monolayer TMD (WS_2 in this case) to make a graphene-WS_2 heterostructure. The stage was heated to 120 °C to release the stack. Subsequently, the sample was cleaned by using toluene, acetone and IPA.

towards the base of the stamp by using a toothpick. The glue was allowed to dry for 5 minutes. On top of the PDMS stamp, the PPC solution was blade coated and the coverslip was baked at 80 °C for 5 minutes to flatten the top surface of the PPC. The PCB board was then mounted to the XYZ stage. hBN crystal was exfoliated on top of the PDMS/PPC stamp and graphene crystal was exfoliated on 285 nm SiO_2/ Si substrate. First, the hBN-containing PDMC/PPC stamp was placed under the optical microscope of the transfer stage and the hBN flake of the required thickness was chosen. The graphene containing SiO_2/ Si substrate was also placed on the sample XYZ stage and a graphene flake of the required thickness was chosen. Then the PDMS/ PPC/ hBN stamp was carefully aligned on top of the identified graphene flake (see Fig. 2.7a). The PDMC/PPC/hBN stamp was then lowered slowly until it completely touched the graphene flake which can be made sure by the progression of the meniscus during lowering (see Fig. 2.7b). The sample stage was then heated to 50 °C (10 °C above the glass transition temperature of PPC) and the configuration was maintained for 5 mins and the PDMS/PPC/hBN stamp was detached quickly from the substrate (see Fig. 2.7c). One can confirm the successful transfer of the graphene by looking at the

PDMS/PPC/hBN stamp and also the empty substrate. The graphene-containing substrate was removed from the sample stage and the monolayer TMD (WS_2 in this case) containing substrate was then placed on the sample XYZ stage. The PDMS/PPC/hBN/graphene stamp was then carefully aligned on top of a desired monolayer WS_2 flake. The stamp was slowly lowered and placed in the required position until the full stamp covered the region. The sample stage was then heated to 120°C. This temperature releases the entire stack including the PPC on the substrate. The PCB cantilever was then taken up quickly. The substrate was then cleaned with toluene, acetone and IPA (10 mins each) to remove PPC. The clean transferred heterostructure can be seen in Fig. 2.7d.

2.3.2.2 Transfer process for CVD grown TMDs using polystyrene

The as-grown SiO_2 /Si substrate containing monolayer WS_2 was spin-coated (3500 rpm, 1 min) with 10% PS solution in chloroform [103] and was heated at 100 °C for 3 min. The PS-coated substrate was then dipped in distilled (DI) water with the four corners slightly scratched using a clean surgical blade. On dipping in DI water, the PS film comes off easily along with the monolayer WS_2 and the film floats in the DI water. The PS film is then placed on the PDMS stamp which was prepared following the steps mentioned earlier. The PDMS/PS stamp was baked at 90 °C for 5 mins for better attachment of PS film with the PDMS. The PDMS/PS stamp was then attached to the glass coverslip and PCB cantilever by following the steps mentioned earlier. The target substrate was then placed on the sample XYZ stage. A monolayer WS_2 flake was chosen by carefully examining the PDMS/PS stamp under an optical microscope. The PDMS/PS stamp was then aligned on top of the target substrate and was lowered slowly till it touched the bottom substrate. After ensuring the complete attachment of PDMS/PS with the substrate the sample stage was heated at 150 °C for completely melting PS from PDMS. The PCB cantilever was then slowly detached and taken up. The substrate was removed from the sample stage and was cleaned in toluene for 3 hrs and in acetone and IPA for 10 mins each[104].

2.3.2.3 Transfer process using transparent commercial nail polish

Among the various techniques developed up to now, the vdW pick-up method is favoured for constructing heterostructures since it ensures that the layers are not exposed to polymers during the stacking process, leading to pristine interfaces[105–107]. An evident limitation of this method is the dependence on thin polycarbonate (PC) or polypropylene carbonate (PPC) layers, which require mixing, preparation, and application via spin coating or direct application to a glass slide prior to use. With PPC, the thin film exhibits significant wear after multiple (>5) stacking sequences, potentially causing extensive delays in fabrication due to flake cracks, folds, and unexpected transfer issues before the process is completed.

It was recently demonstrated that commercially obtainable nitrocellulose polymer solution

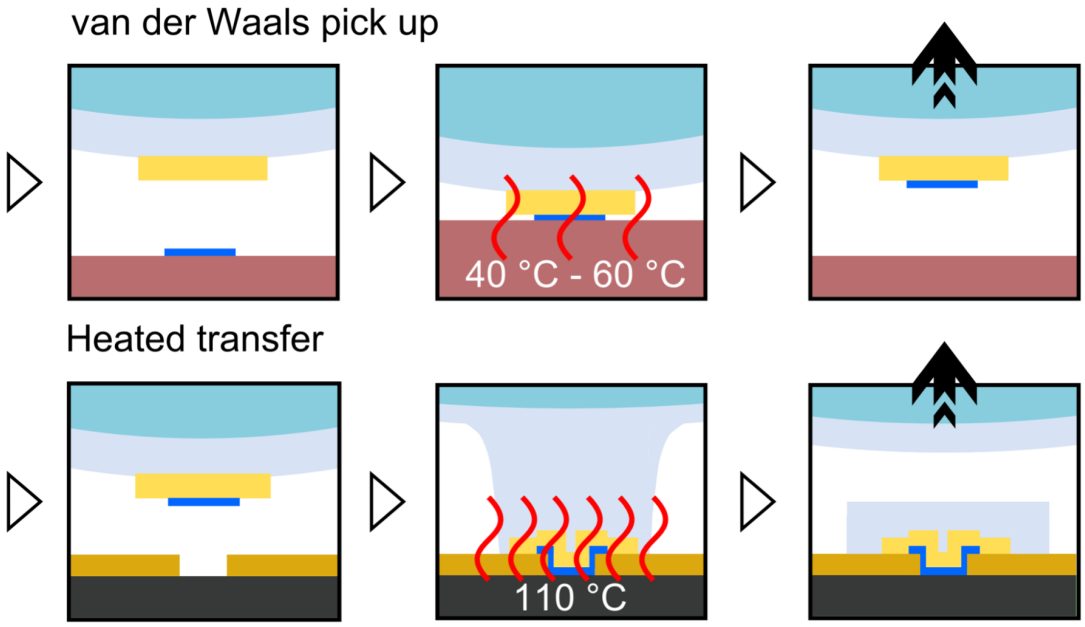

FIGURE 2.8: Initially the exfoliated flake was picked up using nail polish on PDMS by heating the sample stage to 40-60 °C. The flake is then transferred to the target substrate by heating the nail polish to 110 °C, thereby melting it onto the substrate stage. Adapted with permission from [105].

(commonly known as nail polish) can be utilized to pick and drop 2D materials. According to Rebollo et al., [108], these flakes and basic heterostructures can subsequently be relocated to any substrate or trench to form suspended cavities and structures. The emerging advancements have sparked our curiosity in utilizing nail polish for building heterostructures through an adapted vdW pick-up method. While PC and PPC films require careful mixing and preparation before application, a single cured drop of nail polish is sufficient to construct multi-material heterostructures (exceeding 5 layers) without evident polymer fatigue[105]. For our transfers, we utilize either Revlon Nail Enamel Clear 771 or Lakme Absolute Gel Stylist Nail Color in the Top Coat variant (both of them are transparent).

The PDMS stamp is prepared by following the steps mentioned above. A drop of nail polish is extracted from the bottle using a toothpick and is placed on the PDMS stamp and allowed to spread. The glass cover slip is then baked for 5 min at 90°C. This process solidifies and fixes the nail polish, forming a firm adhesive layer for flake collection. The

glass cover slip is then fixed to the PCB cantilever, and the latter is attached to the XYZ stage. The desired flake (exfoliated earlier on a SiO_2/ Si substrate) is positioned beneath the pickup slide with the aid of a microscope. The slide is subsequently lowered gently, ensuring that the surface is not accidentally touched. To pick up the flake the sample stage is heated to 40-60°C (we observed the best temperature to be 50 °C). The slide is subsequently lifted in a single, smooth motion to detach the exfoliated flake from the substrate surface (see Figure 2.8 top panel).

To transfer the exfoliated flake that has been picked up, it is positioned above the target substrate and carefully lowered until it touches the surface. The stage temperature is subsequently increased in increments of 10 °C as the stack is consistently observed. At approximately 90 °C, the stack can be compressed to control the bubbles of adsorbates appearing at the layer interfaces. After compression, the temperature of the stage is increased to 110 °C. At this temperature, the slide can be withdrawn, causing the nail polish to melt and adhere to the surface, thereby depositing the stack onto the substrate (see Figure 2.8 bottom panel). The chip is then rinsed in acetone and IPA for 5 mins each to remove the nail polish and blow-dried with nitrogen gas.

2.4 Conclusion

In conclusion, we have developed a home-built low-pressure chemical vapour deposition (LPCVD) system and 2D van der Waals heterostructure fabrication setup i.e. transfer stage. The home-built setups are less expensive compared to the commercial ones and offer a greater degree of customization according to the needs of the experiments. The twisted GeS nanowires synthesised using a home-built LPCVD setup were used to discover stacking engineered room-temperature ferroelectricity as described in detail in Chapter 5. The samples made using the home-built transfer stage were used for experiments detailed in Chapters 3 and 4 and also various other experiments not included in this thesis. In future, we are trying to add a rotation sample stage in the home-built transfer stage setup for fabricating twisted moiré heterostructures.

Chapter 3

Brightening of dark excitons in WS_2 via tensile strain-induced excitonic valley convergence

Abstract:
Transition-metal dichalcogenides (TMDs) host tightly bound electron-hole pairs named excitons, which can be either optically bright or dark based on spin and momentum selection rules. In tungsten-based TMDs, a momentum-forbidden dark exciton is the energy ground state, and, therefore, it strongly affects the emission properties. In this chapter, I will discuss the brightening of the momentum-forbidden dark exciton by placing monolayer tungsten disulphide on top of nanotextured substrates, which imparts tensile strain, modifying its electronic bandstructure. This enables phonon-assisted exciton scattering between momentum valleys, thereby brightening momentum-forbidden dark excitons. In addition to offering a tuning knob for light-matter interactions in two-dimensional materials, our results pave the way to designing ultrasensitive strain-sensing devices based on TMDs. This chapter is an adaptation of the research article "Phys. Rev. B (Letter), 110, L081405 (2024)" [36].

3.1 Introduction and motivation

TMDs (*e.g.* MX_2, $M = Mo$, W, $X = S$, Se) are known for their novel optical properties [109]. They host excitons - charge neutral electron-hole pairs bound by Coulomb interactions [19, 33, 110–113]. The excitons in monolayer (ML) TMDs have large binding energy ($\sim$ 300 meV in ML WS_2) due to reduced dielectric screening of Coulomb interactions and therefore can be observed even at room temperature[29, 33]. Because of their unique properties, they find applications in novel optoelectronic devices like excitonic interconnects and valleytronic devices. The large spin-orbit coupling in tungsten disulphide (WS_2), due to the heavy mass of the tungsten atom, splits the valance band maxima (VBM) at K point and

conduction band minima (CBM) at K, Λ points in two sub-bands with opposite spin orientations. This results in the formation of 'bright' intravalley KK excitons with the hole at the upper sub-band of K VBM and electron at the upper sub-band of K CB minima (CBM+1) [Fig. 3.1a]. The excitons are called 'bright' (spin-forbidden 'dark') because they satisfy (don't satisfy) the optical selection rule because of their same (opposite) spin and are therefore optically detectable (non-detectable). There is also a possibility for the formation of indirect intervalley excitons $K\Lambda$ with the hole at the upper sub-band of K VBM and electron at the lower sub-band of Λ CBM as well [Fig. 3.1a] [31, 44]. But, because of the large momentum mismatch, they require the assistance of phonons to recombine radiatively [114]. The $K\Lambda$ exciton is therefore called momentum-forbidden dark exciton [115]. In the case of W-based monolayer (ML) TMDs, $K\Lambda$ exciton is the excitonic ground state; it has higher binding energy and longer lifetime than the KK bright excitons [37, 115, 116]. Therefore, $K\Lambda$ plays an important role in the exciton dynamics of the system. Thus, controlling them is essential for designing novel optical devices. The dark exciton can be brightened by exciton-phonon coupling if the energy of the available phonon mode matches the dark-bright exciton energy splitting, which can be effectively tuned by applying strain to ML WS_2 [37, 45, 117]. It is reported that the dark-bright exciton separation changes in the order of $\sim$ 100 meV due to strain[37, 117]. Therefore, strain acts as a tuning knob for the emission of dark excitons [37, 46, 118].

Recent theoretical and experimental works predict that the dark $K\Lambda$ exciton in WS_2 can be brightened only by applying compressive strain [37, 116]. Conversely, two recent studies [119, 120] reported the existence of dark $K\Lambda$ excitons in WSe_2 under tensile strain. However, in these works either the mechanism behind the brightening is not addressed [37, 119] or remains elusive due to the various approximations used in its description, such as not taking the binding energy of the $K\Lambda$ exciton into account [116, 120]. It is highly unlikely that two W-based materials will behave differently in terms of strain-mediated brightening of $K\Lambda$ dark excitons, i.e., requiring compressive strain for WS_2 and tensile strain for WSe_2, despite having similar excitonic band structures with $K\Lambda$ dark excitons as the excitonic ground state in W-based TMDs (unlike in Mo-based TMDs) [31]. Here, we apply tensile strain to ML WS_2 by placing them on nanotextured substrates patterned with nanopillars [Fig. 3.1b, c]. Conically shaped nanopillars of height 'h' and interpillar separation (centre to centre) 'l' were made of Si(100) and capped with insulator Al_2O_3 nanospheres 10 nm on top [Fig. 3.1b, c].

We prepared samples with varied interpillar distances: $l \approx 25$ nm (sample C-48), $l \approx 44$ nm (C-99) and $l \approx 60$ nm (C-132) [121]. By tuning 'l', we tune the amount of strain applied on ML-WS_2. The latter was grown by chemical vapour deposition (CVD) and was transferred on top of the nanotextured substrates [104] [see schematic Fig. 3.1d]. We perform

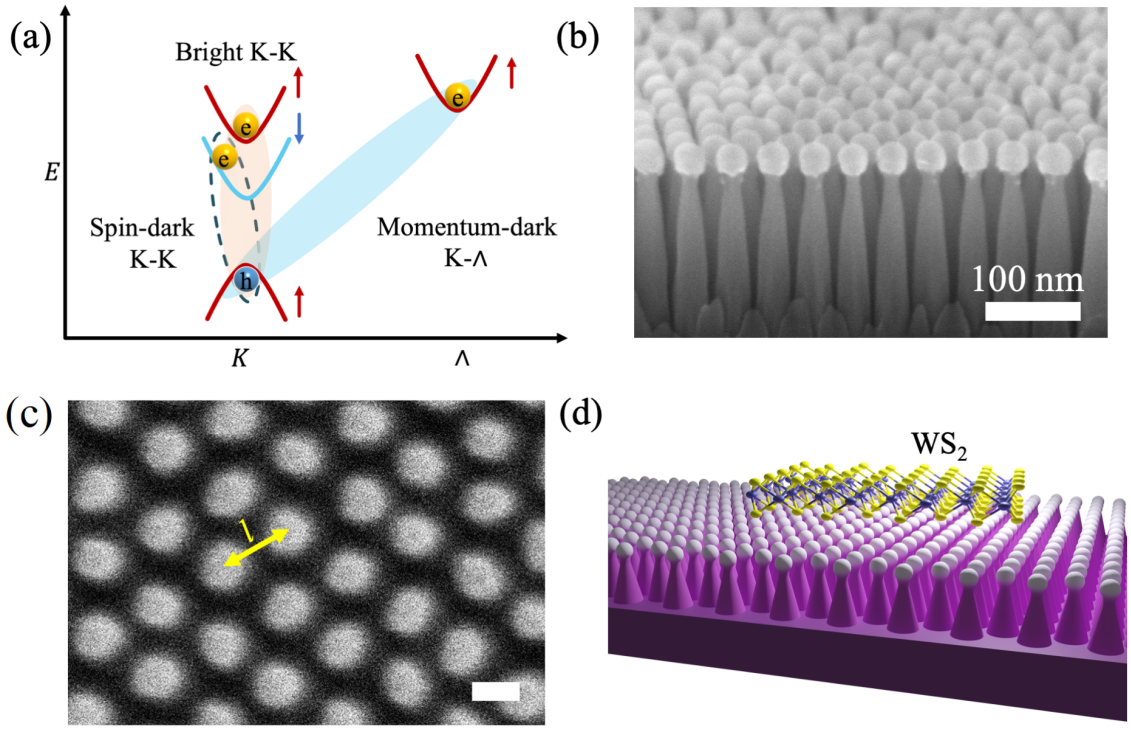

FIGURE 3.1: (a) Schematic showing various excitonic species near the electronic dispersions at K and Λ valley. Arrows indicate the spin orientations. (b) Field Emission Scanning Electron Microscope (FESEM) image of the C-99 nanotextured sample (side view). (c) FESEM image of the C-99 substrate as viewed from the top (scale bar is 20 nm). The yellow line shows the interpillar separation l. (d) Schematic of the substrate with ML WS_2 placed on top.

temperature-dependent photoluminescence (PL) and Raman measurements on the strained and unstrained ML WS_2 samples. Supported by *ab initio* density functional theory (DFT) based calculations, we discover the brightening of $K\Lambda$ dark excitons on the application of tensile strain.

3.2 Sample preparation and optical measurements

The nanotextured (NT) samples were prepared using block-copolymer lithography and inductively coupled plasma etching (ICP-RIE). The NT substrates are patterned with nanopillars of interpillar distance *'l'*. The nanopillars made of Si(100) have a cone-like shape with insulator Al_2O_3 nanospheres of diameter 10 nm on top of each nanopillar [Fig. 3.1d]. We prepared samples of three different l= 25±3, 52±6 and 60±8 nm by varying the molecular weight 'M_W'= 48, 99 and 132 kg mol^{-1} of the cylindrical phase polystyrene block-poly(methyl methacrylate) (PS-b-PMMA) block copolymer respectively[121]. We name the three different substrates according to the molecular weight of PS-b-PMMA used for

their preparation as C-48(l= 25nm), C-99(l= 52 nm) and C-132(l= 60 nm). ML WS_2 were grown by APCVD on 300 nm thermally grown SiO_2 on Si. Properly cleaned and O_2 plasma-treated (60 W, 5 min) substrates were placed on an alumina boat containing 500 mg WO_3. A boat containing WO_3 powder was placed inside a 35 mm quartz tube in the heating zone of the furnace. Another boat containing 500 mg sulphur was placed upstream inside the tube, 15 cm away from the WO_3 boat. The sulphur boat was outside the heating zone and was heated using a heater coil. The tube was flushed with 500 sccm Ar for 20 min. The furnace was kept at 850 °C and the heater coil was kept at 240 °C for evaporation of sulphur. This set of temperatures was maintained for 10 min. After the growth, the system was allowed to cool naturally. The ML WS_2 was then transferred from the growth substrate to the NT substrates by wet-transfer method using polystyrene (PS)[104, 122]. As the layer number increases, the $A_1^{'}$ mode blue shifts by a few wavenumbers and the $E^{'}$ mode redshifts very gradually, as previously reported. Peak position difference of $A_1^{'}$ and $E^{'}$ in ML WS_2 is reported to be $\sim$ 65 cm^{-1} while for bilayer and more the difference become $>$ 68 cm^{-1}[29, 123]. This shows that the WS_2 in our study is indeed a monolayer. However, $A_1^{'}$ and $E^{'}$ mode redshifts due to tensile strain at a rate of -5.7 and $-$ 1.8 $cm^{-1}/\%$[124]. The ML WS_2 on top of C-99 is under a tensile strain of 0.15% (see Sec. XII) which translates into a peak difference increase of 0.6 cm^{-1}. This effect of strain on the peak difference is negligible (Fig.3.2).

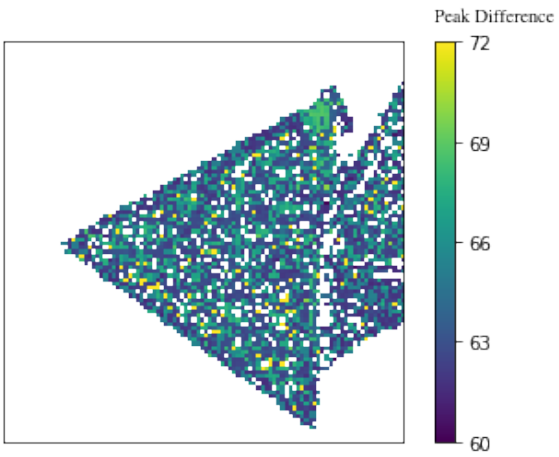

FIGURE 3.2: Raman peak position difference map of ($A_1^{'}$ - $E^{'}$) modes at room temperature.

The temperature-dependent PL and Raman measurements were done using continuous flow Oxford Instruments optical cryostat HiRes. The PL and Raman spectra were obtained in a WiTec Alpha 300 spectrometer mounted with a grating of 600 and 1800 lines/mm respectively using a Nikon 100X objective (numerical aperture (N. A.) = 0.80) lens. The samples were excited with a continuous wave laser of wavelength 514.5 nm and the spot

diameter was $\sim$ 0.4 μm. A water-cooled charged couple device (CCD) was used for detection. All measurements were done at a low pressure of 2×10^{-5} mbar pressure. The spectral resolution was $\sim$ 0.5 meV for PL and $\sim$ 1.3 cm^{-1} for Raman measurements. Liquid nitrogen was used as cryogen and temperature was varied between 77 K and 300 K. All measurements were done at an excitation power of less than 1 mW to prevent laser heating-related damage to the sample. PL and Raman mappings were done at room temperature and ambient pressure by placing the sample on a piezo stage using a Nikon objective lens of 100$\times$ magnification and 0.95 N. A.

Circularly polarized PL measurements, with a spatial resolution of $\sim$ 1.5 μm, were performed using a circularly polarized 532 nm (2.33 eV) laser. The micro-PL setup has a 0.55 m focal length monochromator coupled to a microscope arrangement built using a long working distance (WD) objective (magnification 50$\times$, numerical aperture 0.5, WD =12 mm). The sample was cooled using a liquid nitrogen cryostat with optical access. The PL signal was detected using a thermoelectric-cooled silicon-charged coupled device. For circularly polarized PL excitation we used a polarizer and a quarter waveplate with the laser and an identical combination at the detection end. A 532 nm narrow band pass filter was used in front of the laser and another 532 nm sharp long pass filter was used in front of the monochromator to block detection of the scattered laser.

3.2.1 Characterisation of as grown monolayer WS_2

Temperature-dependent PL of as-grown monolayer WS_2 placed on top of flat SiO_2/ Si substrate is presented in Figure 3.3a. At room temperature, a peak at $\sim$ 1.95 eV can be seen which can be unambiguously assigned to be a trion (X^-) as is widely done in literature [125–127]. The peak shows a characteristic blueshift of the trion with decreasing temperature[128].

Here, in CVD-grown WS_2 placed on top SiO_2/ Si, a well-resolved neutral exciton (X^0) peak cannot be seen because of the presence of charge substrate defects in SiO_2 which dopes the WS_2 channel. This effect is discussed in detail in one of our previous works [104]. This phenomenon in CVD-grown monolayer WS_2 is frequently reported in the literature as well [129, 130].

To observe a noticeable contribution of X^0, we transferred the as-grown monolayer WS_2 from SiO_2/ Si to a hole-patterned SiO_2/ Si substrate (Figure 3.3e) so that the monolayer WS_2 could be suspended freely. In this way, we can eliminate the effects of charge substrate defects in SiO_2 which dopes the WS_2 channel and see a significant contribution of neutral exciton X^0 [104].

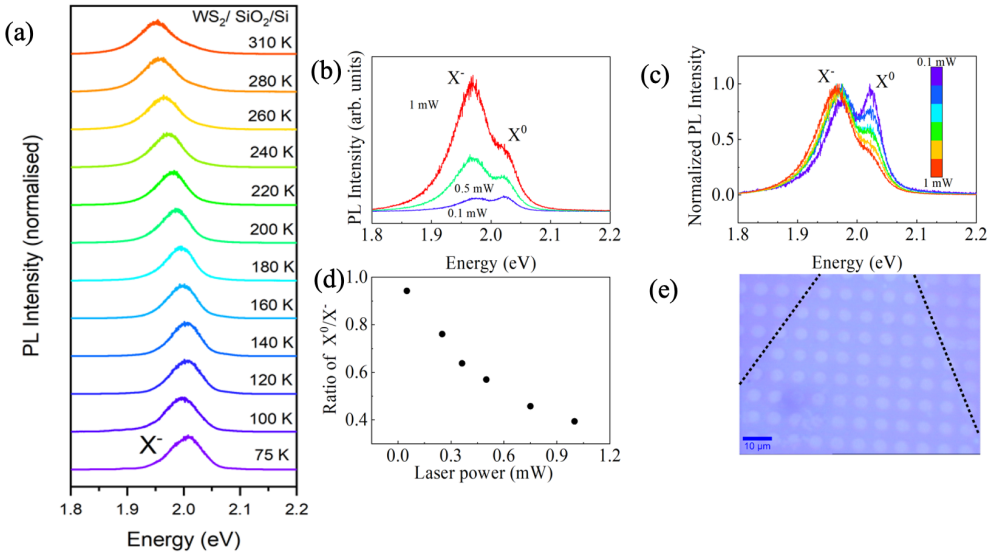

FIGURE 3.3: (a) Temperature-dependent PL of as grown monolayer WS_2 on top of SiO_2/ Si (b) Raw PL spectra of monolayer WS_2 excited with a laser of wavelength 514.5 nm for three different pump power. (c) Normalized PL spectra of monolayer WS_2 for various pump powers (pump power shown in the colour bar). The plot clearly shows that with increasing laser power the X^0 is efficiently getting converted to X^- due to laser-induced doping which increases the carrier density inside the WS_2 monolayer. (d) The ratio of exciton to trion intensity ratio clearly shows a decline in the exciton population and conversion to trion with increasing laser power. (e) Optical microscope image of WS_2 monolayer placed on top of hole patterned SiO_2/Si substrate (monolayer WS_2 shown with dashed lines).

Figure 3.3b shows the PL spectra of suspended WS_2 for three different laser powers. It can be seen that at lower laser power ($\sim$ 0.1mW) exciton and trion contribution are almost equal. But for higher laser powers trion contribution ($\sim$1.95 eV) increases steadily compared to exciton. This phenomenon is commonly observed in WS_2 and other TMDs as with increasing laser power photoinduced doping increases which favour the trion formation [104, 125, 131, 132]. Figure 3.3c is a normalised version of Figure 3.3b and it can be seen that neutral exciton contribution decreases with increasing laser power as a neutral exciton can now easily bind to an excess electron created due to photoinduced doping to form a trion [104]. Figure 3.3d also shows that exciton to trion intensity ratio decreases with increasing laser power [132]. Thus, from this experiment and analysis, we can conclude that the peak at $\sim$ 1.95 eV is a trion (X^-) and the peak at $\sim$ 2.01 eV is an exciton (X^0).

3.3 Theoretical Calculations

First-principle density functional theory-based calculations have been performed using the Quantum ESPRESSO suite of codes (done in collaboration with Dr Prasenjit Ghosh's group) [133, 134]. The electron-ion interactions were described by norm-conserving pseudopotentials [135]. The wavefunctions were expanded in a plane wave basis for which a kinetic energy cut-off of 90 Ry is used. The pseudopotentials were obtained from the Pseudo Dojo website [136]. TMDs show strong spin-orbit interactions that need to be incorporated in calculating their electronic structure [137]. To correctly account for this, we have solved the relativistic Kohn-Sham equations self-consistently [138, 139] using fully relativistic norm-conserving pseudopotentials for all elements. The electron-electron exchange-correlation functional has been described using the Perdew-Burke-Ernzerhof (PBE) parametrization of generalized gradient approximation (GGA) [140]. The Brillouin zone (BZ) was sampled with 6×6×1 Monkhorst-Pack k-point grid for BZ integrations. Since we are using periodic boundary conditions, a vacuum of about 30 Å had been used to minimize the spurious interactions between the periodic images along the direction perpendicular to WS_2 plane. The optimized lattice parameter for the unstrained monolayer is obtained to be a_0= 3.18 Å, which is in good agreement with previous studies[141]. The strained ML WS_2 was modelled via a change of the lattice constant relative to strain with

$$a_0^s = a_0(1 + \epsilon_s) \tag{3.1}$$

where a_0^s is strained lattice constant, and ϵ_s is the applied strain. We relax the atomic positions at each new strained lattice parameter.

The phonon dispersion and density of states (DoS) of ML WS_2 is calculated using the density functional perturbation theory (DFPT) method within the phonon package of Quantum ESPRESSO[142]. We sampled the momentum space with a 6×6×1 Monkhorst-Pack q-point grid. Although the change in the electronic band structure due to strain is much more pronounced, the phonon dispersion does not change considerably with strain. The change in phononic dispersion is less than 0.4 % per cent strain [143]. Therefore their energy and momentum can be considered constant in the range of strain in discussion in this paper. However, for consistency, in the main manuscript, we have considered the phonons for the strained system. The phononic dispersion shows that E$'$ phonon of momentum Λ is required for the scattering of bright KK exciton to the Λ valley to form dark KΛ exciton is available with a considerable density of states.

To calculate the temperature-dependent electronic bandstructure, we have computed the electron self-energies using EPW software[144, 145]. The electron self-energy ($\sum_{nk}^{EP}$) within the Midgal approximation is given by:

$$\sum_{nk}^{EP} = \sum_{q\nu,m} w_q \left| g^{SE}_{mn,\nu}(k,q) \right|^2 \left[\frac{n_{q\nu} + 1 - f_{mk+q}}{\epsilon_{nk} - \epsilon_{mk+q} - \hbar\omega_{q\nu} - i\delta} + \frac{n_{q\nu} + f_{mk+q}}{\epsilon_{nk} - \epsilon_{mk+q} + \hbar\omega_{q\nu} - i\delta} \right] \tag{3.2}$$

where $g^{SE}_{mn,\nu}(k,q) = \sqrt{\frac{\hbar}{2m_0\omega_{q\nu}}} \langle \psi_{mk+q} | \partial_{q\nu} V | \psi_{nk} \rangle$. w_q is the weight associated with phonon wavevector q in the brillouin zone, and ψ_{mk} represents the electronic wavefunction for band m, wavevector k and eigenvalue ϵ_{nk}. $\partial_{q\nu} V$ is the derivative of the self-consistent potential associated with a phonon of wavevector q, branch index ν and frequency $\omega_{q\nu}$.f_{mk+q} is the occupation of the electronic state and is given by Fermi-Dirac distribution. The temperature-dependent electronic eigenvalues are given by:

$$\epsilon_{nk}(T) = \epsilon_{nk} + \sum_{nk}^{EP}(T) \tag{3.3}$$

where ϵ_{nk} denotes the Kohn-Sham eigenvalue of the n, k electronic state.

The electron-phonon matrix elements are first computed using coarse k and q grids as mentioned earlier. These are then interpolated to a dense 200 x 200 x 1 q-mesh for the ML WS_2. We used 25 meV Gaussian broadening to smear the δ function.

3.4 Temperature dependent photoluminescence spectroscopy

The PL measurements were performed using a continuous wave laser of wavelength 514.5 nm (2.41 eV). In the temperature-dependent PL study of ML WS_2 on C-99 substrate [Fig. 3.8a], two well-resolved peaks, one at $\approx$ 2.01 eV (FWHM$\approx$ 24 meV) and other at $\approx$1.95 eV (FWHM$\approx$ 32 meV) were observed at 280 K. The peak position and width were extracted from each PL spectra by fitting with a sum of Gaussian functions because of the large inhomogeneous broadening:

$$I(E) = \sum_j \frac{A_j}{w_j \sqrt{\frac{\pi}{2}}} e^{-\frac{2(E-E_{cj})}{w_j^2}} \tag{3.4}$$

where *I* is intensity, *E* is energy, E_{cj} is peak position, w_j is width and A_j is the integrated area under the curve for j^{th} peak. The fairly good fits obtained with such a lineshape, as shown in Fig. 3.4, indicate that this approximation is reasonable. We attribute the peak at 2.01 eV to a bright exciton KK (X^0) and the peak at 1.95 eV to a negatively charged trion (X^-) since ML WS_2 is a n-doped semiconductor. We further confirm this assignment by varying the laser excitation power which alters the exciton density inside the ML WS_2 channel (see Figure. 3.3) [146]. As we lower the temperature both X^0, X^- blueshift as reported earlier [128]. At around 200 K, a new peak appears at $\approx$1.94 eV. As we further

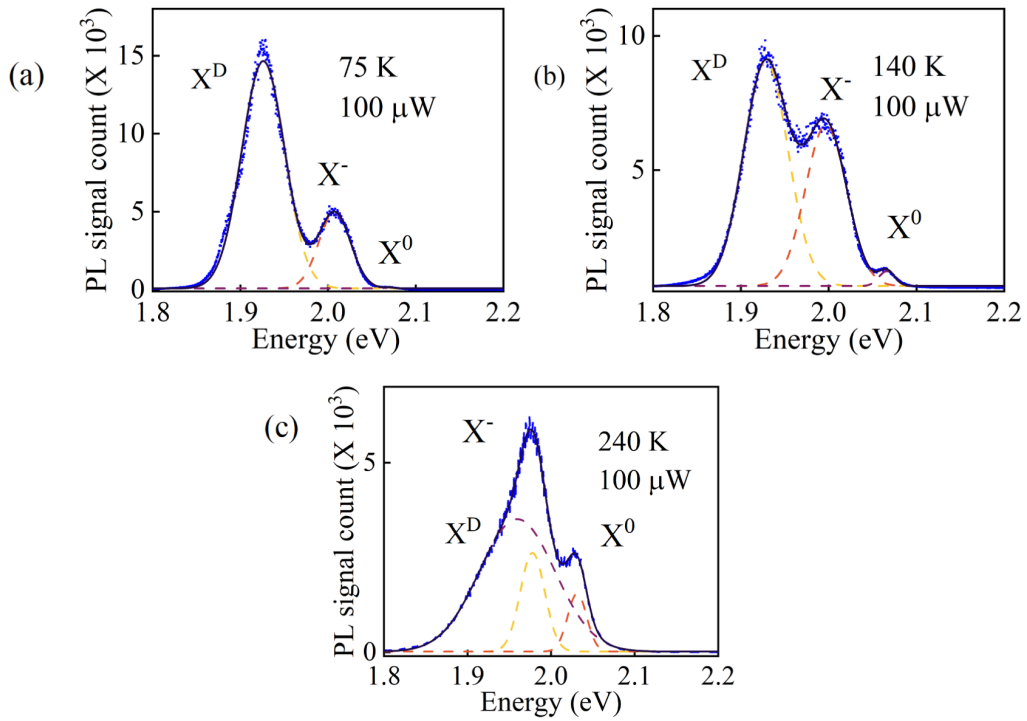

FIGURE 3.4: (a)-(c) PL spectrum of ML WS_2 on C-99 substrate fitted with sum of Gaussians. The dashed lines represent the individual fitted components, the solid black line is the cumulative fit and the blue dots represent the raw data.

decrease the temperature, the intensity of the new peak increases while that corresponding to X^- and X^0 diminishes, consistent with the earlier proposal by Feierabend et al. for $K\Lambda$ dark exciton brightening [38]. The 1.94 eV peak can be attributed to (a) a biexciton, XX (b) a defect-bound exciton (X^L), or (c) a dark exciton (X^D). The exponent α of the power law dependence (integrated intensity as a function of excitation power) for XX and X^L is known to be superlinear ($\sim$2.0) and sublinear ($\sim$0.5), respectively [126, 128, 147]. From the I vs P plot, we obtain a value of $\alpha \sim 1.0$ for the new peak, typical of an exciton [126, 128, 147] (see Fig. 3.8). Also, see excitation power dependence data of X^D for another WS_2/C-99 sample where we extracted $\alpha \sim 1.14$ (see Fig. 3.5). Moreover, the new peak shows no blueshift with increasing excitation power, characteristic of X^L because of its broad energy distribution [148, 149]. However, it showed a red shift due to local heating, a behaviour generally seen in excitons [104] Fig. 3.7a. Furthermore, the new peak also shows anisotropy in circular polarization-dependent PL, uncharacteristic of X^L [149, 150] Fig. 3.7b. Sample is excited with right-handed circularly polarised (σ^+) laser and the emitted PL is measured in both σ^+ and left-handed (σ^-) polarisation. The X^D peak showed a degree of polarization (DoP)= $\frac{I_{\sigma+}-I_{\sigma-}}{I_{\sigma+}+I_{\sigma-}}$ of magnitude 13% even with a off-resonant excitation (off by $\sim$ 380 meV from X^D exciton resonance energy), similar to earlier report[151].The I_{σ^+/σ^-} was

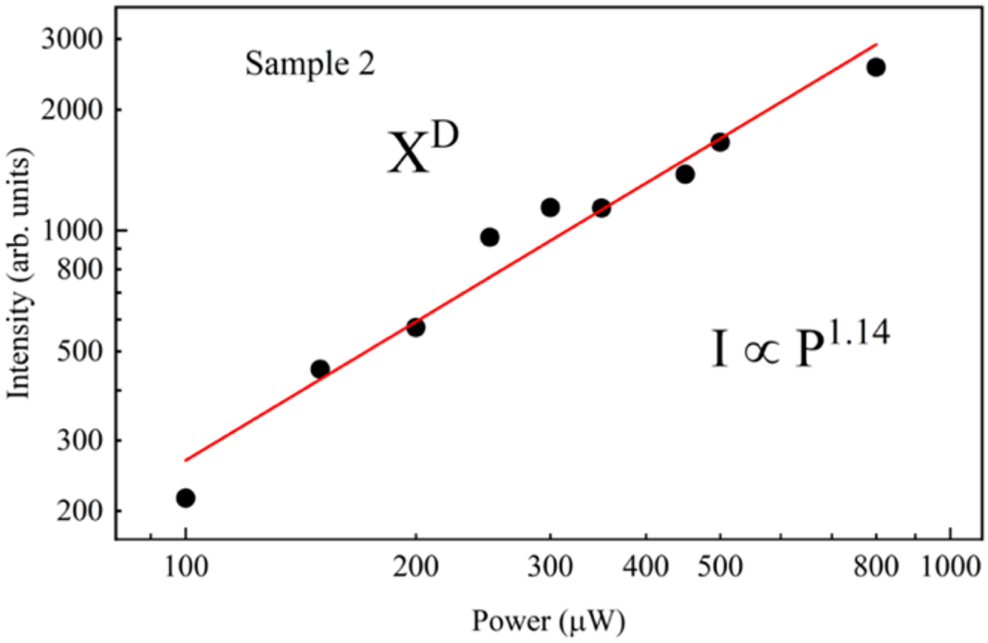

FIGURE 3.5: The integrated intensity (I) of X^D as a function of excitation laser power (P) for WS_2/C-99 Sample 2. The data is fitted with the relation $I \propto P^{\gamma}$ (red solid line). The extracted exponent γ is indicated in the plot.

obtained by spectrally integrated Gaussian fit of the X^D peak (Fig. 3.7b lower panel)[151]. To confirm that the weak polarization anisotropy of X^D is indeed due to valley effects and not measurement artefacts, we excited the sample with linearly polarized light which will initially populate the K and K′ valley equally. The emitted σ^+ and σ^- light showed ~ 0 % DoP (Fig. 3.7b upper panel). This confirms that the polarization anisotropy is due to the coupling of spin and valley degrees of freedom and the origin of X^D is not related to localization of excitons at the defect site (X^L)[149, 150]. Therefore, the new peak is neither XX nor X^L. The value of α and its peak position at 77 K $\sim$ 1.92 eV is similar to recent reports of observation of $K\Lambda$ dark exciton under compressive strain and strong exciton-phonon coupling[116]. We, therefore, attribute the peak at $\sim$ 1.92 eV as X^D. We performed a similar study on the other two samples, namely, C-48 and C-132 [Fig. 3.8b and c]. For the C-48 and C-132 samples, we observed X^0 and X^- peaks at every temperature, but no new peaks were observed as we lowered the temperature to 77 K.

The temperature dependence of the peak position of X^0 in the C-99 sample was studied in detail (Fig. 3.8e). The temperature dependence can be described by the phenomenological

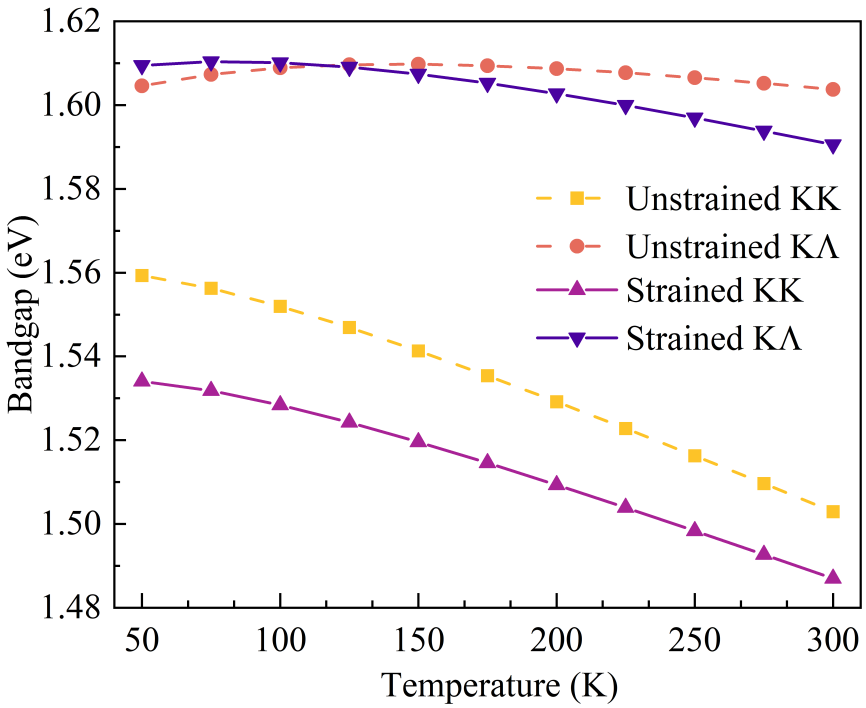

FIGURE 3.6: Temeperature dependence of the renormalized $K - K$ and $K - \Lambda$ electronic bandgap with 0.2% strain within Midgal approximation. We note that the direct band gap ($K - K$) for both the strained and unstrained systems show a much larger variation as a function of temperature compared to that observed for the indirect one ($K - \Lambda$). Moreover, this indirect band gap for the strained system is more sensitive to temperature than that of the unstrained one.

model proposed by O'Donnell and Chen [152]:

$$E(T) = E(0) - S\langle\hbar\omega\rangle\left(\coth\frac{\langle\hbar\omega\rangle}{k_{\mathrm{B}}T} - 1\right) \tag{3.5}$$

where $E(T)$ is the resonance energy of X^0 at temperature T, S is dimensionless exciton-phonon coupling constant, k_{B} is Boltzmann constant and $\langle\hbar\omega\rangle$ is the average phonon energy responsible for the coupling. By fitting the experimental data we obtained the parameters, $E(0) = 2.074 \pm 0.003$ eV, $S = 3.65 \pm 0.98$ and $\langle\hbar\omega\rangle = 43 \pm 10$ meV. The value of $\langle\hbar\omega\rangle$ is close to the energy of $E^{'}$ phonon ($\sim$ 44 meV) mode of ML WS_2. This suggests that the $E^{'}$ phonon mode is crucial in the exciton-phonon coupling. Note that the peak position of X^D changes only by $\sim$2 meV as we increase the temperature from 77 K to 180 K, whereas, in the same temperature range, the X^0 peak position changes by $\sim$20 meV. This observation aligns with our theoretical calculations (Fig 3.6), which shows that the electronic direct bandgap at the K point changes at a much faster rate with temperature in comparison to the indirect $K - \Lambda$ bandgap.

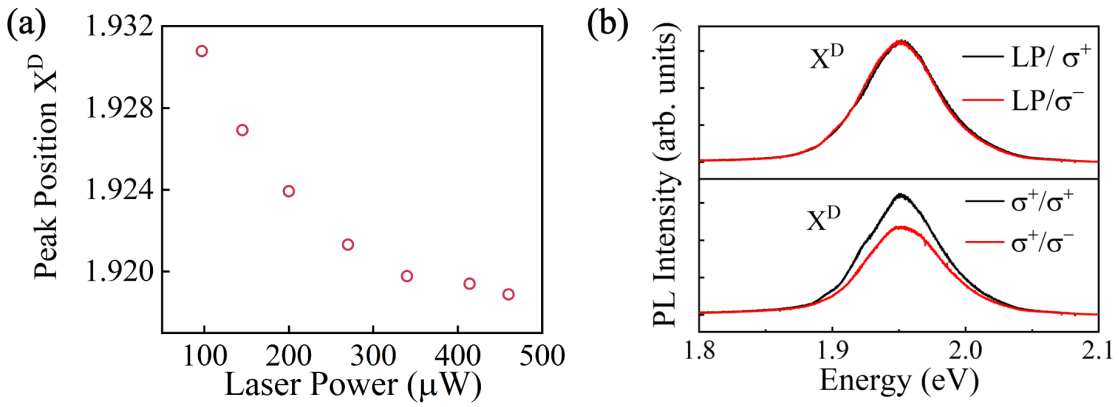

FIGURE 3.7: (a) Variation of emission peak energy of X^D in ML WS_2 on C-99 substrate at 77 K with pump laser (514.5 nm) power. (b) PL spectra of the X^D peak for σ^+ and σ^- polarized detection after excitation with linearly polarized light (upper panel) and σ^+ light (lower panel) at 77 K.

To determine the strength of exciton-phonon coupling, the evolution of the FWHM of X^0 was fitted by a phonon-induced broadening model, Fig. 3.8f [47, 153]:

$$\gamma = \gamma_0 + c_1 T + \frac{c_2}{e^{\frac{\hbar\omega}{k_B T}} - 1} \tag{3.6}$$

where γ_0 is the intrinsic FWHM, the linear term in T is due to the interaction of acoustic phonon modes and the last term describes the interaction with optical phonon modes. The linear term is negligible compared to the last term, as formulated in [154]. The c_2 is the measure of the exciton-optical phonon coupling strength. The value of $\hbar\omega$ obtained by fitting Eq. 3.5 was used for fitting Eq. 3.6. The value of c_2 obtained by fitting Eq. 3.6 is 26.5 $\pm$ 4.6 meV and is significantly higher than the previously reported value of 6.5 for ML WS_2 [47]. This higher value of c_2 further confirms the strong exciton and E′ phonon mode coupling in the C-99 substrate.

3.5 Temperature dependent Raman spectroscopy

We further did a temperature-dependent Raman study on the C-99 sample. The various Raman peaks (E′, 2LA, A_1') were analysed with multiple Lorentzian functions, Fig. 3.11a

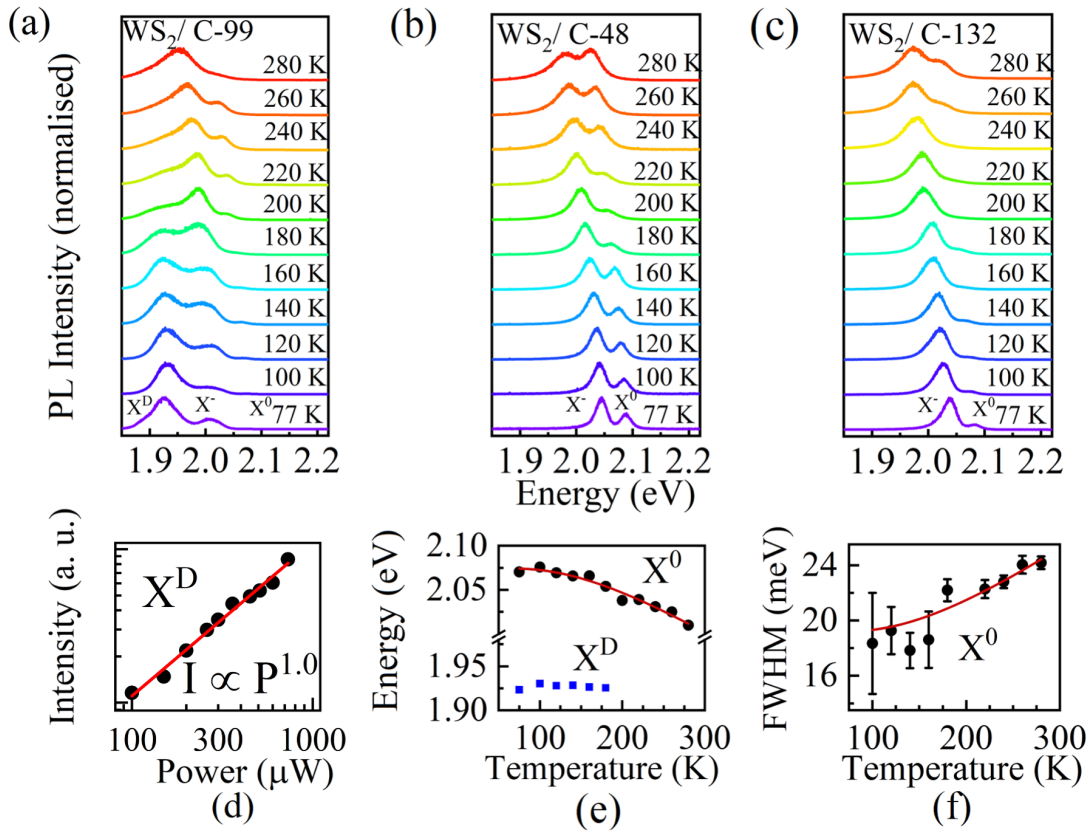

FIGURE 3.8: Temperature dependent PL spectra of ML WS_2 placed on top of (a) C-99 (b) C-48 and (c) C-132 substrates. All the spectra are recorded at an excitation power of $\sim$ 100 μW. The spectra are shifted along the y-axis for clarity. (d) The integrated intensity (I) of X^D as a function of excitation power (P) fitted with the relation $I \propto P^{\alpha}$ where α is the exponent. (e) Temperature dependence of the peak position of X^0 (black solid circles) and X^D(blue solid squares), the temperature dependence of X^0 is fitted with Eq. 3.5 (red line). (f) FWHM of X^0 as a function of temperature fitted with Eq. 3.6.

[155]:

$$I(E) = \sum_j \frac{2A_j w_j}{4\pi(E - E_{cj})^2 + w_j^2} \tag{3.7}$$

where I is intensity, E is energy, E_{cj} is peak position, w_j is width and A_j is the integrated area under the curve for j^{th} peak. The room temperature Raman map of the ML WS_2 flake placed on top of the C-99 substrate is shown in Fig. 3.10. The fairly good fits obtained with such a lineshape, as shown in Fig. 3.9, indicate that this approximation is reasonable.

The E' mode showed unusual blueshift and decreasing linewidth with increasing temperature [see Fig. 3.11b, c]. This anomalous behaviour of E' phonon mode is related to electron-phonon coupling [156–158]. The Raman linewidth with temperature is generally explained by the anharmonic cubic equation [159, 160]:

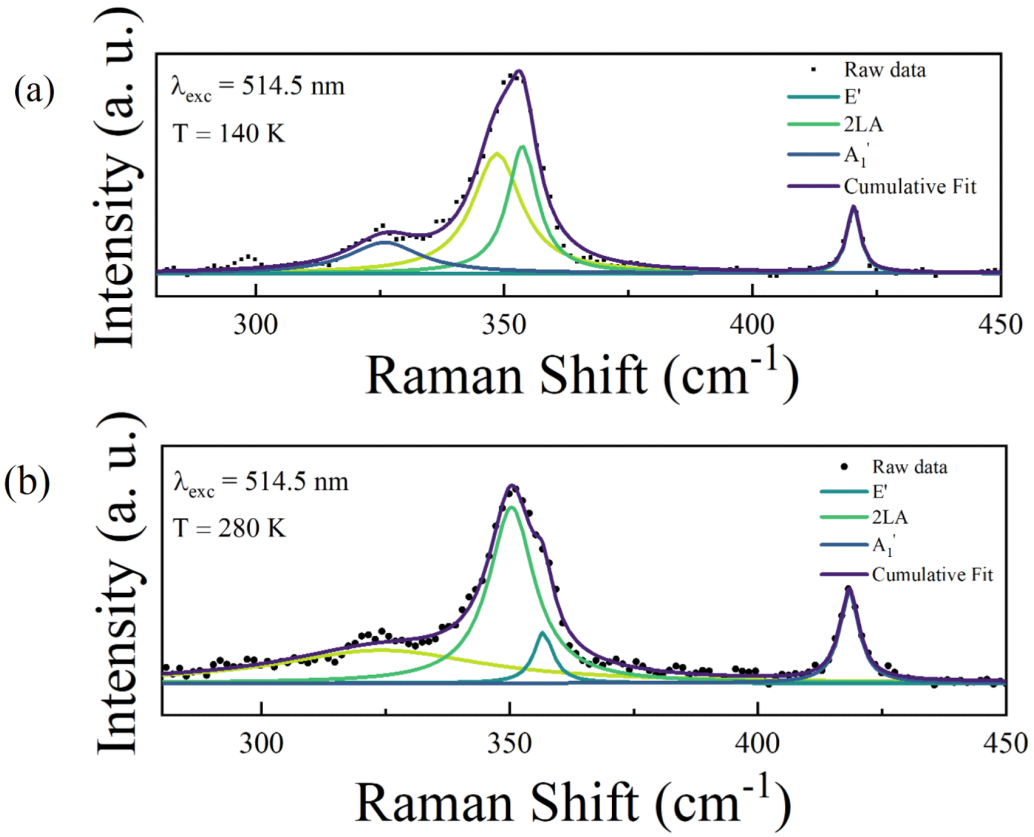

FIGURE 3.9: Raman spectrum of ML WS_2 on C-99 substrate fitted with the sum of Lorentzians at (a) 140 K and (b) 280 K.

$$\gamma_{ph}(T) = \gamma_0 + C\left[1 + 2f_-\left(\frac{\hbar\omega_0}{2k_BT}\right)\right] \tag{3.8}$$

where $\gamma_{ph}(T)$ is the linewidth at temperature T, γ_0 is the linewidth at T= 0 K, $\hbar\omega_0$ is the E$'$ phonon energy, $f_\pm(x) = \frac{1}{e^x \pm 1}$ and C is a constant. Eq. 3.8 is simulated in the inset of Fig. 3.11c (green curve). The E$'$ phonon modes show an opposite trend which is not explained by Eq. 3.8 because it takes into account only phonon-phonon interaction (γ_{ph}) and not the electron-phonon interaction (γ_{e-ph}) term [161]. $\gamma_{e-ph}(T)$ is described by the following equation [157]:

$$\gamma_{e-ph}(T) = \gamma_{e-ph}(0)\left[f_+\left(\frac{-\hbar\omega_0}{2k_BT}\right) - f_+\left(\frac{\hbar\omega_0}{2k_BT}\right)\right] \tag{3.9}$$

where, $\gamma_{e-ph}(0)$ is the linewidth at T= 0 K due to electron-phonon coupling. In the inset of Fig. 3.11c, the red curve is simulated with $\gamma(T) = \gamma_{ph} + \gamma_{e-ph}$ and closely resembles the experimental data, thus showing the role of electron-phonon coupling. The phonon-phonon interaction term in the Raman frequency, $\omega_{ph}(T) = \omega_0 - D\left[1 + 2f_-\left(\frac{\hbar\omega_0}{2k_BT}\right)\right]$ [161], where

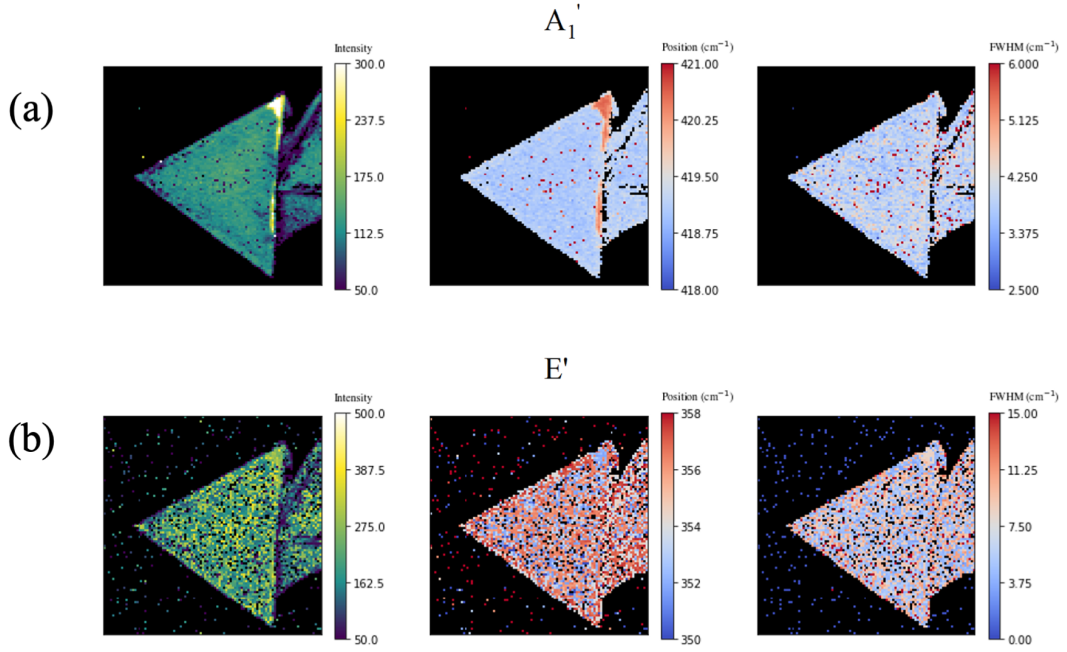

FIGURE 3.10: Room temperature Raman map of the ML WS_2 flake placed on top of C-99 substrate. Intensity, position and FWHM map of the (a) $A_1^{'}$ and (b) $E^{'}$ phonon mode.

ω_0 is the frequency at T= 0 K and D is constant, was simulated in the inset of Fig. 3.11b (blue curve) to show the anomalous behaviour of $E^{'}$ peak position. The non-anomalous behaviour of $A_1^{'}$ peak is shown in Fig. 3.12 a and b.

3.6 Exciton-phonon coupling

To understand the effect of strain on the electronic structure of ML-WS_2 we computed the same within the framework of DFT using full-relativistic norm-conserving pseudopotential with Perdew−Burke−Ernzerhof (PBE) exchange-correlation functionals alongside plane waves, as implemented in Quantum ESPRESSO package [Fig. 3.14a] [133–135, 137–142, 162]. With increasing tensile (compressive) strain, the CBM and CBM+1 at K shift down (up), while the CBM at Λ shifts up (down). The K VBM move up (down) on the application of tensile (compressive) strain, Fig. 3.14a. We denote the direct bandgap at K between CBM+1 and VBM as E^{KK} and the indirect bandgap at Λ as $E^{K\Lambda}$. Note that, in the electronic band structure of the unstrained WS_2, the Λ CBM is at higher energy than the CBM+1 at K by $E^{K\Lambda}-E^{KK} = \Delta E^{K\Lambda} \sim 47$ meV. To get into the exciton picture [Fig. 3.14b] from the electron-hole picture (as described in ref. [31, 37]), we need to calculate the binding energy E_b of the excitons. The exciton binding energy was calculated by determining the quasiparticle band gap corresponding to the energy of a separated electron-hole pair. This is

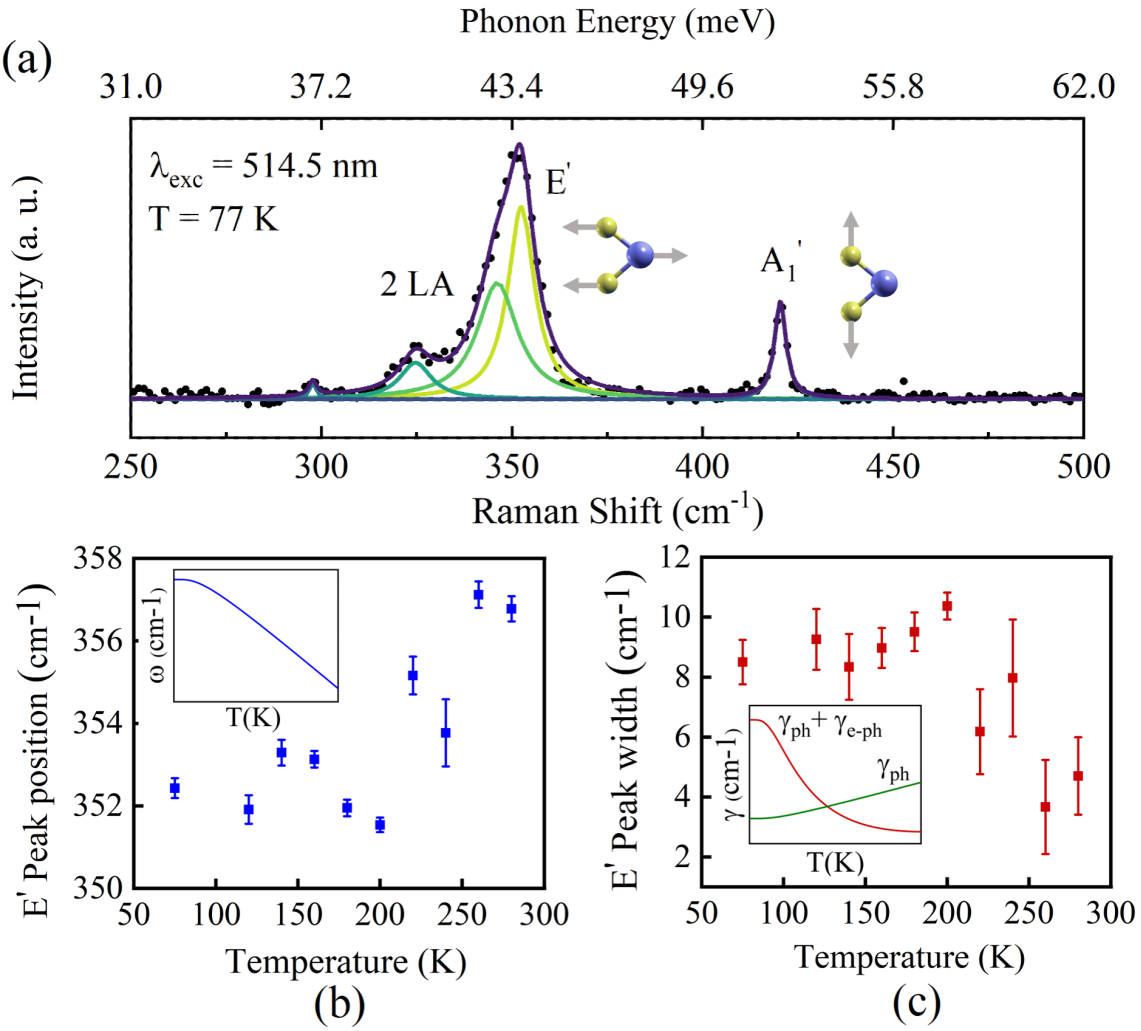

FIGURE 3.11: (a) Raman spectra of ML WS_2 placed on top of C-99 substrate at 77 K. Various peaks are labelled according to ref. [155]. The main vibrational modes $E^{'}$ and $A_1^{'}$ are shown in the schematic. The blue and yellow balls represent tungsten (W) and sulfur (S) atoms respectively. Anomalous behaviour of $E^{'}$ peak (b) position and (c) width as a function of temperature. Simulated ω_{ph} and γ_{ph} are shown in the insets of Fig. 3.11b (blue curve) and Fig. 3.11c (green curve) respectively. $\gamma(T) = \gamma_{ph} + \gamma_{e-ph}$ (red curve) is simulated in the inset of Fig. 3.11c.

done in semiconductors by fitting the excitonic peaks to a hydrogenic Rydberg series[163]. In 2D, this hydrogen model employs an effective mass Hamiltonian[29]:

$$H = -\hbar^2 \frac{\nabla_r^2}{2\mu} + V_{eh}(r) \tag{3.10}$$

where $\frac{1}{\mu} = \frac{1}{m_e} + \frac{1}{m_h}$ is reduced mass of exciton, m_h and m_e are the effective masses of hole and electron respectively. and $V_{eh}(r) = \frac{-e^2}{\epsilon r}$ is a locally screened attractive electron-hole interaction. This model predicts exciton transition energies of E_g-$E_b^{(n)}$, where E_g is the

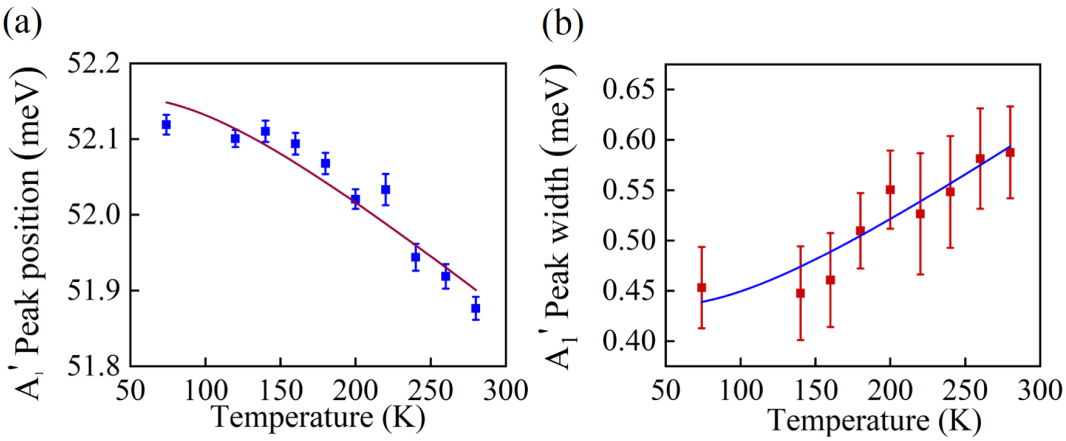

FIGURE 3.12: Non-anomalous behaviour of $A_1^{'}$ peak (a) position and (b) width as a function of temperature. The solid lines in (a) and (b) are fitted lines with Eq 3 and 4 of the main paper respectively.

TABLE 3.1

Strain (%)	E_{el}^{KK}(eV)	$E_{el}^{K\Lambda}$(eV)	E_{ex}^{KK} =E_{el}^{KK}−$E_b^{X^0}$ (eV)	$E_{ex}^{K\Lambda}$ =$E_{el}^{K\Lambda}$−$E_b^{X^D}$ (eV)	E_{ex}^{KK}−$E_{ex}^{K\Lambda}$ (meV)
0.6	1.513	1.661	1.203	1.223	-20
0.5	1.526	1.658	1.216	1.220	-4
0.4	1.539	1.655	1.229	1.217	12
0.3	1.552	1.652	1.242	1.214	28
0.2	1.566	1.649	1.256	1.211	45
0.1	1.578	1.647	1.268	1.208	60
0	1.594	1.641	1.284	1.203	81
-0.1	1.607	1.640	1.297	1.203	94
-0.2	1.621	1.637	1.311	1.199	112
-0.3	1.635	1.633	1.325	1.195	130
-0.4	1.650	1.629	1.340	1.191	149
-0.5	1.664	1.626	1.354	1.188	166
-0.6	1.679	1.623	1.368	1.184	184

quasiparticle gap and

$$E_b^{(n)} = \frac{\mu e^4}{2\hbar^2\epsilon^2(n-\frac{1}{2})^2} \tag{3.11}$$

m_e and m_h are calculated from parabolic band approximation[164] of the electronic bands obtained from DFT calculations. ϵ of ML-WS_2 was taken to be ~ 5 for $n = 1$ as was shown in [29] The effective masses of electrons in CBM+1 at K and in CBM at Λ points of the BZ and those of holes at K point of the BZ are reported in Table 3.2 using the band dispersion obtained from PBE and Gau-PBE functionals. We note that both the functionals yield similar values of effective masses. Using Eq. 3.11 we found E_b of X^0 and X^D $\sim$ 310 meV and 438 meV respectively. Also, we introduce the center-of-mass momentum $\mathbf{Q}= \mathbf{k}_2-\mathbf{k}_1$, where $\mathbf{k}_1$, $\mathbf{k}_2$ are momenta of two bound particles. Now, if we visualize the scenario in the excitonic picture, the bright exciton state is formed at $K - K$, at the energy

TABLE 3.2: The values of the effective masses of electron at the CBM+1 of K point, CBM of Λ point (m^e_K and m^e_Λ respectively) and VB maxima at K point (m^h_K).

Theory	m^e_K	m^h_K	m^e_Λ	μ_{K-K}	$\mu_{K-\Lambda}$
PBE	0.27 m_0	0.36 m_0	0.56 m_0	0.16 m_0	0.22 m_0
Gau-PBE	0.32 m_0	0.40 m_0	0.50 m_0	0.17 m_0	0.22 m_0

TABLE 3.3: Same parameters as reported in Table 3.1 computed using Gau-PBE functional.

Strain (%)	E^{KK}_{el}(eV)	$E^{K\Lambda}_{el}$(eV)	E^{KK}_{ex} =E^{KK}_{el}−$E^{X^0}_b$ (eV)	$E^{K\Lambda}_{ex}$ =$E^{K\Lambda}_{el}$−$E^{X^D}_b$ (eV)	E^{KK}_{ex}−$E^{K\Lambda}_{ex}$ (meV)
0.6	1.948	2.130	1.638	1.692	-54
0.0	2.041	2.111	1.731	1.673	58
-0.6	2.138	2.100	1.828	1.662	166

position $E^{KK}_{exc} = E^{KK} - E^{X^0}_b$ and the dark exciton state is formed at $K-\Lambda$, at the energy position $E^{K\Lambda}_{exc} = E^{K\Lambda} - E^{X^D}_b$ [37]. Our calculations show that, in the unstrained sample, the dark state is below the bright state by energy $E^{KK}_{exc} - E^{K\Lambda}_{exc} = \Delta E_1 \sim 81$ meV. Under tensile (compressive) strain, the excitonic states at $K-K$ and $K-\Lambda$ go down (up) and up (down) respectively. The change of ΔE as a function of strain is plotted in Fig. 3.14c. Values used for generating Fig. 3.14 using PBE functional are shown in Table 3.1. Since strain does not significantly affect the band dispersion [37, 165] we have considered $E^{X^0}_b$ and $E^{X^D}_b$ corresponding to that of the unstrained system. The fitting shows $\sim 170 \pm 1.4$ meV change of ΔE with 1% of applied strain. Note that strain has little influence on E_b [37, 165]. As PBE underestimates the bandgap, we have used Gau-PBE hybrid functionals [166] with $E^{Fock}_{cut} =$ 90 Ry and a 3×3×1 q-mesh for computing the Fock operator. The direct bandgap at K was found to be $\sim$ 2.01 eV which is in close agreement with the experimentally obtained value of $\sim$ 2.05 eV[123]. As shown in Tables 3.2 and 3.3 and Fig. 3.13, the trend in the different energy differences between Kohn-Sham eigenvalues and the effective masses computed using PBE and Gau-PBE are similar. Hence we believe that the results will remain qualitatively unchanged even if we use PBE functional. Since computing electron-phonon coupling with hybrid functionals are prohitively expensive, we have computed those with PBE functional only.

On optically exciting a coherent exciton population at $K-K$, bright excitons are formed. Incoherent excitons are then formed at $K-\Lambda$ by phonon-assisted scattering of excitons from $K-K$, where a phonon compensates for the energy and momentum mismatch [Fig. 3.14b] [45]. However, in the unstrained case, phonon modes with energy $\Delta E_1 \sim 81$ meV are not available, therefore, excitons are not formed at $K-\Lambda$. On applying tensile strain (theoretically) on the ML WS_2, we observe ΔE decreases and under $\sim$0.21% strain the value of ΔE_1 is reduced to $\Delta E_2 \sim 44$ meV, thereby making the optical phonons accessible to couple with the exciton for phonon-assisted scattering. To estimate the amount of strain on ML WS_2 on top of C-99 substrate due to nanopillars, PL mapping was done and the

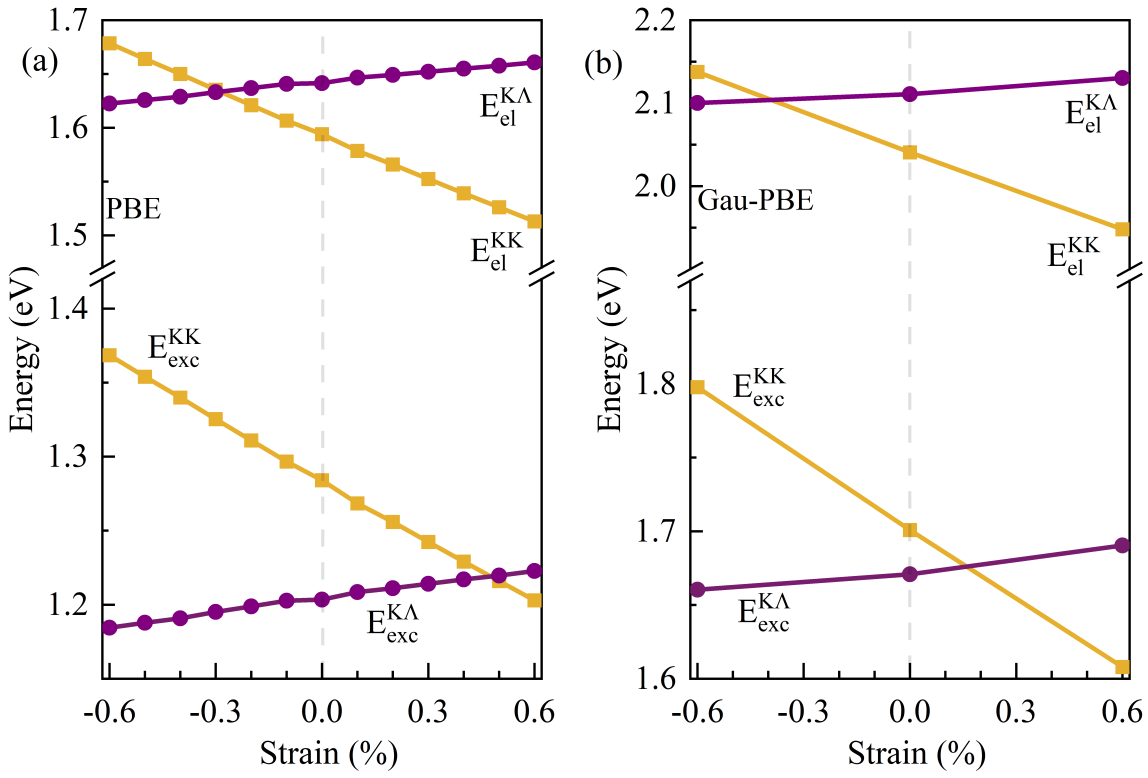

FIGURE 3.13: Electronic and excitonic bandgap KK and KΛ as a function of strain calculated using (a) PBE and (b) Gau-PBE using data from Table 3.1 and Table 3.3. We note that the qualitative trends are independent of the choice of functionals.

average peak position of X^- in the C-99 sample was compared with the average X^- peak position in ML WS_2 on top of flat SiO_2/Si. Therefore, we can experimentally estimate that ML WS_2 on top of C-99 is under a tensile strain of $\sim$ 0.15 % which is in very close agreement with the theoretical value of $\sim$0.21%. In the C-99 sample, phonon-assisted scattering of excitons from $K - K$ to $K - \Lambda$ is possible, thereby forming a population of dark excitons. The scattering process is illustrated in the schematic Fig. 3.14b. An E$'$ phonon with momentum $K - \Lambda$ and energy $\sim$44 meV can make this scattering possible. The calculated phonon density of states shows a large number of phonon states available at $\sim$44 meV, thereby making this scattering more favourable [Fig. 3.14d]. Note that change of phonon energy with strain is very negligible [143]. To estimate the scattering strength we calculate the electron-phonon matrix element $g^{\nu}_{mn}(\mathbf{k}, \mathbf{q})$ [Fig. 3.15a, b] using the formalism described in ref. [144, 167, 168] as,

$$g^{\nu}_{mn}(\mathbf{k}, \mathbf{q}) = \langle \psi_{m,\mathbf{k}+\mathbf{q}} | \partial_{\mathbf{q}\nu} V | \psi_{n\mathbf{k}} \rangle, \tag{3.12}$$

where $\psi_{n\mathbf{k}}$ is the electronic wavefunction for nth band at $\mathbf{k}$ k-point of the Brillouin zone, ν is phonon band index, $\partial_{\mathbf{q}\nu} V$ the derivative of the self-consistent potential associated with E$'$ phonon of momentum q. Here, we consider the hole to be fixed at the K VBM [Fig.

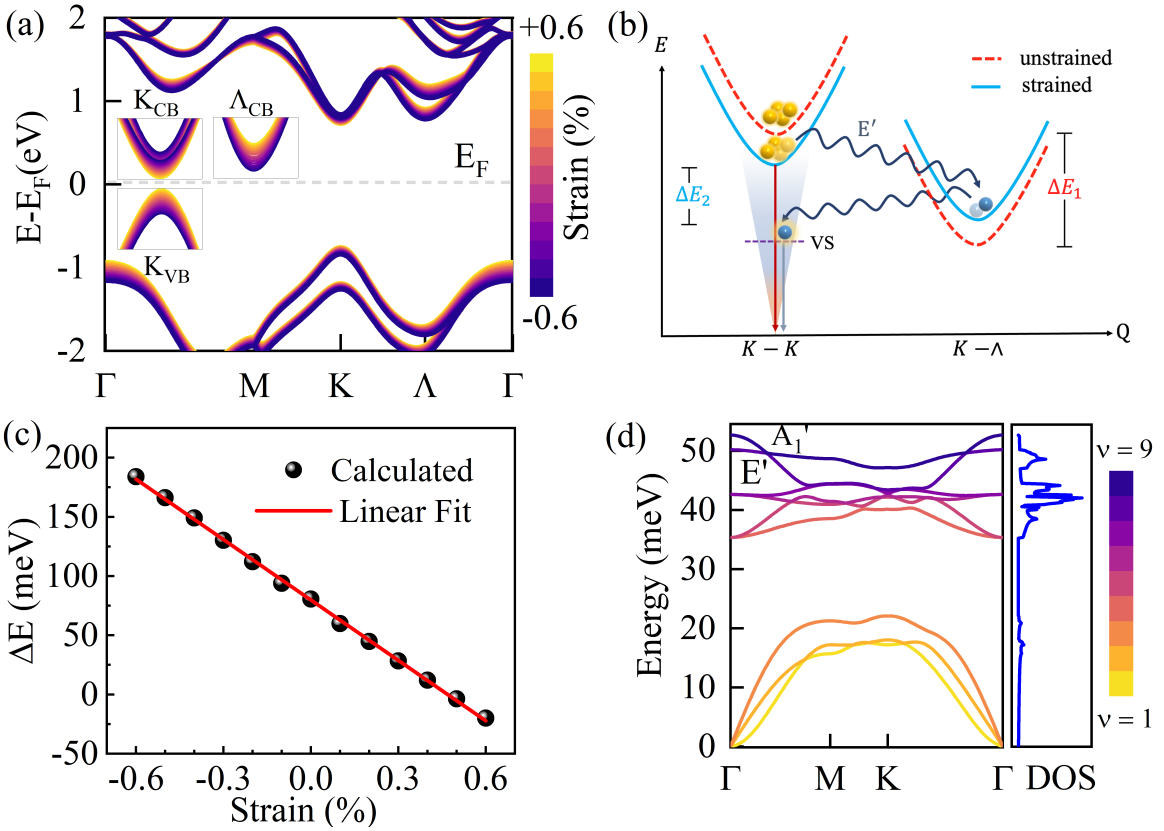

FIGURE 3.14: (a) DFT computed electronic bandstructure of ML WS_2 with different strain values. (b) Schematic showing the E$^{'}$ phonon mediated scattering of the bright $K-K$ excitons to dark $K-\Lambda$ due to tensile strain. The $K-\Lambda$ excitons then decay to a virtual state (dotted violet line marked as VS) inside the light cone (shaded area) by emitting phonons and finally recombine radiatively from the VS by emitting photons. (c) ΔE as a function of strain on ML WS_2. (d) Phonon dispersion (left panel) and phonon density of states (DOS) (right panel). ν represents the phonon band index.

3.15a] and take into account the scattering of electrons from CBM+1 at K to Λ CBM with a phonon of momentum $\mathbf{q} = \mathbf{K} - \mathbf{\Lambda}$ and energy value ΔE_2 = energy of E$^{'}$ phonon mode. Two degenerate E$^{'}$ phonon modes ($\nu = 6, 7$) with momentum $K-\Lambda$ shows significant coupling strength $\sim$ 28 meV for the concerned scattering [Fig. 3.15c]. We note that this value is comparable with the experimentally estimated exciton-phonon coupling strength reported in the previous paragraphs. The dark excitons at $K-\Lambda$ then can scatter non-radiatively to a virtual state inside the light cone at $K-K$ by emitting phonons. Once inside the light cone, the dark excitons can decay radiatively from the virtual state by emitting photons, thus leaving its signature in the PL spectra. A recent study [119] reported the existence of dark exciton in WSe_2 under tensile strain without any mechanism for their brightening. Nevertheless, our model can describe their experimental observation well because both WS_2 and WSe_2 have rather similar excitonic behaviour [31]. The X^D peak was not observed in ML WS_2/C-48 and C-132 samples [Fig. 3.8b, c] as the imparted tensile strain was less and

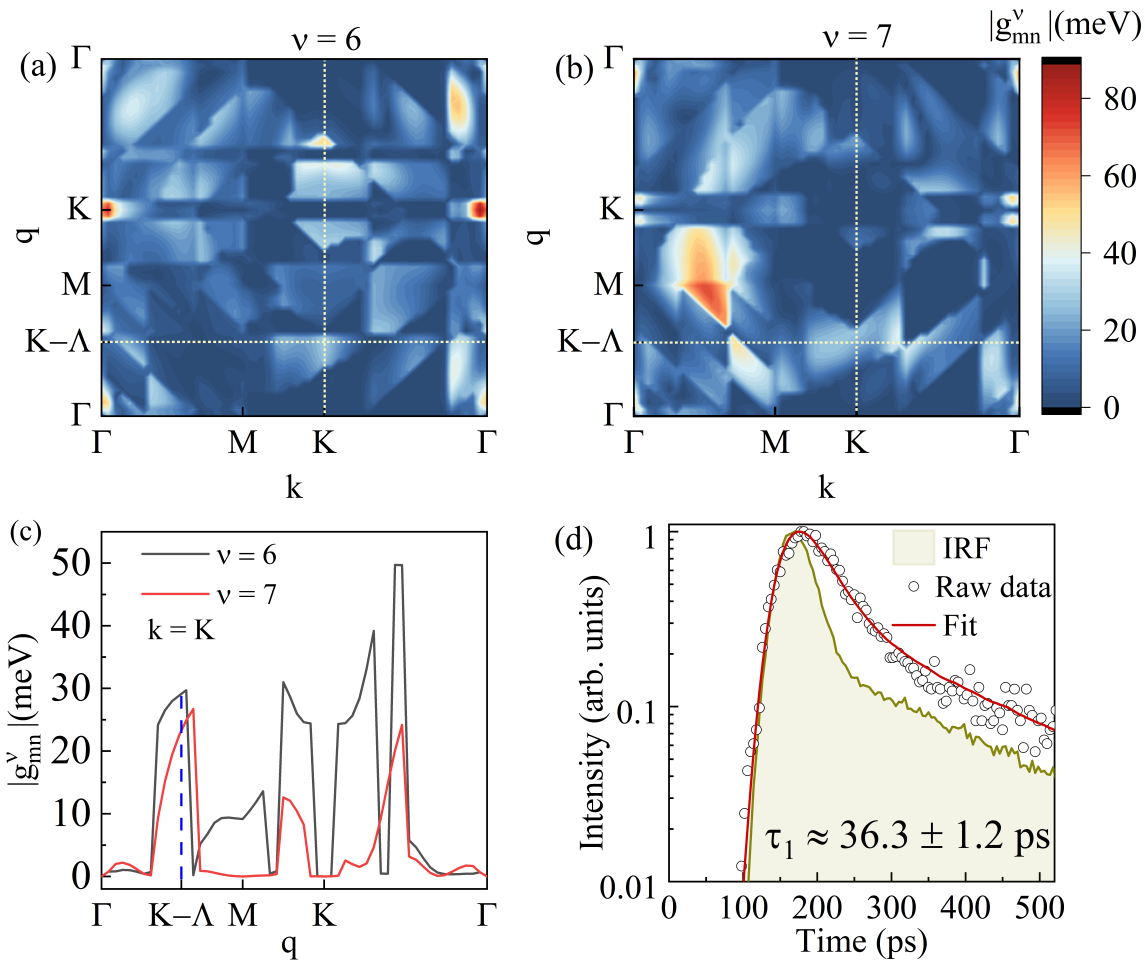

FIGURE 3.15: (a) and (b) Calculated g^{ν}_{mn} value for two degenerate E$'$ phonon modes with $\nu = 6$ and 7 respectively, responsible for the scattering of electrons from CBM+1 at K to CBM at Λ valley. (c) Line-cut along $k = K$ from (a) and (b) to show the g^{ν}_{mn} along the phonon momentum (q), $\Gamma \rightarrow M \rightarrow K \rightarrow \Gamma$ direction. The blue dashed line shows the g^{ν}_{mn} of q= $K - \Lambda$ at $k = K$. (d) TRPL measurement on ML WS_2 at 60 K to determine the lifetime of X^D.

so the ΔE value was not close to the energy of any available phonon mode which can open the scattering channel from $K - K$ to $K - \Lambda$ points.

3.6.1 Experimental Estimation of strain on WS_2 flake on top of C-99 substrate

From the PL map of X^- and X^0 the distribution of their position was plotted. The statistical distribution was fitted with a normal distribution to extract the mean and standard deviation. To find out the amount of strain on ML WS_2 on top of C-99 substrate due to nanopillars, its position of X^- was compared with X^- position in ML WS_2 on top of flat SiO_2/Si. ML WS_2 on top of C-99 was considered to be unstrained. We did not take into account X^0 position for this purpose because X^0 was not resolved in ML WS_2 on top of flat SiO_2/Si. The mean

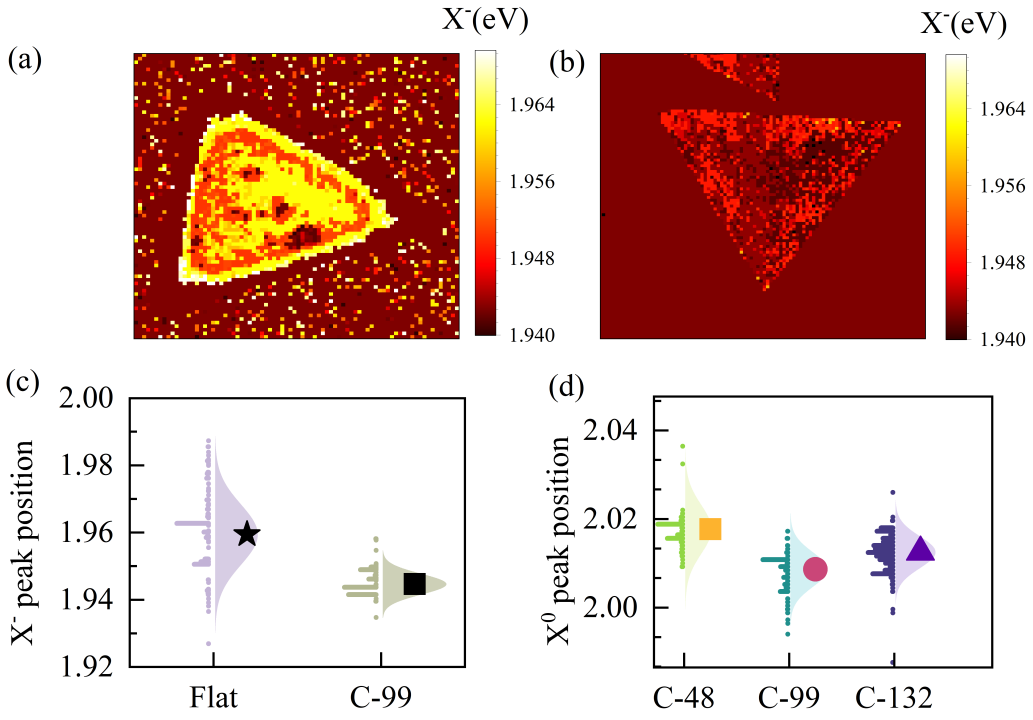

FIGURE 3.16: Trion (X^-) position map in ML WS_2 placed on top of (a) Si/SiO_2 (b) C-99 substrate and (c) Mean peak position of X^- in ML WS_2 on top of SiO_2/Si (flat) and C-99 extracted from the PL map. The normal distribution and the raw data points are also shown.

X^- position was found to be 1.96 eV and 1.94 eV for SiO_2/Si and C-99 respectively. This amounts to $\sim$ 20 meV redshift of X^- in WS_2/C-99. It is reported that X^- redshifts by $\sim$ 130 meV for 1% applied tensile strain[124]. Therefore we can estimate that ML/WS_2 on top of C-99 is under a tensile strain of $\sim$ 0.15 %. The amount of tensile strain on ML WS_2 on top of C-48 and C-132 was determined in the same way by comparing the position of X^0 with respect to the position of X^0 in C-99. Therefore we can estimate that ML WS_2 on top of C-48 and C-132 is under a tensile strain of $\sim$ 0.04 % and 0.08 %.

3.6.2 Comparison of Raman spectra of WS_2 placed on different substrates

From the Raman spectra comparison (Figure 3.18) we can see that the 2LA Raman mode of WS_2/C-132, C-48 and SiO_2/Si are almost at identical positions whereas in WS_2/ C-99 the 2LA mode is redshifted by $\sim$ 1.4 cm^{-1} compared to the other three samples. We have discussed the calculation of the tensile strain imparted on the WS_2 placed on C-132, C-99, C-48 and SiO_2/Si comparing the PL maps. The amount of strain calculated on WS_2 /C-132, C-99 and C-48 considering WS_2/ SiO_2/Si unstrained are 0.08%, 0.15% and 0.04% respectively.

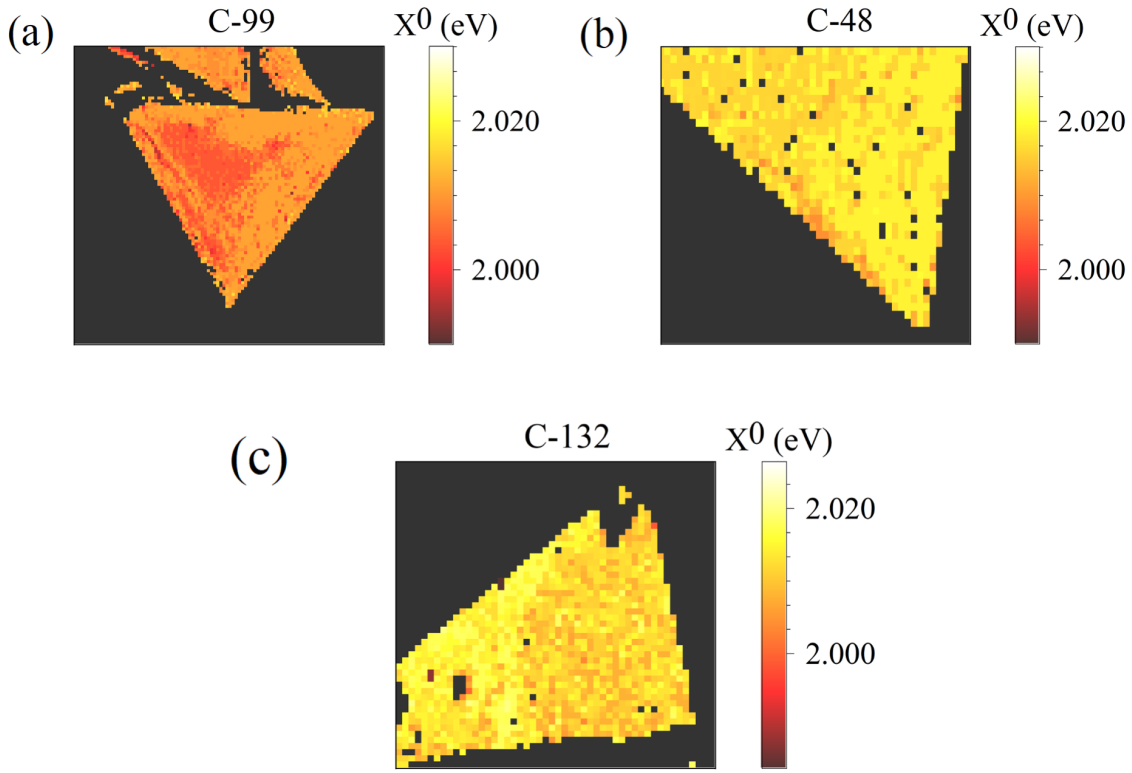

FIGURE 3.17: Exciton (X^0) position map in ML WS_2 placed on top of (a) C-99 (b) C-48 and (c) C-132 substrate.

We can recalculate the strain on various samples using Raman spectra presented in Figure 3.18.

It is known that for 1% tensile strain, the 2LA mode redshifts by 6.8 cm^{-1}. Since in the WS_2/C-99 sample, the redshift of 2LA mode is about $\sim$ 1.4 cm^{-1} compared to SiO_2/Si (unstrained), this amounts to $\sim$ 0.20% tensile strain in WS2/C-99 [124]. This estimated value of strain in WS_2/C-99 using Raman spectra is quite close to the strain value of $\sim$ 0.15% calculated using PL map. Also, this is very close to the theoretically estimated tensile strain value of $\sim$ 0.21% required for the phonon-scattering from K to Λ valley.

In the case of C-48 and C-132, using a PL map, we estimated the tensile strain value to be 0.04% and 0.08% respectively. If these strain values are converted to 2LA Raman mode redshift (considering 6.8 cm^{-1}/% redshift [124]), they come out to be 0.3 cm^{-1} and 0.5 cm^{-1} for C-48 and C-132 respectively which are too small to be detected in a Raman setup with 1800 lines/mm grating (minimum resolution of [124] 1.1 cm^{-1} [104]). Therefore we do not see any considerable 2LA mode redshift in C-48 and C-132 compared to SiO_2/Si (unstrained).

It can be seen that in Figure 3.18 the $A_1^{'}$ does not show any noticeable shift for all four samples. It is reported that $A_1^{'}$ redshifts at a rate of only $\sim$ 1.8 cm^{-1}/% tensile. In our

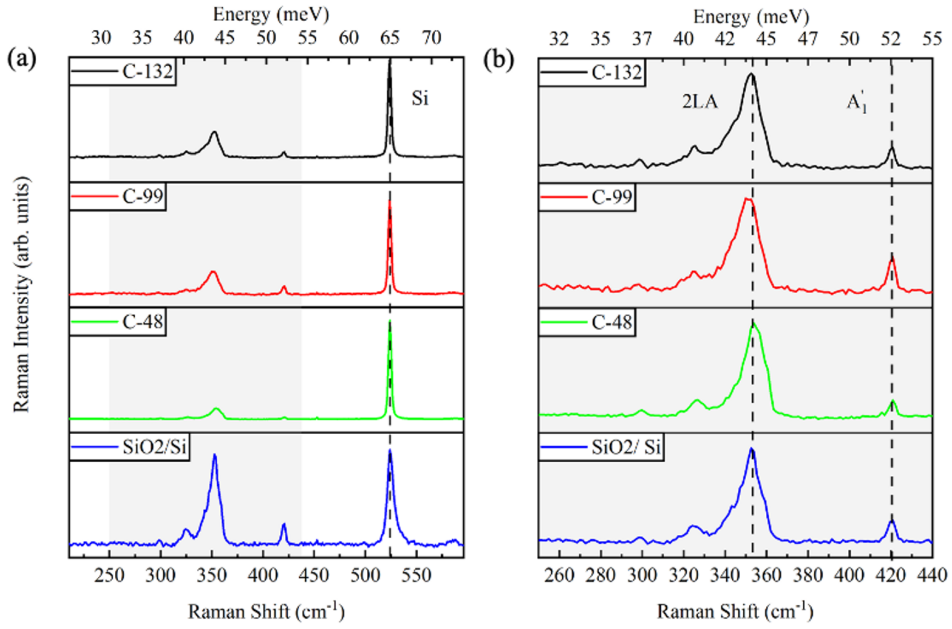

FIGURE 3.18: (a) Raman spectra of WS_2 on top of C-132, C-99, C-48 and SiO_2/ Si at 77 K. The Si Raman peak at $\sim$ 520 cm^{-1} for all the substrates are at identical positions. The grey shaded area is zoomed in (b) which shows the 2LA peak and the $A_1^{'}$ Raman modes of monolayer WS_2.

case, for the above-mentioned calculated strain values of 0.04% (C-48), 0.15% (C-99) and 0.08% (C-132) the redshift in $A_1^{'}$ Raman mode comes out to be 0.07 cm^{-1}, 0.27 cm^{-1} and 0.14 cm^{-1}. The values of the redshift of Raman mode are very small to be detected by the existing Raman setup as discussed above.

3.7 Observation of X^D with a low N.A. objective lens

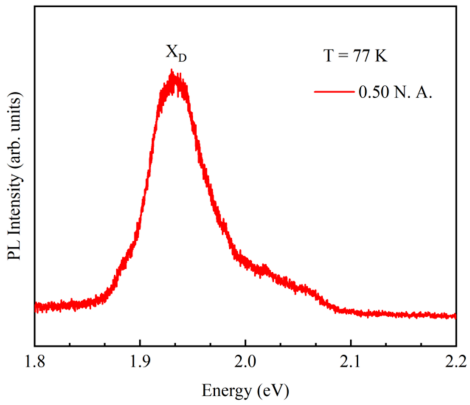

FIGURE 3.19: PL spectra of monolayer WS_2 acquired at 77 K with an objective lens of numerical aperture (0.50 N. A.).

The spin-forbidden dark exciton in WSe_2 only appears when an objective lens of high N. A. $\sim$ 0.82 and could not be detected with an objective lens of low N. A. $\sim$ 0.60 [169]. This is because the spin-forbidden dark exciton has an out-of-plane dipole moment and therefore it has in-plane emission [170, 171]. So, a high N. A. objective lens is required to detect the in-plane emission of spin-forbidden dark exciton. This is not the case with momentum-forbidden dark exciton as the emission is always out-of-plane. However, in our case, we re-performed the PL spectroscopy on WS_2/ C-99 at 77 K with a low N. A. ($\sim$ 0.50) objective lens and we were again able to detect the X^D peak at $\sim$ 1.92 eV (Figure 3.19) similar to what we observed earlier when the PL spectroscopy was performed with a high N. A. $\sim$0.80 objective lens (data in Figure 3.8). Therefore, it can be safely said that in our case, X^D is a KΛ momentum-forbidden dark exciton and not a spin-forbidden dark exciton.

3.8 Time-resolved photoluminescence measurements

To elucidate the kinetics of X^D, we did time-resolved PL (TRPL) on the ML WS_2 on top of C-99 substrate Fig. 3.15d). The sample was excited with a 531 nm pulsed laser having FWHM of 48 ps and a repetition rate of 5 MHz. The sync signal from the laser driver is fed to channel 0 of a TCSPC (PicoHarp 300). The emission from the sample is fed to a single photon detector (Micro Photon Devices), the output of which is connected to channel 1 of the TCSPC. The IRF shows an FWHM of 52 ps and a decay time scale of 23 ps. Using deconvolution, we can accurately estimate down to 10% of the IRF width. To filter out X^D at 1.92 eV only, we use a bandpass filter (FWHM of 10 nm) centred at 635 nm. For *in situ* steady-state PL spectra, a 50:50 beam splitter is used to divert part of the emission to a spectrometer. The measured TRPL data were fitted with two exponentials ($\sum_{n=1}^{2} A_i e^{\frac{-t}{\tau_i}}$)[172] after deconvoluting from the instrument response function (IRF) as implemented in QuCoa software (PicoQuant). The faster and stronger component τ_1 representing the X^D decay time is estimated $\tau_1 \approx 36.3 \pm 1.2$ ps. The lifetime τ of X^D is estimated to be $\tau \approx 36.3 \pm 1.2$ ps which is 30 times larger than the reported decay time of a neutral exciton X^0 ($\tau \sim 1$ ps at T = 60 K) [151, 173] as X^D is the excitonic ground state of ML WS_2 [115, 116]. The slower ($\frac{A_1}{A_2} \sim 294$) and weaker decay component $\tau_2 \sim 100$ ps is expected to be coming from the contribution of the tail of defect-bound exciton complex observed in ML WS_2 at lower temperatures [172].

3.9 Conclusion

In summary, we have reported the experimental observation of momentum-forbidden $K\Lambda$ dark excitons by applying tensile strain on ML WS_2 using a nanotextured substrate. Our

model shows that the $K\Lambda$ dark excitons in both WS_2 and WSe_2 can be brightened by the application of tensile strain, thereby establishing the universality across the W-based TMDs. Also, TMDs are prone to buckling under compressive strain [174] and it is difficult to create at lower temperatures which is necessary for the brightening of $K\Lambda$ dark exciton[116]. Rather they can endure a high tensile strain and are easy to create [175]. Therefore our work paves the way for more application-oriented modulation of the $K\Lambda$ dark exciton, which, being the excitonic ground state, strongly affects exciton dynamics in W-based materials.

Chapter 4

Modulation of trion and exciton formation in monolayer WS_2 by dielectric and substrate engineering

Abstract:
Photoluminescence (PL) of transition metal dichalcogenide (TMD) monolayers is strongly influenced by the dielectric environment. The defect states present in the substrate induce uncontrollable doping in the TMD monolayer and thereby modify the PL spectra. There have been enormous efforts to tune and overcome the effect of inevitable substrate defects in PL spectra, but a proper understanding and a convenient way are still lacking. Here, we systematically studied the effect of surface defects by gradually increasing the separation between WS_2 monolayer and substrate. Hence, we could precisely modulate the exciton and trion contribution in the PL spectra of WS_2. The excitation power-dependent measurements on dielectric engineered and patterned substrates helped us to shed light on the mechanism of PL modulation in monolayer WS_2. We have also studied the influence of the nature of the charge carried by substrate defects on the PL spectra. These results open a new pathway to modulate and obtain the desired PL spectra of TMDs by engineering the substrates. Our findings will be useful for fabricating excitonic interconnects, valleytronic, and single-photon devices. The content of this chapter is adapted from the research article "2D Materials, 8, 045032 (2021)." [104].

4.1 Introduction and motivation

Transition metal dichalcogenides (TMDs) have attracted considerable interest in recent times due to their unique electrical and optical properties [19, 54, 99, 109–113, 176–182] . These TMDs are usually grown in their monolayer form by chemical vapour deposition (CVD) [183–186] or are mechanically exfoliated [187] from their bulk form. TMD monolayers

have high carrier mobility, and a high absorption coefficient which can be harnessed in making optoelectronic devices such as light-emitting diode photodetectors, high-performance optoelectronics [109, 178, 188–190]. Unlike its bulk form, monolayer TMDs exhibit a transition from an indirect to direct bandgap [19, 109, 111, 191, 192]. Additionally, due to the reduced dielectric screening (compared to their bulk form), optical transition phenomena in the monolayer TMDs are highly susceptible [193–195] to the surrounding dielectric medium which includes the underlying substrate as well [196–200]. Inefficient screening of Coulomb interactions between the photoexcited carriers favours the formation of excitons and charged excitons (trions) in these 2D semiconducting materials [29, 201]. The signature of excitons and trions in the optical transition is strongly influenced by the nature of the underlying substrate and the surrounding medium on the top [200, 202]. Usually, thermally grown SiO_2 on silicon is used as a substrate for the monolayer TMDs but the TMD/SiO_2 interface may contain many charge impurities which act as a local doping centre. These doping centres affect the nature of optical transitions like PL to a large extent [47, 203]. It is reported that the effect of these doping centres can be reduced by placing the monolayer TMDs on hBN [47, 200, 204]. The doping centres usually contribute extra carriers (electrons or holes) in the TMD channel and help in trion formation [205]. Thus, by tuning the dielectric environment, one can minimize the effect of doping centres at the TMD/SiO_2 interface and, hence can modulate the contribution of trions and excitons in the PL spectra. There are reports which investigated how various substrates (silicon, hBN, mica, quartz, etc) affect the PL emission of TMDs like WS_2 [200, 202, 206–210]. It has been theoretically predicted that if we increase the spacing between substrate defects and the monolayer WS_2, the neutral exciton starts dominating gradually with respect to the trion. However, the lack of systematic experimental studies [211, 212] motivated us to examine the PL modulation of monolayer TMDs either by inserting different thicknesses of hBN as a spacer layer or by engineering the dielectric environment. The present study sheds light on the mechanism of PL modulation by controlling the effect of impurity via dielectric and substrate engineering and provides a recipe for getting the desired PL from monolayer TMDs. Here we have varied the local dielectric environment and tuned the doping at the interface by taking substrates of varying materials and textures. CVD-grown WS_2 monolayer has been taken as a model 2D system and 300 nm thermally grown SiO_2 on Si and hBN (exfoliated on SiO_2/Si) of varying thickness have been used as substrates, which were patterned with micron-size holes or pillars for further dielectric modulations. First, we have placed a CVD-grown monolayer WS_2 on top of hBN (which is exfoliated on a SiO_2/Si substrate) of varying thickness to reveal the effect of impurities on the PL spectra of WS_2. When the WS_2 was on SiO_2/Si the PL spectra predominantly showed a single trion peak. If WS_2 is placed on a very thin ($\sim$ 6 nm) hBN layer, both the trion and exciton peaks were observed. With increasing thickness of

the hBN layer, the trion peak started diminishing and when WS_2 is placed on a very thick ($\geq$ 90 nm) hBN, only the exciton peak was present. WS_2 monolayers were also placed on a hole and pillar patterned SiO_2 /Si substrate to understand how a gap (air) between WS_2 and SiO_2 is effective in isolating the doping centres. By varying the excitation laser power in each of these cases, we studied how exciton and trion contribution in PL evolves with an increasing number of photogenerated carriers inside the WS_2 channel. We observed that the evolution of the ratio of trion to exciton peak intensity as a function of excitation power in WS_2 on top of hBN is markedly different from that of a suspended WS_2 in the hole region. This illustrates that these two different methods of isolating the doping centres have different effects on the PL of WS_2. We have further placed an hBN layer on top of a WS_2 layer which was partly placed on a bottom hBN layer (the remaining part of this WS_2 is on SiO_2) in such a way that one part of the WS_2 is encapsulated between two hBN layers and the other part has an hBN layer just on top while bottom part was on SiO_2. This was done to understand the contribution of doping centres at the WS2/SiO_2 interface and surroundings on the PL of WS_2. Finally, by modifying the sign of the charge on the substrate surface, we examined how the polarity (+ve or -ve) of the surface defects affects the PL of WS_2. Our study elucidates the effect of impurity on the PL of WS_2 and provides a reliable way to generate excitons and trions selectively, which will have a profound impact on exciton interconnects [213], valleytronic devices [180–182], and single-photon emission processes from the defects of 2D materials [214].

4.2 Sample Preparation and Experimental Details

4.2.1 Synthesis of WS_2 monolayer

Monolayer WS_2 was synthesized using a home-built atmospheric pressure chemical vapour deposition (APCVD) unit. WS_2 monolayers were grown by APCVD on 300 nm thermally grown SiO_2 on Si. Properly cleaned and O_2 plasma-treated (60 W, 5 min) substrates were placed on an alumina boat containing 500 mg WO_3. A boat containing WO_3 powder was placed inside a 35 mm quartz tube in the heating zone of the furnace. Another boat containing 500 mg sulphur was placed upstream inside the tube, 15 cm away from the WO_3 boat. The sulphur boat was outside the heating zone and was heated using a heater coil. The tube was flushed with 500 sccm Ar for 20 min. The furnace was kept at 850 °C and the heater coil was kept at 240 °C for evaporation of sulphur. This set of temperatures was maintained for 10 min. After the growth, the system was allowed to cool naturally.

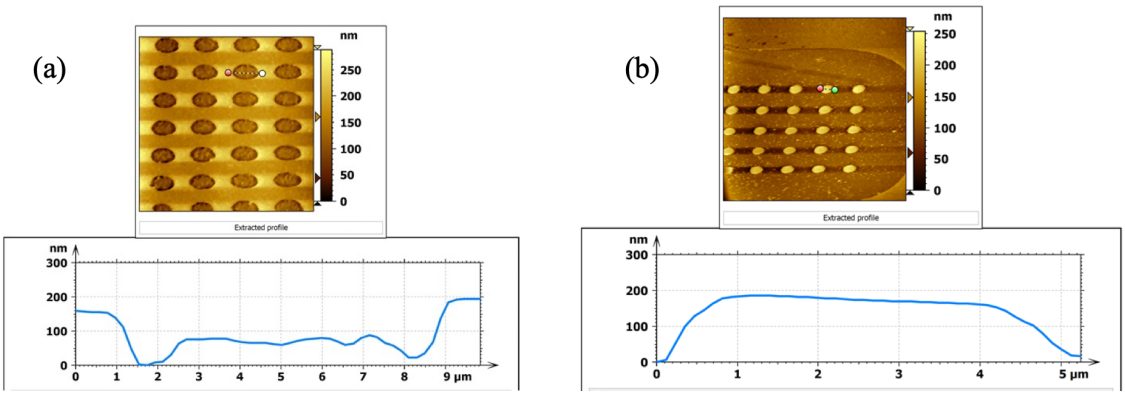

FIGURE 4.1: (a) AFM image of hole structure of depth 194 nm. (b) AFM image of Pillar structure of height 186 nm on Si/ SiO_2.

4.2.2 Substrate Patterning

To study the optical properties of suspended monolayer WS_2, substrate patterning was done. Photolithography and reactive ion etching (RIE) methods were used for the substrate modification of SiO_2/Si substrate. First, photolithography was employed for making circular array patterns on SiO_2/Si substrate. Afterwards, keeping photoresist as a mask, RIE (SF_6 and O_2 plasma, 120 W) was done for 2 min to etch SiO_2 and to get hole structure of depth $\sim$ 194 nm, diameter $\sim$ 4 μm and interpillar separation of 6.5 μm Fig. 4.1a and 4.3g on SiO_2/Si. In another case, to get the pillar structures on SiO_2/Si, aluminium (Al) was sputtered (30 nm) on a circular array patterned SiO_2/Si after the first step of photolithography. Then deep RIE was carried out for 2 min to get Al capped SiO_2/Si pillar structure, where sputtered Al was used as the mask to obtain the circular pillars. Finally, the Al mask was etched using Al etchant to obtain SiO_2/Si pillar structures of height 186 nm, diameter $\sim$ 4 μm and interpillar separation of 6.5 μm Fig. 4.1b and 4.3f. These parameters were chosen such that their dimensions are always greater than the laser spot size ($\sim$2 μm) to avoid any averaging effect in our optical measurement data. These textured substrates were used to minimize the effect of substrate-induced defects since the contact area with SiO_2 will be minimal as part of the WS_2 monolayer will remain suspended.

4.2.3 Transfer process:

The as-grown SiO_2 /Si substrate containing monolayer WS_2 was spin-coated (3500 rpm, 1 min) with 10% PS solution in chloroform [103] and was heated at 100 °C for 3 min. The PS-coated substrate was then dipped in distilled (DI) water with the four corners slightly scratched using a clean surgical blade. On dipping in DI water, the PS film comes off easily along with the monolayer WS_2 and the film floats in the DI water. hBN was exfoliated using scotch tape on an IPA/acetone cleaned and O_2 plasma-treated 300 nm SiO_2/Si substrate. This hBN exfoliated substrate was then used to fish the PS film floating in water (since the WS_2 monolayers were on the surface of the PS film which is facing the water). This substrate was then heated at 80 °C for 1 hr and 150 °C for 30 min for better adhesion of PS film with the substrate. The substrate was then dipped in toluene for 3 h which removed the PS and was then dipped in acetone and IPA for 10 min in succession to remove any organic adsorbates. The substrate was then blow-dried and heated at 110 °C for 10 min to remove water molecules. For transferring monolayer WS_2 on hole and pillar SiO_2/Si substrate, the patterns (hole and pillar) were made covering a large area such that the region of the substrate where the pillars/holes are located is easily visible to the naked eye. The floating PS film containing the monolayer WS_2 (on the surface facing the water) is scooped by a clean tweezer and is placed in the same orientation on the marked area of pillar/hole substrates. Removal of PS and other cleaning processes were the same as discussed earlier. For placing the hBN flake on top of monolayer WS_2, a dry transfer technique involving polydimethylsiloxane (PDMS) stamp and a home-built transfer stage was used. PDMS stamp was made by mixing PDMS liquid and the hardener in a 10:1 ratio and was subsequently cured at 90 °C for 30 min. This PDMS stamp was then attached to a clean glass slide by plasma bonding (O_2 plasma, 80 W, 40 s). hBN was exfoliated by scotch tape on the top surface of the PDMS stamp and a suitable flake was identified by using an optical microscope for transfer. The transfer steps mentioned here [103] were followed with the stage of the transfer setup at 120 °C to remove blisters at the WS_2/hBN interface formed during the transfer process. The sample was then dipped in acetone and IPA in succession for 10 min each to remove any polymer. The substrate was then blow-dried and heated at 110 °C for 10 min to remove water molecules.

4.2.4 Optical setup

The optical measurements were performed using an upright microscope (Olympus). The sample was illuminated using a 100× 0.95 NA lens at wavelength 532 nm laser excitation. The emitted light from the sample upon excitation was collected using the same lens and was projected onto the spectrometer/ EMCCD for spectral analysis/ imaging using relay

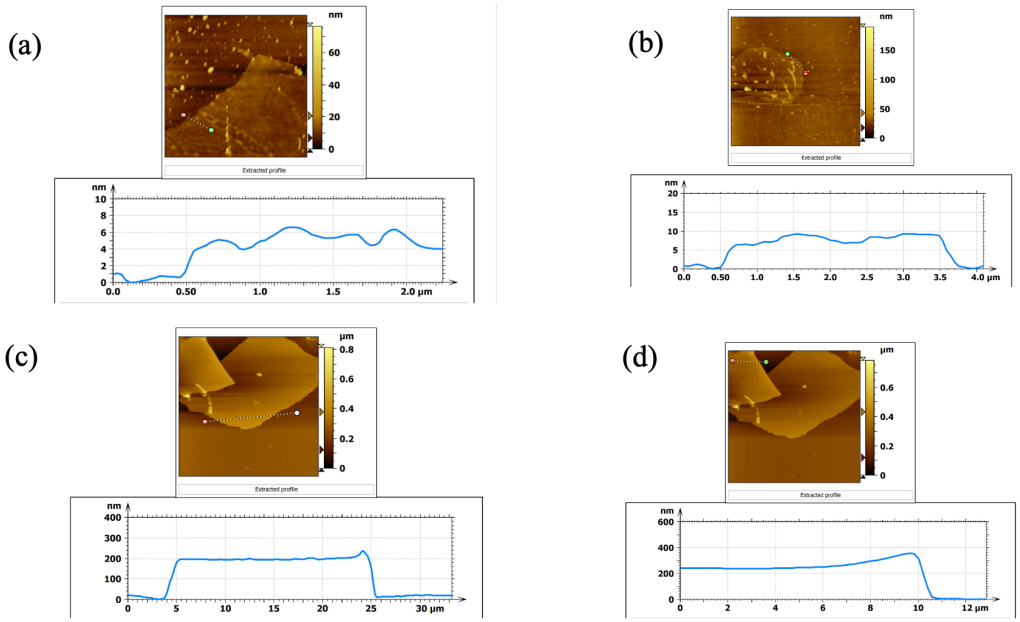

FIGURE 4.2: Atomic Force Microscopy (AFM) images for determining the thickness of various hBN flakes used in the experiments.

optics. Whereas a focused excitation was used for the spectral analysis, a broad illumination configuration was employed for the PL imaging. This was done by placing a lens before the objective lens back aperture at the input path. A combination of half-wave plate and polarizing beam splitter were used for varying the input excitation laser power and 532 nm Edge and 532 nm Notch filters were used to efficiently reject the Rayleigh scattered light in the output path. The Raman spectra measurements were performed with 532 nm as excitation wavelength and dispersing the signal using 1800 lines mm^{-1} grating, keeping the centre wavelength at 540 nm. This allows us a wavelength resolution of $\sim$ 0.034 nm, and consequently, $\sim$ 1.15 cm^{-1} resolution in wavenumber. A combination of polarizer (P), half-wave plate (HWP) and polarizing beam splitter (PBS) is used to smoothly vary the power, by changing the HWP angle. The beam is routed to the microscope entrance port using a mirror (M) and expanded through lenses. A combination of 532 notch and 532 edge filters are used to reject the Rayleigh scattered component in the collected light. The signal is then passed to the spectrometer and CCD using relay optics. BS1, BS2: beam splitters (BS1 is 90% transmitting), L1-L6: lenses, FM: Flip mirror. The power of the incident laser was measured at pos1 (as indicated in Fig. 4.4) and multiplied by the appropriate multiplication factor to get the approximate power in the free space. However, not the entire width of the beam enters the microscope objective lens as well as the microscope's internal optics may cause a further decrease in power. To avoid these factors in determining the power, we kept a detector at the sample plane and then measured the integrated power. Power density was calculated by dividing this value by the approximate beam spot area. This calculation gives

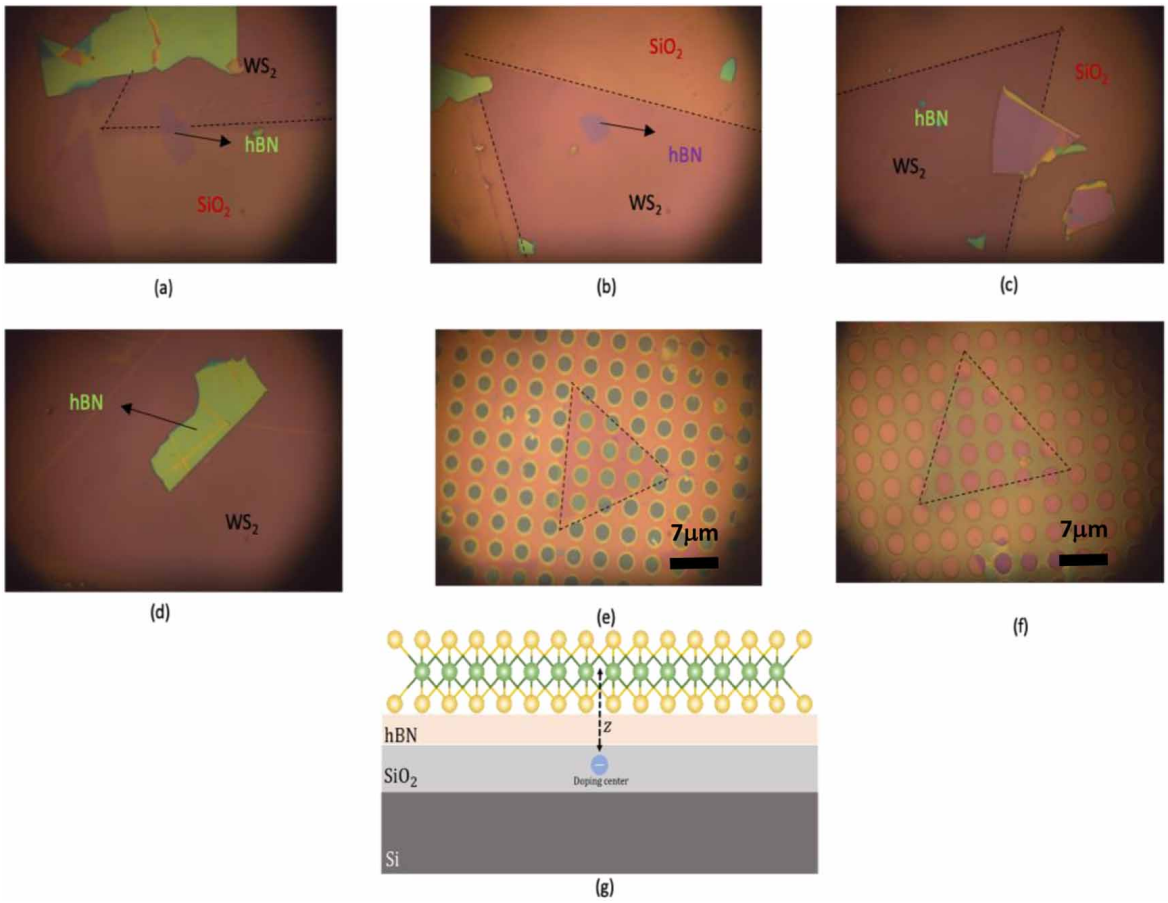

FIGURE 4.3: Optical microscope image (at 100×) of WS_2 monolayer on (a) thinnest (∼ 6 nm) hBN, (b) slightly thicker (∼ 9 nm) hBN, (c) thicker (∼ 90 nm) hBN, and (d) a very thick (∼200 nm) hBN (see figure 4.2 for AFM measurement of hBN flakes). (e) WS_2 on a hole patterned SiO_2/Si substrate (highlighted by dashed black line) and (f) WS_2 on a pillar patterned SiO_2 substrate (highlighted by black line). (g) Schematic showing the role of hBN as spacer.

the highest power density of 0.463 mW/μm^2 while the lowest power density of 30 mW/μm^2 incident on monolayer WS_2. Thus for our experiments, laser power was nowhere near to a very high power density of 5 mW/μm^2 which could have burnt the sample.

4.3 Experimental Results

4.3.1 Modulation of PL

First, we started with investigating PL spectra of a monolayer WS_2 on a 300 nm SiO_2/Si substrate. The PL spectra exhibited a single peak at ∼1.95 eV (see Fig. 4.5a). It has been reported that the PL peak of a transferred WS_2 monolayer is slightly redshifted (almost 50 meV) compared to that of an as-grown WS_2 monolayer. This is due to the relaxation of strain when the WS_2 layer is transferred[130]. There is another report according to which

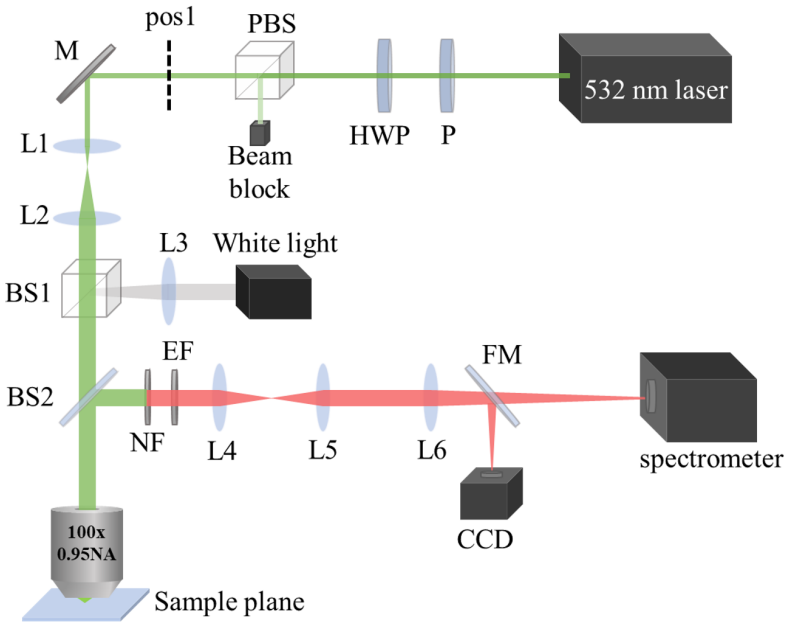

FIGURE 4.4: Schematic of the optical setup.

the PL peak of transferred WS_2 gets blue-shifted compared to the as-grown one because of the trapped water layer in the transferred sample, which acts as a source of doping [202]. We took PL on our as-grown WS_2 monolayer and the shift was less than 10 meV compared to the transferred one Fig. 4.6a. When monolayer WS_2 was placed atop a thin ($\sim$6 nm) hBN layer (Fig. 4.5a, marked as hBN-1), PL spectra Fig. 4.5a showed a prominent peak at $\sim$1.96 eV with another small feature at $\sim$2.00 eV. The low energy peak is attributed to negatively charged trion (X^-) contribution while the higher energy peak is arising due to neutral exciton (X^0) contribution [29, 215]. We compared the PL spectra with another monolayer WS_2 placed on a slightly thicker hBN of 9 nm thickness (Fig. 4.3b, marked as hBN-2). Here we observed that the X^- peak at $\sim$1.96 eV becomes less prominent while the X^0 peak at $\sim$2.01 eV becomes sharper and more prominent (see Fig. 4.5). The study was repeated by increasing the bottom hBN thickness, which led to the observation that with increasing thickness of hBN, the X^- peak (Fig. 4.5a, marked as hBN-3) gradually becomes less prominent while for a very thick bottom hBN ($\sim$ 90 nm for 4.5c and $\sim$200 nm for 4.5d) the X^- peak vanishes and the only prominent peak is X^0 at $\sim$ 2.00 eV (Fig. 4.5a, marked as bulk hBN). Thus, we observed that we are getting a neutral exciton signature in PL just by placing the monolayer WS_2 on the hBN flake which was otherwise dominated by trions when the WS_2 layer was placed directly on SiO_2/Si substrate (Fig. 4.5a). In other words, the trion-to-exciton peak intensity ratio decreases with an increase in the thickness of hBN layers (see Fig. 4.6b). This is in accordance with the theoretical works of Tuan et al [211], which predicted that with the increase in separation of monolayer WS_2 from the surface

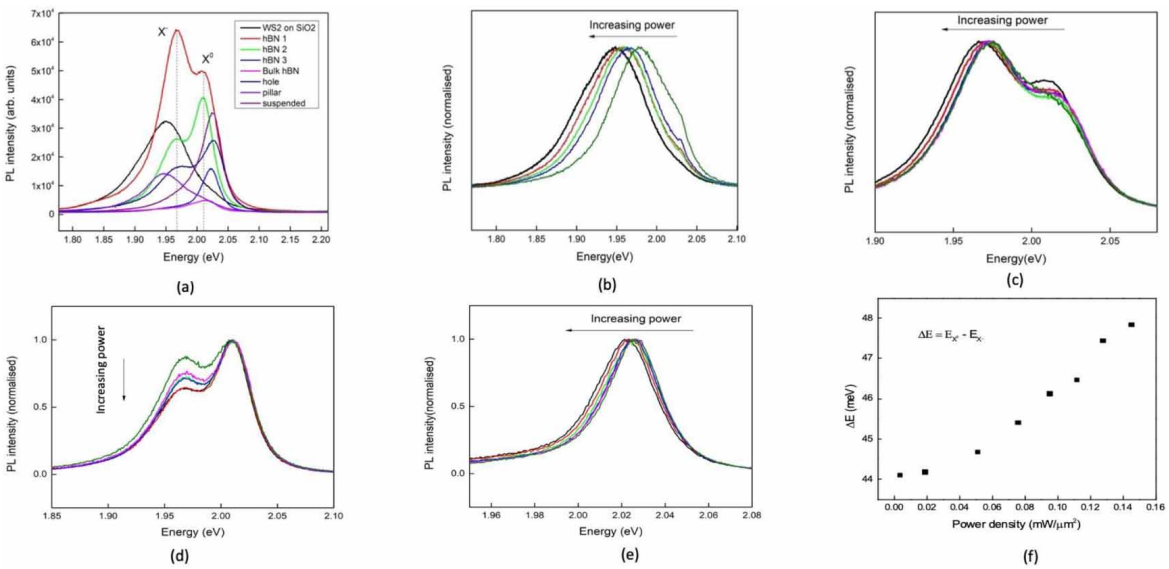

FIGURE 4.5: (a) PL spectra of various cases at 0.394 mW μm^{-2} excitation power density showing exciton and trion peaks. Excitation power density (0.002-0.394 mW μm^{-2}) dependent PL spectra (normalized) of WS_2 on (b) SiO_2/Si substrate, (c) 6 nm hBN, (d) 9 nm hBN, (e) 90 nm hBN. (f) Energy difference of exciton and trion (ΔE) as a function of excitation power density.

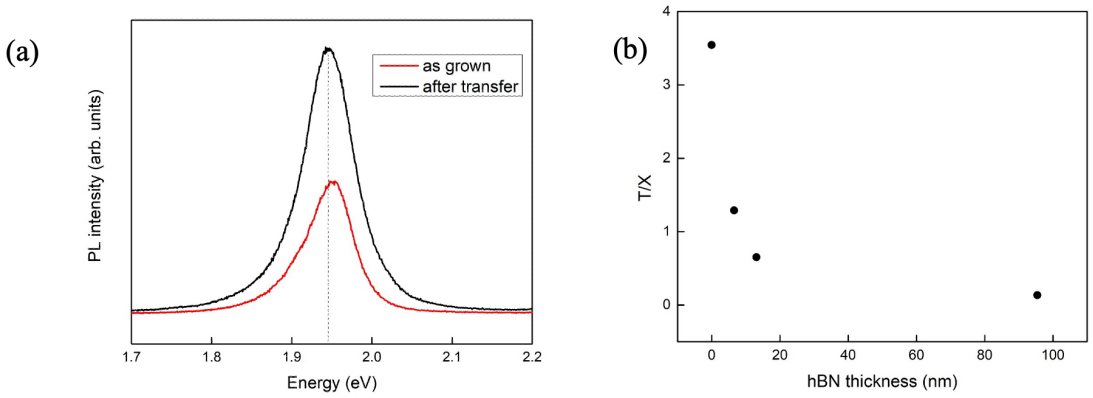

FIGURE 4.6: (a) PL spectra of as-grown (red) and transferred (black) WS_2 monolayer and (b) Trion and exciton peak intensity ratio as a function of the thickness of hBN. Calculation is done for data taken at a fixed excitation power.

defects or impurity (situated on SiO_2) the relative trion to exciton intensity ratio decreases.

The modulation of X and X^0 peaks with hBN thickness can be attributed to the presence of the unintentional source of doping in the SiO_2/WS_2 interface [29]. This source of doping is the charged defects present on the SiO_2 surface. In the presence of doping, the WS_2 PL

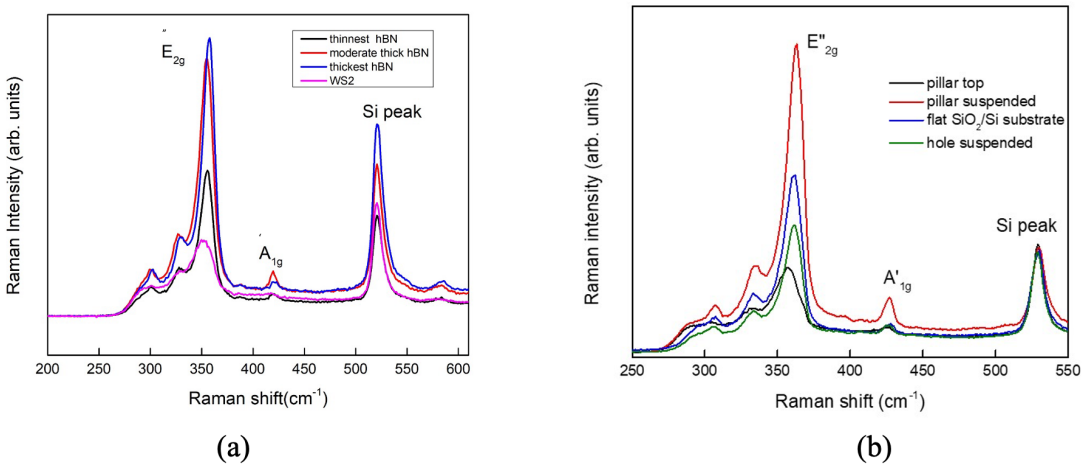

FIGURE 4.7: (a) Raman spectra of monolayer WS_2 placed on hBN of various thicknesses. (b) Raman spectra of monolayer WS_2 placed on the hole, pillar patterned and flat SiO_2/Si substrate.

is dominated by the trions. Formations of trions are more favourable when there is a larger number of carriers inside the WS_2 channel. The unintentional doping sources are providing these additional carriers inside the channel. Because of that, we are seeing a broad X^- peak in the PL of WS_2 placed directly on SiO_2/Si [130]. In other cases, by placing the WS_2 layer on a very thin hBN flake, the effect of the doping source gets screened up to some extent and we can see well-resolved X and X^0 peaks. A little shift of $\sim$5 meV can be due to the flake-to-flake variation of PL. This shift is not due to the strain effect, because Raman spectra of all these samples are similar (Fig. 4.7a) [216]. Now, as we increase the thickness of the hBN flake, the effect of the doping source diminishes further due to dielectric screening by hBN and also due to increasing spatial separation between SiO_2 and WS_2. Thus, for a WS_2 on thick ($\geq$90 nm) hBN, the spectra are dominated by neutral exciton peak X^0.

4.3.2 Laser power dependent study

We have performed laser power-dependent PL for all of these samples to understand the exact mechanism of PL modulation due to dielectric engineering. For the WS_2 on SiO_2/Si, the power-dependent PL (Fig. 4.5b) shows a clear redshift of the X^- PL peak with increasing power. This indicates that the peak is dominated by trions and there is less contribution of neutral excitons. This is because with increasing laser power the carrier density increases, which raises the dissociation energy of trions causing the redshift [132, 203, 215]. Now, in the laser power dependant PL for WS_2 on a very thin (6 nm) hBN (Fig. 4.5b) we see that

the X^- peak has a slight redshift with increasing power but less compared to the previous case of WS_2 on SiO_2/Si. The X^0 peaks show almost no observable shift with increasing excitation power which is consistent with the literature [29, 203, 215]. This less shift in trion peak in WS_2 on hBN case compared to WS_2 on SiO_2/Si can be attributed to the diminishing effect of unintentional sources of doping from the SiO_2/WS_2 interface. In Fig. 4.5f, energy difference of trion and exciton in Fig. 4.5c is plotted as a function of excitation power. The increase of energy separation with increasing laser power indicates an increase in carrier density in the channel [131, 217, 218]. Since a relatively higher excitation power was used in our experiment, the peak intensity of raw PL spectra with laser power density was plotted (Fig. 4.8a-c) to see any signature of Auger effect [219]. However, from the analysis of the data, no signature of the Auger effect was observed and PL is primarily dominated by free carrier and excitonic recombination. We divided each PL spectra by the laser power density and the integration time used to record it (Fig. 4.8c). However, we didn't observe any significant change in the intensity of the PL peaks with laser power density. To clearly see any signature of the Auger effect, we plotted the peak intensity of raw PL spectra with laser power density. Here, we observed that the PL intensity of both trions and excitons are linearly dependent on excitation power for every case (Figure 4.8a and 4.8b). We know from the literature that, in the case of Auger recombination, PL intensity has a sublinear dependence on excitation power density. Ideally, this dependence is (excitation power density)$^{\frac{2}{3}}$ [220]. Therefore, in this case, there is no auger recombination. Probably, the excitation power used in our experiments is not high enough to see an Auger recombination since this happens only at very high excitation power densities. So, the PL is mostly dominated by free carrier recombination and excitonic recombination [220]. Probably, the excitation power used in our experiments is not high enough to see an Auger recombination in WS_2 since this happens only at very high excitation power densities [220]. In the case of WS_2 on SiO_2, photogenerated carriers from unintentional doping centres as well as from donors of the n-doped channel were contributing to the PL. When hBN is introduced between SiO_2 and WS_2, the effect of unintentional doping centres is minimized to some extent but not completely [47] causing lesser redshift of X^- peaks. This suggests that a thin hBN layer screens the effect of charged impurities up to a certain extent at the substrate interface. Excitation power dependant PL of WS_2 on a slightly thicker (9 nm) hBN (Fig. 4.5d) shows that with increasing power, trion peak intensity decreases. The power-dependent PL of WS_2 on a bulk (90 nm thick) hBN (Fig. 4.5e) shows a small redshift of exciton peak with no observable trion peak at any laser power. The small redshift of the exciton peak in Fig. 4.5e can be due to the laser-induced heating of the sample. Although, in the excitation power dependent Raman measurement (Fig. 4.9) no detectable change in the Raman peaks was observed [221, 222]. But it is important to mention that with our measurement setup a

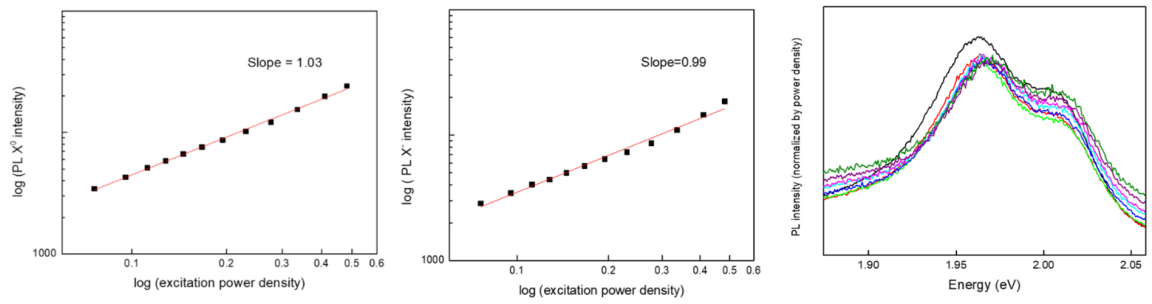

FIGURE 4.8: (a) Intensity of trion peaks vs excitation power density (log-log scale) for WS_2 on top of 6nm hBN (b) Intensity of trion peaks vs excitation power density (log-log scale) for WS_2 on top of 6nm hBN (c) Excitation power dependent PL spectra (power and integration time normalized) for WS_2 on top of 6nm hBN.

maximum resolution of 1.15 cm^{-1} in wavenumber can be achieved, whereas for monolayer WS_2, rate of change of Raman shift has been reported to be -0.0091 cm^{-1} K^{-1} for E''_{2g} [223]. Therefore, at least a temperature difference of $\sim$126 K is required to be detectable in our measurements. Based on our observation we can say that if there is any heating effect, the maximum temperature of our WS_2 samples is less than $\sim$ 419 K (considering ambient temperature to be 293 K). However, the possibility of heating due to laser where the temperature can rise even by a few 10 °C, which can cause such redshift [224], cannot be ruled out. For better understanding, peak width and position as a function of excitation power for trion and exciton in Fig. 4.5c are shown in the Fig. 4.10, respectively. The decrease of intensity of the trion with the increase of excitation power in the case of WS_2 on top of 9 nm hBN is described while explaining Figure 4.16a in the latter half of this chapter. To further study the effect of substrate, we transferred monolayer WS_2 on hole and pillar patterned SiO_2/Si substrate. We took PL spectra on the hole region (Fig. 4.5a) where the WS_2 layer is suspended freely (Fig. 4.3e). The PL spectra exhibit similar characteristics to that of a WS_2 on moderately thick (9 nm) hBN but with a slight blueshift in X^0 and X peaks. This shift is probably due to the strain imparted on the suspended region inside the hole which is evident from the Raman spectra (Fig. 4.7b)[216].

We studied the excitation power dependant spectra on the hole region (Fig. 4.11a) and observed redshift in the X^- peaks and comparatively less redshift in the X^0 peaks (peak

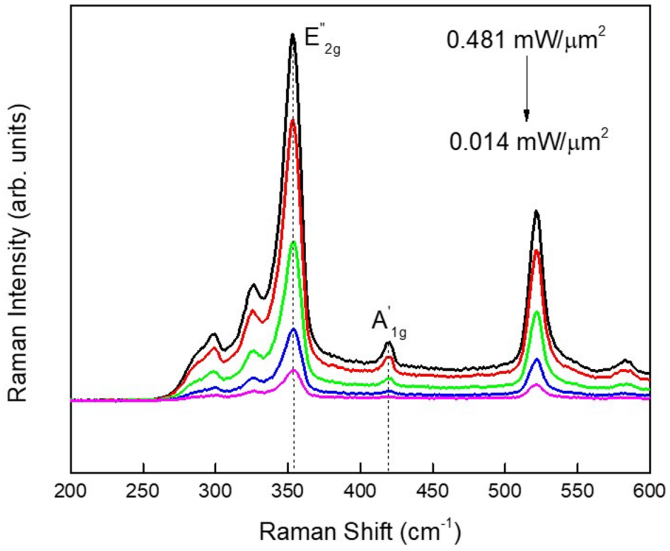

FIGURE 4.9: Raman spectra of WS_2 for various laser power. The sample is placed on a 90 nm thick hBN flake.

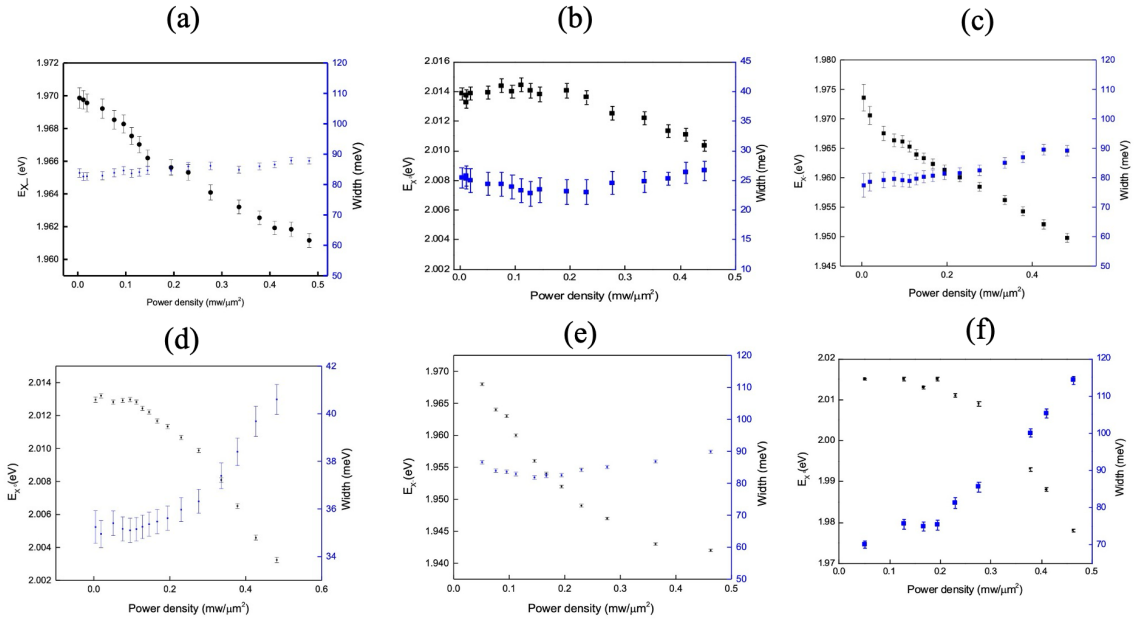

FIGURE 4.10: Peak width and position of (a)trion (b) exciton in WS_2 on top of 6 nm thin hBN, (c) trion (d) exciton in WS_2 on hole patterned substrate, (e) trion and (f) exciton on pillar patterned substrate.

width and position as a function of laser power is plotted in Fig. 4.10c and d). In contrast to the PL spectra of WS_2 on thin (6 nm) hBN (see Fig. 4.5c), in this case, PL spectra at the lowest excitation power exhibited minimal X^- contribution. Probably this is because, at the

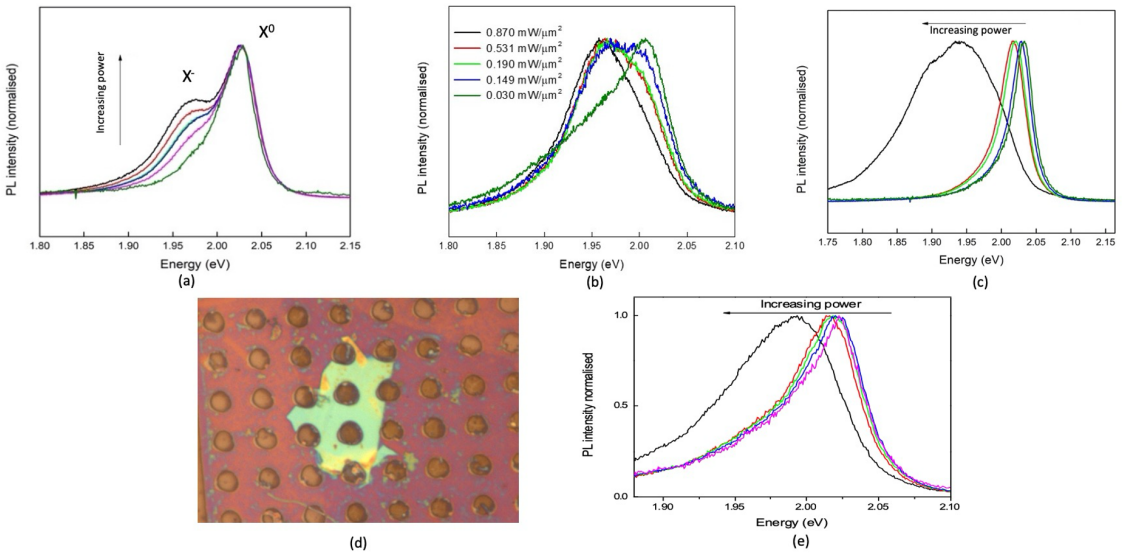

FIGURE 4.11: Excitation power dependent (0.03-0.870 mW μm^2) PL spectra (normalized) of WS_2 on (a) suspended region on hole patterned SiO_2/Si substrate, (b) pillar (WS_2 in contact with SiO_2), (c) the suspended WS_2 region of pillar patterned SiO_2/Si substrate. (d) Optical microscope image (100×) of monolayer WS_2 on hole patterned hBN substrate. (e) Suspended region on hole patterned hBN substrate (shown in fig. 4.11d).

same excitation power, in the WS_2 on hBN case, photon flux was able to ionize the required number of donors so that there is trion formation. On the other hand, in the case of suspended WS_2, the number of donor atoms is less as the WS_2 is freely suspended and the unintentional doping centres at the SiO_2/WS_2 interface are absent. Thus, the same photon flux was unable to ionize the required number of donors for trion formation and hence trion peak is absent in the PL spectra. But as we increase the laser power, the increase in photon flux can ionize sufficient donor atoms and we see X^- peak emerging at higher excitation powers. Whereas, in bulk (90 nm) hBN (Fig. 4.5e), even at the highest excitation power no X^- peak was observed. This suggests that bulk hBN is more efficient in screening surface defects. In the case of WS_2 on hBN, hBN acts as a dielectric medium while for a hole suspended WS_2, air trapped inside the hole acts as a dielectric medium. Since hBN has a higher dielectric constant of ∼3.5 compared to air and because of its large thickness (∼90 nm), electric field lines from the surface defects are screened more effectively [29]. Probably, this is the reason why we don't see a trion peak in the case of WS_2 on top of 90 nm hBN. In the case of a hole suspended WS_2, there is a finite volume of air trapped inside the hole which is not the case in WS_2 placed on thick hBN. O_2 present in the trapped air may get physisorbed in WS_2 and this can deplete the electron concentration inside the channel [225, 226]. The adsorption energy of O_2 in TMDs typically ranges between 0.1-1.9 eV [227, 228]. Thus photons of energy 2.33

eV are sufficient to break this bond. But at low intensity, there are not that many photons available to desorb a significant amount of O_2 and we only see the excitonic feature. As we increase the laser intensity, probably more and more O_2 get desorbed from the channel and electron concentration starts to rise. Thus at higher excitation power, a trion-like feature can be seen [229, 230]. The PL spectra (also excitation power dependence) taken on WS_2 on SiO_2 (non-hole region) showed only X^- feature similar to that of the earlier case of WS_2 on SiO_2. In case of monolayer WS_2 on pillar patterned substrate (Fig. 4.3f), the PL spectra taken on pillars (Fig. 4.5a) (i.e., WS_2 on SiO_2) showed only trion peak while the spectra on the suspended region showed only the exciton peak (peak width and position as a function of laser power is plotted in Fig. 4.10e and f). In the excitation power-dependent spectra of the pillar top region (Fig. 4.11b) we observed that at the lowest power, the exciton peak is dominant. As the laser power is increased, the peak gradually shifts to the trion side and at the highest power, only the trion peak is visible. From the field effect scanning electron microscope (FESEM) image (Fig. 4.12a) of the pillar patterned substrate, we found that the monolayer WS_2 sits conformally on the pillar top which has a diameter of around 4 μm while the laser spot used had a size of 2 μm. Raman spectra were taken on the pillar top and suspended region away from the pillar top at the same excitation power (Fig. 4.12b). From Raman spectra, it was observed that E''_{2g} peak is redshifted by 4.7 cm^{-1} in pillar top compared to the suspended region or flat SiO_2/Si substrate. This observation is a well-known signature of tensile strain in monolayer WS_2 where the Raman peak (especially E''_{2g}) gets redshifted with increasing strain [229, 231]. Our results show that strain is more on the pillar top region compared to the suspended region. It is also known from the literature that, strain gradient in monolayer TMDs creates a force on neutral exciton and pushes them towards maximum strained region i.e. the region where band gap becomes minimum due to strain [232, 233]. Probably, in our case, because of strain, exciton formation becomes more favourable in the pillar top region which is not the case when WS_2 is just placed on a flat SiO_2/Si substrate. But as we increase the laser power, the photo-induced carrier number increases, and now a neutral exciton is more likely to bind with another electron to form a trion. Thus, in the case of WS_2 on pillar top, we see a gradual transition from exciton to trion as we go from lower to higher power. The excitation power dependant PL (Fig. 4.11c) on the area where WS_2 is suspended showed only X^0 peak and no X^- peak (except at the highest excitation power) compared to WS_2 in the hole region. To further investigate the effect of the surrounding donor centres on a suspended WS_2 monolayer, PL spectra were studied on a sample in which monolayer WS_2 was placed on holes made on an hBN flake exfoliated on a SiO_2/Si substrate (Fig. 4.11d). In this study, on the hole pattern (of hBN) we observed only X^0 peak and no X^- peak (Fig. 4.11e). So, the surrounding donor centres cannot affect the PL in this case and the trion peak was not observed at any excitation power.

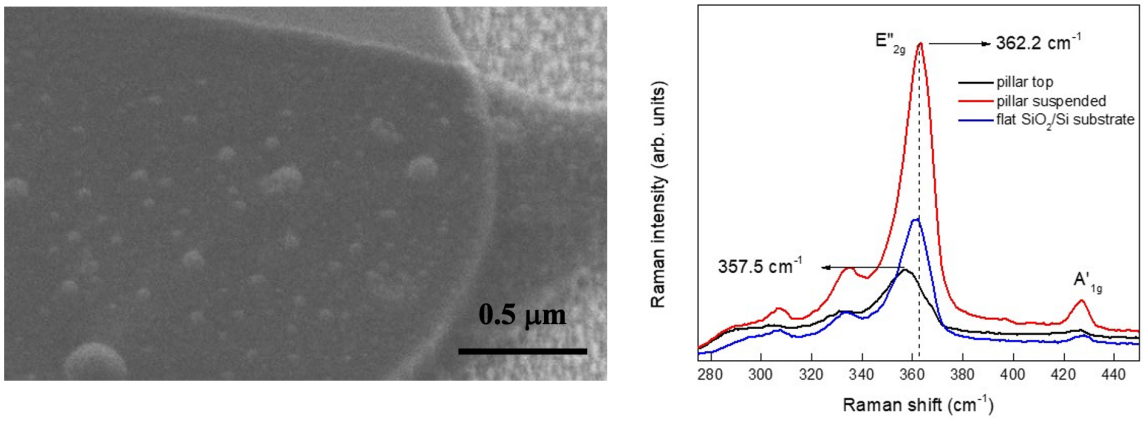

FIGURE 4.12: (a) FESEM images of the monolayer WS_2 on top of pillar patterned substrates. Conformal coating of WS_2 monolayer on pillar top is evident. (b) Raman spectra of WS_2 taken at pillar top, suspended region of pillar patterned substrate and on a flat SiO_2/Si substrate. The shift in Raman E''_{2g} line indicates the presence of strain for the sample on the pillar top.

This also explains the observation of only exciton peak in the case of suspended WS_2 on a pillar patterned substrate.

4.3.3 Electron hole plasma formation

In figures Fig. 4.11c and e, a huge redshift of the exciton peak at the highest power is observed. This can be attributed to the formation of electron-hole plasma (EHP) at higher laser powers. We argue that this shift is probably not due to the heating effect because the observed shift in the figure is $\sim$100 meV and width $\sim$150 meV whereas for the heating effect, shift and width are typically in the range of 40 meV and 35 meV respectively [234]. To find out the effect of heating due to laser power we did Raman measurement (Fig. 4.13) at different excitation powers, and we did not observe any significant change in the peak positions of E''_{2g} and A'_{1g} with excitation [221, 222]. This suggests that, probably, heating due to laser (if there is any) cannot be fully accountable for the observed large shift in the PL spectra. The peak position, width vs. excitation power (Fig. 4.10f) were plotted and the trend is similar to that of electron-hole plasma (EHP) in MoS_2 as was reported by Yilling Yu et. al. [234]. However, this requires further investigation to confirm the presence of EHP and will be explored in our future work.

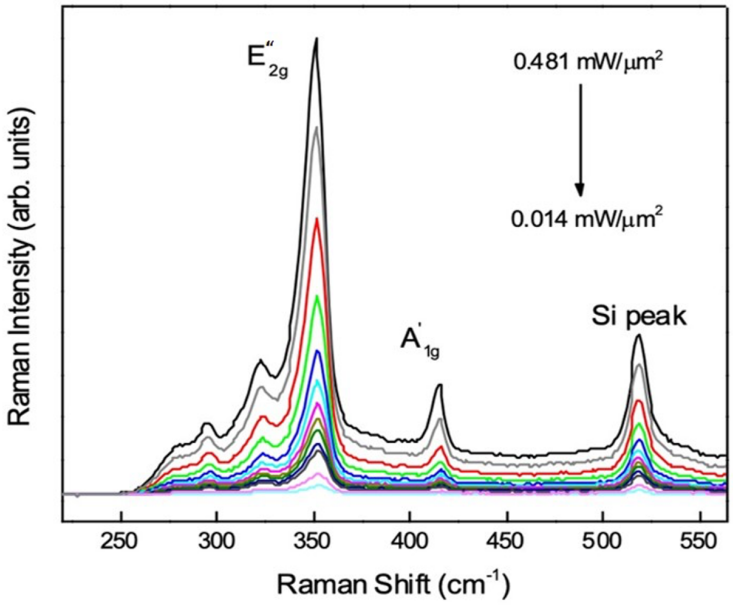

FIGURE 4.13: Power dependent Raman spectra of WS_2 in suspended region of pillar patterned substrate.

4.3.4 Effect of hBN as dielectric on PL of WS_2

To further support our claim that the unintentional source of doping at the SiO_2/WS_2 interface is affecting the PL and not any external factor, we did a PL study on a monolayer WS_2 with different encapsulations. In region I (Fig. 4.14a), WS_2 is on top of hBN, one part is on SiO_2 but the top is covered by an hBN flake (region II) and another part of WS_2 is encapsulated between two hBN flakes (region III). The PL spectra (Fig. 4.14b) on region II showed only trion peak at $\sim$ 1.96 eV. By increasing excitation power, we saw only a small redshift of X^- peak (Fig. 4.14c). At any excitation power, we did not observe any signature of exciton in the spectra. The PL spectra (Fig. 4.14b) of the region I, exhibit an exciton peak at around $\sim$ 2.01 eV, and a small shoulder-like feature in the trion position at around $\sim$1.96 eV (Fig. 4.14d). This confirms our claim that the unintentional source of doping at the SiO_2/WS_2 interface is largely affecting the PL rather than any other factors; also, by screening these doping sources, we can tune the PL emission spectra. Now, in region III where WS_2 is encapsulated between two hBN flakes, we see an X^0 PL peak (Fig. 4.14b) at $\sim$2.01 eV and no X^- peak. The excitation power-dependent spectra (Fig. 4.14e) from region I and region III exhibit similar exciton and trion characteristics. This implies that putting a top layer hBN does not have a significant impact and the impurities at the SiO_2/WS_2 interface play the most crucial role in determining the relative X^- and X^0 contribution in PL. It has been reported that [235, 236] encapsulating a TMD layer by hBN makes the PL peak narrow and sharp. But here we see that when hBN is just at the bottom, the X^0 peak of WS_2 is narrower

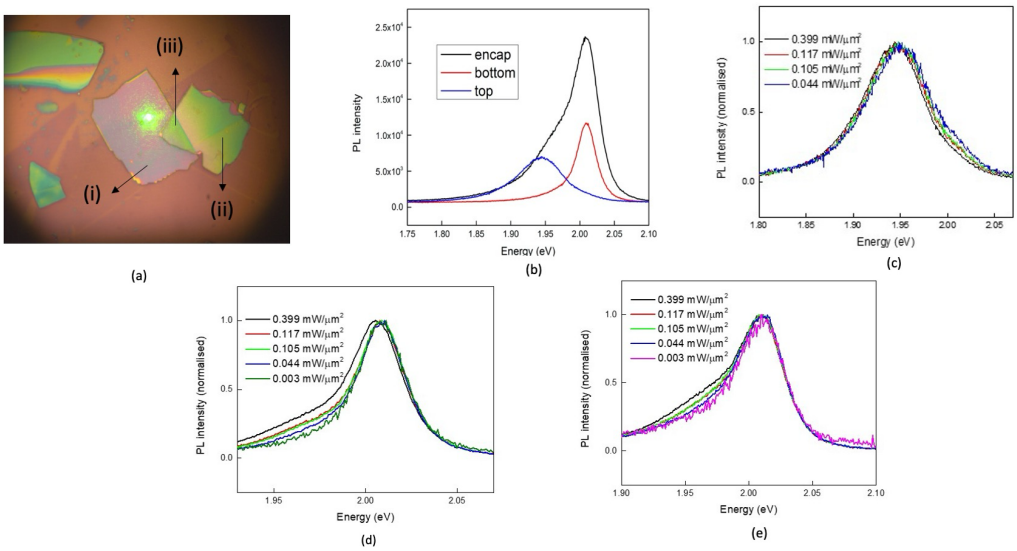

FIGURE 4.14: (a) Optical microscope image (at 100×) of (i) WS_2 on top of hBN, (ii) hBN on top of WS_2, (iii) WS_2 sandwiched between top and bottom hBN. (b) PL spectra from regions (i), (ii) and (iii) of the sample shown in Figure 3(a) Normalized PL with varying excitation power (c) on WS_2 with hBN on top, (d) on the WS_2 on top of hBN, (e) on the WS_2 encapsulated between hBN.

and sharper than the encapsulated one. The PL emission is more enhanced in the case of the encapsulated region compared to other cases.

We also investigated the importance of the thickness of the bottom hBN flake for selective excitation of the X^- in PL of WS_2. As it was seen earlier while discussing the results of Fig. 4.5c (WS_2 on top of 6 nm hBN), at the lowest excitation power we observed that the X^- peak is dominant. Now, as we increase the excitation power, we see an X^0 peak emerging slowly. At the highest excitation power, we see a prominent X^0 peak though for all powers X^- peak was more dominant and intense. To know about relative X^0 and X^- contribution we did Lorentz fitting of the PL spectra of Fig. 4.5c and d for deconvolution of the peaks at these powers Fig. 4.15 using the following Lorentzian equation:

$$I(E) = \sum_j \frac{2A_j w_j}{4\pi(E - E_{cj})^2 + w_j^2} \tag{4.1}$$

where I is intensity, E is energy, E_{cj} is peak position, w_j is width and A_j is the integrated area under the curve for j^{th} peak.

We see that with increasing excitation power, the T/X (ratio of peak intensities of X^-(trion) and X^0(exciton) respectively from the Lorentz fit) ratio decreases Fig. 4.16a. In this case, X^- peak is far more intense than the X^0 peak at all powers. In the case of WS_2 on top of

9 nm hBN (Fig. 4.5d), we see that at lowest power both X^- and X^0 peaks of comparable intensity are present. As we increase the laser power, from Lorentz peak fit of Fig. 4.5d, we see that the T/X ratio decreases Fig. 4.16a. But this time at all excitation powers, X^0 was more intense compared to the X^- peak. Now when we do the same analysis on the PL spectra of WS_2 suspended in the hole region (Fig. 4.11a) we see that at the lowest excitation power, only X^0 peak is present. As we increase the laser power the X^- peak starts appearing gradually. From the deconvolution of the PL spectra (Fig. 4.11a) at all these powers, we see that T/X increases with increasing excitation power (Fig. 4.16a). But the X^0 peak was always far more intense than the X^- peak at all these powers. The T/X intensity ratio decreases as the excitation power is increased for the case when monolayer WS_2 is placed on 9 nm thick hBN. This is because hBN limits the number of doping centers affecting the WS_2 monolayer resulting in decreased excitation of trions to that of excitons as the laser power is increased. A similar effect can also be observed for the 6 nm thick hBN, although the relative intensity of the X^-, in this case, is always higher due to decreased screening (because of less thickness of hBN) of the doping centres. In contrast, in the case of hole-suspended monolayer WS_2, the decreased screening efficiency leads to an increase of trion excitation relative to that of exciton as the excitation power is increased. We have plotted the splitting between X and T as a function of their intensity ratio (Fig. 4.16b) for WS_2 on top of 6 nm hBN and WS_2 suspended on a hole patterned substrate. We observed that in both the cases (hole and hBN) splitting shows a linear dependence with T/X ratio which is expected from the earlier reports in the literature [131]. Therefore, in both cases (hBN and hole) trion dissociation energy increases with the increase of excess carriers. But the slope of the plot in the case of WS_2 suspended on top of the hole is higher than the slope of the plot in the case of WS_2 on top of 6 nm hBN. This suggests that hBN more efficiently screens (due to the high dielectric constant of hBN) the effect of unintentional doping centres at the WS_2/SiO_2 interface compared to the hole suspended WS_2. This increases the T/X ratio as the excitation power is increased. As discussed earlier while explaining Fig. 4.11a light-induced desorption of oxygen in case of holes might also contribute to this observation [225, 226].

4.3.5 Effect of polarity of the substrate defects on the PL of WS_2

To investigate how the polarity of the defects affects the PL of WS_2, we have prepared SiO_2/Si substrate whose surface is made positively charged by coating the substrate with APTES [237]. A piece of 300nm SiO_2/Si was first cleaned by dipping in acetone, IPA and oxygen plasma. It was then dipped in 5% 3-aminopropyltriethoxysilane (APTES) in a toluene solution and kept for 15 minutes. It was taken out and washed in fresh toluene and then blow-dried. This made the SiO_2 surface positively charged [237]. Monolayer

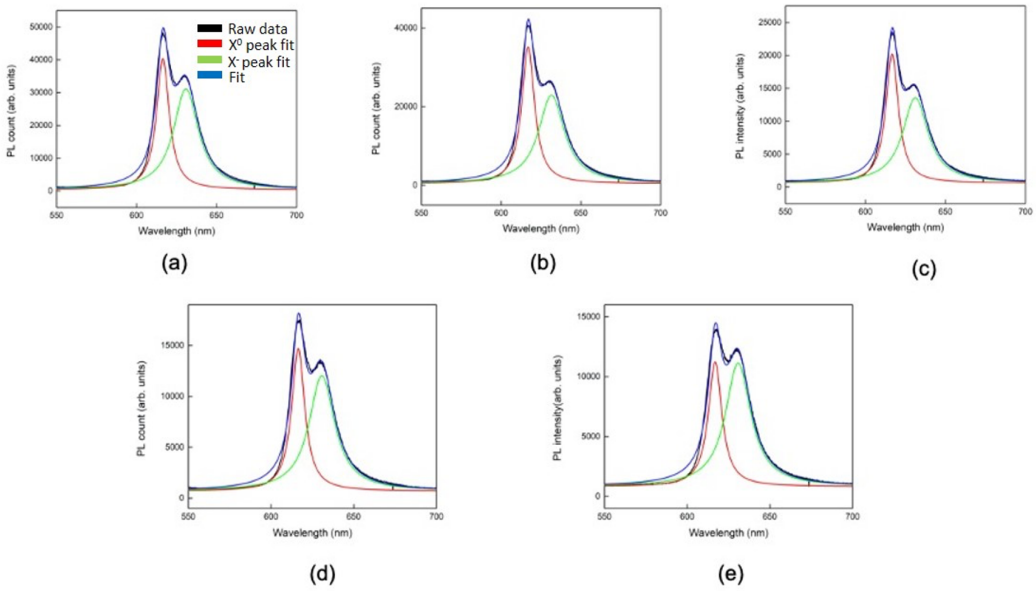

FIGURE 4.15: PL peak deconvolution carried out using Lorentzian peak fit component of excitons and trions in monolayer WS_2 placed on hBN. Figures (a) to (e) are in the order of decreasing excitation power.

TABLE 4.1: Summary of the peak width and position of data shown in Fig. 4.5a

	Trion		Exciton	
Configuration	Peak energy (eV)	Width (meV)	Peak energy (eV)	Width (meV)
WS_2 on SiO_2 /Si	1.946	73.10	———-	———-
WS_2 on 6 nm thick hBN	1.966	64.14	2.015	33.64
WS_2 on 9 nm thick hBN	1.964	60.89	2.010	32.57
WS_2 on 90 nm thick hBN	———-	———-	2.021	33.69
WS_2 suspended on hole	1.969	82.41	2.026	34.49
WS_2 on top of pillar	1.962	90.11	———-	———-
WS_2 suspended on pillar	———-	———-	2.015	43.19
WS_2 encapsulated between hBN	———-	———-	2.008	63.70

WS_2 was then transferred. In the excitation power-dependent PL (Fig. 4.16c) we found that almost for every power, X^0 peak is the dominant one with a little hump at the X^- position. At the highest power, we see an X^- peak and no X^0 peak. This is because the positive charge of the surface neutralizes the excess electrons in the naturally n-doped WS_2 channel and thereby decreases the carrier density inside the channel. As a result, we observe X^0 peak in WS_2 when placed on the positively charged substrate [238]. This also means that the usual SiO_2/Si surface that is being used in our experiments has negatively charged surface defects which aided the trion formation in WS_2. We have confirmed this by treating a SiO_2/Si substrate with oxygen plasma (60W, 10 mins) which turns the SiO_2/Si surface entirely negatively charged [239]. PL spectra taken on a WS_2 monolayer transferred on this substrate showed only trion peak at all excitation power (data not shown).

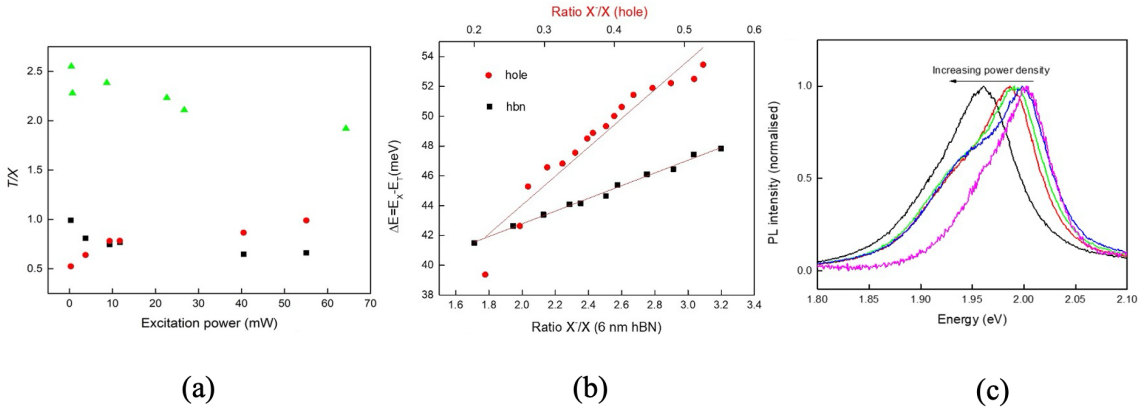

FIGURE 4.16: (a) Ratio of trion peak intensity and exciton peak intensity as a function of excitation power (0.03 to 0.870 mW/μm^2) for i. WS_2 on 6 nm hBN (green triangles) ii. WS_2 on top of a 9 nm hBN (black squares) iii. WS_2 suspended on hole patterned SiO_2/Si substrate (red circles). (b) Splitting energy (ΔE) of exciton and trion as a function of the ratio of the intensity of the exciton and trion for monolayer WS_2 supported on 6 nm thick hBN (black squares) and suspended on top of the hole (red circle). (c) Normalized PL with varying excitation power of WS_2 on positively charged SiO_2/Si surface.

4.4 Conclusions:

In conclusion, we have demonstrated that substrate plays an important role in optical transitions like photoluminescence. The substrate and TMD interface is a major source of charged impurity which modifies the PL spectra significantly. The effect of these charged impurities or doping centres can be screened by inserting a dielectric layer like hBN and by tuning the thickness of hBN one can modify the presence of trions and excitons (see Table 4.1 for peak position and width of trion and exciton in different substrate configuration). In such a way we can study them together or independently which is essential for realizing valleytronic devices. We also studied the screening effect of substrate defects by suspending the WS_2 monolayer. Our study reveals that suspending and inserting an hBN layer has two distinct effects on the ratio of trion and exciton intensity with increasing excitation power. Also, the PL emission of the WS_2 monolayer strongly depends on the polarity of the charge carried by the substrate defects. These results demonstrate a facile way to modulate the PL spectra of TMDs by controlling the effect of impurities through substrate engineering. Our findings will have a profound impact on tailoring single-photon emission processes from the defects of 2D materials and fabricating excitonic interconnects and valleytronic devices.

Chapter 5

Stacking Engineered Room Temperature Ferroelectricity in Twisted Germanium Sulfide Nanowires

Abstract:
Group-IV monochalcogenides have emerged with immense potential to be used as ferroelectric materials in recent times. However, in most of them, ferroelectricity is limited by the presence of inversion symmetry in their natural crystal structure. Here, an experimental observation of ferroelectric order at room temperature by introducing Eshelby twist in Germanium sulfide (GeS) nanowires is reported. The twisted nanowires are synthesized by low-pressure chemical vapour deposition. The existence of room-temperature ferroelectricity in a single nanowire is confirmed by electrical measurements, piezoelectric force microscopy, and second harmonic generation spectroscopy. Density functional theory (DFT) calculations reveal that the twist in the GeS nanowires breaks the inversion symmetry where the inversion symmetry breaking phonon modes get hardened giving rise to ferroelectricity. These results are expected to be useful in making non-volatile memory devices, flexible electronics, electronic sensors, and neuromorphic computing. The content of this chapter is adapted from the research article "Adv. Electron. Mater. 2022, 8, 2101158 (2022)" [15].

5.1 Introduction and motivation

After the successful isolation of graphene, a wide range of van der Waals (vdW) materials have been discovered[240]. Among various vdW materials, transition metal dichalcogenides (TMDCs) and group IV monochalcogenides, with the potential to show piezoelectric and ferroelectric properties have grown considerable interest in recent years. Ferroelectricity involves spontaneous electric polarization which can be tuned by an external electric field[241, 242]. Ferroelectricity in the group IV monochalcogenides may be more advantageous, as such materials display additional features like tuneable band gap and flexibility which are

crucial for applications as sensors and memory devices [241, 242]. Monolayers of many vdW materials such as TMDCs (MoS_2, $MoSe_2$, WS_2, and WSe_2) [241, 242] and group-IV monochalcogenides (GeS, GeSe, and SnS) are promising ferroelectric candidates [222, 241–246]. Materials with broken inversion symmetry are expected to show ferroelectricity but many of the TMDCs and group-IV monochalcogenides in their bulk form have inversion symmetry which forbids spontaneous polarization [243, 247]. However, if the inversion symmetry is broken then these materials might exhibit ferroelectricity[222, 243–245, 248–250]. GeS is one such material with inversion symmetry and lacks spontaneous polarization in its bulk form owing to its centrosymmetric crystal structure[243].

Twist is a very promising degree of freedom through which one not only can break the inversion symmetry, but also control electrical and optical properties of various vdW heterostructures[251–253]. Recently, stacking-engineered ferroelectricity has been discovered in twisted bilayer hBN[254]. In the fabrication of non-centrosymmetric GeS, the main challenge lies in the complexity of the preparation and assembly of GeS layers. One way to achieve that is by the introduction of twists. The fabrication of twisted nanostructures using the transfer stacking method is usually a very challenging task because of poor control over twist angle[255–257]. Liu. Y et. al. and Sutter P. et. al. demonstrated a robust process to grow twisted GeS nanowires by introducing Eshelby twist between two adjacent layers[12, 13]. These nanowires are formed by stacking layers held together via vdW interaction along the transverse direction[258, 259]. We used GeS nanowires made of stacked layers as a model system and introduced the Eshelby twist in consecutive layers to break the inversion symmetry. In the I-V characteristics of the nanowires, hysteresis, a characteristic feature of ferroelectric switching was observed. The ferroelectric nature of these nanowires was further established by PFM measurement and the nanowires exhibited spontaneous polarization also there is a 180°polarization switching in an external field at room temperature. SHG measurement showed a strong signal from these twisted nanowires which confirmed the presence of broken inversion symmetry. Phonon dispersion of the nanowire was calculated using DFT which showed the hardening of the inversion symmetry breaking phonon mode due to twisting. But this induces an instability which is compensated by spreading the twist across several unit cells. This twist results in the breaking of the inversion symmetry which might induce a spontaneous polarization in the nanowire, giving rise to ferroelectricity.

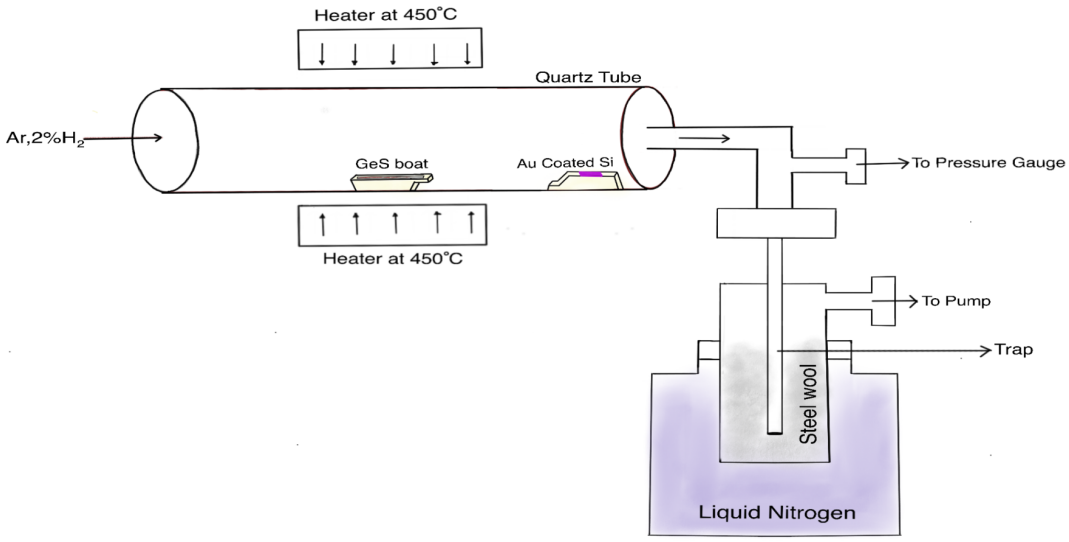

FIGURE 5.1: Schematic of low-pressure chemical vapour deposition (LPCVD) setup.

TABLE 5.1: Elemental Compositions as obtained from EDX analysis:

Element	Weight (%)	Atomic (%)
Ge	69.22	50.16
S	30.78	49.84
Total	100	100

5.2 Synthesis and characterisation

5.2.1 Synthesis

The twisted GeS nanowires were grown by vapour-liquid-solid (VLS) technique using gold as catalyst[12, 13]. A thin layer (3 nm) of gold (Au) was deposited on silicon (Si) substrates by thermal evaporation. These Au-coated substrates were put inside a quartz tube in a low-pressure chemical vapour deposition (LPCVD) setup (Fig. 5.1) along with 30 mg of GeS powder in an alumina boat. The precursor boat containing GeS powder was kept at a temperature of 450°C and the substrate boat was kept at a temperature of 270-300°C. Ar balanced with 2% H_2 was used as a carrier gas with a flow rate of 50 sccm. Pressure is a very crucial parameter for the growth of these twisted nanowires, so we kept the quartz tube at a pressure of 1-2 torr for optimal coverage of twisted nanowires over the substrates[12].

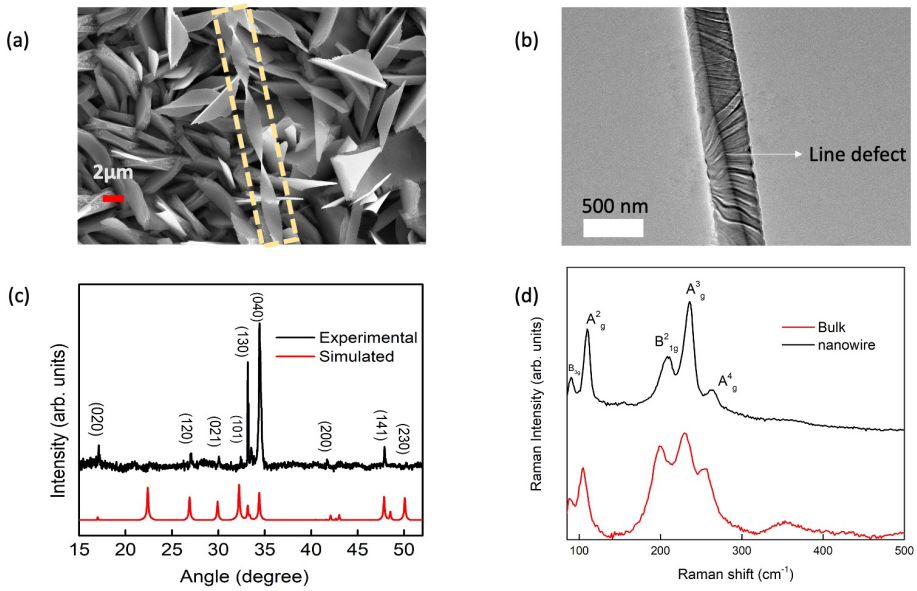

FIGURE 5.2: GeS nanowires with Eshelby twist. (a) FESEM image of a twisted GeS nanowire (inside the box) adhering to the substrate. (b) TEM image of a twisted GeS nanowire with a line defect (shown by arrow) at the centre of the wire. (c) PXRD pattern showing peaks which can be exactly indexed to the orthorhombic structure of pristine GeS. and (d) Raman scattering spectra of twisted GeS nanowires with different phonon modes.

5.2.2 Characterisation

Figure 5.2a shows a representative field emission scanning electron microscope (FESEM) image of a twisted GeS nanowire. The existence of the Eshelby twist was further confirmed by transmission electron microscopy (TEM) studies. In the TEM image (Figure 5.3b) a line defect can be seen at the centre of the nanowire. This line defect can be observed for every GeS nanowire. It was predicted by Eshelby that an axial screw dislocation at the centre of a thin rod will result in twisting by relaxing the elastic energy present due to the dislocation[260]. This energy-relaxing mechanism induces a torque on the ends of the nanowire which results in the chiral structure. Selected area electron diffraction (SAED) was done to confirm the crystallographic twist in the nanowires[12]. The SAED was done at two different locations of the nanowire along its length and the change in the SAED patterns confirms that their crystallographic orientation changes along the length (Figure 5.3). XRD was done from a Bruker D8 Advance diffractometer using Cu Kα radiation ($\lambda = 1.5406\mathring{A}$). The peaks obtained from the powder X-ray diffraction (PXRD) of these nanowires (Figure 5.2c) can be exactly indexed to the orthorhombic structure of pristine GeS (space group pnma, JCPDS No. 00-051-1168) [261, 262]. SAED also confirmed the single-crystalline nature of the nanowires. Raman spectroscopy was done with a laser of wavelength 632.8 nm using

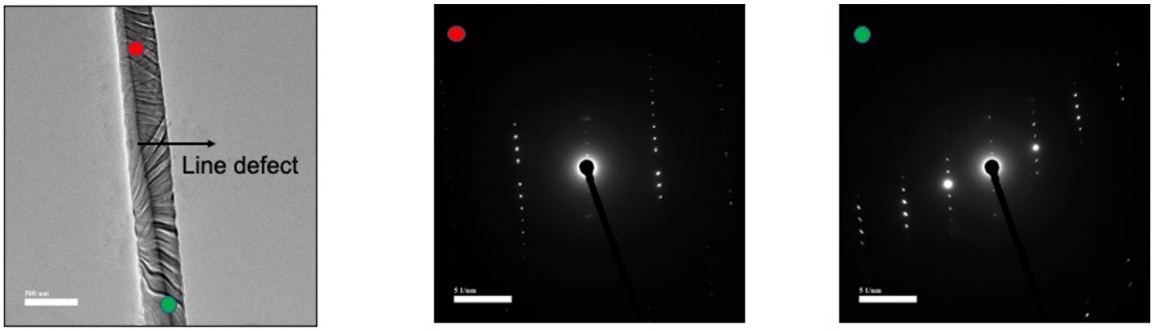

FIGURE 5.3: (a) TEM image of a twisted GeS nanowire with a line defect at the centre of the wire. (b) and (c) are SAED patterns taken from two different locations on the nanowire (marked by red and green dots), showing the changing crystal orientation with respect to the incident electron beam.

a Raman microscope (LabRAM HR, HoribaJobinYvon) having a 50× objective lens. Using Raman spectroscopy phonon modes of the single twisted GeS nanowires were measured (Figure 5.2d), and $A_{1g}(265cm^{-1})$, $B^2{}_{1g}(210cm^{-1})$, $A_{3g}(236cm^{-1})$ and $A_{2g}(110cm^{-1})$ peaks were observed[262–264]. Raman spectra of the bulk and twisted nanowires were compared and a blueshift of the phonon modes was observed in the twisted nanowires. This is probably due to the hardening[265] of phonon mode because of twist as was also seen in our DFT calculations (discussed later). The elemental compositions of the single nanowire were determined by Energy Dispersive X-ray spectroscopy (EDS) which gave the stoichiometric ratio of $Ge : S \simeq 1 : 1$ (Fig. 5.4 and Table 5.1, Supporting Information). We found that these nanowires were very stable over time both in chemical composition and as well as their structure. The stability of LPCVD-grown GeS is attributed to the self-encapsulation of twisted GeS nanowires in a protective GeS_x shell during synthesis, which is thermally and chemically protective[13].

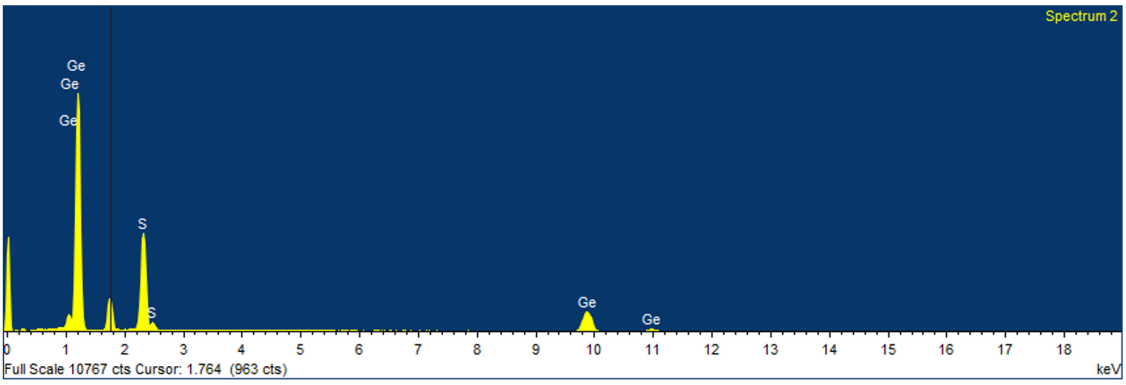

FIGURE 5.4: EDS spectra of twisted GeS nanowires.

5.3 Experimental Measurements

5.3.1 Electrical Studies

To measure current-voltage (I-V) characteristics, field-effect transistor (FET) devices were fabricated on single GeS nanowires. First, from Si substrates, the nanowires were scraped out and dispersed in a 99% ethyl alcohol solution. The nanowires were then drop cast on 300 nm SiO_2 /Si substrate and two probe contacts of Cr/Au (5/65 nm) were made on these nanowires by a standard photolithographic process. All the electrical characterisations were done in a probe station with the help of the Keithley 2450 source measure unit and Yokogawa GS820 multi-channel source measure unit. The source-drain current vs. source-drain voltage (I_{ds}-V_{ds}) characteristics of a single nanowire FET, measured at room temperature, are shown in Figure 5.5a. I-V data exhibited hysteresis, which is a characteristic feature of ferroelectric switching. The hysteresis in I-V data indicates that there is a change in the resistance of the device by polarization switching of ferroelectric GeS nanowire[266, 267]. This is because the width of the Schottky barrier and the height at the Au/GeS interface are changed by the reversal of polarization. The voltage sweep direction in Figure 5.5a. is shown by arrows. From the I-V characteristics, it is clear that when the bias is increased from 0V to a positive value, the device remains in a low resistance state (LRS), this is because the channel stays in negative polarization from the previous negative bias sweep. Further, increasing bias shows a reduction in the current (sweep i in Figure 5.5a). This happens when the applied bias becomes larger than the coercive field (here it is +18V).

The negatively polarized domains of GeS gradually switch to positive polarizations. This increases the resistance hence current decreases (+18 to +20 V region in Figure 5.5a) and the device enters into a high resistance state (HRS). As the voltage is decreased to zero (sweep ii in Figure 5.5a) the direction of net polarization remains in the direction of the external field and the device stays in HRS. In this case, the measured coercive voltage is +18V and the corresponding coercive field is 4.5 kV/cm.

The source-drain vs. gate voltage (I_{ds}-V_{ds}) curve at V_{ds}= +20V (Figure 5.5b) shows that the GeS-FET is p-type. The mobility of charge carriers was calculated by the following formula:

$$\mu = \frac{L}{WCV_{ds}} \frac{dI_{ds}}{dV_g} \tag{5.1}$$

where L is the length and W is the diameter of the twisted GeS nanowires, C is the capacitance between the twisted nanowire and the Si substrate (universal back gate) per unit area $C = \frac{\epsilon_0 \epsilon_r}{d}$, ϵ_r is the relative permittivity, ϵ_0 is the permittivity of vacuum and d is the thickness of the SiO_2). From this formula, the FET mobility of a single twisted GeS nanowire is found to be 0.70 $cm^2 V^{-1} s^1$. This mobility of charge carriers in twisted GeS nanowires is larger than the reported values of mobility in GeS [261, 264, 268]. However, measured mobility for twisted GeS nanowires is low compared to reported values for other 2D materials[261, 264, 268, 269] probably because of a large number of defects in the as-grown twisted GeS nanowire. These defects cause local variation in the conduction and valence band[270] and the holes get localized in the forbidden energy gap[271], which results in a low charge carrier mobility. A sublinear dependence of photocurrent on incident optical power density was observed (Figure 5.5c). This also supports the presence of a large number of defects in these twisted nanowires[272, 273].

5.3.2 Piezoelectric Force Microscopy

To obtain further support for ferroelectricity in GeS we drop cast the twisted nanowires on an indium tin oxide (ITO) coated glass substrate[274] and carried out piezoresponse force microscopy (PFM)[265]. The Curie temperature (T_C) of the ferroelectric GeS nanowire is predicted to be $\sim$ 310 K which is well above the room temperature [222]. An Asylum research AFM (MFP-3D) equipped with a high-voltage amplifier was used for PFM measurements. The sample was mounted on a conducting sample holder that was connected to the ground of the amplifier. The conductive AFM cantilever having a Pt-Ir tip on it was brought in contact with the nanowires. An ac excitation riding on a bias voltage (V_{dc}) was applied between the amplifier ground and the Pt-Ir tip. The electrical stimulus was applied

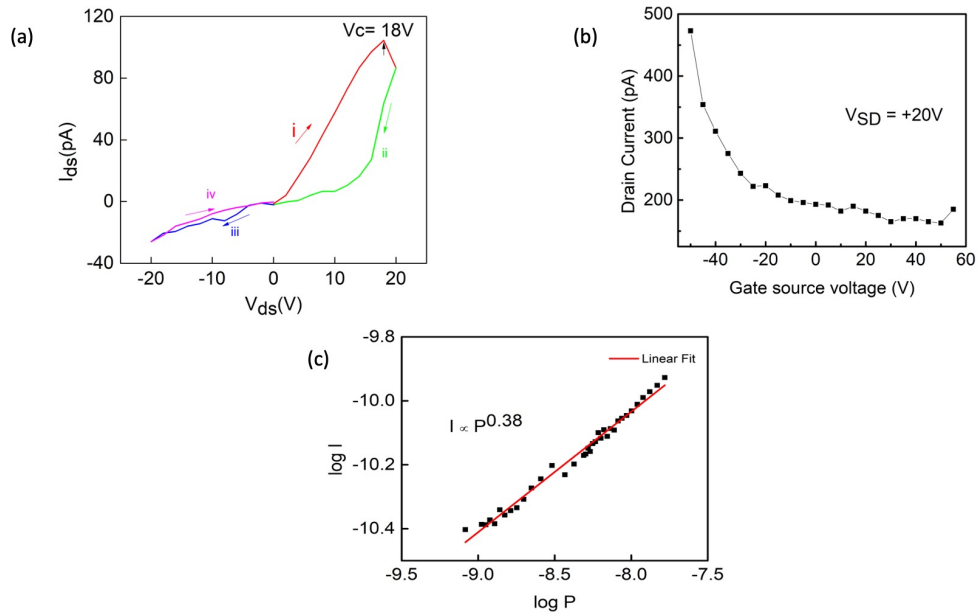

FIGURE 5.5: Electrical characterization. a) I-V hysteresis curve of a twisted GeS nanowire FET device (channel length L = 4 μm, cycled from - 20 to + 20 V). The voltages are swept in order 0 V $\rightarrow$ 20 V $\rightarrow$ 0 V $\rightarrow$ -20 V $\rightarrow$0V as shown by coloured arrows with the four sweeps labeled as i, ii, iii, and iv. The coercive voltage refers to the minimum voltage required for ferroelectric switching is labeled near the current peak. b) The source-drain versus gate voltage at V_{ds} = +20 V and c) dependence of photocurrent (I_{ds}) at Vds = +5 V on incident optical power density.

to the sample and its response was detected through the reflection of a laser from the cantilever end onto a position-sensitive photodiode. To make sure that the hysteretic effects are due to ferroelectricity which can also come from various other reasons, all the measurements were performed following SS-PFM (switching spectroscopy piezoresponse force microscopy) introduced by Jesse et al. [265, 275, 276] A hysteric behaviour of the nanowire can be observed (Figure 5.6a and b) in the "off-state" piezoresponse signal at room temperature. This hysteretic behaviour with a switching of electric polarization at different applied dc bias (V_{dc}) can be seen in Figure 3a. A large coercive field $\geq +10V$ indicates that two opposite polarization states are separated by a very high energy barrier. In PFM, the polarization direction of the domain under the PFM cantilever is shown by the phase of the PFM response signal which shows hysteresis with 180° switching[265] when the domain switches the polarization direction. Hence, the observed hysteresis curve (Figure 5.6a) in twisted GeS indicates the presence of intrinsic ferroelectricity. As it is well known, all ferroelectrics are also piezoelectric, this is seen in the amplitude of PFM response [265]. The PFM signal amplitude of twisted nanowires exhibited a butterfly-shaped hysteresis loop (Figure 3b) which is a hallmark signature of piezoelectricity. We calculated the piezoelectric coefficient "d_3" value of this nanowire and this is found to be 2.97 pm V^{-1} [277]. This was

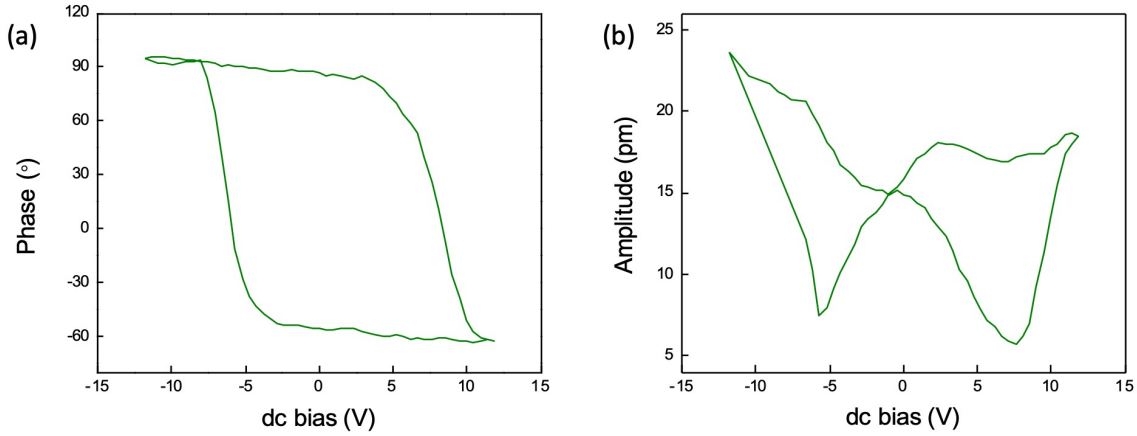

FIGURE 5.6: a) Phase and (b) amplitude of SS-PFM signal from twisted GeS nanowire at room temperature exhibiting ferroelectricity with 180°polarization switching.

calculated from the amplitude versus external dc bias data from PFM (Figure 5.6b). d_{33} is the piezoelectric coefficient that quantifies the change of volume when an external electric field is applied[278].

5.3.3 Second Harmonic Generation spectroscopy

Since the absence of inversion symmetry is the fundamental cause for the emergence of the ferroelectric order[279], these twisted nanowires should show nonlinearity in the SHG signal. SHG is a nonlinear scattering phenomenon in which two photons combine and a photon with twice the frequency is emitted. SHG is prohibited in materials with inversion symmetry[280]. When the twisted GeS nanowires are irradiated with an electric field of frequency ω, then there is an asymmetric charge oscillation about the mean position in the nanowires and due to the cosine term (see supporting information), this is reradiated at a frequency 2ω[281]. Therefore, the materials with a non-zero second-order nonlinear susceptibility $\chi^{(2)}$ i.e. the materials which have broken inversion symmetry will show SHG. The nanowires were excited at 810 nm wavelength (Ti Sapphire Laser operating at 140fs, 80 Hz) through a glass substrate using a high numerical aperture objective lens (100×, 1.49 N.A.). The average power at the entrance port of the objective lens was measured to be 65 mW. It was observed that exposing the wire to 80 mW or more power burnt the structure. The SHG signal was collected through the same objective lens and projected at the spectrometer slit using relay optics. The laser is focused onto a single nanowire using a

high numerical aperture lens through the glass, and the back-scattered light from the wire is collected using the same objective lens. Every twisted nanowire showed an SHG signal at λ = 405 nm (Figure 5.7). A pinhole was used for spatially filtering out the excitation region. A combination of a 680 nm short-pass filter and a 405 nm line pass filter was used for blocking the excitation laser as well as spectrally filtering out the signal of interest. The full optical schematic of the measurement is given in Fig. 5.8. It is known that gold can show SHG due to surface effect and morphology although it has inversion symmetry in bulk[282–285]. To confirm that the SHG is not originating from the gold substrate, the same measurement was performed on a 3nm gold-coated glass substrate heated at 350°C i.e. the temperature at which VLS occurs during LPCVD synthesis of twisted GeS nanowires. No SHG signal was observed from the heated gold-coated glass substrate, (Figure 5.7) which indicates the SHG signal is solely coming from twisted GeS nanowires. As a control experiment, SHG was also done on GeS bulk crystal and it gave no signal (Fig. 5.7). The SHG study re-confirms that inversion symmetry is indeed broken in these twisted GeS nanowires and is the reason for the emergence of ferroelectric order. There are many theoretical predictions that GeS will show strong SHG[286, 287]. As far as we know from the literature, this is the first experimental report of SHG in a GeS system.

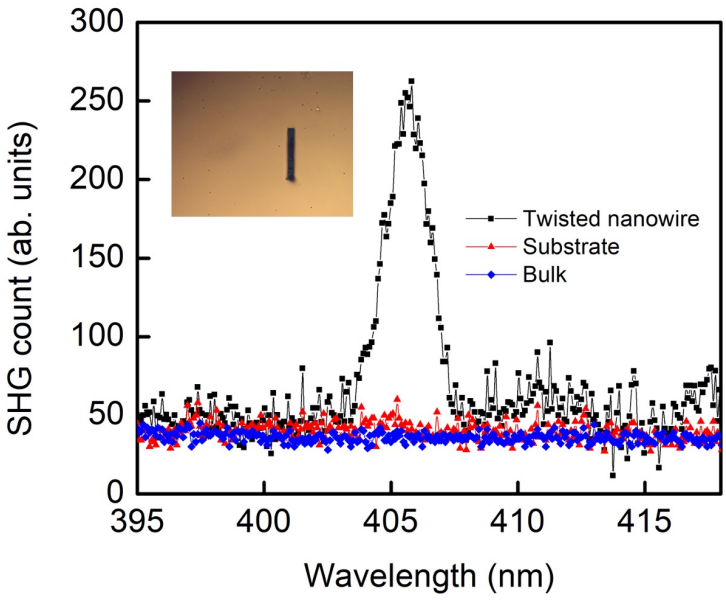

FIGURE 5.7: SHG spectra of twisted GeS nanowire on a glass substrate (red), 3 nm gold-coated glass substrate (black), and bulk GeS (blue). The inset shows the image of the nanowire on which the SHG measurement is done.

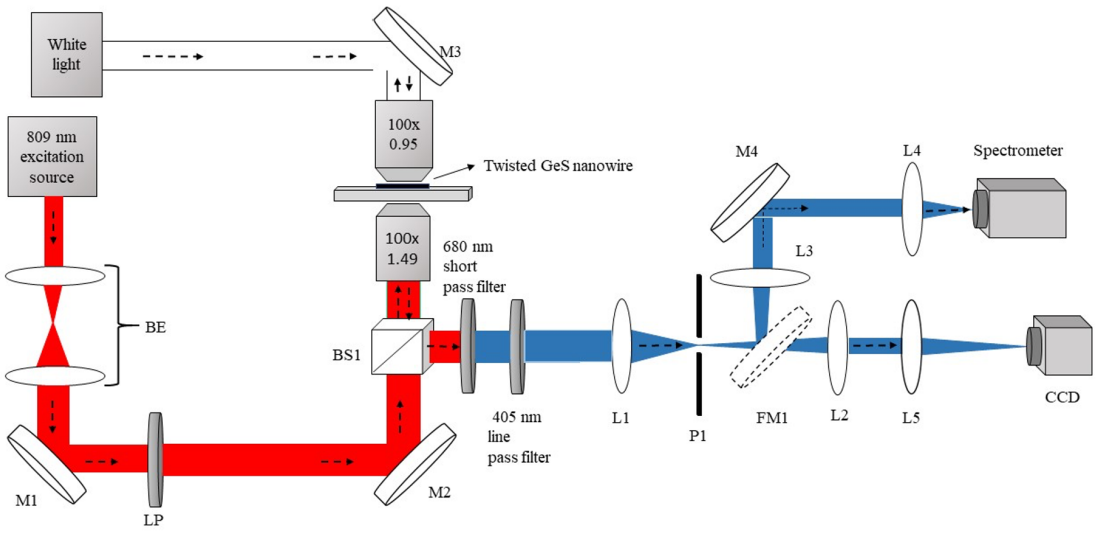

FIGURE 5.8: Schematic of the second harmonic generation (SHG) measurement setup.

5.4 Density Functional Theory calculations

5.4.1 Computational Details

DFT-based calculations were done using the Quantum ESPRESSO software [133, 134] which is a plane wave-based implementation of DFT (done in collaboration with Dr Prasenjit Ghosh's group). The electron-ion interactions were modelled with ultrasoft pseudopotentials For Ge and S, valence electronic of $4s^2 4p^2$ and $3s^2 3p^4$ were used, respectively. The wave functions and charge densities were expanded in a plane wave basis determined by kinetic energy cut-offs of 50 and 500 Ry, respectively. The electron-electron exchange and correlation potential were described with Perdew-Burke-Ernzerhof (PBE) parametrization of the Generalized-Gradient-Approximation (GGA)[133]. Bulk GeS had a layered structure and the layers interacted with each other primarily through van der Waals interactions. However, standard PBE-GGA functionals did not take into account those interactions. Hence, the empirical correction proposed by Grimme et al. was used [140]. For the bulk, a 9 $\times$ 9 $\times$ 3 Monkhorst-Pack k-point grid was used for Brillouin zone (BZ) integrations. To study the dynamical stability of the system, the phonon spectra for the nanowires were computed using density functional perturbation theory[142]. For these calculations, kinetic energy cut-offs of 70 and 600 Ry were used, respectively. To test the pseudopotentials, the optimized structure of bulk GeS was computed. The calculations yielded lattice parameters of a = 3.67, b = 4.34, and c = 10.67 $\mathring{A}$. It was found that the computed lattice parameters were in

excellent agreement with the experimental results [261, 288] and previously reported computational studies[81]. The nanowires in the calculation were aligned along the c-axis. Since the codes used periodic boundary conditions, there was spurious periodicity along the a and b directions. To minimize these spurious interactions, about 14 $\mathring{A}$ separation was ensured between the nanowires along both directions. In these cases, a $1 \times 1 \times 6$ Monkhorst-Pack k-point grid was used for BZ integrations. Berry phase-based calculations were performed to compute the magnitude and direction of spontaneous polarization.

5.4.2 Results

The origin of ferroelectricity in a material is usually associated with a breaking of inversion symmetry that leads to non-zero charge polarization. Bulk GeS has an inversion symmetry and hence is nonpolar. However, as we have shown experimentally, the twisted nanowires are ferroelectric. To understand the origin of the observed ferroelectricity we have performed density functional theory (DFT) based calculations. Since the nanowires have a large spatial extent in the plane perpendicular to the c-axis, modelling the full system using DFT is prohibitively expensive. Therefore, we have considered a small model nanowire (NW1) cut from the bulk system as shown in Fig. 5.9a. The nanowire is periodic along the c-axis and analogous to bulk and it consists of two bilayers of GeS. This structure is nonpolar with D_{2h} symmetry. NW1 has a periodicity of 12.13 $\mathring{A}$ along the c-direction, which is larger than that observed in bulk GeS (10.67 $\mathring{A}$). Computation of the phonon dispersion (Fig. 5.9d) shows that two optical modes are unstable in the whole Brillouin zone (BZ). Additionally, we observe instability in an acoustic mode at some points of the BZ. To move to a dynamically stable structure, we considered the unstable mode at Γ-point with the largest imaginary frequency and displaced the atoms along the eigenvector of this mode. After a displacement of about 1.40 $\mathring{A}$ in the multidimensional Hilbert space, we observe a local minimum in the potential energy space that is about 137 meV lower in energy than NW1. The structure of the nanowire at this minimum (NW2), after a full geometry relaxation, is shown in Fig. 5.9b. The computed phonon spectrum (Fig. 5.9e) shows that there is no unstable frequency in the whole BZ, suggesting that this structure is dynamically stable. Compared to NW1, the symmetry of NW2 is reduced to C_{2h} and the lattice parameter along the c-axis is slightly reduced to 11.63 $\mathring{A}$. However, NW2 still has an inversion symmetry that makes it non-polar.

To understand what is the driving force behind the twisting of the nanowires, we looked into the low-frequency optical modes of NW2 at $\Gamma-$point of the BZ. We find that the mode with 32 cm^{-1} frequency at Γ-point of the BZ is not only the softest mode but also corresponds to the lowest frequency inversion symmetry breaking mode (highlighted by a red line in Fig. 5.9e). The vibrational motion corresponding to that mode results in the twisting

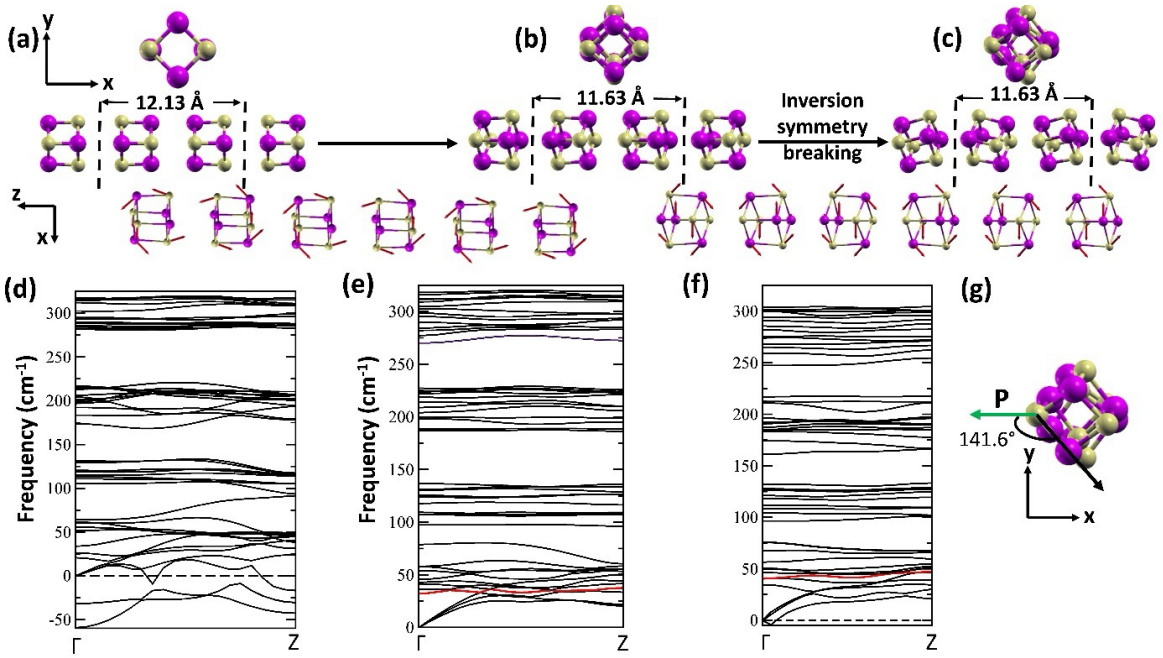

FIGURE 5.9: Density functional theory studies. a,d) Dynamically unstable structure and phonon dispersion of NW1 with inversion symmetry, b,e) dynamically stable structure and phonon dispersion of NW2 with inversion symmetry. c,f) Twisted nanowire without inversion symmetry and the phonon dispersion curve. In (e) and (f), the phonon mode corresponding to the twist is highlighted in red. g) The direction of the polarization vector P for the twisted NW2 with an imaginary acoustic mode. In (a), (b), and (c), the top panel shows the top view while the bottom one shows the side view. Yellow and magenta spheres denote S and Ge atoms, respectively.

of NW2. Upon twisting NW2 by displacing the atoms along with the eigenvector corresponding to this soft mode, we observe that instabilities start setting in at a displacement of 1.5 $\mathring{A}$ in the multi-dimensional space. The twisted NW2 structure shown in Fig. 5.9c is about 0.30 eV higher in energy than the parent one. Moreover, in this case, the instability is observed in the long-wavelength acoustic modes as shown in Fig. 5.9e. The vibrational pattern corresponds to a rippling in the wire. This suggests that NW2 will be unstable if the wavelength of this mode $\lambda > 20c$. However, finite-sized nanowires will be stable. Thus, our calculations suggest that the introduction of a twist in the nanowire will increase the periodicity of the unit cell along the c-direction. Additionally, we also observe that this mode is hardened to 40.5 cm^{-1} upon twisting. Thus our results suggest that by introducing a twist into these nanowires, the corresponding soft mode is strengthened. However, this comes at the cost of instability in terms of rippling. We envisage that this energy cost is compensated by spreading the twist across several unit cells along the c-direction. Further, the twist results in the breaking of the inversion symmetry that might induce a spontaneous polarization in the nanowire, giving rise to ferroelectricity. To verify this, we have computed the spontaneous polarization induced in the twisted NW2 (Figure 5.9c). We find that this model system has a polarization 408.6 μC m^1. The polarization vector makes an angle of

141.6°with the in-plane S-Ge bond as shown in Figure 5.9g. At this point, we would like to note that the DFT calculations are done on a model system, and the magnitude and direction of the spontaneous polarization might be different in the actual system. In this case, the Eshelby twist in these LPCVD-grown GeS nanowires is breaking the inversion symmetry.

5.5 Conclusions

In summary, we demonstrated the growth of twisted GeS nanowires using LPCVD. Raman scattering, PXRD, SAED, and EDS were done on these twisted nanowires to confirm the chemical composition and crystallinity. The twist in these nanowires was seen in FESEM. Also, the crystallographic twist is confirmed by TEM and SAED. Transfer characteristics of these nanowires showed that the twisted nanowires were p-type. The FET mobility of the twisted GeS nanowire is found to be 0.70 $cm^2V^{-1}s^1$ which is the highest reported so far for any GeS system. The I-V characteristics of the twisted GeS nanowires showed hysteresis which is a characteristic feature of ferroelectric materials, observed due to polarization switching. PFM measurement showed that these twisted GeS nanowires have intrinsic ferroelectric order which is absent in bulk GeS. The presence of broken inversion symmetry, a fundamental cause for ferroelectricity, is further confirmed by SHG spectroscopy which showed that the twisted nanowires are SHG active. Our experimental observations are further supported by DFT calculations which showed that inversion symmetry is broken due to Eshelby twist in GeS nanowires. Our findings will have a profound impact on the development of ultrathin non-volatile memory devices, flexible electronics and quantum optical communication because of their chiro-optical nature[289].

Chapter 6

Overall summary and future directions

6.1 Summary

This thesis primarily aims at adjusting the optoelectronic properties of layered two-dimensional materials such as monolayer WS_2, specifically TMDs, and group-IV monochalcogenides like GeS. The methods include applying strain and altering the surrounding dielectric to tune the photoluminescence and Raman spectra of WS_2, as well as utilizing interlayer twists in GeS nanowires to induce unconventional ferroelectricity arising from broken inversion symmetry.

In Chapter 2, we detailed the process of designing and assembling custom-built setups, specifically the LPCVD system and the transfer stage, for fabricating twisted GeS nanowires and van der Waals heterostructures. The constructed setups are economically efficient and can be easily modified to meet experimental requirements.

In Chapter 3, we demonstrate how external influences, such as strain, can adjust the electronic band structure of monolayer TMDs (e.g. WS_2) to brighten the dark K-Λ exciton state, which is the excitonic ground state of monolayer WS_2. We applied strain to the monolayer WS_2 by placing the CVD-grown monolayer WS_2 onto nanotextured substrates fabricated using block copolymer lithography. We subsequently carried out temperature-dependent photoluminescence spectroscopy and observed the brightening of the K-Λ dark exciton forbidden momentum in WS_2. Furthermore, we performed temperature-dependent Raman spectroscopy to reveal the robust exciton-phonon coupling induced by tensile strain, which accounts for the brightening of the K-Λ dark exciton. Furthermore, we performed DFT-based calculations to analyze the behaviour of the electronic and phononic bands under applied strain. We also determined the exciton-phonon coupling strength specific to phonon modes to corroborate our experimental findings. Being an excitonic ground state, it affects nearly all types of optical emission properties. Hence, brightening this dark state state is crucial for various fundamental studies and technological applications such as ultrasensitive strain sensing device.

In Chapter 4, we demonstrate how dielectric and substrate engineering can modulate exciton and trion formation in monolayer WS_2. Specifically, we placed the monolayer WS_2 on hBN flakes of varying thickness situated on conventional SiO_2/Si substrates, as well as on SiO_2 / Si substrates with holes and pillar patterns. Thus, we can separate the monolayer WS_2 channel from the impact of substrate defects located at the interface between the TMD and SiO_2/Si, which introduce doping into the TMD layer and influence the formation of quasiparticles such as excitons and trions. This allows us to adjust the proportion of trions and excitons in the photoluminescence spectra. We also demonstrated that the exciton and trion spectra varied with different laser excitation powers, as laser excitation acts as a photodoping source for the WS_2 channel in all the previously mentioned samples. Moreover, we detected the funnelling of excitons in regions subjected to significant strain, and the emergence of electron-hole plasma when higher laser excitation powers were applied, which was previously observed only in monolayer MoS_2. Finally, we present an analysis demonstrating that separating the monolayer WS_2 from the SiO_2/Si substrate using hBN is more effective than suspending it in air with a hole and patterned SiO_2/Si substrate. Our results will significantly influence the customization of single-photon emission processes originating from 2D material defects and in the creation of excitonic interconnects and valleytronic devices, where the selective excitation of trions, excitons, or both, is essential.

In Chapter 5 we discussed the emergence of unconventional ferroelectricity in GeS nanowires due to interlayer twist. GeS exhibits a centrosymmetric crystal structure in its bulk form, meaning that ferroelectricity is inherently prohibited. Nevertheless, the interlayer twist in GeS nanowires leads to the spontaneous breaking of inversion symmetry, resulting in the appearance of stacking-induced ferroelectricity. We fabricated the twisted GeS nanowires through low-pressure chemical vapour deposition, employing the vapour-liquid-solid (VLS) growth mechanism. We validated the twisting in each nanowire by employing SEM, TEM, and SAED techniques. After fabricating the devices on individual nanowires, we observed a hysteresis loop in their I-V characteristics, which hinted at the presence of ferroelectricity. Next, we carried out piezoelectric force microscopy (PFM), which revealed hysteresis in the phase versus DC bias plot and exhibited a butterfly loop in the amplitude versus DC bias plot, a definitive indicator of ferroelectricity. Our theoretical calculations further underpin the experimental findings by demonstrating the stabilization and hardening of phonon modes that break inversion symmetry owing to the twist in GeS nanowires. We observed that the truncated twisted GeS nanowire, utilized in our calculations due to computational constraints of simulating the entire nanowire, exhibited an electrical polarization of 408.6 μC m^{-1}. Our research outcomes hold significant potential for advancing ultrathin nonvolatile memory devices, flexible electronics, and quantum optical communication due to their chiro-optical properties[15, 36, 104].

All these observations demonstrated that external perturbation plays a significant role in revealing new optoelectronic properties of layered materials. In terms of future research on the optoelectronic characteristics of 2D TMDs, our objective is to explore the mechanisms of charge and energy transfer within the graphene-MoS_2 heterostructure. The subsequent section presents some of our initial findings regarding the electronic transport studies of the graphene-MoS_2 heterostructure.

6.2 Future directions

6.2.1 Introduction and motivation

Two-dimensional (2D) materials like graphene and MoS_2 show significant potential for future electronic and photonic applications due to their unique characteristics derived from their ultrathin planar forms, such as pronounced electron-hole confinement, exceptional flexibility, and high transparency, enabling the creation of thinner, more bendable, and more effective devices. Graphene has garnered significant interest in optoelectronic applications because of its excellent carrier mobility, wide range of absorption, and quick response time. Recent research has demonstrated that graphene is an outstanding material for converting light into photocurrent, achieving near 100% quantum efficiency due to its extended mean-free path and elevated Fermi velocity. Nonetheless, graphene captures just 2.3% of the light across the broad spectrum of visible wavelength. Despite employing several methods such as graphene plasmons, microcavities, and metallic plasmons to boost light absorption in graphene, there remains significant potential for improving the photogain in graphene-based photodetectors. While the rapid recombination of photoexcited carriers in graphene might be detrimental to photoresponsivity, the high carrier mobility in graphene provides a promising opportunity to achieve high photoresponsivity given an appropriate graphene device design. The integration of graphene with different 2D layers into synthetic heterostructures to exhibit unique or customized properties has been suggested and achieved in tunnelling field-effect transistors. The photoresponse performance of graphene devices can, in theory, be significantly improved by utilizing a vertical structure, such as a graphene/2D semiconductor heterostructural arrangement, enabling the entire graphene area to function as a junction. Layered MoS_2 is a two-dimensional material characterized by a finite and direct band gap. MoS_2 monolayers exhibit a photoluminescence that is four times greater than that of their bulk form, due to the quantum confinement effect leading to the change from an indirect band gap in the bulk to a direct band gap in the monolayer. MoS_2 thin-layer photodetectors have demonstrated notably high photoresponsivity in ambient conditions, with values ranging from 7.5 mA/W to 780 A/W. At the interfaces of MoS_2 and graphene, the photogenerated

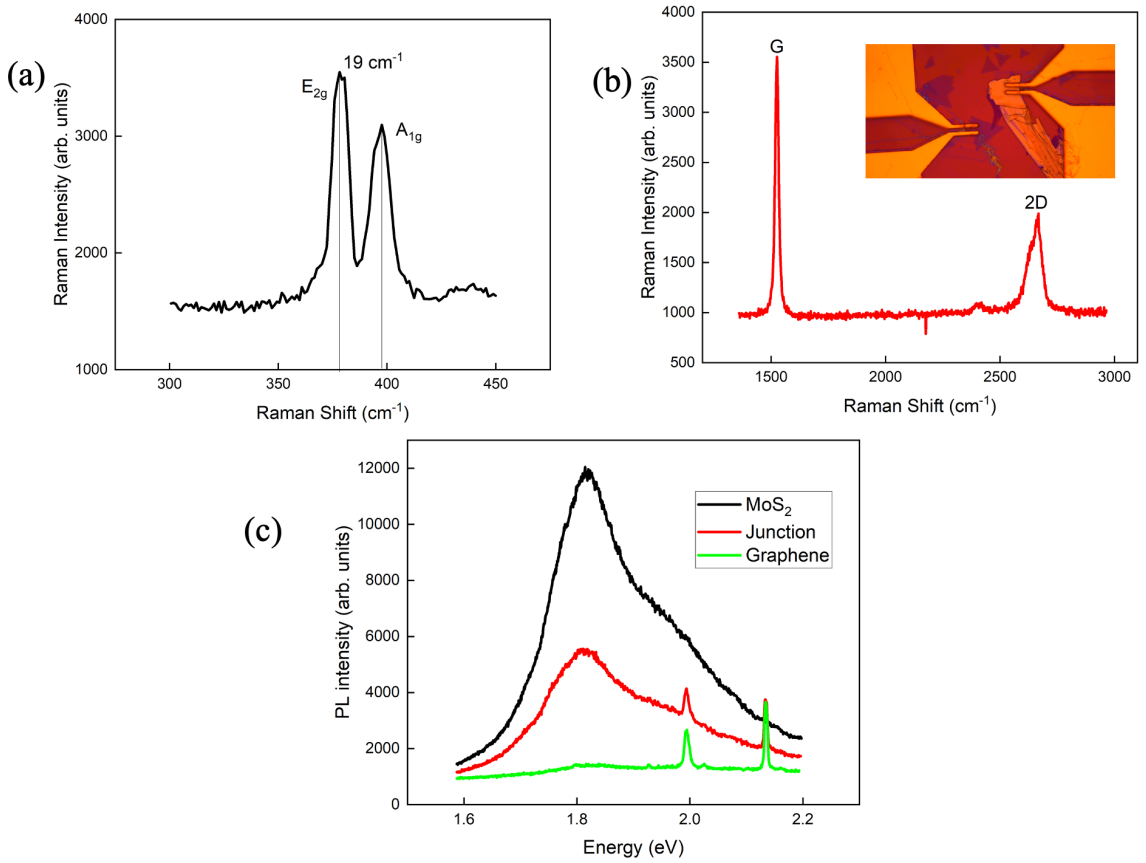

FIGURE 6.1: (a) Raman spectra of CVD grown monolayer MoS_2 shown in the inset of (b). The separation of 19 cm^{-1} between in-plane (E_{2g}) and out-of-plane A^1_{2g} Raman mode indicates that the thickness of MoS_2 is one-layer. (b) The Raman spectra of FLG. The thickness is confirmed by the intensity ratio of G and 2D peak ($\frac{I_G}{I_{2D}} > 1$). (c) The PL spectra were taken at three different regions of the sample shown in (b), namely monolayer MoS_2 flake (black), FLG (green) and FLG-MoS_2 junction.

electron-hole pairs are separated, with electrons migrating to the graphene layer. This movement is prompted by a perpendicular effective electric field, which is a result of the interplay between the inherent electric field, the applied electrostatic field, and any charged impurities or adsorbed molecules. The photodetector utilizing the graphene/MoS_2 heterostructure can achieve a photoresponsivity exceeding 10^7 A/W and a photogain of approximately 10^8 at ambient temperature[290–293].

In the upcoming sections, we present initial data on optical spectroscopy, photoresponse, and photocurrent spectroscopy, deriving from our ongoing study on the electronic transport characteristics of the graphene-MoS_2 heterostructure.

6.2.2 Electronic Transport study of graphene-MoS_2 heterostructure

6.2.2.1 Sample Preparation

The sample was made using a CVD-grown monolayer of MoS_2 and few-layer graphene (FLG) obtained by exfoliation from Kish graphite crystals available commercially. The sample was fabricated utilizing the procedures outlined in Chapter 2, employing a transfer stage and nail polish as the polymer (see Figure 6.1a for an optical microscope image of the sample).

6.2.2.2 Raman and PL spectroscopy

We performed PL and Raman spectroscopy on the Graphene-MoS_2 heterostructure sample shown in the inset of Figure 6.1b. We excited the sample with a laser excitation wavelength of 532 nm. The Raman spectrum of the monolayer (see Figure 6.1a) MoS_2 flake displays in-plane (E_{2g}) and out-of-plane A^1_{2g} Raman modes, separated by 19 cm^{-1}. This confirms that the MoS_2 flake is a monolayer. The Raman spectra of FLG graphene show two distinct Raman modes G and 2D (see Figure 6.1b). The thickness was confirmed by the intensity ratio of the G and 2D peak, $\frac{I_G}{I_{2D}} > 1$.

Figure 6.1b illustrates the photoluminescence (PL) of monolayer MoS_2 flake (black), FLG (green), and the junction between FLG and monolayer MoS_2. As shown in figure 6.1b, the PL of monolayer MoS_2 at the interface with FLG is greatly quenched in comparison to the PL of pure monolayer MoS_2 (by about $\simeq 3$ times). This quenching of PL is due to the interlayer charge transfer from MoS_2 to graphene[294].

6.2.2.3 Photoresponse of graphene-MoS_2 heterostructure

Figure 6.2 illustrates the photoresponse characteristics of both pristine MoS_2 and graphene-MoS_2 junctions, varying with the wavelength of light emitting diodes (LEDs) (Figure 6.2a and b) and gate voltage (Figure 6.2b and c). As shown in Figure 6.2 a, with a 535 nm wavelength LED and on time $\tau = 200$ secs, the rise time of the junction is faster than that of pristine MoS_2, but no distinct pattern for the fall time is observed. Alternatively, under illumination with a 385-nm wavelength LED and $\tau = 200$ s, the junction exhibits a faster fall time in comparison to pristine monolayer MoS_2, but no definitive pattern for the rise time is observed.

In the study of gate dependence of photoresponse of the junction, a clear variation in the rise time for $\lambda = 535$ nm and in the fall time for $\lambda = 385$ nm is observed. Furthermore, it is notable that the photocurrent saturates rapidly for all gate voltages at $\lambda = 385$ nm in contrast to the slower saturation observed at $\lambda = 535$ nm.

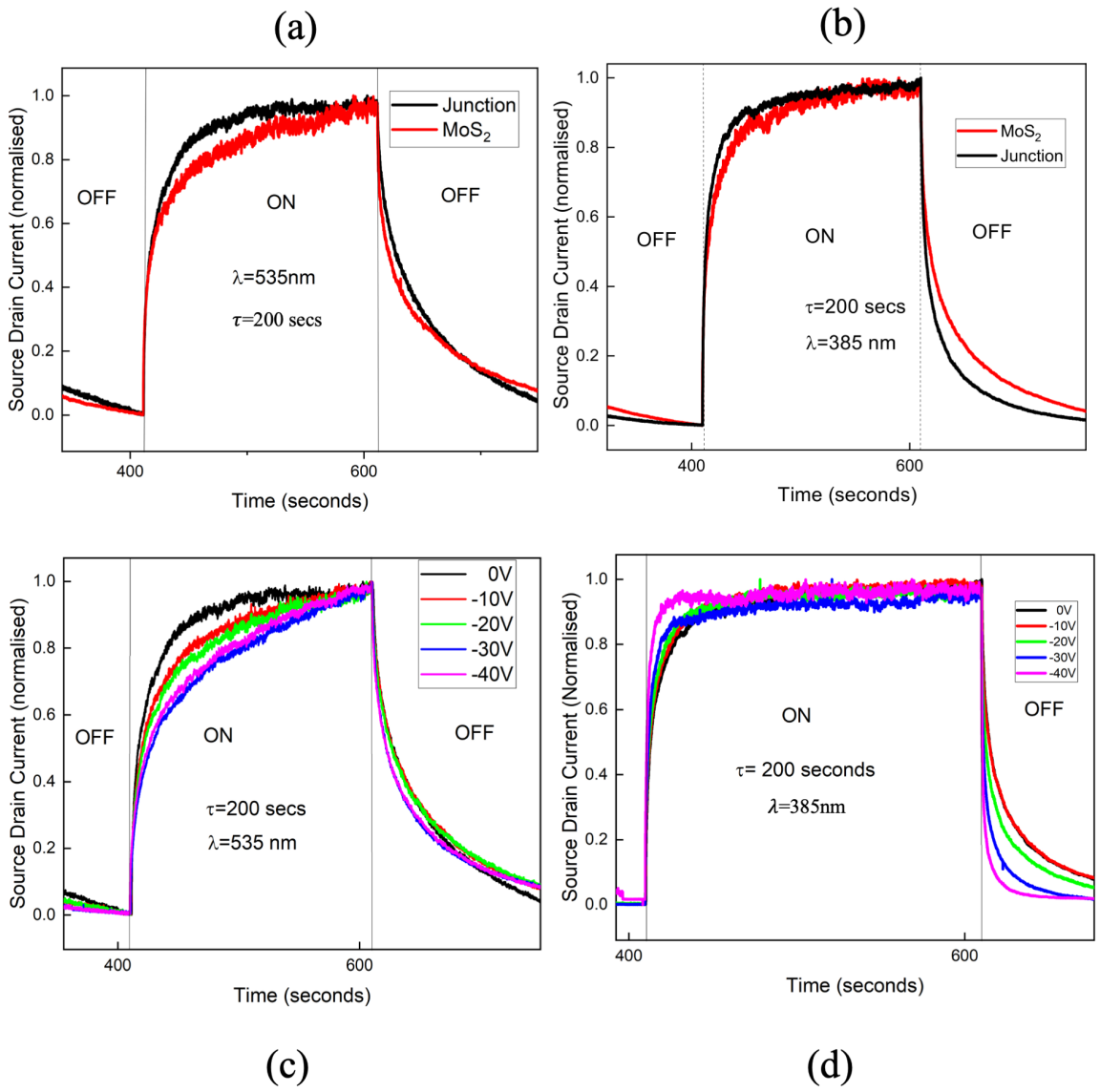

FIGURE 6.2: Photoresponse of pristine MoS_2 (red) and graphene-MoS_2 junction with source-drain voltage V_{ds} = -1V subjected to (a) an LED of λ =535 nm and on-off time, τ =200 secs, (b)an LED of λ =385 nm and on-off time, τ =200 secs. Photoresponse of graphene-MoS_2 junction as a function of gate voltage V_g= 0 to -40 V and V_{ds} = -1V with (c) an LED of λ =535 nm and on-off time, τ =200 secs, (d) an LED of λ =385 nm and on-off time, τ =200 secs.

The observed photoresponse in the graphene-MoS_2 system is likely attributed to the different contributions from deep and shallow-level trap states. Nonetheless, further investigation is necessary to elucidate the precise mechanism, and this work is currently in progress.

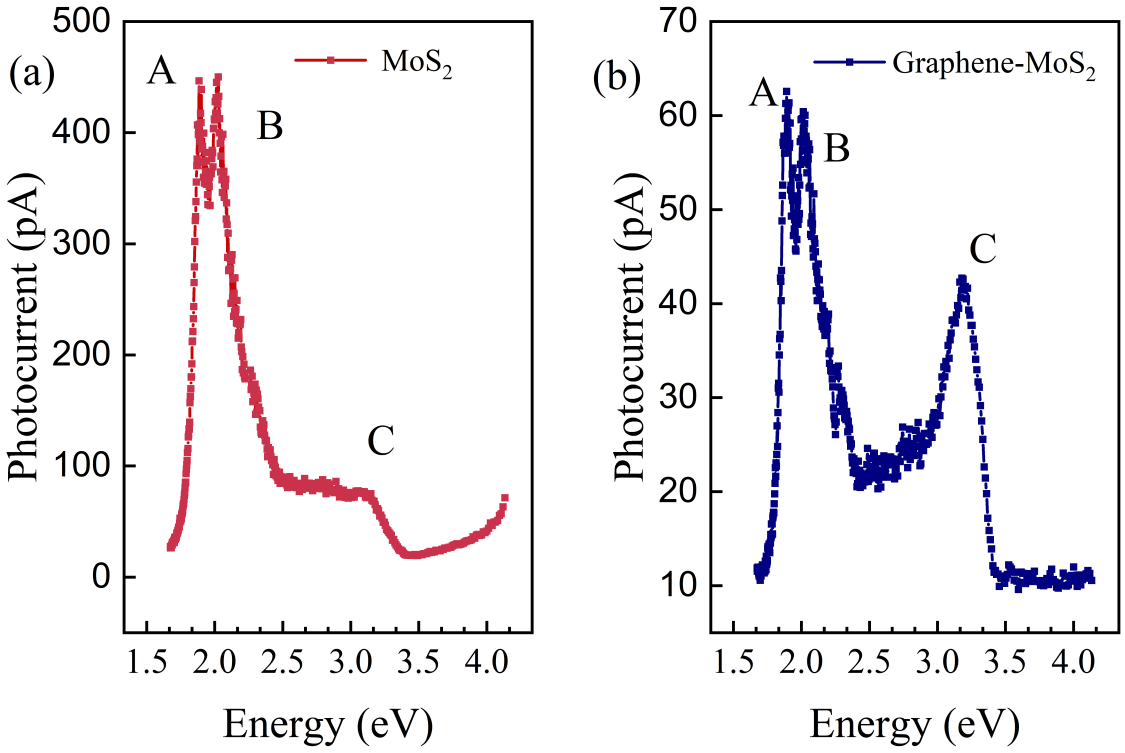

FIGURE 6.3: Photocurrent spectra taken with a laser excitation wavelength of 532 nm and $V_{ds} = -1$V, showing A, B and C exciton in (a) pristine monolayer MoS_2 and (b) Graphene-MoS_2 junction.

6.2.2.4 Photocurrent spectroscopy

The photocurrent spectroscopy of pristine MoS_2 and the junction was done using a laser of wavelength 532 nm and source-drain bias of -1 V. The photocurrent spectra show three dominant peaks at 1.85 eV, 2.0 eV, and 3.1 eV, corresponding to the A, B, and C exciton, respectively. At the Schottky junction, the photocurrent is produced due to the built-in potential which facilitates the separation of photo-generated charge carriers. As a result, electron-hole pairs formed at the corresponding optical transition energies contribute to the net photocurrent. In contrast, in the PL process, light is primarily emitted from the MoS_2 flake distant from the Schottky junction, leading to higher energy electron-hole pairs relaxing to the band edge prior to light emission.

From figures 6.3a and b it can be seen that, the relative intensity of A and B exciton peaks in both the cases are similar. However, at the graphene-MoS_2 junction, the C-exciton peak has a high relative intensity compared to the C-exciton peak in the pristine monolayer MoS_2. Within a single-electron band structure framework, the C-exciton pertains to the area of the Brillouin zone characterized by nested valence and conduction bands. The oscillator

strength of the C-exciton peak is associated with the spontaneous dissociation of electron-hole pairs in the k-space resulting from band nesting. Consequently, we think that graphene significantly influences the band nesting in the MoS_2 monolayer. Nevertheless, thorough research on carrier relaxation processes [295] is necessary to elucidate the precise mechanism underlying this phenomenon.

6.2.3 Conclusion

The significant interactions between light and matter in semiconducting two-dimensional transition metal dichalcogenides (TMDs) make them particularly appealing for cutting-edge optoelectronic applications. Notably, vertically stacked van der Waals (vdW) heterostructures of graphene and MoS_2 are highly promising for next-generation optoelectronic devices with high performance, including broadband, high-responsivity, and high-speed photodetectors. Such heterostructures offer efficient charge transfer while minimizing recombination losses, resulting in devices with superior performance compared to those made from traditional materials. Beyond photodetection, the integration of TMD/graphene heterostructures into photonic and quantum technologies might open up entirely new possibilities. For example, by incorporating TMDs with graphene in cavity quantum electrodynamics systems, one can enhance exciton-photon interactions, paving the way for tunable quantum emitters, polaritonic devices, and room-temperature single-photon sources. These advancements are critical for applications in quantum computing, communication, and cryptography. In chiral optics, the circular dichroism and spin-valley coupling selective to valleys in TMDs can be exploited to develop chiral photonic devices, enabling unidirectional light propagation and selective interaction with light of specific handedness, thus making them ideal for optical isolators and sensors. In the emerging field of opto-valleytronics, TMD/graphene heterostructures, which exhibit remarkable valley coherence and polarization (up to 60% and 50%, respectively), could be employed to encode, process, and transmit information using the valley degree of freedom. This could result in valleytronic devices that offer ultra-low energy dissipation and high-speed data processing, essential for future information technologies. Furthermore, these structures might facilitate the development of novel valleytronic memory and logic devices, taking advantage of the extended valley coherence times possible within these systems. The unique excitonic properties of TMDs, coupled with graphene's high carrier mobility, also indicate their potential in energy-harvesting applications, like efficient solar cells and photothermal devices. Moreover, combining TMD/graphene structures with flexible or transparent substrates could lead to lightweight, flexible, and wearable optoelectronic devices, vital for applications in augmented reality (AR) displays, health monitoring, and environmental sensing. Lastly, hybrid structures consisting of TMDs and graphene

might enable the creation of ultra-thin optical meta-devices with tunable photonic properties for imaging, spectroscopy, and holography. By accurately controlling heterostructure layer thickness and twist angle, highly adaptable optical responses across a broad spectral range can be engineered, opening pathways for compact, on-chip photonic systems for light manipulation, sensing, and telecommunications[295].

Bibliography

[1]N. O. Weiss, H. Zhou, L. Liao, Y. Liu, S. Jiang, Y. Huang, and X. Duan, "Graphene: an emerging electronic material", Advanced Materials **24**, 5782–5825 (2012).

[2]F. Schwierz, "Graphene transistors", Nature Nanotechnology **5**, 487–496 (2010).

[3]K. S. Novoselov, L. Colombo, P. Gellert, M. Schwab, K. Kim, et al., "A roadmap for graphene", Nature **490**, 192–200 (2012).

[4]Y. Liu, N. O. Weiss, X. Duan, H.-C. Cheng, Y. Huang, and X. Duan, "Van der waals heterostructures and devices", Nature Reviews Materials **1**, 1–17 (2016).

[5]Q. H. Wang, K. Kalantar-Zadeh, A. Kis, J. N. Coleman, and M. S. Strano, "Electronics and optoelectronics of two-dimensional transition metal dichalcogenides", Nature Nanotechnology **7**, 699–712 (2012).

[6]A. K. Geim and I. V. Grigorieva, "Van der waals heterostructures", Nature **499**, 419–425 (2013).

[7]Y. Liu, R. Cheng, L. Liao, H. Zhou, J. Bai, G. Liu, L. Liu, Y. Huang, and X. Duan, "Plasmon resonance enhanced multicolour photodetection by graphene", Nature Communications **2**, 579 (2011).

[8]G. Konstantatos, M. Badioli, L. Gaudreau, J. Osmond, M. Bernechea, F. P. G. De Arquer, F. Gatti, and F. H. Koppens, "Hybrid graphene–quantum dot phototransistors with ultrahigh gain", Nature Nanotechnology **7**, 363–368 (2012).

[9]L. Liao, J. Bai, Y. Qu, Y.-c. Lin, Y. Li, Y. Huang, and X. Duan, "High-κ oxide nanoribbons as gate dielectrics for high mobility top-gated graphene transistors", Proceedings of the National Academy of Sciences **107**, 6711–6715 (2010).

[10]L. Liao, Y.-C. Lin, M. Bao, R. Cheng, J. Bai, Y. Liu, Y. Qu, K. L. Wang, Y. Huang, and X. Duan, "High-speed graphene transistors with a self-aligned nanowire gate", Nature **467**, 305–308 (2010).

[11]C. R. Dean, A. F. Young, I. Meric, C. Lee, L. Wang, S. Sorgenfrei, K. Watanabe, T. Taniguchi, P. Kim, K. L. Shepard, et al., "Boron nitride substrates for high-quality graphene electronics", Nature Nanotechnology **5**, 722–726 (2010).

[12]Y. Liu, J. Wang, S. Kim, H. Sun, F. Yang, Z. Fang, N. Tamura, R. Zhang, X. Song, J. Wen, B. Z. Xu, M. Wang, S. Lin, Q. Yu, K. B. Tom, Y. Deng, J. Turner, E. Chan, D. Jin, R. O. Ritchie, A. M. Minor, D. C. Chrzan, M. C. Scott, and J. Yao, "Helical van der waals crystals with discretized eshelby twist", Nature **570**, 358–362 (2019).

[13]P. Sutter, S. Wimer, and E. Sutter, "Chiral twisted van der waals nanowires", Nature **570**, 354–357 (2019).

[14]E. Sutter, H.-P. Komsa, A. A. Puretzky, R. R. Unocic, and P. Sutter, "Stacking fault induced symmetry breaking in van der waals nanowires", ACS Nano **16**, 21199–21207 (2022).

[15]T. Chowdhury, C. Taneja, A. Vasdev, P. Ghosh, G. Sheet, G. P. Kumar, and A. Rahman, "Stacking engineered room temperature ferroelectricity in twisted germanium sulfide nanowires", Advanced Electronic Materials **8**, 2101158 (2022).

[16]A. K. Geim and K. S. Novoselov, "The rise of graphene", Nature Materials **6**, 183–191 (2007).

[17]C. Lee, X. Wei, J. W. Kysar, and J. Hone, "Measurement of the elastic properties and intrinsic strength of monolayer graphene", Science **321**, 385–388 (2008).

[18]A. H. Castro Neto, F. Guinea, N. M. R. Peres, K. S. Novoselov, and A. K. Geim, "The electronic properties of graphene", Rev. Mod. Phys. **81**, 109–162 (2009).

[19]K. F. Mak, C. Lee, J. Hone, J. Shan, and T. F. Heinz, "Atomically thin MoS_2: a new direct-gap semiconductor", Phys. Rev. Lett. **105**, 136805 (2010).

[20]B. Radisavljevic, A. Radenovic, J. Brivio, V. Giacometti, and A. Kis, "Single-layer MoS_2 transistors.", Nature Nanotechnology **6**, 147–50 (2011).

[21]F. Withers, O. Del Pozo-Zamudio, A. Mishchenko, A. P. Rooney, A. Gholinia, K Watanabe, T. Taniguchi, S. J. Haigh, A. Geim, A. Tartakovskii, et al., "Light-emitting diodes by band-structure engineering in van der waals heterostructures", Nature Materials **14**, 301–306 (2015).

[22]L. Britnell, R. V. Gorbachev, R. Jalil, B. D. Belle, F. Schedin, M. I. Katsnelson, L. Eaves, S. V. Morozov, A. S. Mayorov, N. M. Peres, et al., "Electron tunneling through ultrathin boron nitride crystalline barriers", Nano Letters **12**, 1707–1710 (2012).

[23]A. S. Mayorov, R. V. Gorbachev, S. V. Morozov, L. Britnell, R. Jalil, L. A. Ponomarenko, P. Blake, K. S. Novoselov, K. Watanabe, T. Taniguchi, et al., "Micrometer-scale ballistic transport in encapsulated graphene at room temperature", Nano Letters **11**, 2396–2399 (2011).

[24]P. Sutter and E. Sutter, "Unconventional van der waals heterostructures beyond stacking", iScience **24** (2021).

[25]T. Mueller and E. Malic, "Exciton physics and device application of two-dimensional transition metal dichalcogenide semiconductors", npj 2D Materials and Applications **2**, 29 (2018).

[26]G. Wang, A. Chernikov, M. M. Glazov, T. F. Heinz, X. Marie, T. Amand, and B. Urbaszek, "Colloquium: excitons in atomically thin transition metal dichalcogenides", Rev. Mod. Phys. **90**, 021001 (2018).

[27]D. Y. Qiu, T. Cao, and S. G. Louie, "Nonanalyticity, valley quantum phases, and lightlike exciton dispersion in monolayer transition metal dichalcogenides: theory and first-principles calculations", Phys. Rev. Lett. **115**, 176801 (2015).

[28]C. Pöllmann, P. Steinleitner, U. Leierseder, P. Nagler, G. Plechinger, M. Porer, R Bratschitsch, C. Schüller, T. Korn, and R. Huber, "Resonant internal quantum transitions and femtosecond radiative decay of excitons in monolayer WSe_2", Nature Materials **14**, 889–893 (2015).

[29]A. Chernikov, T. C. Berkelbach, H. M. Hill, A. Rigosi, Y. Li, B. Aslan, D. R. Reichman, M. S. Hybertsen, and T. F. Heinz, "Exciton binding energy and nonhydrogenic rydberg series in monolayer WS_2", Phys. Rev. Lett. **113**, 076802 (2014).

[30]G. Wang, X. Marie, I Gerber, T. Amand, D. Lagarde, L. Bouet, M Vidal, A. Balocchi, and B. Urbaszek, "Giant enhancement of the optical second-harmonic emission of WSe_2 monolayers by laser excitation at exciton resonances", Phys. Rev. Lett. **114**, 097403 (2015).

[31]E. Malic, M. Selig, M. Feierabend, S. Brem, D. Christiansen, F. Wendler, A. Knorr, and G. Berghäuser, "Dark excitons in transition metal dichalcogenides", Phys. Rev. Mater. **2**, 014002 (2018).

[32]M. M. Ugeda, A. J. Bradley, S. F. Shi, F. H. D. Jornada, Y. Zhang, D. Y. Qiu, W. Ruan, S. K. Mo, Z. Hussain, Z. X. Shen, F. Wang, S. G. Louie, and M. F. Crommie, "Giant bandgap renormalization and excitonic effects in a monolayer transition metal dichalcogenide semiconductor", Nature Materials **13**, 1091–1095 (2014).

[33]K. He, N. Kumar, L. Zhao, Z. Wang, K. F. Mak, H. Zhao, and J. Shan, "Tightly bound excitons in monolayer WSe_2", Phys. Rev. Lett. **113**, 026803 (2014).

[34]A. Raja, A. Chaves, J. Yu, G. Arefe, H. M. Hill, A. F. Rigosi, T. C. Berkelbach, P. Nagler, C. Schüller, T. Korn, et al., "Coulomb engineering of the bandgap and excitons in two-dimensional materials", Nature Communications **8**, 15251 (2017).

[35]A. V. Stier, N. P. Wilson, G. Clark, X. Xu, and S. A. Crooker, "Probing the influence of dielectric environment on excitons in monolayer WSe_2: insight from high magnetic fields", Nano Letters **16**, 7054–7060 (2016).

[36]T. Chowdhury, S. Chatterjee, D. Das, I. Timokhin, P. D. Núñez, G. M. A., S. Chatterjee, K. Majumdar, P. Ghosh, A. Mishchenko, and A. Rahman, "Brightening of dark excitons in WS_2 via tensile strain-induced excitonic valley convergence", Phys. Rev. B **110**, L081405 (2024).

[37]M. Feierabend, Z. Khatibi, G. Berghäuser, and E. Malic, "Dark exciton based strain sensing in tungsten-based transition metal dichalcogenides", Phys. Rev. B **99**, 195454 (2019).

[38]M. Feierabend, G. Berghäuser, A. Knorr, and E. Malic, "Proposal for dark exciton based chemical sensors", Nature Communications **8**, 14776 (2017).

[39]M. R. Molas, C. Faugeras, A. O. Slobodeniuk, K. Nogajewski, M. Bartos, D. Basko, and M. Potemski, "Brightening of dark excitons in monolayers of semiconducting transition metal dichalcogenides", 2D Materials **4**, 021003 (2017).

[40]X.-X. Zhang, T. Cao, Z. Lu, Y.-C. Lin, F. Zhang, Y. Wang, Z. Li, J. C. Hone, J. A. Robinson, D. Smirnov, et al., "Magnetic brightening and control of dark excitons in monolayer WSe_2", Nature Nanotechnology **12**, 883–888 (2017).

[41]A. Kormányos, G. Burkard, M. Gmitra, J. Fabian, V. Zólyomi, N. D. Drummond, and V. Falko, "k.p theory for two-dimensional transition metal dichalcogenide semiconductors", 2D Materials **2**, 022001 (2015).

[42]X.-X. Zhang, Y. You, S. Y. F. Zhao, and T. F. Heinz, "Experimental evidence for dark excitons in monolayer WSe_2", Phys. Rev. Lett. **115**, 257403 (2015).

[43]Y. Zhou, G. Scuri, D. S. Wild, A. A. High, A. Dibos, L. A. Jauregui, C. Shu, K. De Greve, K. Pistunova, A. Y. Joe, et al., "Probing dark excitons in atomically thin semiconductors via near-field coupling to surface plasmon polaritons", Nature Nanotechnology **12**, 856–860 (2017).

[44]M. Selig, G. Berghäuser, A. Raja, P. Nagler, C. Schüller, T. F. Heinz, T. Korn, A. Chernikov, E. Malic, and A. Knorr, "Excitonic linewidth and coherence lifetime in monolayer transition metal dichalcogenides", Nat. Commun. **7**, 13279 (2016).

[45]M. Selig, G. Berghäuser, M. Richter, R. Bratschitsch, A. Knorr, and E. Malic, "Dark and bright exciton formation, thermalization, and photoluminescence in monolayer transition metal dichalcogenides", 2D Mater. **5**, 035017 (2018).

[46]I. Niehues, R. Schmidt, M. Drëppel, P. Marauhn, D. Christiansen, M. Selig, G. Berghäuser, D. Wigger, R. Schneider, L. Braasch, R. Koch, A. Castellanos-Gomez, T. Kuhn, A. Knorr, E. Malic, M. Rohlfing, S. Michaelis de Vasconcellos, and R. Bratschitsch, "Strain control of exciton–phonon coupling in atomically thin semiconductors", Nano Lett. **18**, 1751–1757 (2018).

[47]F. Cadiz, E. Courtade, C. Robert, G. Wang, Y. Shen, H. Cai, T. Taniguchi, K. Watanabe, H. Carrere, D. Lagarde, M. Manca, T. Amand, P. Renucci, S. Tongay, X. Marie, and B. Urbaszek, "Excitonic linewidth approaching the homogeneous limit in MoS_2-based van der waals heterostructures", Phys. Rev. X **7**, 021026 (2017).

[48]P. Tonndorf, R. Schmidt, R. Schneider, J. Kern, M. Buscema, G. A. Steele, A. Castellanos-Gomez, H. S. van der Zant, S. M. de Vasconcellos, and R. Bratschitsch, "Single-photon emission from localized excitons in an atomically thin semiconductor", Optica **2**, 347–352 (2015).

[49]M. Koperski, K Nogajewski, A. Arora, V Cherkez, P. Mallet, J.-Y. Veuillen, J Marcus, P. Kossacki, and M Potemski, "Single photon emitters in exfoliated WSe_2 structures", Nature Nanotechnology **10**, 503–506 (2015).

[50]H. J. Conley, B. Wang, J. I. Ziegler, R. F. Haglund Jr, S. T. Pantelides, and K. I. Bolotin, "Bandgap engineering of strained monolayer and bilayer MoS_2", Nano Letters **13**, 3626–3630 (2013).

[51]D. Yoon, Y.-W. Son, and H. Cheong, "Strain-dependent splitting of the double-resonance raman scattering band in graphene", Phys. Rev. Lett. **106**, 155502 (2011).

[52]O. Frank, M. Mohr, J. Maultzsch, C. Thomsen, I. Riaz, R. Jalil, K. S. Novoselov, G. Tsoukleri, J. Parthenios, K. Papagelis, et al., "Raman $2D-$band splitting in graphene: theory and experiment", ACS Nano **5**, 2231–2239 (2011).

[53]H. Shi, H. Pan, Y.-W. Zhang, and B. I. Yakobson, "Quasiparticle band structures and optical properties of strained monolayer MoS_2 and WS_2", Phys. Rev. B **87**, 155304 (2013).

[54]H. Shi, R. Yan, S. Bertolazzi, J. Brivio, B. Gao, A. Kis, D. Jena, H. G. Xing, and L. Huang, "Exciton dynamics in suspended monolayer and few-layer MoS_2 2D crystals", ACS Nano **7**, 1072–1080 (2013).

[55]Z. Peng, X. Chen, Y. Fan, D. J. Srolovitz, and D. Lei, "Strain engineering of $2D$ semiconductors and graphene: from strain fields to band-structure tuning and photonic applications", Light: Science & Applications **9**, 190 (2020).

[56]R. Roldán, A. Castellanos-Gomez, E. Cappelluti, and F. Guinea, "Strain engineering in semiconducting two-dimensional crystals", Journal of Physics: Condensed Matter **27**, 313201 (2015).

[57]E. Scalise, M. Houssa, G. Pourtois, V. Afanasév, and A. Stesmans, "Strain-induced semiconductor to metal transition in the two-dimensional honeycomb structure of MoS_2", Nano Research **5**, 43–48 (2012).

[58]J. Feng, X. Qian, C.-W. Huang, and J. Li, "Strain-engineered artificial atom as a broad-spectrum solar energy funnel", Nature Photonics **6**, 866–872 (2012).

[59]M. Ghorbani-Asl, S. Borini, A. Kuc, and T. Heine, "Strain-dependent modulation of conductivity in single-layer transition-metal dichalcogenides", Phys. Rev. B **87**, 235434 (2013).

[60]B. Chakraborty, A. Bera, D. V. S. Muthu, S. Bhowmick, U. V. Waghmare, and A. K. Sood, "Symmetry-dependent phonon renormalization in monolayer MoS_2 transistor", Phys. Rev. B **85**, 161403 (2012).

[61]B. Chakraborty, H. R. Matte, A. Sood, and C. Rao, "Layer-dependent resonant raman scattering of a few layer MoS_2", Journal of Raman Spectroscopy **44**, 92–96 (2013).

[62]K. He, C. Poole, K. F. Mak, and J. Shan, "Experimental demonstration of continuous electronic structure tuning via strain in atomically thin MoS_2", Nano Letters **13**, 2931–2936 (2013).

[63]R. Schmidt, I. Niehues, R. Schneider, M. Drueppel, T. Deilmann, M. Rohlfing, S. M. De Vasconcellos, A. Castellanos-Gomez, and R. Bratschitsch, "Reversible uniaxial strain tuning in atomically thin WSe_2", 2D Materials **3**, 021011 (2016).

[64]C. R. Zhu, G. Wang, B. L. Liu, X. Marie, X. F. Qiao, X. Zhang, X. X. Wu, H. Fan, P. H. Tan, T. Amand, and B. Urbaszek, "Strain tuning of optical emission energy and polarization in monolayer and bilayer MoS_2", Phys. Rev. B **88**, 121301 (2013).

[65]A. Raja, A. Chaves, J. Yu, G. Arefe, H. M. Hill, A. F. Rigosi, T. C. Berkelbach, P. Nagler, C. SchÃijller, T. Korn, C. Nuckolls, J. Hone, L. E. Brus, T. F. Heinz, D. R. Reichman, and A. Chernikov, "Coulomb engineering of the bandgap and excitons in two-dimensional materials", Nature Communications **8**, 1–7 (2017).

[66]A Chaves, J. G. Azadani, H. Alsalman, D. Da Costa, R Frisenda, A. Chaves, S. H. Song, Y. D. Kim, D. He, J. Zhou, et al., "Bandgap engineering of two-dimensional semiconductor materials", npj 2D Materials and Applications **4**, 29 (2020).

[67]S. Borghardt, J.-S. Tu, F. Winkler, J. Schubert, W. Zander, K. Leosson, and B. E. Kardynał, "Engineering of optical and electronic band gaps in transition metal dichalcogenide monolayers through external dielectric screening", Phys. Rev. Mat. **1**, 054001 (2017).

[68]L. Keldysh, "Coulomb interaction in thin semiconductor and semimetal films", Sov. J. Exp. Theor. Phys. Lett. **29**, 658 (1979).

[69]N. S. Rytova, "Screened potential of a point charge in a thin film", arXiv:1806.00976 (2018).

[70]A. Weston, E. G. Castanon, V. Enaldiev, F. Ferreira, S. Bhattacharjee, S. Xu, H. Corte-León, Z. Wu, N. Clark, A. Summerfield, et al., "Interfacial ferroelectricity in marginally twisted 2D semiconductors", Nature Nanotechnology **17**, 390–395 (2022).

[71]T Mikolajick, S Slesazeck, H Mulaosmanovic, M. Park, S Fichtner, P. Lomenzo, M Hoffmann, and U Schroeder, "Next generation ferroelectric materials for semiconductor process integration and their applications", Journal of Applied Physics **129** (2021).

[72]S. Bertolazzi, P. Bondavalli, S. Roche, T. San, S.-Y. Choi, L. Colombo, F. Bonaccorso, and P. Samorì, "Nonvolatile memories based on graphene and related 2D materials", Advanced Materials **31**, 1806663 (2019).

[73]K. Chang, J. Liu, H. Lin, N. Wang, K. Zhao, A. Zhang, F. Jin, Y. Zhong, X. Hu, W. Duan, et al., "Discovery of robust in-plane ferroelectricity in atomic-thick $SnTe$", Science **353**, 274–278 (2016).

[74]A. Belianinov, Q. He, A. Dziaugys, P. Maksymovych, E. Eliseev, A Borisevich, A Morozovska, J. Banys, Y. Vysochanskii, and S. V. Kalinin, "$CuInP_2S_6$ room temperature layered ferroelectric", Nano Letters **15**, 3808–3814 (2015).

[75]Y. Zhou, D. Wu, Y. Zhu, Y. Cho, Q. He, X. Yang, K. Herrera, Z. Chu, Y. Han, M. C. Downer, et al., "Out-of-plane piezoelectricity and ferroelectricity in layered $\alpha - In_2Se_3$ nanoflakes", Nano Letters **17**, 5508–5513 (2017).

[76]C. Zheng, L. Yu, L. Zhu, J. L. Collins, D. Kim, Y. Lou, C. Xu, M. Li, Z. Wei, Y. Zhang, et al., "Room temperature in-plane ferroelectricity in van der waals In_2Se_3", Science Advances **4**, eaar7720 (2018).

[77]A. P. Rooney, A. Kozikov, A. N. Rudenko, E. Prestat, M. J. Hamer, F. Withers, Y. Cao, K. S. Novoselov, M. I. Katsnelson, R. Gorbachev, et al., "Observing imperfection in atomic interfaces for van der waals heterostructures", Nano Letters **17**, 5222–5228 (2017).

[78]A. Weston, Y. Zou, V. Enaldiev, A. Summerfield, N. Clark, V. Zólyomi, A. Graham, C. Yelgel, S. Magorrian, M. Zhou, et al., "Atomic reconstruction in twisted bilayers of transition metal dichalcogenides", Nature Nanotechnology **15**, 592–597 (2020).

[79]M. R. Rosenberger, H.-J. Chuang, M. Phillips, V. P. Oleshko, K. M. McCreary, S. V. Sivaram, C. S. Hellberg, and B. T. Jonker, "Twist angle-dependent atomic reconstruction and moiré patterns in transition metal dichalcogenide heterostructures", ACS Nano **14**, 4550–4558 (2020).

[80]C. Woods, P Ares, H Nevison-Andrews, M. Holwill, R Fabregas, F. Guinea, A. Geim, K. Novoselov, N. Walet, and L Fumagalli, "Charge-polarized interfacial superlattices in marginally twisted hexagonal boron nitride", Nature Communications **12**, 347 (2021).

[81]L. C. Gomes and A Carvalho, "Phosphorene analogues: isoelectronic two-dimensional group-IV monochalcogenides with orthorhombic structure", Physical Review B **92**, 85406 (2015).

[82]S. Barraza-Lopez, T. P. Kaloni, S. P. Poudel, and P. Kumar, "Tuning the ferroelectric-to-paraelectric transition temperature and dipole orientation of group-IV monochalcogenide monolayers", Phys. Rev. B **97**, 024110 (2018).

[83]H. Wang and X. Qian, "Two-dimensional multiferroics in monolayer $\mathrm{group}-\mathrm{IV}$ monochalcogenides", 2D Materials **4**, 015042 (2017).

[84]P. Sutter, S. Wimer, and E. Sutter, "Chiral twisted van der waals nanowires", Nature **570**, 354–357 (2019).

[85]P. A. Murgatroyd, M. J. Smiles, C. N. Savory, T. P. Shalvey, J. E. Swallow, N. Fleck, C. M. Robertson, F. Jäckel, J. Alaria, J. D. Major, et al., "GeSe : optical spectroscopy and theoretical study of a van der waals solar absorber", Chemistry of Materials **32**, 3245–3253 (2020).

[86]L. Tang, J. Tan, H. Nong, B. Liu, and H.-M. Cheng, "Chemical vapor deposition growth of two-dimensional compound materials: controllability, material quality, and growth mechanism", Accounts of Materials Research **2**, 36–47 (2021).

[87]X. Liu, J. Liu, L. Y. Antipina, J. Hu, C. Yue, A. M. Sanchez, P. B. Sorokin, Z. Mao, and J. Wei, "Direct fabrication of functional ultrathin single-crystal nanowires from quasi-one-dimensional van der waals crystals", Nano Letters **16**, 6188–6195 (2016).

[88]G. Liu, S. Rumyantsev, M. A. Bloodgood, T. T. Salguero, M. Shur, and A. A. Balandin, "Low-frequency electronic noise in $\mathrm{quasi}-\mathrm{1D}\ \mathrm{TaSe_3}$ van der waals nanowires", Nano Letters **17**, 377–383 (2017).

[89]R. S. Wagner and W. Ellis, "Vapor-liquid-solid mechanism of single crystal growth", Applied Physics Letters **4**, 89–90 (1964).

[90]E. Sutter and P. Sutter, "Phase diagram of nanoscale alloy particles used for vapor- liquid-solid growth of semiconductor nanowires", Nano Letters **8**, 411–414 (2008).

[91]S. A. Dayeh and S. Picraux, "Direct observation of nanoscale size effects in Ge semiconductor nanowire growth", Nano Letters **10**, 4032–4039 (2010).

[92]E. Sutter and P. Sutter, "$\mathrm{1D}$ wires of $\mathrm{2D}$ layered materials: germanium sulfide nanowires as efficient light emitters", ACS Applied Nano Materials **1**, 1042–1049 (2017).

[93]C.-J. Kim, A Sánchez-Castillo, Z. Ziegler, Y. Ogawa, C. Noguez, and J. Park, "Chiral atomically thin films", Nature Nanotechnology **11**, 520–524 (2016).

[94]J. C. Song and N. M. Gabor, "Electron quantum metamaterials in van der waals heterostructures", Nature Nanotechnology **13**, 986–993 (2018).

[95] Y. Cao, V. Fatemi, A. Demir, S. Fang, S. L. Tomarken, J. Y. Luo, J. D. Sanchez-Yamagishi, K. Watanabe, T. Taniguchi, E. Kaxiras, et al., "Correlated insulator behaviour at half-filling in magic-angle graphene superlattices", Nature **556**, 80–84 (2018).

[96] Y. Cao, V. Fatemi, S. Fang, K. Watanabe, T. Taniguchi, E. Kaxiras, and P. Jarillo-Herrero, "Unconventional superconductivity in magic-angle graphene superlattices", Nature **556**, 43–50 (2018).

[97] K. Liu, L. Zhang, T. Cao, C. Jin, D. Qiu, Q. Zhou, A. Zettl, P. Yang, S. G. Louie, and F. Wang, "Evolution of interlayer coupling in twisted molybdenum disulfide bilayers", Nature Communications **5**, 4966 (2014).

[98] I. V. Grigorieva, A. A. Firsov, K. S. Novoselov, A. K. Geim, S. V. Morozov, D. Jiang, Y. Zhang, and S. V. Dubonos, "Electric field effect in atomically thin carbon films", Science **306**, 666–669 (2016).

[99] K. S. Novoselov, D. Jiang, F Schedin, T. Booth, V. Khotkevich, S. Morozov, and A. K. Geim, "Two-dimensional atomic crystals", Proc. Natl. Acad. Sci. U.S.A. **102**, 10451–10453 (2005).

[100] R. Frisenda, E. Navarro-Moratalla, P. Gant, D. Pérez De Lara, P. Jarillo-Herrero, R. V. Gorbachev, and A. Castellanos-Gomez, "Recent progress in the assembly of nanodevices and van der waals heterostructures by deterministic placement of 2D materials", Chem. Soc. Rev. **47**, 53–68 (2018).

[101] Q. Zhao, T. Wang, Y. K. Ryu, R. Frisenda, and A. Castellanos-Gomez, "An inexpensive system for the deterministic transfer of 2D materials", Journal of Physics: Materials **3**, 016001 (2020).

[102] M. Yankowitz, Q. Ma, P. Jarillo-Herrero, and B. J. LeRoy, "Van der waals heterostructures combining graphene and hexagonal boron nitride", Nature Reviews Physics **1**, 112–125 (2019).

[103] A. Castellanos-Gomez, M. Buscema, R. Molenaar, V. Singh, L. Janssen, H. S. Van Der Zant, and G. A. Steele, "Deterministic transfer of two-dimensional materials by all-dry viscoelastic stamping", 2D Materials **1**, 011002 (2014).

[104] T. Chowdhury, D. Paul, D. Nechiyil, G. M. A, K. Watanabe, T. Taniguchi, G. V. P. Kumar, and A. Rahman, "Modulation of trion and exciton formation in monolayer WS_2 by dielectric and substrate engineering", 2D Mater. **8**, 045032 (2021).

[105] K. L. Haley, J. A. Cloninger, K. Cerminara, R. M. Sterbentz, T. Taniguchi, K. Watanabe, and J. O. Island, "Heated assembly and transfer of van der waals heterostructures with common nail polish", Nanomanufacturing **1**, 49–56 (2021).

[106]L. Wang, I Meric, P. Huang, Q Gao, Y Gao, H Tran, T Taniguchi, K. Watanabe, L. Campos, D. Muller, et al., "One-dimensional electrical contact to a two-dimensional material", Science **342**, 614–617 (2013).

[107]F. Pizzocchero, L. Gammelgaard, B. S. Jessen, J. M. Caridad, L. Wang, J. Hone, P. Bøggild, and T. J. Booth, "The hot pick-up technique for batch assembly of van der waals heterostructures", Nature Communications **7**, 11894 (2016).

[108]I. Rebollo, F. Rodrigues-Machado, W Wright, G. Melin, and A. Champagne, "Thin-suspended 2D materials: facile, versatile, and deterministic transfer assembly", 2D Materials **8**, 035028 (2021).

[109]K. F. Mak and J. Shan, "Photonics and optoelectronics of 2D semiconductor transition metal dichalcogenides", Nature Photonics **10**, 216–226 (2016).

[110]J. S. Ross, S. Wu, H. Yu, N. J. Ghimire, A. M. Jones, G. Aivazian, J. Yan, D. G. Mandrus, D. Xiao, W. Yao, and X. Xu, "Electrical control of neutral and charged excitons in a monolayer semiconductor", Nat. Commun. **4**, 1474 (2013).

[111]A. Splendiani, L. Sun, Y. Zhang, T. Li, J. Kim, C.-Y. Chim, G. Galli, and F. Wang, "Emerging photoluminescence in monolayer MoS_2", Nano Lett. **10**, 1271–1275 (2010).

[112]A. Ramasubramaniam, "Large excitonic effects in monolayers of molybdenum and tungsten dichalcogenides", Phys. Rev. B **86**, 115409 (2012).

[113]H.-P. Komsa and A. V. Krasheninnikov, "Effects of confinement and environment on the electronic structure and exciton binding energy of MoS_2 from first principles", Phys. Rev. B **86**, 241201 (2012).

[114]S. Brem, A. Ekman, D. Christiansen, F. Katsch, M. Selig, C. Robert, X. Marie, B. Urbaszek, A. Knorr, and E. Malic, "Phonon-assisted photoluminescence from indirect excitons in monolayers of transition-metal dichalcogenides", Nano Lett. **20**, 2849–2856 (2020).

[115]J. Madéo, M. K. L. Man, C. Sahoo, M. Campbell, V. Pareek, E. L. Wong, A. Al-Mahboob, N. S. Chan, A. Karmakar, B. M. K. Mariserla, X. Li, T. F. Heinz, T. Cao, and K. M. Dani, "Directly visualizing the momentum-forbidden dark excitons and their dynamics in atomically thin semiconductors", Science **370**, 1199–1204 (2020).

[116]S. B. Chand, J. M. Woods, E. Mejia, T. Taniguchi, K. Watanabe, and G. Grosso, "Visualization of dark excitons in semiconductor monolayers for high-sensitivity strain sensing", Nano Lett. **22**, 3087–3094 (2022).

[117]K. Zollner, P. E. F. Junior, and J. Fabian, "Strain-tunable orbital, spin-orbit, and optical properties of monolayer transition-metal dichalcogenides", Phys. Rev. B **100**, 195126 (2019).

[118]R. Rosati, R. Schmidt, S. Brem, R. Perea-Causín, I. Niehues, J. Kern, J. A. Preuß, R. Schneider, S. Michaelis de Vasconcellos, R. Bratschitsch, and E. Malic, "Dark exciton anti-funneling in atomically thin semiconductors", Nature Communications **12**, 7221 (2021).

[119]R. J. Gelly, D. Renaud, X. Liao, B. Pingault, S. Bogdanovic, G. Scuri, K. Watanabe, T. Taniguchi, B. Urbaszek, H. Park, and M. Lončar, "Probing dark exciton navigation through a local strain landscape in a WSe_2 monolayer", Nature Communications **13**, 232 (2022).

[120]S. Chand, "Exciton dynamics, interaction, and transport in monolayers of transition metal dichalcogenides", Ph.D. Thesis, City University of New York (CUNY Academic Works) (2024).

[121]A. Rahman, A. Ashraf, H. Xin, X. Tong, P. Sutter, M. D. Eisaman, and C. T. Black, "Sub-50-nm self-assembled nanotextures for enhanced broadband antireflection in silicon solar cells", Nat. Commun. **6**, 5963 (2015).

[122]A. Gurarslan, Y. Yu, L. Su, Y. Yu, F. Suarez, S. Yao, Y. Zhu, M. Ozturk, Y. Zhang, and L. Cao, "Surface-energy-assisted perfect transfer of centimeter-scale monolayer and few-layer MoS_2 films onto arbitrary substrates", ACS Nano **8**, 11522–11528 (2014).

[123]H. R. Gutiérrez, N. Perea-López, A. L. Elías, A. Berkdemir, B. Wang, R. Lv, F. López-Urías, V. H. Crespi, H. Terrones, and M. Terrones, "Extraordinary room-temperature photoluminescence in triangular WS_2 monolayers", Nano Letters **13**, 3447–3454 (2013).

[124]A. Michail, D. Anestopoulos, N. Delikoukos, S. Grammatikopoulos, S. A. Tsirkas, N. N. Lathiotakis, O. Frank, K. Filintoglou, J. Parthenios, and K. Papagelis, "Tuning the photoluminescence and raman response of single-layer WS_2 crystals using biaxial strain", J. Phys. Chem. C **127**, 3506–3515 (2023).

[125]R. Kesarwani, K. B. Simbulan, T.-D. Huang, Y.-F. Chiang, N.-C. Yeh, Y.-W. Lan, and T.-H. Lu, "Control of trion-to-exciton conversion in monolayer WS_2 by orbital angular momentum of light", Science Advances **8**, eabm0100 (2022).

[126]J. Shang, X. Shen, C. Cong, N. Peimyoo, B. Cao, M. Eginligil, and T. Yu, "Observation of excitonic fine structure in a 2D transition-metal dichalcogenide semiconductor", ACS Nano **9**, 647–655 (2015).

[127]K. Wei, Y. Liu, H. Yang, X. Cheng, and T. Jiang, "Large range modification of exciton species in monolayer WS_2", Appl. Opt. **55**, 6251–6255 (2016).

[128]G. Plechinger, P. Nagler, J. Kraus, N. Paradiso, C. Strunk, C. Schüller, and T. Korn, "Identification of excitons, trions and biexcitons in single-layer WS_2", Phys. Status Solidi (RRL) **9**, 457–461 (2015).

[129]M. Sledzinska, P. Xiao, E. Puig Vilardell, E. Chávez Angel, M. J. Esplandiu, and C. M. Sotomayor Torres, "Exciton tuning and strain imaging in WS_2 supported on PDMS micropillars", Applied Physics Letters **121**, 253101 (2022).

[130]K. M. Mccreary, A. T. Hanbicki, S. Singh, R. K. Kawakami, G. G. Jernigan, M. Ishigami, A. Ng, T. H. Brintlinger, R. M. Stroud, and B. T. Jonker, "The effect of preparation conditions on Raman and photoluminescence of monolayer WS_2", Sci. Rep. **6**, 35154 (2016).

[131]N. Lundt, E. Cherotchenko, O. Iff, X. Fan, Y. Shen, P. Bigenwald, A. V. Kavokin, S. Höfling, and C. Schneider, "The interplay between excitons and trions in a monolayer of $MoSe_2$", Applied Physics Letters **112**, 031107 (2018).

[132]A. A. Mitioglu, P Plochocka, J. N. Jadczak, W Escoffier, G. L. J. A. Rikken, L Kulyuk, and D. K. Maude, "Optical manipulation of the exciton charge state in single-layer tungsten disulfide", Physical Review B **88**, 245403 (2013).

[133]P. Giannozzi et al., "Quantum espresso: a modular and open-source software project for quantum simulations of materials", Journal of Physics: Condensed Matter **21**, 395502 (2009).

[134]P Giannozzi et al., "Advanced capabilities for materials modelling with quantum espresso", Journal of Physics: Condensed Matter **29**, 465901 (2017).

[135]D. R. Hamann, M. Schlüter, and C. Chiang, "Norm-conserving pseudopotentials", Phys. Rev. Lett. **43**, 1494–1497 (1979).

[136]M. van Setten, M. Giantomassi, E. Bousquet, M. Verstraete, D. Hamann, X. Gonze, and G.-M. Rignanese, "The pseudodojo: training and grading a 85 element optimized norm-conserving pseudopotential table", Computer Physics Communications **226**, 39–54 (2018).

[137]Z. Y. Zhu, Y. C. Cheng, and U. Schwingenschlögl, "Giant spin-orbit-induced spin splitting in two-dimensional transition-metal dichalcogenide semiconductors", Phys. Rev. B **84**, 153402 (2011).

[138]A. H. MacDonald and S. H. Vosko, "A relativistic density functional formalism", Journal of Physics C: Solid State Physics **12**, 2977 (1979).

[139]A. K. Rajagopal and J. Callaway, "Inhomogeneous electron gas", Phys. Rev. B **7**, 1912–1919 (1973).

[140]J. P. Perdew, K. Burke, and M. Ernzerhof, "Generalized gradient approximation made simple", Phys. Rev. Lett. **77**, 3865–3868 (1996).

[141]A. Molina-Sánchez and L. Wirtz, "Phonons in single-layer and few-layer MoS_2 and WS_2", Phys. Rev. B **84**, 155413 (2011).

[142]S. Baroni, S. de Gironcoli, A. Dal Corso, and P. Giannozzi, "Phonons and related crystal properties from density-functional perturbation theory", Rev. Mod. Phys. **73**, 515–562 (2001).

[143]Z. Khatibi, M. Feierabend, M. Selig, S. Brem, C. Linderálv, P. Erhart, and E. Malic, "Impact of strain on the excitonic linewidth in transition metal dichalcogenides", 2D Materials **6**, 015015 (2018).

[144]F. Giustino, M. L. Cohen, and S. G. Louie, "Electron-phonon interaction using wannier functions", Phys. Rev. B **76**, 165108 (2007).

[145]S. Poncé, E. Margine, C. Verdi, and F. Giustino, "EPW: electron-phonon coupling, transport and superconducting properties using maximally localized wannier functions", Computer Physics Communications **209**, 116–133 (2016).

[146]C. Poellmann, P. Steinleitner, U. Leierseder, P. Nagler, G. Plechinger, M. Porer, R. Bratschitsch, C. Schüller, T. Korn, and R. Huber, "Resonant internal quantum transitions and femtosecond radiative decay of excitons in monolayer WSe_2", Nature Materials **14**, 889–893 (2015).

[147]I Paradisanos, S Germanis, N. Pelekanos, C Fotakis, E Kymakis, G Kioseoglou, and E Stratakis, "Room temperature observation of biexcitons in exfoliated WS_2 monolayers", Appl. Phys. Lett. **110** (2017).

[148]R. Kaupmees, M. Grossberg, M. Ney, A. Asaithambi, A. Lorke, and J. Krustok, "Tailoring of bound exciton photoluminescence emission in WS_2 monolayers", Physica Status Solidi (RRL) - Rapid Research Letters **14**, 1900355 (2020).

[149]N. Saigal and S. Ghosh, "Phonon induced luminescence decay in monolayer MoS_2 on SiO_2/Si substrates", Applied Physics Letters **107**, 242103 (2015).

[150]N. Saigal and S. Ghosh, "Evidence for two distinct defect related luminescence features in monolayer MoS_2", Applied Physics Letters **109**, 122105 (2016).

[151]P. Nagler, M. V. Ballottin, A. A. Mitioglu, M. V. Durnev, T. Taniguchi, K. Watanabe, A. Chernikov, C. Schüller, M. M. Glazov, P. C. M. Christianen, and T. Korn, "Zeeman splitting and inverted polarization of biexciton emission in monolayer WS_2", Phys. Rev. Lett. **121**, 057402 (2018).

[152]K. P. O'donnell and X. Chen, "Temperature dependence of semiconductor band gaps", Appl. Phys. Lett. **58**, 2924–2926 (1991).

[153]S Rudin, T. Reinecke, and B Segall, "Temperature-dependent exciton linewidths in semiconductors", Phys. Rev. B **42**, 11218 (1990).

[154]A. Arora, M. Koperski, K. Nogajewski, J. Marcus, C. Faugeras, and M. Potemski, "Excitonic resonances in thin films of WSe_2: from monolayer to bulk material", Nanoscale **7**, 10421–10429 (2015).

[155]A. Berkdemir, H. R. Gutiérrez, A. R. Botello-Méndez, N. Perea-López, A. L. Elías, C.-I. Chia, B. Wang, V. H. Crespi, F. López-Urías, J.-C. Charlier, H. Terrones, and M. Terrones, "Identification of individual and few layers of WS_2 using raman spectroscopy", Sci. Rep. **3**, 1755 (2013).

[156]A. C. Ferrari, "Raman spectroscopy of graphene and graphite: disorder, electron–phonon coupling, doping and nonadiabatic effects", Solid State Commun. **143**, 47–57 (2007).

[157]N. Bonini, M. Lazzeri, N. Marzari, and F. Mauri, "Phonon anharmonicities in graphite and graphene", Phys. Rev. Lett. **99**, 176802 (2007).

[158]D.-H. Chae, B. Krauss, K. Von Klitzing, and J. H. Smet, "Hot phonons in an electrically biased graphene constriction", Nano Lett. **10**, 466–471 (2010).

[159]M Balkanski, R. Wallis, and E Haro, "Anharmonic effects in light scattering due to optical phonons in silicon", Phys. Rev. B **28**, 1928 (1983).

[160]J. Joshi, I. R. Stone, R. Beams, S. Krylyuk, I. Kalish, A. V. Davydov, and P. M. Vora, "Phonon anharmonicity in bulk $T_d - MoTe_2$", Appl. Phys. Lett. **109** (2016).

[161]S. Paul, S. Karak, M. Mandal, A. Ram, S. Marik, R. Singh, and S. Saha, "Tailoring the phase transition and electron-phonon coupling in 1 $T' - MoTe_2$ by charge doping: a raman study", Phys. Rev. B **102**, 054103 (2020).

[162]A. D. Corso and A. M. Conte, "Spin-orbit coupling with ultrasoft pseudopotentials: application to Au and Pt", Phys. Rev. B **71**, 115106 (2005).

[163]C. F. Klingshirn, *Semiconductor optics* (Springer Science & Business Media, 2012).

[164]N. Ashcroft and N. Mermin, *Solid state physics* (Cengage, 2021).

[165]M. Feierabend, A. Morlet, G. Berghäuser, and E. Malic, "Impact of strain on the optical fingerprint of monolayer transition-metal dichalcogenides", Phys. Rev. B **96**, 045425 (2017).

[166]J.-W. Song, K. Yamashita, and K. Hirao, "Communication: A new hybrid exchange correlation functional for band-gap calculations using a short-range Gaussian attenuation (Gaussian-Perdue-Burke-Ernzerhof)", The Journal of Chemical Physics **135**, 071103 (2011).

[167]E. R. Margine and F. Giustino, "Anisotropic migdal-eliashberg theory using wannier functions", Phys. Rev. B **87**, 024505 (2013).

[168]H. Lee, S. Poncé, K. Bushick, S. Hajinazar, J. Lafuente-Bartolome, J. Leveillee, C. Lian, J.-M. Lihm, F. Macheda, H. Mori, H. Paudyal, W. H. Sio, S. Tiwari, M. Zacharias, X. Zhang, N. Bonini, E. Kioupakis, E. R. Margine, and F. Giustino, "Electron–phonon physics from first principles using the EPW code", npj Computational Materials **9**, 156 (2023).

[169]G. Wang, C. Robert, M. M. Glazov, F. Cadiz, E. Courtade, T. Amand, D. Lagarde, T. Taniguchi, K. Watanabe, B. Urbaszek, and X. Marie, "In-plane propagation of light in transition metal dichalcogenide monolayers: optical selection rules", Phys. Rev. Lett. **119**, 047401 (2017).

[170]A. Arora, "Magneto-optics of layered two-dimensional semiconductors and heterostructures: Progress and prospects", Journal of Applied Physics **129**, 120902 (2021).

[171]E. Liu, J. van Baren, T. Taniguchi, K. Watanabe, Y.-C. Chang, and C. H. Lui, "Valley-selective chiral phonon replicas of dark excitons and trions in monolayer WSe_2", Phys. Rev. Res. **1**, 032007 (2019).

[172]S. Chatterjee, S. Das, G. Gupta, K. Watanabe, T. Taniguchi, and K. Majumdar, "Probing biexciton in monolayer WS_2 through controlled many-body interaction", 2D Materials **9**, 015023 (2021).

[173]C. Robert, D. Lagarde, F. Cadiz, G. Wang, B. Lassagne, T. Amand, A. Balocchi, P. Renucci, S. Tongay, B. Urbaszek, and X. Marie, "Exciton radiative lifetime in transition metal dichalcogenide monolayers", Phys. Rev. B **93**, 205423 (2016).

[174]K.-A. N. Duerloo, Y. Li, and E. J. Reed, "Structural phase transitions in two-dimensional mo-and w-dichalcogenide monolayers", Nat. Commun. **5**, 4214 (2014).

[175]A. Castellanos-Gomez, M. Poot, G. A. Steele, H. S. Van Der Zant, N. Agraït, and G. Rubio-Bollinger, "Elastic properties of freely suspended MoS_2 nanosheets", Adv. Mat. **24**, 772–775 (2012).

[176]H. L. Liu, C. C. Shen, S. H. Su, C. L. Hsu, M. Y. Li, and L. J. Li, "Optical properties of monolayer transition metal dichalcogenides probed by spectroscopic ellipsometry", Applied Physics Letters **105**, 201905 (2014).

[177]Q. H. Wang, K. Kalantar-Zadeh, A. Kis, J. N. Coleman, and M. S. Strano, "Electronics and optoelectronics of two-dimensional transition metal dichalcogenides", Nature Nanotechnology **7**, 699–712 (2012).

[178]R. S. Sundaram, M. Engel, A. Lombardo, R. Krupke, A. C. Ferrari, P. Avouris, and M. Steiner, "Electroluminescence in single layer MoS_2", Nano Letters **13**, 1416–1421 (2013).

[179]K. F. Mak, K. He, C. Lee, G. H. Lee, J. Hone, T. F. Heinz, and J. Shan, "Tightly bound trions in monolayer MoS_2", Nature Materials **12**, 207–211 (2013).

[180]C. Mai, A. Barrette, Y. Yu, Y. G. Semenov, K. W. Kim, L. Cao, and K. Gundogdu, "Many-body effects in valleytronics: direct measurement of valley lifetimes in single-layer MoS_2", Nano Letters **14**, 202–206 (2014).

[181]K. F. Mak, K. He, J. Shan, and T. F. Heinz, "Control of valley polarization in monolayer MoS_2 by optical helicity", Nature Nanotechnology **7**, 494–498 (2012).

[182]H. Zeng, J. Dai, W. Yao, D. Xiao, and X. Cui, "Valley polarization in MoS_2 monolayers by optical pumping", Nature Nanotechnology **7**, 490–493 (2012).

[183]K. Kang, S. Xie, L. Huang, Y. Han, P. Y. Huang, K. F. Mak, C. J. Kim, D. Muller, and J. Park, "High-mobility three-atom-thick semiconducting films with wafer-scale homogeneity", Nature **520**, 656–660 (2015).

[184]N. Briggs, S. Subramanian, Z. Lin, X. Li, X. Zhang, K. Zhang, K. Xiao, D. Geohegan, R. Wallace, L. Q. Chen, M. Terrones, A. Ebrahimi, S. Das, J. Redwing, C. Hinkle, K. Momeni, A. V. Duin, V. Crespi, S. Kar, and J. A. Robinson, "A roadmap for electronic grade $2D$ materials", 2D Materials **6**, 022001 (2019).

[185]V. Narayanan P, G. MA, T. Chowdhury, C. K. Singh, S. K. Chaubey, T. Taniguchi, K. Watanabe, M. Kabir, G. P. Kumar, and A. Rahman, "Giant photoresponse enhancement in mixed-dimensional van der waals heterostructure through dielectric engineering", Adv. Mater. Interfaces **9**, 2102054 (2022).

[186]M. A. Gokul, V. Narayanan, and A. Rahman, "Modulating flow near substrate surface to grow clean and large-area monolayer MoS_2", Nanotechnology **31**, 415706–415717 (2020).

[187]A. K. Geim and K. S. Novoselov, "The rise of graphene", Nature Materials **6**, 183–191 (2007).

[188]K. Roy, M. Padmanabhan, S. Goswami, T. P. Sai, G. Ramalingam, S. Raghavan, and A. Ghosh, "Graphene-MoS_2 hybrid structures for multifunctional photoresponsive memory devices", Nature Nanotechnology **8**, 826–830 (2013).

[189]O. Lopez-Sanchez, D. Lembke, M. Kayci, A. Radenovic, and A. Kis, "Ultrasensitive photodetectors based on monolayer MoS_2", Nature Nanotechnology **8**, 497–501 (2013).

[190]J. S. Ross, P. Klement, A. M. Jones, N. J. Ghimire, J. Yan, D. G. Mandrus, T. Taniguchi, K. Watanabe, K. Kitamura, W. Yao, D. H. Cobden, and X. Xu, "Electrically tunable excitonic light-emitting diodes based on monolayer WSe_2 p-n junctions", Nature Nanotechnology **9**, 268–272 (2014).

[191]W. Jin, P. C. Yeh, N. Zaki, D. Zhang, J. T. Sadowski, A. Al-Mahboob, A. M. V. D. Zande, D. A. Chenet, J. I. Dadap, I. P. Herman, P. Sutter, J. Hone, and R. M. Osgood, "Direct measurement of the thickness-dependent electronic band structure of MoS_2 using angle-resolved photoemission spectroscopy", Physical Review Letters **111**, 106801 (2013).

[192]Y. Zhang, T. R. Chang, B. Zhou, Y. T. Cui, H. Yan, Z. Liu, F. Schmitt, J. Lee, R. Moore, Y. Chen, H. Lin, H. T. Jeng, S. K. Mo, Z. Hussain, A. Bansil, and Z. X. Shen, "Direct observation of the transition from indirect to direct bandgap in atomically thin epitaxial $MoSe_2$", Nature Nanotechnology **9**, 111–115 (2014).

[193]B. Radisavljevic and A. Kis, "Mobility engineering and a metal-insulator transition in monolayer MoS_2", Nature Materials **12**, 815–820 (2013).

[194]S. L. Li, K. Wakabayashi, Y. Xu, S. Nakaharai, K. Komatsu, W. W. Li, Y. F. Lin, A. Aparecido-Ferreira, and K. Tsukagoshi, "Thickness-dependent interfacial coulomb scattering in atomically thin field-effect transistors", Nano Letters **13**, 3546–3552 (2013).

[195]N. Ma and D. Jena, "Charge scattering and mobility in atomically thin semiconductors", Physical Review X **4**, 11043 (2014).

[196]V. Perebeinos, J. Tersoff, and P. Avouris, "Scaling of excitons in carbon nanotubes", Physical Review Letters **92**, 257402 (2004).

[197]A. G. Walsh, A. N. Vamivakas, Y. Yin, S. B. Cronin, M. S. Ünlü, B. B. Goldberg, and A. K. Swan, "Scaling of exciton binding energy with external dielectric function in carbon nanotubes", Physica E: Low-Dimensional Systems and Nanostructures **40**, 2375–2379 (2008).

[198]M. Kumagai and T. Takagahara, "Excitonic and nonlinear-optical properties of dielectric quantum-well structures", Physical Review B **40**, 12359–12381 (1989).

[199]L. Kulik, V. Kulakovskii, M. Bayer, and A. Forchel, "Dielectric enhancement of excitons in near-surface quantum wells", Physical Review B - Condensed Matter and Materials Physics **54**, R2335–R2338 (1996).

[200]L. M. Schneider, S. Lippert, J. Kuhnert, O. Ajayi, D. Renaud, S. Firoozabadi, Q. Ngo, R. Guo, Y. D. Kim, W. Heimbrodt, J. C. Hone, and A. Rahimi-Iman, "The influence of the environment on monolayer tungsten diselenide photoluminescence", Nano-Structures and Nano-Objects **15**, 84–97 (2018).

[201]Y. Lin, X. Ling, L. Yu, S. Huang, A. L. Hsu, Y. H. Lee, J. Kong, M. S. Dresselhaus, and T. Palacios, "Dielectric screening of excitons and trions in single-layer MoS_2", Nano Letters **14**, 5569–5576 (2014).

[202]Y. Yu, Y. Yu, C. Xu, Y. Q. Cai, L. Su, Y. Zhang, Y. W. Zhang, K. Gundogdu, and L. Cao, "Engineering substrate interactions for high luminescence efficiency of transition-metal dichalcogenide monolayers", Advanced Functional Materials **26**, 4733–4739 (2016).

[203]A. O. Tanoh, J. Alexander-Webber, J. Xiao, G. Delport, C. A. Williams, H. Bretscher, N. Gauriot, J. Allardice, R. Pandya, Y. Fan, Z. Li, S. Vignolini, S. D. Stranks, S. Hofmann, and A. Rao, "Enhancing photoluminescence and mobilities in WS_2 monolayers with oleic acid ligands", Nano Letters **19**, 6299–6307 (2019).

[204]M. K. Man, S. Deckoff-Jones, A. Winchester, G. Shi, G. Gupta, A. D. Mohite, S. Kar, E. Kioupakis, S. Talapatra, and K. M. Dani, "Protecting the properties of monolayer MoS_2 on silicon based substrates with an atomically thin buffer", Scientific Reports **6**, 1–9 (2016).

[205]T. C. Berkelbach, M. S. Hybertsen, and D. R. Reichman, "Theory of neutral and charged excitons in monolayer transition metal dichalcogenides", Physical Review B - Condensed Matter and Materials Physics **88**, 045318 (2013).

[206]M. Currie, A. T. Hanbicki, G. Kioseoglou, and B. T. Jonker, "Optical control of charged exciton states in tungsten disulfide", Applied Physics Letters **106** (2015).

[207]M. Buscema, G. A. Steele, H. S. van der Zant, and A. Castellanos-Gomez, "The effect of the substrate on the raman and photoluminescence emission of single-layer MoS_2", Nano Research **7**, 561–571 (2014).

[208]D. Sercombe, S. Schwarz, O. D. Pozo-Zamudio, F. Liu, B. J. Robinson, E. A. Chekhovich, I. I. Tartakovskii, O. Kolosov, and A. I. Tartakovskii, "Optical investigation of the natural electron doping in thin MoS_2 films deposited on dielectric substrates", Scientific Reports **3**, 1–6 (2013).

[209]N. Scheuschner, O. Ochedowski, A. M. Kaulitz, R. Gillen, M. Schleberger, and J. Maultzsch, "Photoluminescence of freestanding single- and few-layer MoS_2", Physical Review B - Condensed Matter and Materials Physics **89**, 125406 (2014).

[210]R. Yan, S. Bertolazzi, J. Brivio, T. Fang, A. Konar, A. G. Birdwell, N. V. Nguyen, A. Kis, D. Jena, and H. G. Xing, "Raman and photoluminescence study of dielectric and thermal effects on atomically thin MoS_2", arXiv.1211.4136 (2012).

[211]D. V. Tuan, A. M. Jones, M. Yang, X. Xu, and H. Dery, "Virtual trions in the photoluminescence of monolayer transition-metal dichalcogenides", Physical Review Letters **122**, 217401 (2019).

[212]J Jadczak, L Bryja, J Kutrowska-Girzycka, P Kapuściński, M Bieniek, Y.-S. Huang, and P Hawrylak, "Room temperature multi-phonon upconversion photoluminescence in monolayer semiconductor WS_2", Nature Communications **10**, 107 (2019).

[213]M. Baldo and V. Stojanovi, "Optical switching: excitonic interconnects", Nature Photonics **3**, 558–560 (2009).

[214]B. Schuler, K. A. Cochrane, C. Kastl, E. S. Barnard, E. Wong, N. J. Borys, A. M. Schwartzberg, D. F. Ogletree, F. J. G. D. Abajo, and A. Weber-Bargioni, "Electrically driven photon emission from individual atomic defects in monolayer WS_2", Science Advances **6**, 5988–6004 (2020).

[215]Y. Kwon, K. Kim, W. Kim, S. Ryu, and H. Cheong, "Variation of photoluminescence spectral line shape of monolayer WS_2", Current Applied Physics **18**, 941–945 (2018).

[216]C. Rice, R. J. Young, R. Zan, U. Bangert, D. Wolverson, T. Georgiou, R. Jalil, and K. S. Novoselov, "Raman-scattering measurements and first-principles calculations of strain-induced phonon shifts in monolayer MoS_2", Physical Review B - Condensed Matter and Materials Physics **87**, 081307 (2013).

[217]N. Zhang, A. Surrente, M. Baranowski, D. Dumcenco, Y.-C. Kung, D. K. Maude, A. Kis, and P. Plochocka, "Impact of photodoping on inter- and intralayer exciton emission in a MoS_2/$MoSe_2$/MoS_2 heterostructure", Applied Physics Letters **113**, 062107 (2018).

[218]V. Huard, R. T. Cox, K. Saminadayar, A. Arnoult, and S. Tatarenko, "Bound states in optical absorption of semiconductor quantum wells containing a two-dimensional electron gas", Physical Review Letters **84**, 187 (2000).

[219]M. Danovich, V. Zólyomi, V. I. Fal'ko, and I. L. Aleiner, "Auger recombination of dark excitons in WS_2 and WSe_2 monolayers", 2D Materials **3**, 035011 (2016).

[220]A. R. S. Kandada, S. Neutzner, V. D'Innocenzo, F. Tassone, M. Gandini, Q. A. Akkerman, M. Prato, L. Manna, A. Petrozza, and G. Lanzani, "Nonlinear carrier interactions in lead halide perovskites and the role of defects", Journal of the American Chemical Society **138**, 13604–13611 (2016).

[221]N. Peimyoo, J. Shang, W. Yang, Y. Wang, C. Cong, and T. Yu, "Thermal conductivity determination of suspended mono- and bilayer WS_2 by raman spectroscopy", Nano Research **8**, 1210–1221 (2015).

[222]J. J. Zhang, J. Guan, S. Dong, and B. I. Yakobson, "Room temperature ferroelectricity in $\mathrm{Group-IV}$ metal chalcogenide nanowires", Journal of the American Chemical Society **141**, 15040–15045 (2019).

[223]X. Huang, Y. Gao, T. Yang, W. Ren, H.-M. Cheng, and T. Lai, "Quantitative analysis of temperature dependence of raman shift of monolayer WS_2", Scientific Reports **6**, 1–8 (2016).

[224]H.-L. Liu, T. Yang, J.-H. Chen, H.-W. Chen, H. Guo, R. Saito, M.-Y. Li, and L.-J. Li, "Temperature-dependent optical constants of monolayer MoS_2, $MoSe_2$, WS_2, and WSe_2: spectroscopic ellipsometry and first-principles calculations", Scientific Reports **10**, 15282 (2020).

[225]S. Tongay, J. Zhou, C. Ataca, J. Liu, J. S. Kang, T. S. Matthews, L. You, J. Li, J. C. Grossman, and J. Wu, "Broad-range modulation of light emission in two-dimensional semiconductors by molecular physisorption gating", Nano Letters **13**, 2831–2836 (2013).

[226]S. Tongay, J. Suh, C. Ataca, W. Fan, A. Luce, J. S. Kang, J. Liu, C. Ko, R. Raghunathanan, J. Zhou, et al., "Defects activated photoluminescence in two-dimensional semiconductors: interplay between bound, charged and free excitons", Scientific Reports **3**, 2657 (2013).

[227]B. Zhao, C. Shang, N. Qi, Z. Y. Chen, and Z. Q. Chen, "Stability of defects in monolayer MoS_2 and their interaction with O_2 molecule: a first-principles study", Applied Surface Science **412**, 385–393 (2017).

[228]S. Zhao, J. Xue, and W. Kang, "Gas adsorption on MoS_2 monolayer from first-principles calculations", Chemical Physics Letters **595-596**, 35–42 (2014).

[229]Y. Wang, Z. He, J. Zhang, H. Liu, X. Lai, B. Liu, Y. Chen, F. Wang, and L. Zhang, "UV illumination enhanced desorption of oxygen molecules from monolayer MoS_2 surface", Nano Research **13**, 358–365 (2020).

[230]P. Sun, M. Zhu, K. Wang, M. Zhong, J. Wei, D. Wu, Y. Cheng, and H. Zhu, "Photoinduced molecular desorption from graphene films", Applied Physics Letters **101**, 053107 (2012).

[231]F. Wang, I. A. Kinloch, D. Wolverson, R. Tenne, A. Zak, E. O'Connell, U. Bangert, and R. J. Young, "Strain-induced phonon shifts in tungsten disulfide nanoplatelets and nanotubes", 2D Materials **4**, 015007 (2016).

[232]J. Feng, X. Qian, C.-W. Huang, and J. Li, "Strain-engineered artificial atom as a broad-spectrum solar energy funnel", Nature Photonics **6**, 866–872 (2012).

[233]P. San-Jose, V. Parente, F. Guinea, R. Roldén, and E. Prada, "Inverse funnel effect of excitons in strained black phosphorus", Physical Review X **6**, 031046 (2016).

[234]Y. Yu, A. W. Bataller, R. Younts, Y. Yu, G. Li, A. A. Puretzky, D. B. Geohegan, K. Gundogdu, and L. Cao, "Room-temperature $\mathrm{Electron} - \mathrm{Hole}$ liquid in monolayer MoS_2 MoS_2", ACS Nano **13**, 10351–10358 (2019).

[235]C. Cong, J. Shang, X. Wu, B. Cao, N. Peimyoo, C. Qiu, L. Sun, and T. Yu, "Synthesis and optical properties of large-area single-crystalline $2D$ semiconductor WS_2 monolayer from chemical vapor deposition", Advanced Optical Materials **2**, 131–136 (2014).

[236]Y. Zhang, Y. Zhang, Q. Ji, J. Ju, H. Yuan, J. Shi, T. Gao, D. Ma, M. Liu, Y. Chen, X. Song, H. Y. Hwang, Y. Cui, and Z. Liu, "Controlled growth of high-quality monolayer WS_2 layers on sapphire and imaging its grain boundary", ACS Nano **7**, 8963–8971 (2013).

[237]M. Qin, S. Hou, L. K. Wang, X. Z. Feng, R. Wang, Y. L. Yang, C. Wang, L. Yu, B. Shao, and M. Q. Qiao, "Two methods for glass surface modification and their application in protein immobilization", Colloids and Surfaces B: Biointerfaces **60**, 243–249 (2007).

[238]C. H. Li, K. M. McCreary, and B. T. Jonker, "Spatial control of photoluminescence at room temperature by ferroelectric domains in monolayer WS_2 /PZT hybrid structures", ACS Omega **1**, 1075–1080 (2016).

[239]X. Zhang and J. P. Raskin, "Low-temperature wafer bonding optimal O_2 plasma surface pretreatment time", Electrochemical and Solid-State Letters **7**, G172 (2004).

[240]K. S. Novoselov, A. K. Geim, S. V. Morozov, D. Jiang, Y. Zhang, S. V. Dubonos, I. V. Grigorieva, and A. A. Firsov, "Electric field in atomically thin carbon films", Science **306**, 666–669 (2004).

[241]C. Cui, F. Xue, W. J. Hu, and L. J. Li, "Two-dimensional materials with piezoelectric and ferroelectric functionalities", npj 2D Materials and Applications **2** (2018).

[242]Z. Guan, H. Hu, X. Shen, P. Xiang, N. Zhong, J. Chu, and C. Duan, "Recent progress in two-dimensional ferroelectric materials", Advanced Electronic Materials **6**, 1–30 (2020).

[243]T. Rangel, B. M. Fregoso, B. S. Mendoza, T. Morimoto, J. E. Moore, and J. B. Neaton, "Large bulk photovoltaic effect and spontaneous polarization of single-layer monochalcogenides", Phys. Rev. Lett. **119**, 067402 (2017).

[244]H. Wang and X. Qian, "Two-dimensional multiferroics in monolayer group IV monochalcogenides", 2D Materials **4**, 015042 (2017).

[245]M. Wu and X. C. Zeng, "Intrinsic ferroelasticity and/or multiferroicity in two-dimensional phosphorene and phosphorene analogues", Nano Letters **16**, 3236–3241 (2016).

[246]Y. Yan, Q. Deng, S. Li, T. Guo, X. Li, Y. Jiang, X. Song, W. Huang, J. Yang, and C. Xia, "In-plane ferroelectricity in few-layered ges and its van der waals ferroelectric diodes", Nanoscale **13**, 16122–16130 (2021).

[247]K.-A. N. Duerloo, M. T. Ong, and E. J. Reed, "Intrinsic piezoelectricity in two-dimensional materials", The Journal of Physical Chemistry Letters **3**, 2871–2876 (2012).

[248]H. Yin, C. Liu, G.-P. Zheng, Y. Wang, and F. Ren, "Ab initio simulation studies on the room-temperature ferroelectricity in two-dimensional β-phase ges", Applied Physics Letters **114** (2019).

[249]R. Fei, W. Li, J. Li, and L. Yang, "Giant piezoelectricity of monolayer group iv monochalcogenides: SnSe, SnS, GeSe, andGeS", Applied Physics Letters **107** (2015).

[250]R. Fei, W. Kang, and L. Yang, "Ferroelectricity and phase transitions in monolayer group-iv monochalcogenides", Physical Review Letters **117**, 097601 (2016).

[251]A. L. Sharpe, E. J. Fox, A. W. Barnard, J. Finney, K. Watanabe, T. Taniguchi, M. A. Kastner, and D. Goldhaber-Gordon, "Emergent ferromagnetism near three-quarters filling in twisted bilayer graphene", Science **365**, 605–608 (2019).

[252]S. Carr, D. Massatt, S. Fang, P. Cazeaux, M. Luskin, and E. Kaxiras, "Twistronics: manipulating the electronic properties of two-dimensional layered structures through their twist angle", Phys. Rev. B **95**, 075420 (2017).

[253]Y. Cao, V. Fatemi, S. Fang, K. Watanabe, T. Taniguchi, E. Kaxiras, and P. Jarillo-Herrero, "Unconventional superconductivity in magic-angle graphene superlattices", Nature **556**, 43–50 (2018).

[254]K. Yasuda, X. Wang, K. Watanabe, T. Taniguchi, and P. Jarillo-Herrero, "Stacking-engineered ferroelectricity in bilayer boron nitride", Science **372**, 1458–1462 (2021).

[255]E. Y. Andrei and A. H. MacDonald, "Graphene bilayers with a twist", Nature Materials **19**, 1265–1275 (2020).

[256]L. Cai and G. Yu, "Fabrication strategies of twisted bilayer graphenes and their unique properties", Advanced Materials **33**, 2004974 (2021).

[257]A. C. Gadelha, D. A. A. Ohlberg, F. C. Santana, G. S. N. Eliel, J. S. Lemos, V. Ornelas, D. Miranda, R. B. Nadas, K. Watanabe, T. Taniguchi, C. Rabelo, P. P. de Mello Venezuela, G. Medeiros-Ribeiro, A. Jorio, L. G. Cançado, and L. C. Campos, "Twisted bilayer graphene: a versatile fabrication method and the detection of variable nanometric strain caused by twist-angle disorder", ACS Applied Nano Materials **4**, 1858–1866 (2021).

[258]E. Sutter and P. Sutter, "1D wires of 2D layered materials: germanium sulfide nanowires as efficient light emitters", ACS Applied Nano Materials **1**, 1042–1049 (2018).

[259]C. Li, Y. Yu, M. Chi, and L. Cao, "Epitaxial nanosheet-nanowire heterostructures", Nano Letters **13**, 948–953 (2013).

[260]J. D. Eshelby, "Screw dislocations in thin rods", Journal of Applied Physics **24**, 176 (2004).

[261]R. K. Ulaganathan, Y. Y. Lu, C. J. Kuo, S. R. Tamalampudi, R. Sankar, K. M. Boopathi, A. Anand, K. Yadav, R. J. Mathew, C. R. Liu, F. C. Chou, and Y. T. Chen, "High photosensitivity and broad spectral response of multi-layered germanium sulfide transistors", Nanoscale **8**, 2284–2292 (2016).

[262]K. Kushnir, M. Wang, P. D. Fitzgerald, K. J. Koski, and L. V. Titova, "Ultrafast zero-bias photocurrent in ges nanosheets: promise for photovoltaics", ACS Energy Letters **2**, 1429–1434 (2017).

[263]H. B. Ribeiro, S. L. Ramos, L. Seixas, C. J. D. Matos, and M. A. Pimenta, "Edge phonons in layered orthorhombic ges and gese monochalcogenides", Physical Review B **100**, 1–8 (2019).

[264]S. R. Tamalampudi, S. Patole, B. Alfakes, R. Sankar, I. Almansouri, M. Chiesa, and J. Y. Lu, "High-temperature defect-induced hopping conduction in multilayered germanium sulfide for optoelectronic applications in harsh environments", ACS Applied Nano Materials **2**, 2169–2175 (2019).

[265]T. Ghosh, M. Samanta, A. Vasdev, K. Dolui, J. Ghatak, T. Das, G. Sheet, and K. Biswas, "Ultrathin free-standing nanosheets of Bi_2O_2Se: room temperature ferroelectricity in self-assembled charged layered heterostructure", Nano Letters **19**, 5703–5709 (2019).

[266]Y. Bao, P. Song, Y. Liu, Z. Chen, M. Zhu, I. Abdelwahab, J. Su, W. Fu, X. Chi, W. Yu, W. Liu, X. Zhao, Q. H. Xu, M. Yang, and K. P. Loh, "Gate-tunable in-plane ferroelectricity in few-layer SnS", Nano Letters **19**, 5109–5117 (2019).

[267]F. Liu, L. You, K. L. Seyler, X. Li, P. Yu, J. Lin, X. Wang, J. Zhou, H. Wang, H. He, S. T. Pantelides, W. Zhou, P. Sharma, X. Xu, P. M. Ajayan, J. Wang, and Z. Liu, "Room-temperature ferroelectricity in $CuInP_2S_6$ ultrathin flakes", Nature Communications **7**, 12357 (2016).

[268]D. Tan, H. E. Lim, F. Wang, N. B. Mohamed, S. Mouri, W. Zhang, Y. Miyauchi, M. Ohfuchi, and K. Matsuda, "Anisotropic optical and electronic properties of two-dimensional layered germanium sulfide", Nano Research **10**, 546–555 (2017).

[269]D. Tan, W. Zhang, X. Wang, S. Koirala, Y. Miyauchi, and K. Matsuda, "Polarization-sensitive and broadband germanium sulfide photodetectors with excellent high-temperature performance", Nanoscale **9**, 12425–12431 (2017).

[270]T. Karakostas, "Planar defects in $GeSe$ and GeS crystals", Journal of Materials Science **23**, 3099–3105 (1988).

[271]G. K. Solanki, D. B. Patel, S. Unadkat, and M. K. Agarwal, "Synthesis and characterization of germanium monosulphide (GeS) single crystals grown using different transporting agents", Pramana - Journal of Physics **74**, 813–825 (2010).

[272]L.-H. Zeng, M.-Z. Wang, H. Hu, B. Nie, Y.-Q. Yu, C.-Y. Wu, L. Wang, J.-G. Hu, C. Xie, F.-X. Liang, and L.-B. Luo, "Monolayer graphene/germanium schottky junction as high-performance self-driven infrared light photodetector", ACS Applied Materials and Interfaces **5**, 9362–9366 (2013).

[273]L. Zeng, L. Tao, C. Tang, B. Zhou, H. Long, Y. Chai, S. P. Lau, and Y. H. Tsang, "High-responsivity $\mathrm{UV}-\mathrm{Vis}$ photodetector based on transferable WS_2 film deposited by magnetron sputtering", Scientific Reports **6**, 1–8 (2016).

[274]P. C. Joshi, A. Mansingh, M. N. Kamalasanan, and S. Chandra, "Structural and optical properties of ferroelectric $\mathrm{Bi}_4\mathrm{Ti}_3\mathrm{O}_{12}$ thin films by sol-gel technique", Applied Physics Letters **59**, 2389–2390 (1991).

[275]S. Jesse, A. P. Baddorf, and S. V. Kalinin, "Switching spectroscopy piezoresponse force microscopy of ferroelectric materials", Applied Physics Letters **88**, 1–4 (2006).

[276]S. Jesse, B. Mirman, and S. V. Kalinin, "Resonance enhancement in piezoresponse force microscopy: mapping electromechanical activity, contact stiffness, and q factor", Applied Physics Letters **89**, 11–14 (2006).

[277]L. Aggarwal, A. Banik, S. Anand, U. V. Waghmare, K. Biswas, and G. Sheet, "Local ferroelectricity in thermoelectric snte above room temperature driven by competing phonon instabilities and soft resonant bonding", Journal of Materiomics **2**, Special Issue on Advances in Thermoelectric Research, 196–202 (2016).

[278]K. Lefki and G. J. M. Dormans, "Measurement of piezoelectric coefficients of ferroelectric thin films", Journal of Applied Physics **76**, 1764–1767 (1994).

[279]N. Higashitarumizu, H. Kawamoto, C. J. Lee, B. H. Lin, F. H. Chu, I. Yonemori, T. Nishimura, K. Wakabayashi, W. H. Chang, and K. Nagashio, "Purely in-plane ferroelectricity in monolayer SnS at room temperature", Nature Communications **11**, 1–9 (2020).

[280]M. Galanty, O. Shavit, A. Weissman, H. Aharon, D. Gachet, E. Segal, and A. Salomon, "Second harmonic generation hotspot on a centrosymmetric smooth silver surface", Light: Science & Applications **7**, 49 (2018).

[281]M. Fox, "Optical properties of solids", Oxford Master Series in Physics (2011).

[282]M. I. Stockman, D. J. Bergman, C. Anceau, S. Brasselet, and J. Zyss, "Enhanced second-harmonic generation by metal surfaces with nanoscale roughness: nanoscale dephasing, depolarization, and correlations", Physical Review Letters **92**, 4 (2004).

[283]R. T. Deck and R. K. Grygier, "Surface-plasmon enhanced harmonic generation at a rough metal surface", Applied Optics **23**, 3202 (1984).

[284]A. Wokaun, J. G. Bergman, J. P. Heritage, A. M. Glass, P. F. Liao, and D. H. Olson, "Surface second-harmonic generation from metal island films and microlithographic structures", Physical Review B **24**, 849–856 (1981).

[285]F. X. Wang, F. J. Rodréguez, W. M. Albers, and M. Kauranen, "Enhancement of bulk-type multipolar second-harmonic generation arising from surface morphology of metals", New Journal of Physics **12**, 63009 (2010).

[286]S. R. Panday and B. M. Fregoso, "Strong second harmonic generation in two-dimensional ferroelectric", Journal of Physics: Condensed Matter **29**, 43LT01 (2017).

[287]H. Wang and X. Qian, "Giant optical second harmonic generation in two-dimensional multiferroics", Nano Letters **17**, 5027–5034 (2017).

[288]H. Wiedemeier, H. Georg, and G. von Schnering, "Refinement of the structures of ges, gese, sns and snse", Zeitschrift für Kristallographie - Crystalline Materials **148**, 295–304 (1978).

[289]Z. Wang, M. Gao, X. Hao, and W. Qin, "Helical-chiroptical nanowires generated orbital angular momentum for the detection of circularly polarized light", Applied Physics Letters **116**, 053301 (2020).

[290]W. Zhang, C.-P. Chuu, J.-K. Huang, C.-H. Chen, M.-L. Tsai, Y.-H. Chang, C.-T. Liang, Y.-Z. Chen, Y.-L. Chueh, J.-H. He, et al., "Ultrahigh-gain photodetectors based on atomically thin graphene-MoS_2 heterostructures", Scientific Reports **4**, 3826 (2014).

[291]F. H. Koppens, D. E. Chang, and F. J. García de Abajo, "Graphene plasmonics: a platform for strong light–matter interactions", Nano Letters **11**, 3370–3377 (2011).

[292]M. Furchi, A. Urich, A. Pospischil, G. Lilley, K. Unterrainer, H. Detz, P. Klang, A. M. Andrews, W. Schrenk, G. Strasser, et al., "Microcavity-integrated graphene photodetector", Nano Letters **12**, 2773–2777 (2012).

[293]J. C. Song, M. S. Rudner, C. M. Marcus, and L. S. Levitov, "Hot carrier transport and photocurrent response in graphene", Nano Letters **11**, 4688–4692 (2011).

[294]Y. Zou, Z. Zhang, C. Wang, Y. Cheng, C. Wang, K. Sun, W. Zhang, P. Suo, X. Lin, H. Ma, Y. Leng, W. Liu, J. Du, and G. Ma, "Charge transfer in graphene-MoS_2 vertical heterostructures tuned by stacking order and substrate-introduced electric field", ACS Applied Materials & Interfaces **16**, 30589–30597 (2024).

[295]D. Kozawa, R. Kumar, A. Carvalho, K. Kumar Amara, W. Zhao, S. Wang, M. Toh, R. M. Ribeiro, A. H. Castro Neto, K. Matsuda, et al., "Photocarrier relaxation pathway in two-dimensional semiconducting transition metal dichalcogenides", Nature Communications **5**, 4543 (2014).

Copyrights and Permissions

American Physical Society
Reuse and Permissions License

12-Aug-2024

This license agreement between the American Physical Society ("APS") and Tamaghna Chowdhury ("You") consists of your license details and the terms and conditions provided by the American Physical Society and SciPris.

Licensed Content Information

License Number:	**RNP/24/AUG/082200**
License date:	12-Aug-2024
DOI:	10.1103/PhysRevB.110.L081405
Title:	Brightening of dark excitons in ${\mathrm{WS}}_{2}$ via tensile strain-induced excitonic valley convergence
Author:	Tamaghna Chowdhury et al.
Publication:	Physical Review B
Publisher:	American Physical Society
Cost:	USD $ 0.00

Request Details

Does your reuse require significant modifications: No

Specify intended distribution locations:	Worldwide
Reuse Category:	Reuse in a thesis/dissertation
Requestor Type:	Author of requested content
Items for Reuse:	Whole Article
Format for Reuse:	Print and Electronic
Total number of print copies:	Up to 1000

Information about New Publication:

University/Publisher:	Indian Institute of Science Education and Research Pune
Title of dissertation/thesis:	Modulation of optoelectronic properties of layered two-dimensional materials by strain, twist and dielectric engineering
Author(s):	Tamaghna Chowdhury
Expected completion date:	Jul. 2024

License Requestor Information

Name:	Tamaghna Chowdhury
Affiliation:	Individual
Email Id:	tamaghna.chowdhury@students.iiserpune.ac.in
Country:	India

Marketplace

Order Date	27-Jun-2024	Type of Use	Republish in a thesis/dissertation
Order License ID	1498982-1		
ISSN	2053-1583	Publisher	IOP Publishing
		Portion	Chapter/article

LICENSED CONTENT

Publication Title	2D materials	Country	United Kingdom of Great Britain and Northern Ireland
Author / Editor	Institute of Physics (Great Britain),	Rightsholder	IOP Publishing, Ltd
Date	01/01/2014	Publication Type	e-Journal
Language	English		

REQUEST DETAILS

Portion Type	Chapter/article	Rights Requested	Main product
Page Range(s)	1-13	Distribution	Worldwide
Total Number of Pages	13	Translation	Original language of publication
Format (select all that apply)	Print, Electronic	Copies for the Disabled?	No
Who Will Republish the Content?	Academic institution	Minor Editing Privileges?	No
Duration of Use	Life of current and all future editions	Incidental Promotional Use?	No
Lifetime Unit Quantity	Up to 499	Currency	USD

NEW WORK DETAILS

Title	Modulation of optoelectronic properties of layered two-dimensional materials by strain, twist, and dielectric engineering.	Institution Name	Indian Institute of Science Education and Research Pune
Instructor Name	Dr Atikur Rahman	Expected Presentation Date	2024-07-31

ADDITIONAL DETAILS

Order Reference Number	N/A	The Requesting Person / Organization to Appear on the License	Tamaghna Chowdhury

REQUESTED CONTENT DETAILS

Title, Description or Numeric Reference of the Portion(s)	Modulation of trion and exciton formation in monolayer WS2 by dielectric and substrate engineering	**Title of the Article / Chapter the Portion Is From**	Modulation of trion and exciton formation in monolayer WS2 by dielectric and substrate engineering
Editor of Portion(s)	N/A	**Author of Portion(s)**	Tamaghna Chowdhury, Diptabrata Paul, Divya Nechiyil, Gokul M A, Kenji Watanabe, Takashi Taniguchi, G V Pavan Kumar and Atikur Rahman
Volume / Edition	8		
Page or Page Range of Portion	045032	**Issue, if Republishing an Article From a Serial**	N/A
		Publication Date of Portion	2021-09-22

RIGHTSHOLDER TERMS AND CONDITIONS

These special terms and conditions are in addition to the standard terms and conditions for CCC's Republication Service and, together with those standard terms and conditions, govern the use of the Works. As the User you will make all reasonable efforts to contact the author(s) of the article which the Work is to be reused from, to seek consent for your intended use. Contacting one author who is acting expressly as authorised agent for their co-author(s) is acceptable. User will reproduce the following wording prominently alongside the Work: the source of the Work, including author, article title, title of journal, volume number, issue number (if relevant), page range (or first page if this is the only information available) and date of first publication; and a link back to the article (via DOI); and if practicable, and IN ALL CASES for new works published under any of the Creative Commons licences, the words "© IOP Publishing. Reproduced with permission. All rights reserved" Without the express permission of the author(s) and the Rightsholder of the article from which the Work is to be reused, User shall not use it in any way which, in the opinion of the Rightsholder, could: (i) distort or alter the author(s)' original intention(s) and meaning; (ii) be prejudicial to the honour or reputation of the author(s); and/or (iii) imply endorsement by the author(s) and/or the Rightsholder. This licence does not apply to any article which is credited to another source and which does not have the copyright line '© IOP Publishing Ltd'. User must check the copyright line of the article from which the Work is to be reused to check that IOP Publishing Ltd has all the necessary rights to be able to grant permission. User is solely responsible for identifying and obtaining separate licences and permissions from the copyright owner for reuse of any such third party material/figures which the Rightsholder is not the copyright owner of. The Rightsholder shall not reimburse any fees which User pays for a republication license for such third party content. This licence does not apply to any material/figure which is credited to another source in the Rightsholder's publication or has been obtained from a third party. User must check the Version of Record of the article from which the Work is to be reused, to check whether any of the material in the Work is third party material. Third party citations and/or copyright notices and/or permissions statements may not be included in any other version of the article from which the Work is to be reused and so cannot be relied upon by the User. User is solely responsible for identifying and obtaining separate licences and permissions from the copyright owner for reuse of any such third party material/figures where the Rightsholder is not the copyright owner. The Rightsholder shall not reimburse any fees which User pays for a republication license for such third party content. User and CCC acknowledge that the Rightsholder may, from time to time, make changes or additions to these special terms and conditions without express notification, provided that these shall not apply to permissions already secured and paid for by User prior to such change or addition. User acknowledges that the Rightsholder (which includes companies within its group and third parties for whom it publishes its titles) may make use of personal data collected through the service in the course of their business. If User is the author of the Work, User may automatically have the right to reuse it under the rights granted back when User transferred the copyright in the article to the Rightsholder. User should check the copyright form and the relevant author rights policy to check whether permission is required. If User is the author of the Work and does require permission for proposed reuse of the Work, User should select 'Author of requested content' as the Requestor Type. The Rightsholder shall not reimburse any fees which User pays for a republication license. If User is the author of the article which User wishes to reuse in User's thesis or dissertation, the republication licence covers the right to include the Version of Record of the article, provided it is not then shared or deposited online. User must include citation details. Where User wishes to share their thesis or dissertation online, they should remove the Version of Record before uploading it. User may include a Preprint or the Accepted Manuscript (after the embargo period) in the online version of the thesis or dissertation, provided they do so in accordance with the Rightsholder's policies on sharing Preprints or Accepted Manuscripts. User may need to obtain separate permission for any third party content included within the article. User must check this with the copyright owner of such third party content. Any online or commercial use of User's thesis or dissertation containing the article, including publication via ProQuest, would need to be expressly notified in writing to the Rightsholder at the time of request and would require separate written permission from the Rightsholder. As well as CCC, the Rightsholder shall have the right to bring any legal action that it deems necessary to enforce its rights should it consider that the Work infringes those rights in any way. For content reuse requests that qualify for permission under the STM Permissions Guidelines, which may be

JOHN WILEY AND SONS LICENSE
TERMS AND CONDITIONS

Jun 22, 2024

This Agreement between Tamaghna Chowdhury ("You") and John Wiley and Sons ("John Wiley and Sons") consists of your license details and the terms and conditions provided by John Wiley and Sons and Copyright Clearance Center.

License Number	5814150552755
License date	Jun 22, 2024
Licensed Content Publisher	John Wiley and Sons
Licensed Content Publication	Advanced Electronic Materials
Licensed Content Title	Stacking Engineered Room Temperature Ferroelectricity in Twisted Germanium Sulfide Nanowires
Licensed Content Author	Atikur Rahman, G.V. Pavan Kumar, Goutam Sheet, et al
Licensed Content Date	Jan 17, 2022
Licensed Content Volume	8
Licensed Content Issue	5
Licensed Content Pages	8
Type of use	Dissertation/Thesis
Requestor type	Author of this Wiley article
Format	Print and electronic
Portion	Full article

Will you be translating?	No
Title of new work	Modulation of optoelectronic properties of layered two-dimensional materials by strain, twist, and dielectric engineering.
Institution name	Indian Institute of Science Education and Research Pune
Expected presentation date	Jul 2024
The Requesting Person / Organization to Appear on the License	Tamaghna Chowdhury
Requestor Location	Mr. Tamaghna Chowdhury Hostel 2 IISER Pune Pune, Maharashtra 411008 India Attn: Mr. Tamaghna Chowdhury
Publisher Tax ID	EU826007151
Total	0.00 USD

Terms and Conditions

TERMS AND CONDITIONS

This copyrighted material is owned by or exclusively licensed to John Wiley & Sons, Inc. or one of its group companies (each a"Wiley Company") or handled on behalf of a society with which a Wiley Company has exclusive publishing rights in relation to a particular work (collectively "WILEY"). By clicking "accept" in connection with completing this licensing transaction, you agree that the following terms and conditions apply to this transaction (along with the billing and payment terms and conditions established by the Copyright Clearance Center Inc., ("CCC's Billing and Payment terms and conditions"), at the time that you opened your RightsLink account (these are available at any time at http://myaccount.copyright.com).

Terms and Conditions

- The materials you have requested permission to reproduce or reuse (the "Wiley Materials") are protected by copyright.
- You are hereby granted a personal, non-exclusive, non-sub licensable (on a stand-alone basis), non-transferable, worldwide, limited license to reproduce the Wiley

SPRINGER NATURE LICENSE
TERMS AND CONDITIONS

Jul 03, 2024

This Agreement between Tamaghna Chowdhury ("You") and Springer Nature ("Springer Nature") consists of your license details and the terms and conditions provided by Springer Nature and Copyright Clearance Center.

License Number	5821401461224
License date	Jul 03, 2024
Licensed Content Publisher	Springer Nature
Licensed Content Publication	Nature
Licensed Content Title	Helical van der Waals crystals with discretized Eshelby twist
Licensed Content Author	Yin Liu et al
Licensed Content Date	Jun 19, 2019
Type of Use	Thesis/Dissertation
Requestor type	academic/university or research institute
Format	print and electronic
Portion	figures/tables/illustrations
Number of figures/tables/illustrations	2
Would you like a high resolution image with your order?	no

Will you be translating?	no
Circulation/distribution	1 - 29
Author of this Springer Nature content	no
Title of new work	Modulation of optoelectronic properties of layered two-dimensional materials by strain, twist, and dielectric engineering.
Institution name	Indian Institute of Science Education and Research Pune
Expected presentation date	Jul 2024
Portions	Figure 3a, Figure 3b, Extended data Figure 5d
The Requesting Person / Organization to Appear on the License	Tamaghna Chowdhury
Requestor Location	Mr. Tamaghna Chowdhury Hostel 2 IISER Pune Pune, Maharashtra 411008 India Attn: Mr. Tamaghna Chowdhury
Billing Type	Invoice
Billing Address	Mr. Tamaghna Chowdhury Hostel 2 IISER Pune Pune, India 411008 Attn: Tamaghna Chowdhury
Total	0.00 USD
Terms and Conditions	

Springer Nature Customer Service Centre GmbH Terms and Conditions

SPRINGER NATURE LICENSE
TERMS AND CONDITIONS

Jul 04, 2024

This Agreement between Tamaghna Chowdhury ("You") and Springer Nature ("Springer Nature") consists of your license details and the terms and conditions provided by Springer Nature and Copyright Clearance Center.

License Number	5821910130490
License date	Jul 04, 2024
Licensed Content Publisher	Springer Nature
Licensed Content Publication	Nature Reviews Materials
Licensed Content Title	Van der Waals heterostructures and devices
Licensed Content Author	Yuan Liu et al
Licensed Content Date	Jul 12, 2016
Type of Use	Thesis/Dissertation
Requestor type	academic/university or research institute
Format	print and electronic
Portion	figures/tables/illustrations
Number of figures/tables/illustrations	2
Would you like a high resolution image with your order?	no
Will you be translating?	no

Circulation/distribution	1 - 29
Author of this Springer Nature content	no
Title of new work	Modulation of optoelectronic properties of layered two-dimensional materials by strain, twist, and dielectric engineering.
Institution name	Indian Institute of Science Education and Research Pune
Expected presentation date	Jul 2024
Portions	Figure 1
The Requesting Person / Organization to Appear on the License	Tamaghna Chowdhury
Requestor Location	Mr. Tamaghna Chowdhury Hostel 2 IISER Pune Pune, Maharashtra 411008 India Attn: Mr. Tamaghna Chowdhury
Billing Type	Invoice
Billing Address	Mr. Tamaghna Chowdhury Hostel 2 IISER Pune Pune, India 411008 Attn: Tamaghna Chowdhury
Total	0.00 USD

Terms and Conditions

Springer Nature Customer Service Centre GmbH Terms and Conditions

The following terms and conditions ("Terms and Conditions") together with the terms specified in your [RightsLink] constitute the License ("License") between you as Licensee and Springer Nature Customer Service Centre GmbH as Licensor. By clicking 'accept' and completing the transaction for your use of the material ("Licensed

SPRINGER NATURE LICENSE
TERMS AND CONDITIONS

Jul 13, 2024

This Agreement between Tamaghna Chowdhury ("You") and Springer Nature ("Springer Nature") consists of your license details and the terms and conditions provided by Springer Nature and Copyright Clearance Center.

License Number	5827121309711
License date	Jul 13, 2024
Licensed Content Publisher	Springer Nature
Licensed Content Publication	Nature
Licensed Content Title	Van der Waals heterostructures
Licensed Content Author	A. K. Geim et al
Licensed Content Date	Jul 24, 2013
Type of Use	Thesis/Dissertation
Requestor type	academic/university or research institute
Format	print and electronic
Portion	figures/tables/illustrations
Number of figures/tables/illustrations	1
Would you like a high resolution image with your order?	no
Will you be translating?	no

Circulation/distribution	1 - 29
Author of this Springer Nature content	no
Title of new work	Modulation of optoelectronic properties of layered two-dimensional materials by strain, twist, and dielectric engineering.
Institution name	Indian Institute of Science Education and Research Pune
Expected presentation date	Jul 2024
Portions	Figure 1
The Requesting Person / Organization to Appear on the License	Tamaghna Chowdhury
Requestor Location	Mr. Tamaghna Chowdhury Hostel 2 IISER Pune Pune, Maharashtra 411008 India Attn: Mr. Tamaghna Chowdhury
Billing Type	Invoice
Billing Address	Mr. Tamaghna Chowdhury Hostel 2 IISER Pune Pune, India 411008 Attn: Tamaghna Chowdhury
Total	0.00 USD

Terms and Conditions

Springer Nature Customer Service Centre GmbH Terms and Conditions

The following terms and conditions ("Terms and Conditions") together with the terms specified in your [RightsLink] constitute the License ("License") between you as Licensee and Springer Nature Customer Service Centre GmbH as Licensor. By clicking 'accept' and completing the transaction for your use of the material ("Licensed

SPRINGER NATURE LICENSE
TERMS AND CONDITIONS

Jul 13, 2024

This Agreement between Tamaghna Chowdhury ("You") and Springer Nature ("Springer Nature") consists of your license details and the terms and conditions provided by Springer Nature and Copyright Clearance Center.

License Number	5827160067021
License date	Jul 13, 2024
Licensed Content Publisher	Springer Nature
Licensed Content Publication	Nature
Licensed Content Title	Chiral twisted van der Waals nanowires
Licensed Content Author	Peter Sutter et al
Licensed Content Date	Apr 22, 2019
Type of Use	Thesis/Dissertation
Requestor type	academic/university or research institute
Format	print and electronic
Portion	figures/tables/illustrations
Number of figures/tables/illustrations	1
Would you like a high resolution image with your order?	no
Will you be translating?	no

Circulation/distribution	1 - 29
Author of this Springer Nature content	no
Title of new work	Modulation of optoelectronic properties of layered two-dimensional materials by strain, twist, and dielectric engineering.
Institution name	Indian Institute of Science Education and Research Pune
Expected presentation date	Jul 2024
Portions	Figure 2
The Requesting Person / Organization to Appear on the License	Tamaghna Chowdhury
Requestor Location	Mr. Tamaghna Chowdhury Hostel 2 IISER Pune Pune, Maharashtra 411008 India Attn: Mr. Tamaghna Chowdhury
Billing Type	Invoice
Billing Address	Mr. Tamaghna Chowdhury Hostel 2 IISER Pune Pune, India 411008 Attn: Tamaghna Chowdhury
Total	0.00 USD

Terms and Conditions

Springer Nature Customer Service Centre GmbH Terms and Conditions

The following terms and conditions ("Terms and Conditions") together with the terms specified in your [RightsLink] constitute the License ("License") between you as Licensee and Springer Nature Customer Service Centre GmbH as Licensor. By clicking 'accept' and completing the transaction for your use of the material ("Licensed

SPRINGER NATURE

Strain engineering of 2D semiconductors and graphene: from strain fields to band-structure tuning and photonic applications

Author: Zhiwei Peng et al
Publication: Light: Science & Applications
Publisher: Springer Nature
Date: Nov 23, 2020

Creative Commons

RightsLink

Exciton physics and device application of two-dimensional transition metal dichalcogenide semiconductors

Author: Thomas Mueller et al
Publication: npj 2D Materials and Applications
Publisher: Springer Nature
Date: Sep 10, 2018

Creative Commons

Stacking Fault Induced Symmetry Breaking in van der Waals Nanowires

Author: Eli Sutter, Hannu-Pekka Komsa, Alexander A. Puretzky, et al
Publication: ACS Nano
Publisher: American Chemical Society
Date: Dec 1, 2022

Quick Price Estimate

This service provides permission for reuse only. If you do not have a copy of the portion you are using, you may copy and paste the content and reuse according to the terms of your agreement. Please be advised that obtaining the content you license is a separate transaction not involving RightsLink.

If credit is given to another source for the material you requested from RightsLink, permission must be obtained from that source.

Note: Individual Scheme and Structure reuse is free of charge and does not require a license. If the scheme or structure is identified as a Figure in the article, permission is required.

Permission for this particular request is granted for print and electronic formats, and translations, at no charge. Figures and tables may be modified. Appropriate credit should be given. Please print this page for your records and provide a copy to your publisher. Requests for up to 4 figures require only this record. Five or more figures will generate a printout of additional terms and conditions. Appropriate credit should read: "Reprinted with permission from {COMPLETE REFERENCE CITATION}. Copyright {YEAR} American Chemical Society." Insert appropriate information in place of the capitalized words.

I would like to...	reuse in a Thesis/Dissertation	**Format**	Print and Electronic
Requestor Type	Non-profit	**Select your currency**	USD - $
Portion	Table/Figure/Micrograph	**Quick Price**	Click Quick Price
Number of Table/Figure/Micrograph	1		

QUICK PRICE CONTINUE

To request permission for a type of use not listed, please contact the publisher directly.

Stacking Fault Induced Symmetry Breaking in van der Waals Nanowires

Author: Eli Sutter, Hannu-Pekka Komsa, Alexander A. Puretzky, et al

Publication: ACS Nano

Publisher: American Chemical Society

Date: Dec 1, 2022

PERMISSION/LICENSE IS GRANTED FOR YOUR ORDER AT NO CHARGE

This type of permission/license, instead of the standard Terms and Conditions, is sent to you because no fee is being charged for your order. Please note the following:

- Permission is granted for your request in both print and electronic formats, and translations.
- If figures and/or tables were requested, they may be adapted or used in part.
- Please print this page for your records and send a copy of it to your publisher/graduate school.
- Appropriate credit for the requested material should be given as follows: "Reprinted (adapted) with permission from {COMPLETE REFERENCE CITATION}. Copyright {YEAR} American Chemical Society." Insert appropriate information in place of the capitalized words.
- One-time permission is granted only for the use specified in your RightsLink request. No additional uses are granted (such as derivative works or other editions). For any uses, please submit a new request.

If credit is given to another source for the material you requested from RightsLink, permission must be obtained from that source.

BACK CLOSE WINDOW

Share and Cite

MDPI and ACS Style

Haley, K.L.; Cloninger, J.A.; Cerminara, K.; Sterbentz, R.M.; Taniguchi, T.; Watanabe, K.; Island, J.O. Heated Assembly and Transfer of Van der Waals Heterostructures with Common Nail Polish. *Nanomanufacturing* **2021**, *1*, 49-56. https://doi.org/10.3390/nanomanufacturing1010005

AMA Style

Haley KL, Cloninger JA, Cerminara K, Sterbentz RM, Taniguchi T, Watanabe K, Island JO. Heated Assembly and Transfer of Van der Waals Heterostructures with Common Nail Polish. *Nanomanufacturing*. 2021; 1(1):49-56. https://doi.org/10.3390/nanomanufacturing1010005

Chicago/Turabian Style

Haley, Kristine L., Jeffrey A. Cloninger, Kayla Cerminara, Randy M. Sterbentz, Takashi Taniguchi, Kenji Watanabe, and Joshua O. Island. 2021. "Heated Assembly and Transfer of Van der Waals Heterostructures with Common Nail Polish" *Nanomanufacturing* 1, no. 1: 49-56. https://doi.org/10.3390/nanomanufacturing1010005

American Physical Society
Reuse and Permissions License

25-Jul-2024

This license agreement between the American Physical Society ("APS") and Tamaghna Chowdhury ("You") consists of your license details and the terms and conditions provided by the American Physical Society and SciPris.

Licensed Content Information

License Number:	**RNP/24/JUL/081621**
License date:	25-Jul-2024
DOI:	10.1103/PhysRevLett.113.076802
Title:	Exciton Binding Energy and Nonhydrogenic Rydberg Series in Monolayer ${\mathrm{WS}}_{2}$
Author:	Alexey Chernikov et al.
Publication:	Physical Review Letters
Publisher:	American Physical Society
Cost:	USD $ 0.00

Request Details

Does your reuse require significant modifications: No

Specify intended distribution locations:	Worldwide
Reuse Category:	Reuse in a thesis/dissertation
Requestor Type:	Academic Institution
Items for Reuse:	Figures/Tables
Number of Figure/Tables:	1
Figure/Tables Details:	Figure 1
Format for Reuse:	Print and Electronic
Total number of print copies:	Up to 1000

Information about New Publication:

University/Publisher:	Indian Institute of Science Education and Research Pune
Title of dissertation/thesis:	Modulation of optoelectronic properties of layered two-dimensional materials by strain, twist and dielectric engineering
Author(s):	Tamaghna Chowdhury
Expected completion date:	Jul. 2024

License Requestor Information

Name:	Tamaghna Chowdhury
Affiliation:	Individual
Email Id:	tamaghna.chowdhury@students.iiserpune.ac.in
Country:	India